Contribution to the study of magnetostrictive energy conversion : from material to device

Otmane Lahyaoui

Par **Otmane LAHYAOUI**

Contribution to the study of magnetostrictive energy conversion : from material to the device

Thèse présentée
pour l'obtention du grade
de Docteur de l'UTC

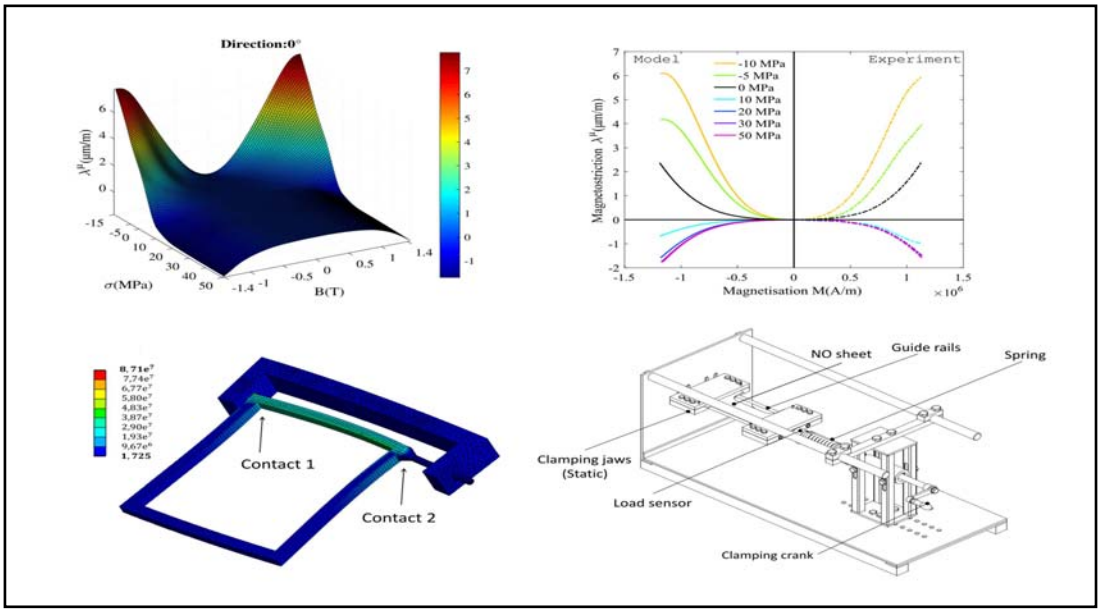

Soutenue le 28 février 2019
Spécialité : Génie Électrique : Unité de recherche en Mécanique - Laboratoire Roberval (FRE UTC - CNRS 2012)

D2472

UNIVERSITÉ DE TECHNOLOGIE DE COMPIÈGNE

DOCTORAL THESIS

CONTRIBUTION TO THE STUDY OF MAGNETOSTRICTIVE ENERGY CONVERSION: FROM MATERIAL TO THE DEVICE

presented by

OTMANE LAHYAOUI

A thesis submitted in fulfillment of the requirements for the degree of Doctor in

ELECTRICAL ENGINEERING

Génie Électrique

Publicly defended at Université de Technologie de Compiègne on February 28, 2019 in front of the jury panel :

Referees	M. Abdelkader Benabou	Université de Lille 1
	M. Xavier Mininger	Université Paris-Sud
Examiners	Mme. Christine Prelle	UTC Compiègne
	M. Jean-Philippe Lecointe	Université d'Artois
Supervisors	M. Vincent Lanfranchi	UTC Compiègne
	M. Nicolas Buiron	UTC Compiègne

Sorbonne Universités, Université de Technologie de Compiègne, CNRS, FRE 2012 Roberval, Centre de recherche Royallieu, CS 60 319, 60203 Compiègne Cedex, France (2015-2018).

﴿ وَقُل رَّبِّ زِدْنِي عِلْمًا ﴾

(سورة طه الآية 114)

« And say: My Lord! Increase me in knowledge »

Holy Qur'an, surat Taha 20:114

« Et dis : ô Mon Seigneur, accroît mes connaissances ! »

Le saint Quoran, sourate Taha 20:114

REMERCIEMENTS/ACKNOWLEDGEMENT

Tout d'abord, je souhaite exprimer ma sincère gratitude à mes directeurs de thèse, M. Vincent Lanfranchi et M. Nicolas Buiron. Je les remercie de m'avoir donné l'occasion de faire mon doctorat au laboratoire Roberval (Equipe M2EI) à l'Univérsité de Technologie de Compiègne. Leurs conseils m'ont aidé tout au long de la réalisation de ce travail, leur expertise, leur ambition et leur optimisme ont fourni une plateforme stable pour entreprendre les travaux de cette thèse.

Je remercie chaleureusement Messieurs Abdelkader Benabou et Xavier Mininger de m'avoir fait l'honneur de rapporter cette thèse. Leurs compétences dans le domaine et leurs conseils avisés ont permis de rendre ce manuscrit plus passionnant et constructif.

J'exprime également ma profonde reconnaissance aux Professeurs Jean-philippe Lecointe et Christine Prelle de m'avoir fait le plaisir de s'intéresser à mes travaux en acceptant de faire partie du Jury de thèse.

Je souhaite de plus remercier doublement le Pr. Jean-philippe Lecointe de m'avoir fait l'honneur de présider le Jury.

J'adresse également mes plus vifs remerciements au Prof. Anouar Belahcen, qui m'a accepté dans son laboratoire pour faire un séjour de recherche en tant que chercheur invité à l'univérsité d'Aalto.

J'ai beaucoup apprécié les interactions avec les membres du laboratoire. Les beaux moments qu'on a passés ensemble pendant ces 3 années resteront gravés à jamais. Merci pour la bonne ambiance de travail. Je souhaite aussi les remercier d'avoir répondu à mes questions lorsqu'ils ont croisé leur domaine de compétence.

Ce m'est un devoir très doux que de remercier, en terminant, les doctorants que j'ai côtoyés au cours d'une si belle expérience. La liste est trop étendue pour que je les nomme tous ici. Un merci tout particulier à mes anciens et récents collègues de bureau : Marie, Olfa, Iman, Zakaria, Youssef et Ahmed pour toutes les discussions et les bons moments passés ensemble.

Dernier point mais non le moindre, ma plus profonde gratitude va à ma famille, mes parents et mes deux frères, pour leur soutien inconditionnel sans lequel ce travail ne serait pas possible. Un grand merci à ma mère Zohra, qui a toujours été une source constante d'amour et d'énergie pour moi.

Et comme disait Victor Hugo : « Et puis, il y a ceux que l'on croise, que l'on connaît

à peine, qui vous disent un mot, une phrase, vous accordent une minute, une demi-heure et changent le cours de votre vie.», je leur dit Merci !

Il s'en faut de beaucoup, cependant, et je ne me le dissimule en aucune façon, que toutes les problématiques soient résolue dans ce travail de thèse. L'exercice auquel je me suis dévoué exige le séquentiellement de plusieurs générations de chercheur : l'effort d'un seul n'y suffit pas.

Lahyaoui Otmane

UTC (Compiègne), Mars 2019

LIST OF PUBLICATIONS

1. Lahyaoui Otmane, Lanfranchi Vincent, Mbengue Serigne Saliou, and Buiron Nicolas "Macroscopic model of magnetostriction based on energy minimization," Mechatronics (MECATRONICS)/17th International Conference on Research and Education in Mechatronics (REM), 2016 11th France-Japan & 9th Europe-Asia Congress on. IEEE, 2016. p. 230-235.

2. Lahyaoui Otmane, Lanfranchi Vincent, and Buiron Nicolas "Magnetostriction deformation of NO ferromagnetic laminated structure in embedded applications," 7th International Symposium on Aircraft Materials (ACMA2018) April 24-26, 2018, Compiègne (France).

3. Lahyaoui Otmane, Lanfranchi Vincent, et Nicolas Buiron "Etude de la résonance mécanique induite par la magnétostriction dans une structure à base de tôles FeSi," Symposium de Genie Electrique (SGE 2018), 3-5 Juillet 2018, Nancy, France.

4. Lahyaoui Otmane, Lanfranchi Vincent, Buiron Nicolas, jean-daniel Chazot, and Christophe Langlois "Investigation on Mechanical Resonance Induced by Magnetostriction in a Structure Based on Si-Fe Sheets," *IEEE Transactions on Magnetics*, 2018, vol. 54, no 12, p. 1-12.

5. Lahyaoui Otmane, Lanfranchi Vincent, Buiron Nicolas, Martin Floran, Aydin Ugur, and Belahcen Anouar "Effect of mechanical stress on magnetization and magnetostriction strain behavior of non-oriented Si-Fe steels at different directions and under pseudo-DC conditions," *International Journal of Applied Electromagnetics and Mechanics Preprint (2019), p. 1-14*.

RÉSUMÉ

Titre : Contribution à l'étude de la conversion d'énergie magnétostrictive : du matériau au dispositif.

Résumé : Dans cette ère du tout électrique, la demande en technologie électrique est en nette augmentation dans plusieurs secteurs (automobile, ferroviaire et aéronautique). Malheureusement, le bruit et les vibrations d'origine magnétiques provenant de ces technologies restent une problématique préoccupante dans ces moyens de transports, perturbant ainsi le confort des passagers. Sachant que le fonctionnement de ces dispositifs électriques comme les moteurs, les générateurs, les transformateurs... repose en grande partie sur les matériaux ferromagnétiques, les principales sources d'émission acoustiques sont la magnétostriction et les forces magnétostatiques. Les travaux de thèse discutés dans ce manuscrit visent à améliorer les connaissances actuelles sur les propriétés magnétiques et magnétostrictives des matériaux ferromagnétiques (NO Fe-3%Si) dans une perspective de compréhension et de maitrise de leur comportement sous différentes sollicitations (contrainte mécanique, effet des fréquences d'excitation...). L'étude présentée offre une approche complète d'investigation partant du matériau jusqu'au dispositif électrique. Un premier volet expérimental présente les caractérisations magnétiques et magnéto-élastiques effectuées sur des tôles magnétiques et sur une structure stratifiée. S'ajoute à cela, une étude sur la résonance mécanique induite par la magnétostriction dans une structure stratifiée ressemblant à un transformateur. Un deuxième volet traite de la modélisation du comportement magnéto-élastique de la magnétostriction et de son intégration dans un outil basé sur la méthode des éléments finis pour permettre de prédire la magnétostriction sur une structure plus complexe qu'une simple tôle. Enfin, une étude impliquant l'interaction de la magnétostriction avec les forces de magnétiques est décrite avec une comparaison des résultats de simulation avec une méthode analytique et avec des mesures expérimentales.

Mots clés : Magnétostriction, forces de Maxwell, matériaux ferromagnétiques, couplage magnéto-élastique, vibromètre laser, caractérisation, structure stratifié, simulation éléments finis, modélisation, analyse modale expérimentale.

ABSTRACT

Title : Contribution to the study of magnetostrictive energy conversion : from material to device

Abstract : In this era of all-electric, the demand for electrical technology is clearly increasing in several sectors (automotive, rail and aeronautics). Unfortunately, magnetic noise and vibrations originating from these technologies remain a worrying issue in these means of transport, thus disrupting passenger comfort. Knowing that the operation of these electrical devices such as motors, generators and transformers...relies largely on ferromagnetic materials, the main noise sources are magnetostriction and magnetic forces. The thesis works discussed in this manuscript aim to improve the current knowledge on the magnetic and magnetostrictive properties of ferromagnetic materials (NO Fe-3% Si) in a perspective of understanding and control of their behavior under different solicitations (mechanical stress, frequencies ...). The presented study offers a complete investigation approach from the material to the electrical device. A first experimental part presents the magnetic and magneto-elastic characterizations carried out on magnetic sheets and on a laminated structure. A study on the magnetic resonance induced by the magnetostriction including on an experimental modal analysis is presented as well. A second part deals with the modeling of the magneto-elastic behavior of magnetostriction and its integration into a finite element tool to predict the impact of the magnetostriction on a more complex structure than simple electrical sheet. Finally, a study of a possible interaction of magnetostriction with magnetic forces is described with a comparison of simulation results with an analytical method and experimental measurements.

Keywords : Magnetostriction, Maxwell forces, ferromagnetic materials, magneto-elastic coupling, laser vibrometer, characterization, laminated structure, finite element simulation, modeling, experimental modal analysis, homogenization methods.

CONTENTS

LIST OF FIGURES

List of Tables

NOTATIONS

List of Symbols

Symbol	Meaning
E_{exch}	Exchange energy [J]
E_{ani}	Magneto-crystalline anisotropy energy [J]
E_{an}	Macroscopic anisotropy energy [J]
E_{ms}	Magneto-static energy [J]
E_z	Zeeman energy [J]
E_σ	Magneto-elastic energy [J]
E_d	Demagnetizing field energy [J]
$\overrightarrow{M}, M$	Magnetization [A/m]
M_s	Saturation magnetization [A/m]
K_1, K_2	Anisotropy constants [J/m^3]
$\overrightarrow{H}, H$	Magnetic field [A/m]
s	Spontaneous strain
M_r	Remanant magnetization [A/m]
H_c	Coercive field [A/m]
B	Magnetic induction [T]
$I, i/u, U$	Current [A] and voltage [V]
M_{anh}	Anhysteretic magnetization [A/m]
k	Boltzmann constant
W	Work

Symbol	Meaning
T	Temperature [K]
m	Local magnetic moment [A/m^2]
M_{rev}, M_{irr}	Reversible and irreversible magnetization [A/m]
$\overline{\overline{N_d}}$	Demagnetizing field tensor
$\overrightarrow{H}^{\sigma}$	Configuration demagnetizing field [A/m]
$\overline{\overline{T}}^{Maxwell}$	Maxwell stress tensor [Pa]
$\overline{\overline{I}}$	Identity tensor
$\mathfrak{R}$	Magnetic reluctance [H^{-1}]
S	Surface [m^2]
N	Number of turns
E	Young modulus [MPa]
G	Shear modulus [MPa]
R	Transformation matrix
f	Frequency [Hz]
C	Torque [N.m]
p	Screw pitch
K	Stiffness matrix [N/m]

List of Greek letter

Symbol	Meaning
$\alpha_1, \alpha_2, \alpha_3$	Direction cosines between magnetization and crystallographic axes
θ, ϕ	Angles [rad]
μ_0	Permeability of free space ($4\pi 10^{-7}$) [H/m]
$\overline{\overline{\sigma}}, \sigma$	Stress [Pa]
$\overline{\overline{\sigma}}^{Maxwell}$	Maxwell stress tensor [Pa]
$\overline{\overline{\varepsilon^{\mu}}}, \varepsilon^{\mu}, \varepsilon$	Strain
$\lambda_{100}, \lambda_{111}$	Saturation magnetostrictions in the $< 100 >$and $< 111 >$directions
λ_s	Saturation magnetostriction
λ	Magnetostrictive strain
$\beta_1, \beta_2, \beta_3$	Direction cosines between saturation magnetostriction λ_s and crystallographic axes
$\gamma_1, \gamma_2, \gamma_3$	Direction cosines between stress σ and crystallographic axes
ε^{el}	Elastic strain
ϕ	Magnetic flux [Wb]
μ	Magnetic permeability [H/m]
μ_r	Magnetic relative permeability [H/m]
ω	Angular velocity [rad/s]
$\mu(\alpha, \beta)$	Distribution function of Preisach
χ_0, χ_i	Initial magnetic susceptibility
ν	Poisson's ratio
ρ	density [kg.m^{-3}]

Abbreviations

Symbol	Meaning
SST	Single Sheet Tester
NO	Non-oriented material
GO	Grain-Oriented material
EBSD	Electron Back Scattering Diffraction
RD	Rolling direction
TD	Transverse direction
FE	Finite Element
2D	Two dimension
LDV	Laser Doppler Vibrometry
He-Ne	Helium-Neon
SP-S	Single Point Serie
BS	Beam Splitter
RB	Reference Beam
OB	Object Beam
SEU	Supply and Evaluation Unit
AEM	Elastomer
DOF	Degree of Freedom
FRF	Frequency Response Function
PWM	Pulse Width Modulation

INTRODUCTION

Context and technological issues

For several years, electricity consumption has been growing steadily. This situation is due to new uses of electricity (electro-mobility, building techniques and appliances), which replace or complement those of other energy sources such as oil and natural gas in the field of heating and mobility. Electricity will therefore become more important in the future for energy supply and thus also for the economy and society. Having electricity available at all times has become a matter of course, but it is easy to forget that this complex task cannot be carried out without the electricity transmission network. Indeed, electricity grids play a key role in this supply. Among the electrical systems involved in electrical transport there are electrical transformers. Transformers are essential components in the transmission, distribution and conversion of electrical energy. Today, in the age of the all-electric era, they are increasingly used in electric means of transport such as trains and airplanes (figure 0.0.1).

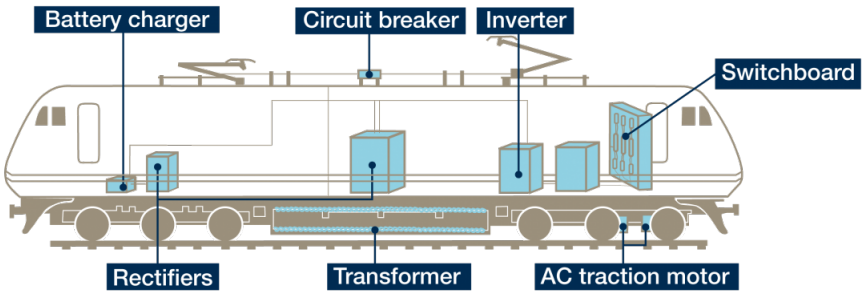

Figure 0.0.1: *Transformer in train locomotive (VonRoll website).*

Unfortunately, these electromagnetic devices can generate, through their operation, very annoying acoustic noise, which causes noise pollution that can disturb passengers in all circumstances. The main sources of noise in such system are traditionally classified into two types:

- Mechanical sources

- Electromagnetic sources

However, the noise from electromagnetic sources is the most typical noise component of transformers and electrical machines. Besides the contribution of Laplace forces in conductors (in the coils), electromagnetic noise in these electrical devices is caused mainly by magnetostriction (in the ferromagnetic core) and Maxwell forces (near the air gap). As a consequence, noise and vibration are inherent characteristics of electrical devices and can not be completely eliminated. This work focuses on vibration from the transformer core considered as the dominant sources of noise in transformer.

The transformer core is made of stacked electrical steels which are fabricated from ferromagnetic material. Consequently, when they are magnetized, a deformation takes place creating undesirable vibration of the core called magnetostriction. In fact, ferromagnetic materials constitute the main elements in magnetic circuits, therefore, they must satisfy several requirements, with priorities that depend on the specific application, such as high magnetic permeability, low hysteresis losses and so on. The demand for smaller, lighter, more powerful and more efficient electrical machines is the driving force for the development of efficient electrical steel sheets. The most common alloys are iron, cobalt (aerospace industry), Nickel and some rare earths. However, because of their good quality-price ratio, iron alloys are by far the most used. In the context of this thesis, we will be interested in the study of 3%Si-Fe non-oriented grain materials. Non-oriented electrical steel sheets are incorporated into a wide range of equipment, from the simplest domestic appliances to hybrid and pure electric train. However, their magnetic and magnetostrictive properties can be harmfully influenced by mechanical stress whose sources can be various and varied (manufacturing process, cutting, assembly ...). In the work of this thesis, we seek to understand this magneto-elastic coupling and identify its effect on the magnetic and magnetostrictive behavior of the material.

In addition to the magnetostriction, following the assembly of magnetic circuit, small air gaps are involuntarily created, which gives rise to the creation of magnetic forces of Maxwell type. These forces are attractive and can be present in the plane of the sheets (assembly UI, EI ..) or out of plane (overlaps of sheets at corners). As a result, the noise generated by Maxwell forces is added to that of magnetostriction. Knowing that the two phenomena are quadratic functions of the magnetization, the determination of the main source of vibration is often difficult as they are always present and not separable in a magnetic circuit. The study presented here initially concerns magnetostriction alone and then its interaction with Maxwell forces later on. Then, we will see that the magnetostriction can interact with the dynamic behavior of a laminated structure (transformer type) and can be at the origin of a mechanical resonance.

Scientific challenges and objectives

The study presented here concerns the magneto-elastic coupling which reflects the stress effect on the magnetostrictive deformation and the magnetic properties of ferromagnetic materials. This coupling is very difficult to model and especially to observe and explain the mechanism that governs it. Another difficulty lies in the state of stress applied, a material subjected to a multi-axial stress (as in rotating machine) differs from that of a material subjected to uniaxial loading. Since the focus in this work is on transformer application, the stress state applied will be mainly uniaxial.

In addition to the stress effect, there is the anisotropy effect introduced by the manufacturing process of the materials. Whether it is a magnetic or magnetostrictive anisotropy, the description of this effect requires huge experimental means (e.g. many samples cut in different directions) which introduces a technical complexity in the modeling. To the difficulty of modeling the two phenomena in a distinct way is added that of modeling both phenomena together. That is to say, the response of the materials in different directions of magnetization (anisotropy effect) and under uniaxial loading (stress effect). The coupling of anisotropy and the stress effect has been less studied and constitute one of the main topic of this thesis.

For this investigation not to be limited to the study of the material alone, it seemed necessary to extend it to a device that is closer to an industrial application (transformer). This strategic choice involves an additional difficulty that lies in considering other phenomena in addition to the previously mentioned effects, of which the main ones are: the cutting effect, the assembly, the dynamic behavior, the magnetic forces. We took care for decreasing as much as possible the cutting effect by adopting a cutting of ferromagnetic sheets by water jet to generate the least residual stresses and a clean cut. For the others, each effect has been studied in a targeted and precise way. Besides, a finite element tools is developed to validate on a the ferromagnetic structure, in addition to magnetostriction, some of these effects such as anisotropy and magnetic forces.

The main objective of this thesis is to gain a better understanding of the electromagnetic phenomena that cause vibration and noise, mainly due to magnetostriction and then to Maxwell forces. This step is essential to then allow the creation of model and software tools to lead to efficient methods of vibration and noise reduction on sets of electromagnetic components (transformers or others ...).

Scope of the thesis work

The thesis focuses on the contribution to the development of a model for predicting magnetostrictive deformation, considered as one of the causes of electromagnetic noise from electromechanical devices. These noises can also come from the Maxwell forces present in the gap (transformer and electric motor). This work takes into account the

interaction between the two phenomena in terms of vibrations generated on a laminated structure approaching more a transformer core and seeks to establish solutions that can be applied as early as the assembly stage. The present dissertation is divided into four chapters:

In a first chapter, a state of the art relating to magnetic materials is presented as well as the theory that governs the magnetization and magnetostriction processes within these materials. Then, the influence of mechanical stress on these processes is described at microscopic and macroscopic scales. Also, the different sources of mechanical stresses are discussed. Finally, the different modeling approaches used to predict magnetostriction are exposed.

In the second chapter, the magneto-elastic behavior of the plates in 3%Si-Fe electrical steel is characterized. Measurements under mechanical stress are made on different samples cut in several directions relative to the rolling direction (0°, 10°, ..., 90°) to take into account the effect of magnetic and magnetostrictive anisotropy. Then, the results of these measurements are analyzed and the variations of the magnetic and magnetostrictive properties of the material are discussed. Moreover, the studied model is presented and the consideration of the mechanical stresses effect in addition to the anisotropy is detailed. The different assumptions and parameter identification operations are illustrated. Finally, the modeling results are compared to the measurements and allow us to conclude on the robustness of the model.

In the third chapter, a laminated structure without gaps is designed from the same material previously characterized. Magnetic and magnetostrictive measurements under mechanical stresses and under two types of excitations (voltage or imposed current) are carried out. Then, two methods of measuring the magnetostriction deformation are confronted. The limits of each method are discussed. Moreover, a second structure integrating this time air gaps is set up to study the interaction between the magnetostrictive deformation and the Maxwell forces. The model already integrated in the finite element tool is developed to take into account also the influence of the Maxwell forces generated in the air gap in addition to the magnetostrictive deformation. The simulation results are initially compared with results from an analytical approach and then with measurements made on the structure.

In the fourth chapter, a study of magnetostriction-induced mechanical resonance in a laminated structure is presented. A model of the studied structure is developed including the contact effect between the sheets. Finite element calculations lead to frequencies and eigen modes. An experimental modal analysis is performed and the measurement results are compared to the simulation results. To further approach the behavior of the structure (in frequencies and modes), a numerical model based on the homogenization principle is developed. Finally, mechanical resonance due to magnetostriction is studied and the results are described.

“What one man calls God, another calls the laws of physics.”

(Nicolas Tesla)

CHAPTER 1

MAGNETOSTRICTION AND MAGNETO-ELASTIC COUPLING

1.1 Introduction

This introductory chapter will focus on literature review related to magnetic materials. For enabling the readers who might not be familiar with the theory behind, all basic notions are detailed as well as magnetization and magnetostriction process. Then, an emphasis is put on the influence of mechanical stress on magnetization and magnetostriction behavior of magnetic materials, from microscopic and macroscopic points of view. Next, the main sources of stress are presented and an overview of measurement techniques is described. Finally, different modeling approaches found in literature are detailed.

1.2 Basic notions on ferromagnetic materials

For a good understanding of the specific characters of ferromagnetic materials, we present in this part in the simplest possible way the basic principles that govern their behavior.

Atomic moments in ferromagnetic materials such as Iron (Fe), Nickel (Ni) and Cobalt (Co) present very strong inter-atomic interactions (figure 1.2.1a). These quantum exchange interactions give birth to parallel or anti-parallel alignment of atomic magnetic moments which leads to spontaneous magnetization even in absence of external magnetic field [113]. The parallel alignment of magnetic moments in one direction is subdivided into small regions (microscopic) within a material, known as «domains» (Pierre Weiss 1907 [119]) in order to minimize the magneto-static stray field energy of the sys-

tem (figure 1.2.1b). Adjacent domains are separated by domain boundaries or walls called Bloch walls (in-plane rotation of walls) or Neel walls (out of plane rotation of walls) in which the direction of the magnetic moment gradually and continuously changes from one domain to adjacent domains (figure 1.2.1c).

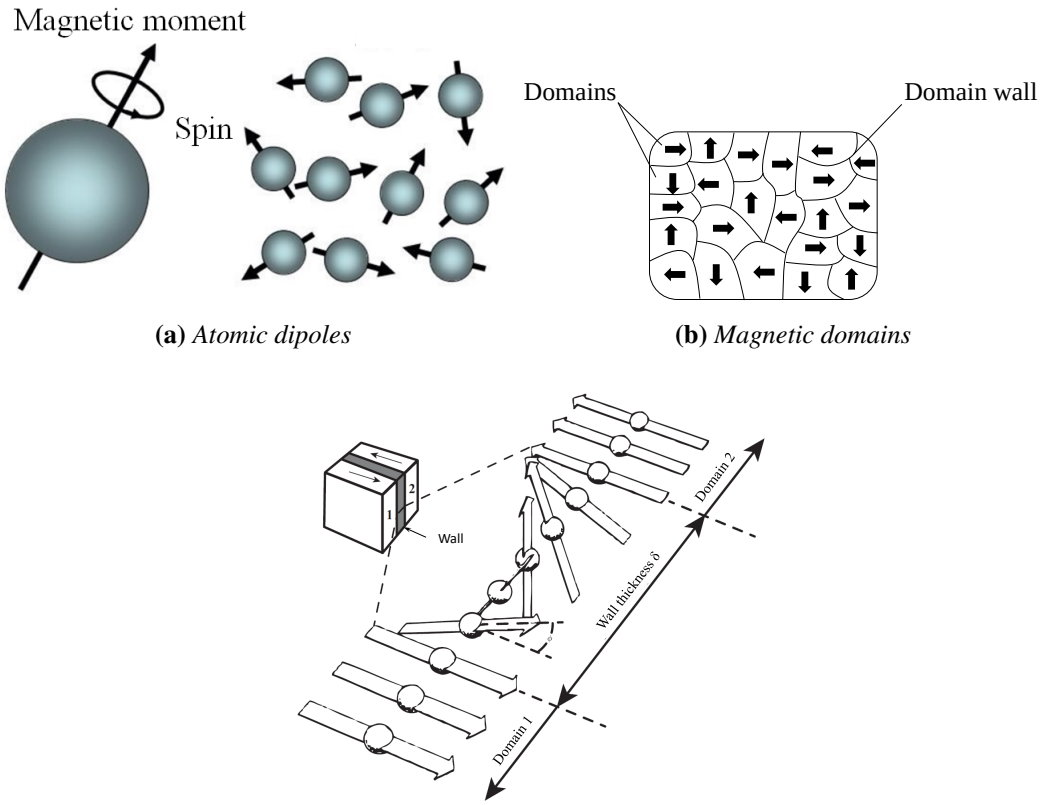

(a) *Atomic dipoles*

(b) *Magnetic domains*

(c) *Domain wall*

Figure 1.2.1: *Description of atomic dipoles, domains and domain walls in ferromagnetic materials.*

The state of magnetic equilibrium of the ferromagnetic material can be explained by the competition of different energy terms (microscopic scale):

$$E_{total} = E_{exch} + E_{ani} + E_d + E_\sigma + E_z \tag{1.2.1}$$

- E_{exch} means Exchange energy
- E_{ani} means Magneto-crystalline anisotropy energy
- E_d means Demagnetizing field energy

- E_z means Zeeman energy
- E_σ means Magneto-elastic energy

All the energy terms presented thereafter are energy densities (energy per volume unit).

This total energy depends on the magnetization state of the material, and always tends towards an equilibrium state with a minimum energy value. A brief description of the main energy terms will be explained here but for more detailed description, you can see [65] and [120]. Every magnetic domain is characterized by its magnetization vector that can be written as follows:

$$\overrightarrow{M} = M_s \overrightarrow{\alpha} = M_s{}^t[\alpha_1, \alpha_2, \alpha_3] = M_s \begin{pmatrix} \sin(\theta)\cos(\phi) \\ \sin(\theta)\sin(\phi) \\ \cos(\theta) \end{pmatrix} \tag{1.2.2}$$

with:

$$\overrightarrow{||M||} = M_s \tag{1.2.3}$$

$\overrightarrow{\alpha}$ is a unity vector whose direction is defined by its direction cosines α_1, α_2 and α_3 ($\alpha_1^2 + \alpha_2^2 + \alpha_3^2 = 1$), figure 1.2.2.

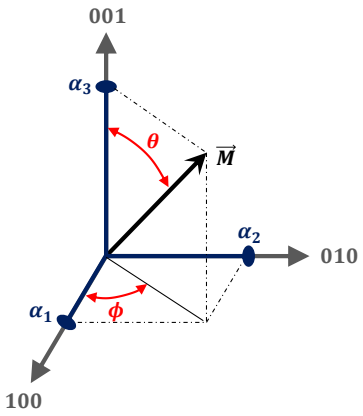

Figure 1.2.2: *Magnetization vector in the cubic crystal reference frame.*

Exchange energy

The exchange energy quantifies the exchange interactions between neighboring atomic spins which align moments:

$$E_{exch} = A.(\overrightarrow{\overline{grad}\,\alpha})^2 \tag{1.2.4}$$

Where A is the exchange constant, depending on the material. This energy is equal to zero when spatial variations of magnetization direction are null. Hence, this energy is generally supposed to be negligible in a magnetic domain, but plays a role in the domain wall energy, which mainly results from exchange and anisotropy energies.

Anisotropy energy

Figure 1.2.3 shows that the work ($W = \int \vec{M} d\vec{H}$) required to saturate the magnetization depends on the crystallographic direction. It is therefore possible to identify «easy directions». This extra energy obeys to material symmetries. Hence, for a cubic structures, a two parameters equation is generally used:

$$E_{ani} = K_1(\alpha_1^2\alpha_2^2 + \alpha_2^2\alpha_3^2 + \alpha_3^2\alpha_1^2) + K_2(\alpha_1^2\alpha_2^2\alpha_3^2) \tag{1.2.5}$$

Where $\alpha_i\,(i = 1,2,3)$ corresponds to the local magnetization direction with respect to the crystallographic direction of the material ($\alpha_1 = cos(\vec{M}, < 100 >), \alpha_2 = cos(\vec{M}, < 010 >), \alpha_3 = cos(\vec{M}, < 001 >)$) . The anisotropy coefficients K_1 and K_2 are energy densities by volume (For Iron (Fe) $K_1 = 4,8.10^4 J/m^3$ and $K_2 = 5.10^3 J/m^3$). They decrease very quickly with temperature and can vary according to the metallurgical preparation and in case of application of large stresses on the material.

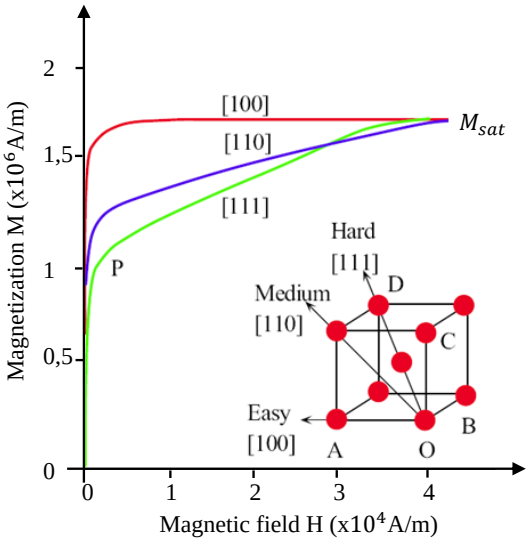

Figure 1.2.3: *Magneto-crystalline anisotropy: Cubic crystal lattice of iron showing the easy magnetization directions (< 100 >), the medium (< 101 >) and the hard magnetization directions (< 111 >) [61].*

Demagnetizing field energy

By contrast to the exchange energy (interaction of narrowed atoms), the demagnetizing field energy corresponds to the interaction between magnetic moments of distant atoms. These interactions tend to cancel the overall polarization of the material. In other words, avoid the alignment of magnetic moments in the same direction, hence the name of demagnetizing energy [47]. Therefore, a demagnetizing field $\overrightarrow{H_d}$ linked with the magnetization $\overrightarrow{M}$ is defined (equation (1.2.6)). This field created by and opposite to magnetization ($\overrightarrow{H_d} = -\alpha\overrightarrow{M}$, $\overrightarrow{\alpha}$ is the direction vector), tends to demagnetize the material.

$$\overrightarrow{\nabla}.\overrightarrow{H_d} = -\overrightarrow{\nabla}.\overrightarrow{M} \tag{1.2.6}$$

If we consider the $\overrightarrow{H}$ as the magnetic field modified by the material presence, the work of magnetization $\overrightarrow{M}$ can be written as follow:

$$W = \int \mu_0 \overrightarrow{H}\, d\overrightarrow{M} = \int \mu_0 \overrightarrow{H_0} d\overrightarrow{M} + \int \mu_0 \overrightarrow{H_d} d\overrightarrow{M} \tag{1.2.7}$$

where $\overrightarrow{H_0}$ is the external magnetic field and $\overrightarrow{H_d}$ is the magnetic field due to the material magnetization ($\overrightarrow{H_d} = -\alpha\overrightarrow{M}$). Thus equation (1.2.7) becomes:

$$\begin{array}{rc} W = & \int \mu_0 \overrightarrow{H_0} d\overrightarrow{M} - \int \mu_0 \alpha \overrightarrow{M} d\overrightarrow{M} \\ = & \int \mu_0 \overrightarrow{H_0} d\overrightarrow{M} - \frac{\mu_0}{2}\alpha M^2 \\ = & \int \mu_0 \overrightarrow{H_0} d\overrightarrow{M} + \frac{\mu_0}{2}\overrightarrow{H_d}\overrightarrow{M} \end{array} \tag{1.2.8}$$

Consequently, the demagnetizing field energy is defined as:

$$E_d = -\int \mu_0 \overrightarrow{H_d} d\overrightarrow{M} = -\frac{1}{2}\mu_0 \overrightarrow{H_d}.\overrightarrow{M} \tag{1.2.9}$$

Zeeman energy

This potential energy reflects the interaction between the external magnetic field ($\overrightarrow{H}$) and the magnetization of the material, different from the demagnetizing field energy.

$$E_z = -\mu_0.\overrightarrow{H}.\overrightarrow{M} \tag{1.2.10}$$

Magneto-elastic energy

As its name indicates, this energy comes from the interaction between the elastic and magnetic properties of the material. In fact, it is known that the deformation of the magnetic material, whatever its origin (magnetic forces or following the application of mechanical stress) induces a variation of its anisotropy coefficients [112] and hence, a

variation of the magnetization state of the material. In other words, there is a magneto-crystalline anisotropy energy induced by crystal. Such energy can be described as follows:

$$E_\sigma = -\overline{\overline{\sigma}} : \overline{\overline{\varepsilon^\mu}} \tag{1.2.11}$$

Where $\overline{\overline{\varepsilon^\mu}}$ is the magnetostrictive strain tensor and $\overline{\overline{\sigma}}$ the applied stress tensor. In the case of a material with cubic symmetry, three parameters are sufficient to describe the magnetostriction deformation. Moreover, assuming the hypothesis of isochoric deformation [47], the number of these parameters is reduced to two (λ_{100} and λ_{111}). Thus, the magnetostriction deformation is written in the crystallographic reference (CR: [100],[010],[001]):

$$\overline{\overline{\varepsilon^\mu}} = \frac{3}{2}\begin{pmatrix} \lambda_{100}(\alpha_1^2 - \frac{1}{3}) & \lambda_{111}\alpha_1\alpha_2 & \lambda_{111}\alpha_1\alpha_3 \\ \lambda_{111}\alpha_1\alpha_2 & \lambda_{100}(\alpha_2^2 - \frac{1}{3}) & \lambda_{111}\alpha_2\alpha_3 \\ \lambda_{111}\alpha_1\alpha_3 & \lambda_{111}\alpha_2\alpha_3 & \lambda_{100}(\alpha_3^2 - \frac{1}{3}) \end{pmatrix}_{CR} \tag{1.2.12}$$

where λ_{100} and λ_{111} denote both magnetostrictive constants, λ_{100} (or λ_{111}) being equal to the deformation of magnetostriction measured in the direction $< 100 >$ (or $< 111 >$) of a single crystal when it is magnetized at saturation in that direction.

All energy terms constituting the total energy E_{total} (equation (1.2.1)) have been discussed. The equilibrium state of the material is the result of this total energy. There is an interaction between all the different contributing energy terms and they are balanced with each other to ensure a minimal total energy. Any change such as a variation in the applied external magnetic field, an applied external stress or a temperature, disrupts the equilibrium and causes a change in these factors. Thus, once again all energy terms are competing to achieve a new balance and keep the total energy minimum.

Magnetic domains formation

Domains distribute themselves to minimize the magneto-static energy (equation (1.2.9) and equation (1.2.10)) due to the leakage field during the demagnetization process as shown in figure 1.2.4. At the demagnetized state, domains re-arrange themselves with narrower domains and flux-closure domains arise to provide return paths for the spontaneous magnetization of the main domains.

Imagine for example the simple model shown in figure 1.2.4, the configuration (a) minimizes exchange energy but magneto-static energy is important due to distance between the north and south poles. Hence, there is a single domain material and large stray fields are introduced in the surrounding air. The formation of domain walls separating two anti-parallel bar domains are shown in figure 1.2.4 (b)-(c), they are called 180° domain walls [18]. They correspond to the boundaries where the magnetic moments change their direction and alignment, leading to an increase of exchange energy,

however, the magneto-static energy is greatly decreased. Finally, additional domains named closure domains appear (classified as 90°domain wall) and cancel the magneto-static energy by removing the poles (figure 1.2.4 (d)-(e)). The appearance of the closure domains takes place early in the domain formation process and disappears late in the saturation process.

Weiss domains arise spontaneously from the competition between the exchange energy and the magneto-static energy, which oppose to the appearance of positive and negative poles. The pattern in figure 1.2.4 (e) favors reaching the minimum energy state explained in the previous paragraph.

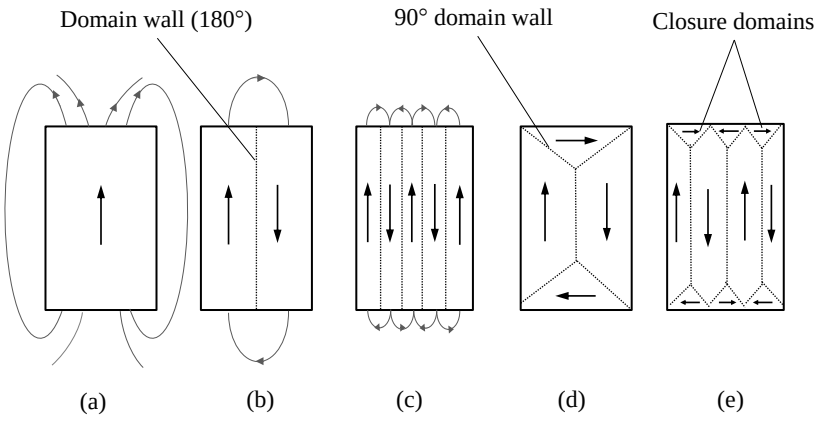

Figure 1.2.4: *Magnetic domains formation at the demagnetized state with the aim of the minimum energy level.*

1.3 Magnetization process

In the absence of external field $H = 0$ (figure 1.3.1, configuration a), the domains are oriented in such a way that the macroscopic magnetization of the material is equal to zero (minimum energy principle). This magnetization is aligned spontaneously in the direction of easy magnetization (figure 1.2.3). When a magnetic field is applied, the magnetic equilibrium is modified by movement of the magnetic walls (figure 1.2.1c) and two distinct mechanisms of magnetization appear: first, by size change of the domains, and then by rotation of the magnetization inside domains. At lower field, the domains lying more or less in the direction of the applied field start to grow at the expense of other domains until most favorably oriented domains remains when the external field is high enough (figure 1.3.1, configuration b). Further increase in the magnetic field causes domains to rotate and align parallel to the applied field (figure 1.3.1, configuration c and d). At this stage the material is saturated as shown in figure 1.3.1, configuration d. It is worth noticing that during the growth of magnetic domain there has been no change in

the magnitude of the local magnetization, only the domain walls move and the external field provides the force required for this movement.

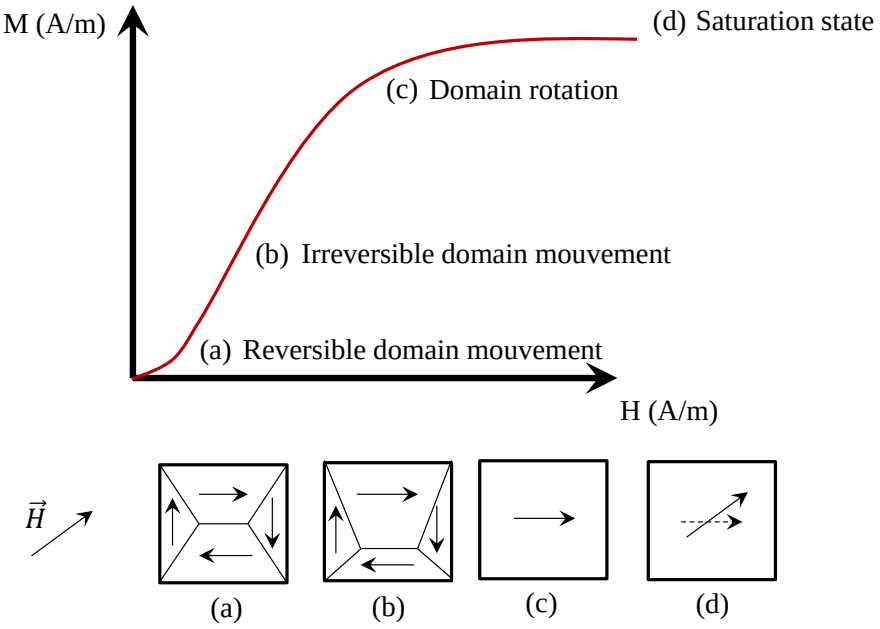

Figure 1.3.1: *Magnetization process (first magnetization curve) and corresponding domain configurations (microscopic mechanism).*

It is possible to link the microscopic mechanisms of wall movement and rotation with the magnetization process seen on a macroscopic scale. This is illustrated in figure 1.3.1. Point c on the figure corresponds to the "bend" of the magnetization curve which announces the beginning of magnetization rotation in the domains. In this zone, two magnetization mechanisms are superimposed: wall movement and magnetization rotation. From practical point of view, it is an interesting area because we obtain a strong magnetization without having to push the magnetic field to higher magnitude. That is why, the operating point of the electric machines (transformer and rotating machines) is often found in this bend where the two magnetization mechanisms are superimposed.

Magnetic Hysteresis

The hysteresis loop express a non linear and irreversible relationship between the magnetization M and the applied magnetic field H. This irreversibility is essentially linked with:

- For low frequency: the pinning of the magnetic domain walls to the material defects. The unpinning induces high speed motion of the domain wall, and generates

micro Eddy currents.

- For high frequency: macroscopic Eddy currents induced by magnetic field variations, which lead to an additional dissipation.

A typical hysteresis loop for a ferromagnetic material is shown in figure 1.3.2. The shape of this loop depends also on the shape of the excitation wave of magnetic field.

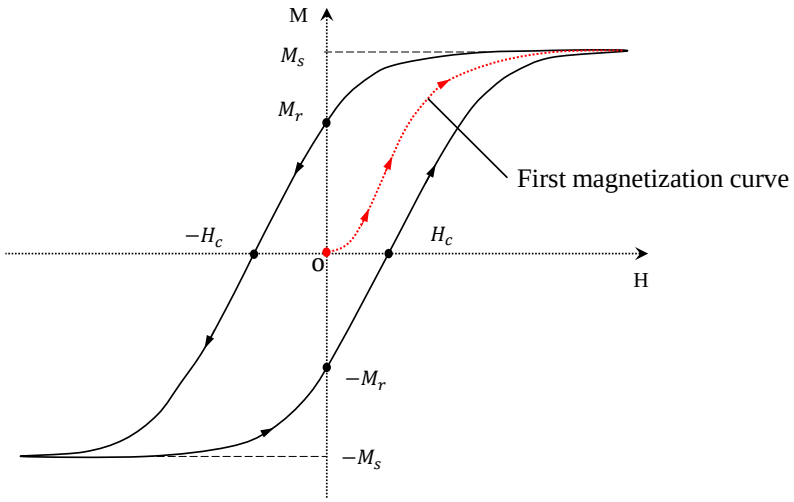

Figure 1.3.2: *Typical hysteresis loop of a ferromagnetic material.*

Point o (origin) presents the demagnetized state of the material, with increasing applied field H in positive direction, the favorable domains of the material start to increase in the direction of H as shown in figure 1.3.2 from o to M_s. With increasing external field, the magnetization M in the material reaches a saturated state denoted M_s, by aligning all domains in the direction of H. Further increase in the external field produce no significant change in the magnetization M. The first curve from the demagnetized state (point o) to the saturation point M_s is called «first magnetization curve» of the M(H) hysteresis. After saturation, when the external field H is reduced to zero the magnetization M does not reduce to zero but it retains in a remanent state which is known as remanence (M_r). To demagnetize the material, that means to reduce M_r to zero, the external field H has to be applied in the negative direction. This negative value of H where the magnetization M becomes zero is described by H_c and is called coercive field or coercivity. A further increase of H in the negative direction can saturate the material but in the opposite direction (-M_s). If now the negative H field reduces to zero, the material achieves again a remanent magnetization (-M_r). The hysteresis loop traced out from M_s to $-M_s$ is called the major hysteresis loop. If the field H is not sufficient to saturate the sample, the formed loop is called minor loop.

Barkhausen noise

As mentioned above, the magnetization process in a ferromagnetic material is governed by the movement of the Weiss domains which are separated by Bloch walls. Subjected to a variable magnetic field H, the magnetic structure of this material changes, accompanied by Bloch wall movements. These movements are at the origin of the creation of a "magnetic noise" called Barkhausen noise (figure 1.3.3). When the Bloch walls meet a micro-structural defect, they tend to be retained, we speak then of anchoring (figure 1.3.3, configuration 2). When released, the wall generates an electromagnetic wave (Barkhausen noise) and discontinuities in the hysteresis cycle appear (stair shape in figure 1.3.3). These discontinuities can be observed as electrical voltage pulses across an induction circuit surrounding the ferromagnetic sample. Depending on the microstructure and the state of stress in the material, wall movements are more or less facilitated or slowed down, and generate very different noises.

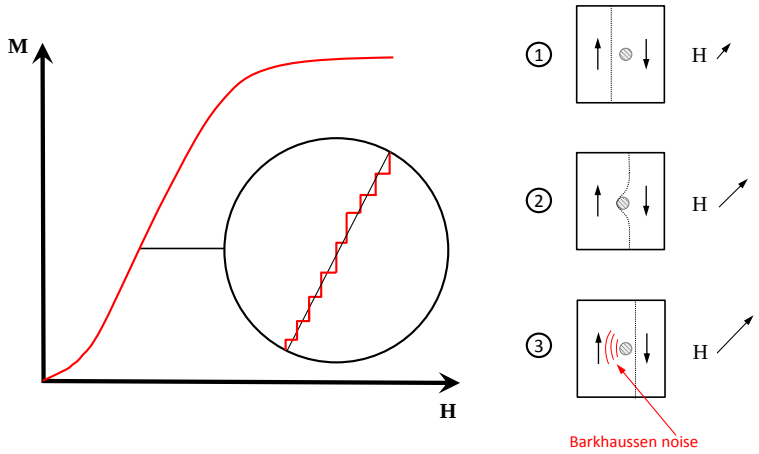

Figure 1.3.3: *Generation of Barkhausen noise due to Bloch wall movement.*

1.4 Magnetostriction process

In 1942, the physicist Joule discovered that an iron rod subjected to a longitudinal magnetic field extended along this field, at the same time it contracted transversely, as under the effect of a mechanical traction. He called this phenomenon magnetostriction [57]. In general sense of term, magnetostriction can be presented as the set of relations linking the mechanical state of a material to its magnetic state. Looking at microscopic scale, besides saturation magnetostriction λ_s we distinguish two principal phenomena:

- Spontaneous magnetostriction λ_0
- Joule magnetostriction

Spontaneous magnetostriction λ_0

When the temperature decreases below the Curie point, the material becomes ferromagnetic and magnetic domains are formed. At the same time, a spontaneous strain appears corresponding to spontaneous magnetostriction λ_0. In the para-magnetic phase, above the Curie temperature, the material is composed of a disordered spherical regions of isotropic solid, figure 1.4.1 (configuration (a)). When the material becomes ferromagnetic and ordered, this sphere becomes ellipsoids (figure 1.4.1, configuration (b)). This transition is accompanied with a spontaneous strain of the domain s. According to author in [17] the change in length with respect to the magnetization direction with an angle θ can be written as follow:

$$s(\theta) = s\cos^2(\theta) \tag{1.4.1}$$

The sum of the spontaneous magnetostriction of each domains in the material corresponds to the total spontaneous magnetostriction λ_0 :

$$\begin{aligned} \lambda_0 &= \int_0^{\pi/2} s\cos^2(\theta)\sin(\theta)d\theta \\ \lambda_0 &= s\int_0^1 x^2 dx \quad (x = \cos(\theta)) \\ \lambda_0 &= \frac{s}{3} \end{aligned} \tag{1.4.2}$$

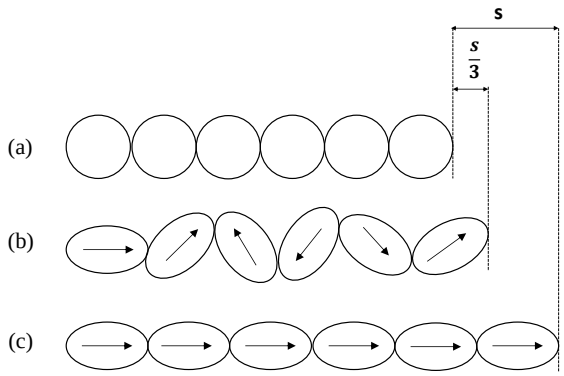

Figure 1.4.1: *Sphere used to model ferromagnetic material: (a) A disorder behavior in para-magnetic regime (above Curie temperature). (b) Ordered behavior in ferromagnetic regime (below Curie temperature). (c) ferromagnetic regime with completely aligned domains with respect to the magnetic field.*

Saturation magnetostriction λ_s

When a magnetic field is applied, an increase in the length of the material is observed due to the rotation of domains in the field direction producing the total strain s (fig-

ure 1.4.1, configuration (c)). A further increase in the magnetic field leads to magnetization saturation state and consequently the magnetostriction saturation λ_s is reached. The latter can be compared to strain in demagnetized state from the relation:

$$\lambda_s = s - \lambda_0 = \frac{2}{3}s \tag{1.4.3}$$

At saturation all domains are completely aligned with the direction of the magnetic field (figure 1.4.1, configuration (c)). The combination of equation (1.4.2) and (1.4.3) gives us the saturation magnetostriction for an isotropic material (with no preferred orientation of the crystal axis) with respect to the applied field with an angle θ:

$$\lambda_s(\theta) = \frac{3}{2}\lambda_s(\cos^2(\theta) - \frac{1}{3}) \tag{1.4.4}$$

Magnetostriction of single crystal

Magnetostriction strain of a single crystal can be obtain by:

$$\lambda = \overrightarrow{n}.\overline{\overline{\varepsilon^{\mu}}}.\overrightarrow{n} \tag{1.4.5}$$

where $\overrightarrow{n}$ is a vector corresponding to the field direction along which the saturation magnetostriction is measured and $\overline{\overline{\varepsilon^{\mu}}}$ is the magnetostriction strain tensor:

$$\overline{\overline{\varepsilon^{\mu}}} = \frac{3}{2}\begin{pmatrix} \lambda_{100}(\alpha_1^2 - \frac{1}{3}) & \lambda_{111}\alpha_1\alpha_2 & \lambda_{111}\alpha_1\alpha_3 \\ \lambda_{111}\alpha_1\alpha_2 & \lambda_{100}(\alpha_2^2 - \frac{1}{3}) & \lambda_{111}\alpha_2\alpha_3 \\ \lambda_{111}\alpha_1\alpha_3 & \lambda_{111}\alpha_2\alpha_3 & \lambda_{100}(\alpha_3^2 - \frac{1}{3}) \end{pmatrix}_{CR} \overrightarrow{n} = \begin{pmatrix} \beta_1 \\ \beta_2 \\ \beta_3 \end{pmatrix} \tag{1.4.6}$$

When dealing with single crystal structure, the equation (1.4.4) defining the saturation magnetostriction must be generalized to take into account the crystal axis along which the magnetization lies. According to equation (1.4.5), it can be expressed as follow:

$$\lambda_s = \frac{3}{2}\lambda_{100}(\alpha_1^2\beta_1^2 + \alpha_2^2\beta_2^2 + \alpha_3^2\beta_3^2 - \frac{1}{3}) + 3\lambda_{111}(\alpha_1\alpha_2\beta_1\beta_2 + \alpha_2\alpha_3\beta_2\beta_3 + \alpha_3\alpha_1\beta_3\beta_1) \tag{1.4.7}$$

where λ_{100} corresponds to saturation magnetostriction along the <100> direction and λ_{111} corresponds to saturation magnetostriction along the <111> direction. α_i and β_i respectively denotes the direction cosines relative to the domain magnetization orientation and the field direction along which the saturation magnetostriction is measured.

A positive value of λ_{100} and λ_{111} corresponds to an elongation and negative value to a contraction. Gersdorf's measurements on pure iron (Fe) gives an order of magnitude of magnetostriction constants [121]:

$$\lambda_{100} = 2.4\,10^{-5}, \lambda_{111} = -2.3\,10^{-5}$$

Joule Magnetostriction (poly-crystal)

The joule effect is the most important magnetostrictive phenomenon. It corresponds to a Δl elongation of a ferromagnetic material of length l subjected to a magnetic field. This magnetostrictive strain depends strongly on the crystal structure of the material. Figure 1.4.2 shows the magnetostrictive strain of some ferromagnetic materials.

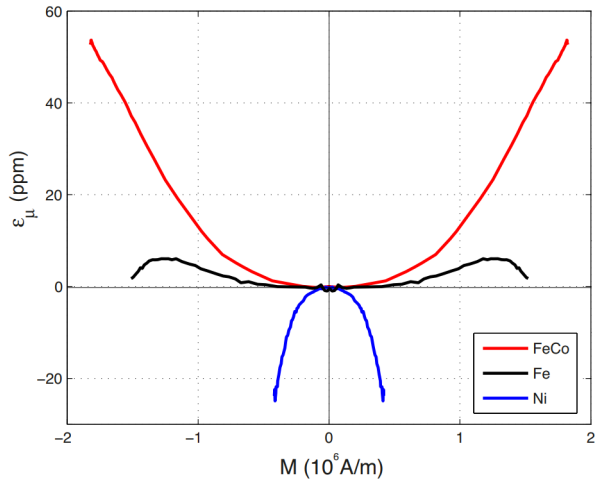

Figure 1.4.2: *Longitudinal joule effect or longitudinal magnetostriction of some ferromagnetic materials versus magnetization [34].*

We have seen in section 1.3, figure 1.3.2, that after the application of a magnetic field, a magnetization is created in the material following a first magnetization curve (dotted line) and then, it describes an hysteresis cycle. The longitudinal joule effect also presents an hysteresis while keeping the same sign whatever the direction of the field. The variations of $\frac{\Delta l}{l}$ with the applied field are shown in figure 1.4.3, curve (b). These variations take a different shape if they are plotted as a function of the magnetization M (figure 1.4.3, curve (c)). $\frac{\Delta l}{l}$ varies practically like the square of the magnetization M:

$$\lambda = \frac{\Delta l}{l} = \sum_{i=1}^{\infty} \alpha_i M^{2i} \tag{1.4.8}$$

where α_i (i = 1,2,3) is the local magnetization with respect to the crystallographic direction of the material. If the magnetization $M \ll M_s$, equation (1.4.8) becomes:

$$\lambda = \frac{\Delta l}{l} = \alpha_1 M^2 \propto M^2 \tag{1.4.9}$$

if the magnetization frequency is f_M, magnetostriction will occur at double this frequency f_λ=2×f_M. Thus, magnetostriction strain will contain only even harmonics of magnetization frequency.

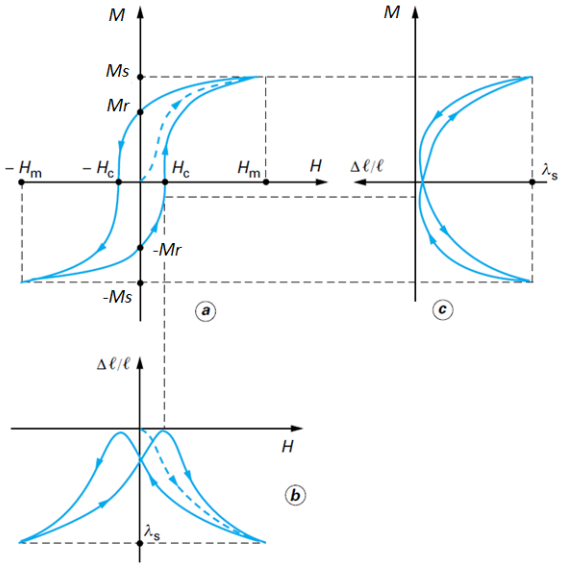

Figure 1.4.3: *Magnetic hysteresis: (a) hysteresis loop, (b) magnetostriction as a function of the magnetic field H and (c) magnetostriction as a function of the magnetization M [45].*

Besides the influence of magnetic field, the sign and the amplitude of magnetostriction strain are significantly affected by several factors, whose the most relevant are: fabrication process, material structure, harmonics, excitation mode (current/voltage), frequency and stress. The latter is one of the main factors affecting the magnetic and magnetostrictive properties of ferromagnetic materials.

1.5 Influence of stress

The first observations on the influence of stress on ferromagnetic materials behavior were carried out by Villari in 1865 when he applied stresses to ferromagnetic samples. The châtelier's principal (equation (1.5.1)) states that the change in magnetization can be linked to the stress dependence on magnetostriction, saturation magnetization and the crystallographic anisotropy [14].

$$\left(\frac{\partial \lambda}{\partial H}\right)_{\sigma} = \left(\frac{\partial B}{\partial \sigma}\right)_{H} \tag{1.5.1}$$

1.5.1 Effect of stress on magnetization

The application of stress causes elastic deformation which induces magneto-elastic anisotropy in the material. This stress affects the behavior of magnetization and consequently the magnetic properties especially at low and medium fields. Dependence of magnetic behavior on applied stress has been extensively studied in the past ([20, 13, 58, 83]). They proved that there is a strong link between stress, magnetization and magnetostriction. When a uniaxial stress σ is applied, these three quantities are involved in the expression of magneto-elastic energy that can be written in the case of cubic crystal lattice as follow:

$$\begin{gathered} E_\sigma = -\bar{\bar{\sigma}} : \bar{\bar{\varepsilon^\mu}} \\ E_\sigma = -\tfrac{3}{2}\lambda_{100}\sigma(\alpha_1^2\gamma_1^2 + \alpha_2^2\gamma_2^2 + \alpha_3^2\gamma_3^2) \\ -3\lambda_{111}\sigma(\alpha_1\alpha_2\gamma_1\gamma_2 + \alpha_2\alpha_3\gamma_2\gamma_3 + \alpha_3\alpha_1\gamma_1\gamma_3) \end{gathered} \tag{1.5.2}$$

where $\alpha_1, \alpha_2, \alpha_3$ and $\gamma_1, \gamma_2, \gamma_3$ are the direction cosines of magnetization M and the direction cosines of stress σ with respect to the cube axes, respectively. λ_{100} and λ_{111} are the saturation magnetostriction in $< 100 >$ direction and $< 111 >$ direction respectively. Thus, a stress σ applied parallel to an easy magnetization direction ($\gamma_1 = 1, \gamma_2 = \gamma_3 = 0$) and forming an angle θ with the magnetization M causes the appearance of an additional anisotropy that is equivalent in case of axial symmetry to:

$$E_\sigma = -\frac{3}{2}\lambda_{100}\sigma\alpha^2 = -\frac{3}{2}\lambda_{100}\sigma\cos^2(\theta) \tag{1.5.3}$$

Relation (1.5.3) will allow to determine the effect of stress on magnetic behavior. In fact, the material's response to stress depends only on the sign of the product $\lambda_{100}\sigma$. If the product $\lambda_{100}\sigma$ is positive, as it is the case for iron ($\lambda_{100} > 0$) under tension or for nickel ($\lambda_{100} < 0$) under compression, the magneto-elastic anisotropy favors direction [100] over the other two crystal directions [110] and [111] (figure 1.2.3). The opposite happens when the product $\lambda_{100}\sigma$ is negative. This magneto-elastic energy reaches its minimum (or maximum) when the magnetization M is parallel to stress direction providing that $\lambda_{100}\sigma$ is positive (or negative) [104]. E_σ is zero when M and σ are at right angles ($\theta = \pm\frac{\pi}{2}$).

Figure 1.5.1 illustrates the effect of tensile stress on magnetic properties of iron and nickel. These two materials have magnetostriction constants of opposite signs. It is obvious that the application of the same tensile stress has an opposite effects on these two materials.

Under low magnetic field conditions, in the case of iron, when the tensile stress is parallel to the direction of applied field, the permeability (or susceptibility) improves, while it degrades for compressive stress. In the case of nickel, the magnetostriction being negative, the application of a tensile stress makes the magnetization more difficult

and leads to a degradation of permeability (or susceptibility). The curves crossing in figure 1.5.1a corresponds to the Villari inversion, and can be related to the non-monotonic behavior of magnetostriction curves for iron.

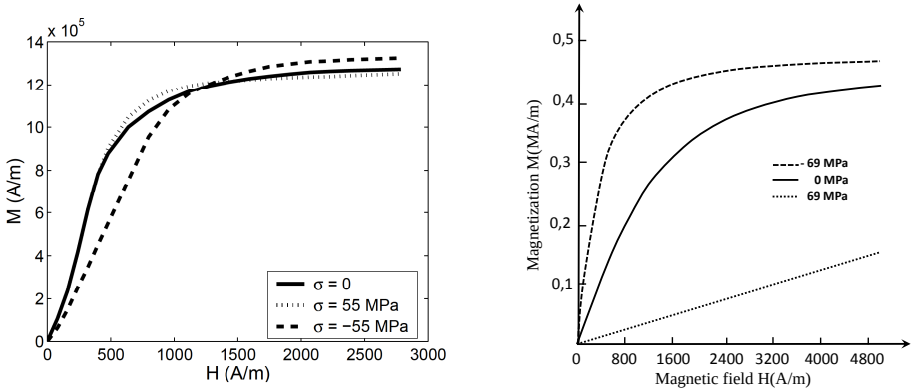

(a) *Poly-crystal of iron (Fe).* **(b)** *Poly-crystal of nickel (Ni).*

Figure 1.5.1: *Stress effect on magnetization [22].*

Villari effect application

The Villari effect is a consequence of the changes in magnetization due to the applied stress (figure 1.5.1a). It is due to many mechanisms that are coupled (magneto-mechanical effect) and it is also called inverse magnetostriction. This changes or variations is equivalent to the level of the applied stress (if low magnitude stress) and can be detected by a pickup coil for sensing applications (figure 1.5.2).

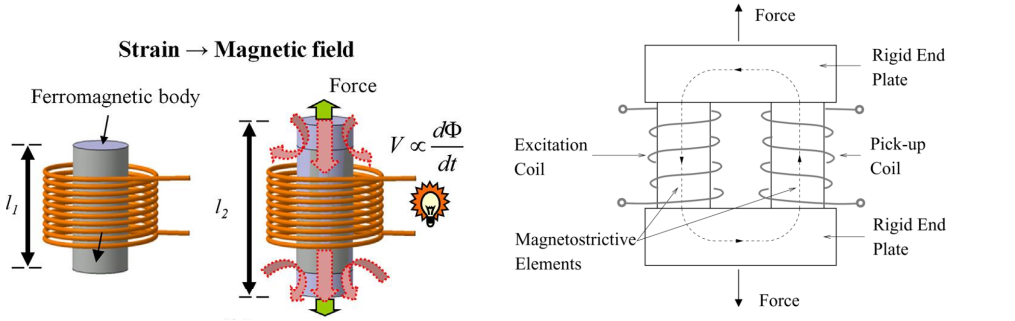

(a) *Villari effect [64].* **(b)** *Magnetostrictive force sensor based on the Villari effect [29].*

Figure 1.5.2: *Villari effect : (a) principal, (b) application.*

1.5.2 Effect of stress on domain structure

The mechanism of figure 1.5.3 describes the transformation of four magnetic domains structure under stress, configuration (a) in figure 1.5.3 represents the unstressed state. When a tensile stress is applied (figure 1.5.3, configuration (b)), the domain walls start to move in such a way to increase the volume of domains parallel to the direction of stress to the detriment of domains perpendicular to the direction of stress (closure domains 90°). The latter completely disappear in case of high tensile stress. The opposite occurs when a compression is applied (figure 1.5.3, configuration (c)). The stress direction becomes a hard axis as the volume of 90° domains increases, much more energy will be needed to rotate the magnetization of 90° domains in the magnetic field direction (applied parallel to the stress direction). Therefore, if the field is in the direction of stress, for iron, tensile stress makes the magnetization easier and the compression stress makes it harder. The opposite is true for Nikel.

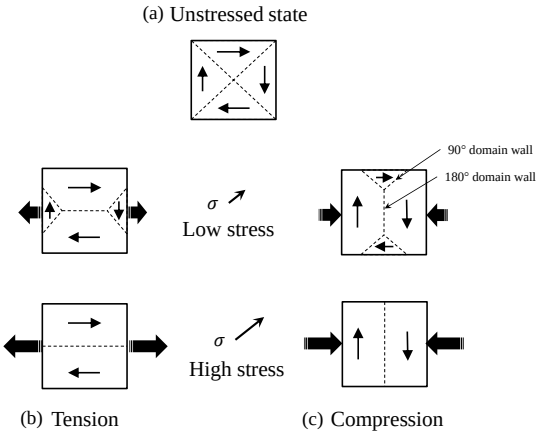

Figure 1.5.3: *Magnetic domains: magnetization process under stress of a material with positive magnetostriction like iron ($\lambda_{100} > 0$) .*

As we have seen, stress has an effect on magnetization and domain structure of ferromagnetic materials. It also alters magnetostrictive strain.

1.5.3 Effect of stress on magnetostriction

It has been shown up to now that when a compressive or tensile stress is applied to a ferromagnetic material, it causes a change in the magnetization process. This introduces also in addition to the deformation created by elasticity, a variation of the magnetostrictive deformation; this is well illustrated by measurements results shown figure 1.5.4. Non-oriented steel sample cut in the rolling direction were subjected to uniaxial tensile and compressive stresses, then the longitudinal magnetostriction strain was measured.

Figure 1.5.4a shows that a tensile stress reduces the maximum magnetostriction and at a stress of about 25 MPa, the magnetostriction is nearly null, beyond that value of stress, magnetostriction becomes negative and saturates for high tensile stresses. On the other hand, compression increases the maximum magnetostriction, and at -40 MPa, it becomes 1.5 times greater than the magnetostriction value at unstressed state.

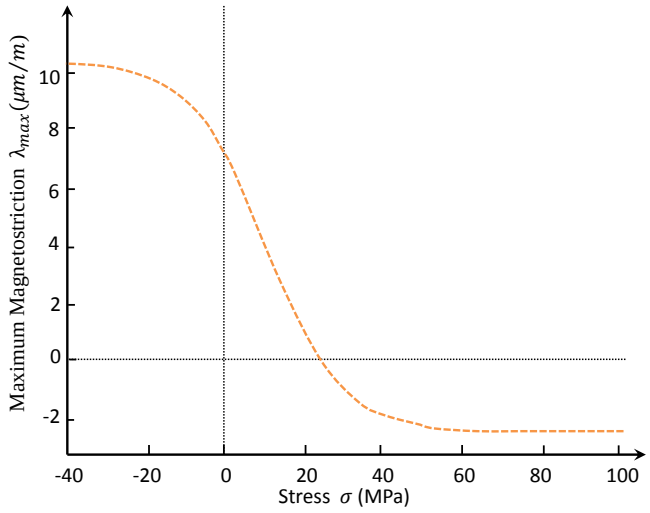

(a) *Maximum magnetostriction variation under mechanical stress* $\lambda_{max}(\sigma)$.

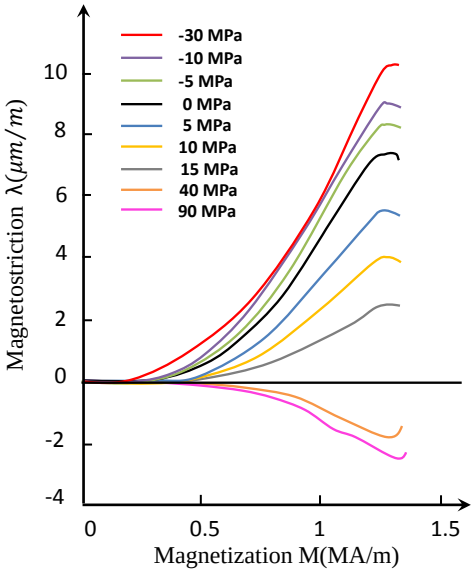

(b) *Magnetostrictive deformation* $\lambda(M)$ *under different stresses (Si-Fe).*

Figure 1.5.4: *Magnetostrictive deformation behavior under uniaxial stress for non oriented 3%Si-Fe steel cut in the rolling direction (RD) [106].*

Considering the magnetic domain structure under stress shown in figure 1.5.3, domains with 180° domain walls grow and the closure domains (90°) decrease under tensile stress. Therefore, the sample will be brought to saturation mostly by 180° domains

walls movements, which produces no magnetostrictive change in length. However, for compressive stress, the structure (iron based) is strongly affected because we favor 90° domains walls that are stress sensitive as illustrated in configuration (c), figure 1.5.3. This explains the high magnetostriction deformation when a compressive stress is exerted and the lower magnetostrictive deformation when tensile stress is applied (figure 1.5.5).

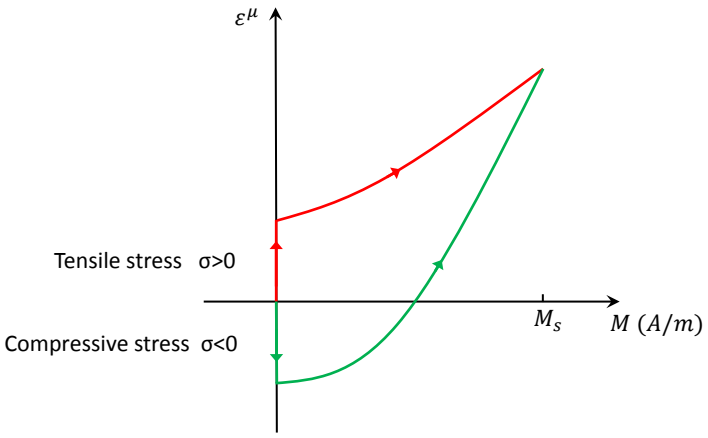

Figure 1.5.5: *Magnetostriction evolution under compressive and tensile stress ($\overrightarrow{M}$ parallel to σ).*

The magnitude variation of the curves representing $\lambda(M)$ in figure 1.5.4b is due to the magneto-elastic energy which modifies the anisotropy of the material and hence its magnetostrictive deformation at demagnetized state. As stated before, the magneto-elastic energy for a single grain can be defined by the equation (1.5.3). Thus, the increase or the decrease of this energy depends on the product $\lambda_s\sigma$. Assuming that saturation magnetostriction is positive for iron sample ($\lambda_s > 0$), when a tensile stress is applied it can be deduced that no increase in magneto-elastic energy happens and therefore no increase in magnetostriction:

$$\begin{aligned} &\text{if } \lambda_s > 0 \text{ and } \sigma > 0 \text{ then } E_\sigma < 0 \\ &\text{if } \lambda_s > 0 \text{ and } \sigma < 0 \text{ then } E_\sigma > 0 \end{aligned} \tag{1.5.4}$$

At medium amplitude of tensile stress, closure structure leads to small magnetostriction and for high tensile stress, a small negative strain appears. But, when compressive stress is applied, the magneto-elastic energy increases leading to the appearance of closure domains resulting in increase of magnetostrictive strain.

△E effect

Another consequence of stress is the dependence of Young modulus E of magnetic materials on its state of magnetization. When a demagnetized ferromagnetic material

is submitted to a tensile test, we observe a nonlinear variation in the curve $\sigma(\varepsilon)$ due to magnetostriction strain, figure 1.5.6a. Thus, magnetostriction leads to an apparent loss of linearity in the elastic behavior of demagnetized magnetic samples, called ΔE effect [23].

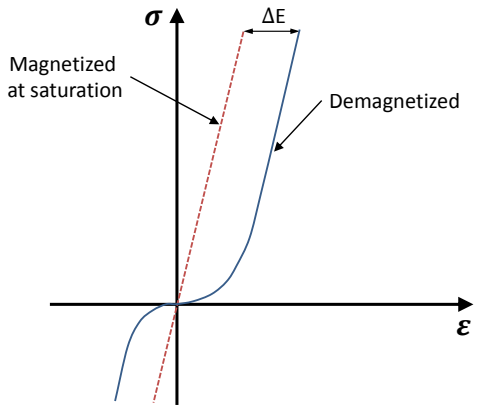

(a) $\sigma(\varepsilon)$*: Non linearity in ferromagnetic material due to mechanical stress.*

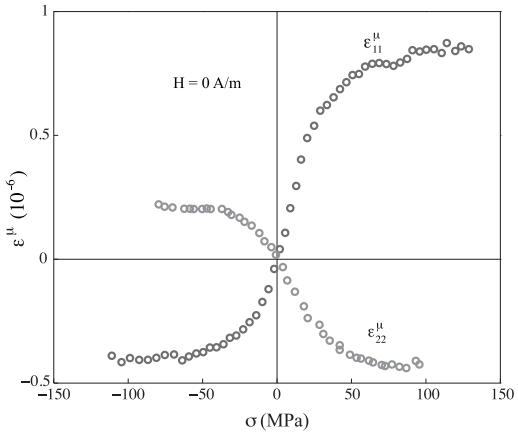

(b) $\varepsilon^{\mu}(\sigma)$*: Influence of stress on the longitudinal and transverse magnetostrictive strain* ($M_s = 1.9 \times 10^6 \mathrm{A/m}$) *[51].*

Figure 1.5.6: $\triangle E$ *effect illustration.*

In the case of uniaxial stress applied to a demagnetized material, two types of deformation are generated:

- Elastic deformation ε^{el} which occurs in any material, magnetic or not.
- Magnetostriction deformation ε^{μ}, due to the reorientation of domain structure by application of stress σ.

As a consequence, the apparent Young modulus of a ferromagnetic material in the demagnetized state is equal to :

$$\mathrm{E_d} = \frac{\sigma}{\varepsilon^{el} + \varepsilon^{\mu}} \tag{1.5.5}$$

When a strong magnetic field is applied, magnetostriction saturation is reached, no reorientation of domain is possible, therefore, magnetostriction strain ε^{μ} is zero. The Young modulus at saturation state is written as :

$$\mathrm{E_d} = \frac{\sigma}{\varepsilon^{el}} \tag{1.5.6}$$

Equations (1.5.5) and (1.5.6) give the expression of the ΔE effect as a function of elastic and magnetostrictive deformation:

$$\frac{\Delta E}{E} = \frac{E_s - E_d}{E_d} = \frac{\varepsilon^{\mu}(\sigma)}{\varepsilon^{el}(\sigma)} \tag{1.5.7}$$

A description of the effect of stress on the longitudinal and transverse magnetostrictive strain behavior $\varepsilon^{\mu}(\sigma)$ is reported in figure 1.5.6b.

Figure 1.5.7 shows a device based on ΔE effect employed as an acoustic wave-guide. The principle of operation of the sensor is the following: the magnet interacts with the magnetostrictive wave-guide and locally changes its material properties. These material property change can be detected by the stiffness discontinuity produced by the magnet ($\triangle$E effect) which partially reflects back an acoustic pulse sent by the emitter. This sensor can be used to measure fluid levels by connecting the magnet to a float or for generic position sensing [29].

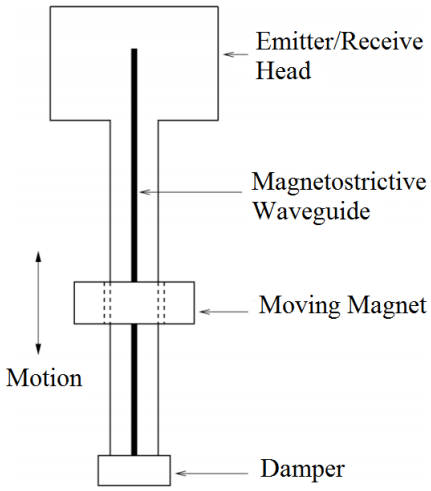

Figure 1.5.7: *Magnetostrictive wave-guide position sensor based on ΔE effect [29].*

1.5.4 Different sources of stress

It has been established that magnetostriction and magnetization of electrical steel sheet are stress sensitive. Nevertheless, various factors cause mechanical stress to appear, starting from the manufacturing process to the assembling of electrical steel. Let's focus on factors that have relevance in being the main sources of stress such as cutting process, coating, clamping and magnetic forces.

1.5.4.1 Cutting induced stress

Electrical steel sheets have to be cut in order to produce rotating machines and transformers components. However, cutting operations induce stresses in electrical steels; consequently magnetic properties are partially deteriorated: the magnetic losses increase and permeability decreases [33, 62, 63]. Figure 1.5.8 shows the edge profiles of a non-oriented electrical steel samples cut by four methods. Plastic deformation can be observed for guillotine and punching and the deformed area seems to extend for about 0.3 mm, the deformed grains recrystallize after annealing. On the other hand, the laser technique caused no deformation on the grains. While, the sample cut by photo-corrosion had a sharp edge of approximately 0.2 mm and grain deformation is not observed either.

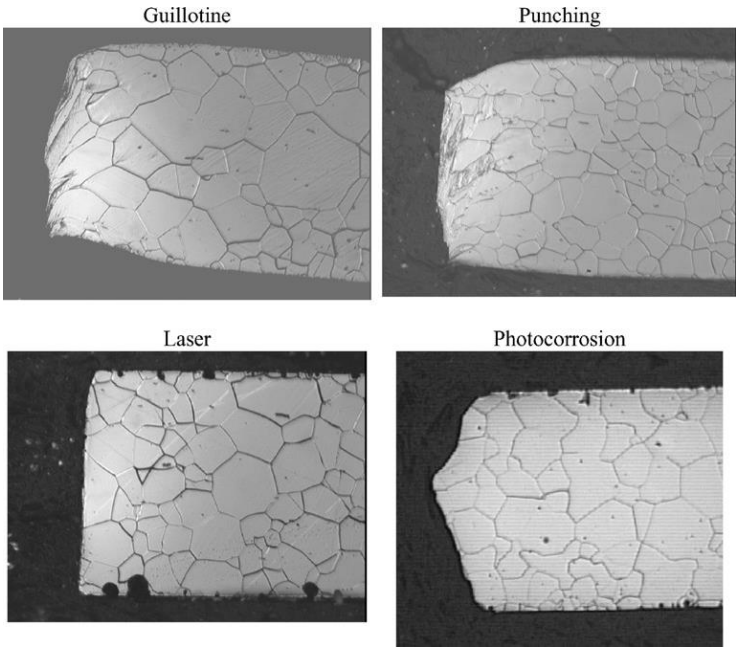

Figure 1.5.8: *Optical micro-graph of a non-oriented Si-Fe electrical steel cut by different techniques: guillotine, punching, laser and photocorrosion [33].*

Figure 1.5.9 illustrates the magnetic results obtained on non-oriented (NO) electrical steel sheets 300 mm x 100 mm magnetized in a Single Sheet Tester (SST) at 50 Hz and cut into strips in different width and a length of 100 mm. It can be observed that the $B(H)$ curves at 50 Hz deteriorated progressively as the width of the strips decreased. Similar degradation of the $B(H)$ curves was found at 400 Hz.

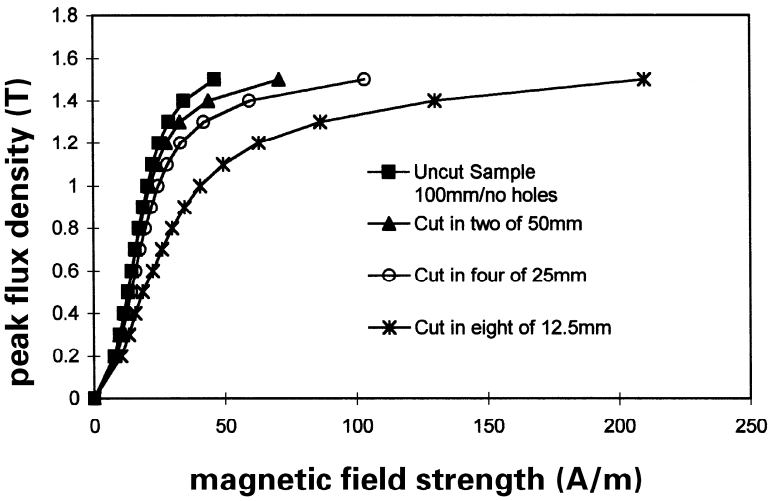

Figure 1.5.9: *Variation of $B(H)$ characteristics caused by guillotine cutting [83].*

1.5.4.2 Coating stress

The coating of electrical steel sheets has the benefit of electrically insulating them, and reduces the losses generated by eddy currents. It also protects them against corrosion. More interesting, it turns out that the coating has an effect of imposing a beneficial tensile elastic stress in the rolling direction (RD) which reduces the magnetostriction strain [110, 42]. Figure 1.5.10 shows the effect of coating stress on two types of electrical steel (NO and GO). The magnetostriction strain decreases for both materials because of the coating. However, the reduction of magnetostriction deformation is much larger for GO than NO steel sheets. In fact, for GO steel, the majority of domains are aligned with the rolling direction of the material, and just a few closure domains (90° domain wall) exist. By applying the coating, a tensile stress is generated which helps remove the rest of closure domain (figure 1.5.10a). But for non-oriented steel, there is no preferred direction for the domains, and much more closure domains are still present when the steel sheets are coated, and hence, the effect of tensile stress induced by coating is less striking (figure 1.5.10b).

The cutting method used for the electrical steel under study in this PhD work is called water jet technology. It uses high pressure water flow in combination with air injected abrasive particles. It has a high accuracy of cutting with a minimum applied stress on the electrical steel.

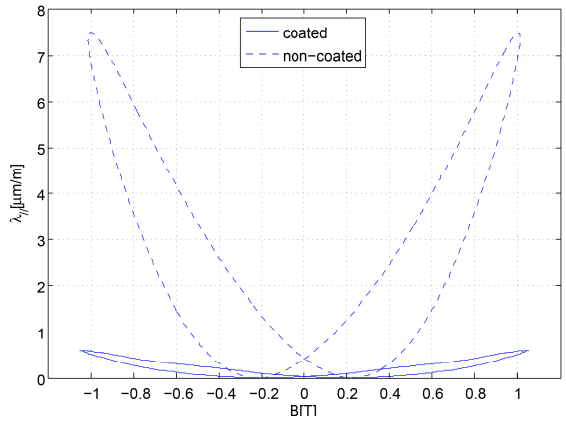

(a) *Grain-oriented electrical steel (GO)*

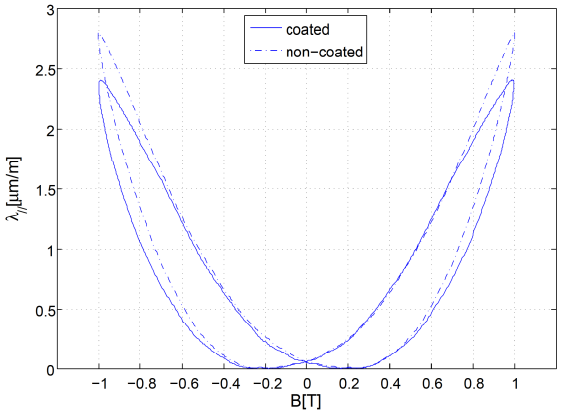

(b) *Non-oriented electrical steel (NO)*

Figure 1.5.10: *Effect of coating on magnetostrictive strain of electrical steel sheets (B =1T, f = 50 Hz) [42].*

1.5.4.3 Clamping stress

Clamping is an important element in the assembly of transformers since it allows the assembly of the magnetic circuit to be maintained. This pressure will also influence the performance of the magnetic core. In fact, excessive tightening torque will tend to increase the iron losses and deformation of the magnetic circuit. Also, imperfections in clamping due to lack of care when assembling are one of the main source of stress. Depending on the type of clamping, the stress generated can be advantageous or not. A well adjusted compressive stress applied in the normal direction of the sheets to hold them together (called C-clamping), helps to reduce the air gap in the z-direction and lowering the noise level due mainly to magnetic forces in this direction [91]. But in the case of compression in the rolling or transverse direction (in the plane of the sheets), the magnetostriction deformation increases dramatically leading to more vibration and noise in the transformer [79]. Figure 1.5.11 shows a general schematic of the mechanism for applying compression to a limb.

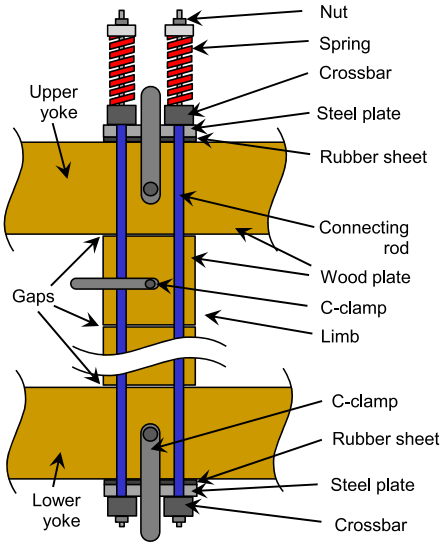

Figure 1.5.11: *Schematic of the mechanism for applying compression to a limb [79].*

1.6 Magnetostrictive strain measurements methods

Magnetostrictive deformation is a magneto-mechanical quantity of very small amplitude, in the order of micrometer per meter, which cannot be directly measured as it is (deformation). The magnetostrictive deformation measurement is often carried out by converting the deformation into an electrical quantity. This signal will then be measured and reconverted to evaluate the deformation. In addition to the small strain scale, the sensitivity of such measurements to any external stress requires an accurate method. The following paragraphs are devoted to classify the deformation measurement methods according to the principles of conversion, and more concretely, according to the physical phenomenon at the origin of which the transduction of physical quantities takes place.

1.6.1 Contact techniques

1.6.1.1 Strain gauge

This is the most widely used method in the field of strain sensors. The deformation causes a proportional variation in the resistance of the gauge, which is then translated into a signal by an electronic circuit. As illustrated in figure 1.6.1, the strain gauge consists of a thin film with a wire attached to it, which meanders over an area of the film. The electrical resistance of the wire changes in proportion to the amount of strain it undergoes. This coefficient of proportionality is called Gauge Factor GF :

$$GF = \frac{\frac{\triangle R}{R}}{\frac{\triangle l}{l}} = \frac{\frac{\triangle R}{R}}{\varepsilon} \tag{1.6.1}$$

The terms $\frac{\triangle R}{R}$ and $\frac{\triangle l}{l}$ represent the relative changes in resistance and in wire length, respectively. The gauge factor is simply the ratio of these percentage changes, with the length variation term corresponding to mechanical strain. Therefore, the strain gauge's change in resistance as a function of strain is:

$$\triangle R = GF \times R \times \varepsilon \tag{1.6.2}$$

Gauge factor values are approximately 2, though they can deviate from this value by several percent.

However, as the variation of strain is very small, an electronic circuit is necessary to amplify the signal. To carry out more accurate measurement, a dummy gauge can be used for calibration to compensate for temperature change. The advantage of this method can be stated as:

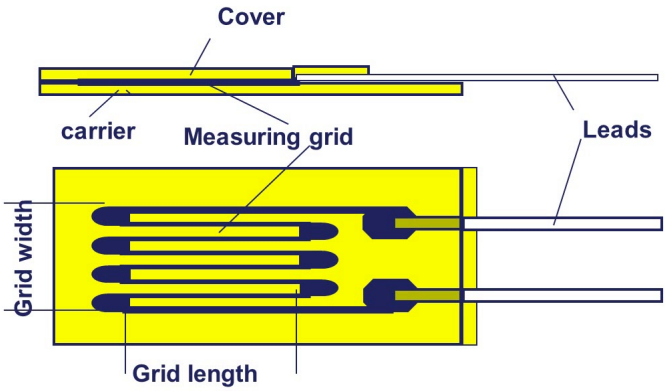

Figure 1.6.1: *A strain gauge for one direction strain measurement.*

- It can be applied to the measurement of magnetostriction on samples of a variety of shapes and geometries.
- In the case of thin laminated samples, errors due to bending can be eliminated by applying gauges on both sides of the sample and connecting them in series.
- Regions over which strain measurements are made are small so that variables such as end effects, shearing stresses and non-uniformity are eliminated.
- The effect of temperature variations and other ambient variables are eliminated by the use of a dummy gauge.
- Possibility of a closed magnetic path setup may be used, assuring a greater uniformity of flux distribution (easy access).
- Easy repeatability of the measurements

1.6.1.2 Piezoelectric strain sensor

The piezoelectric effect is based on the fact that quartz generates, under a pressure load, an electrical charge directly proportional to the force introduced. Using an amplifier, this load is then converted into a proportional output voltage. Piezoelectric accelerometers are generally used for vibration measurement. They are not suited for static or dc applications because the electrical charge produced decays with time due to the internal impedance of the sensor and the input impedance of the signal conditioning circuits. However, they are well suited for dynamic or ac applications. Axial sensors are typically used to measure dynamic forces while flexional sensors are used to measure changes in strain (like magnetostriction) and curvature (figure 1.6.2). The measured quantity is

acceleration, displacement is obtained by double integration of acceleration. The deformation can be deduced by the relative variation of displacement divided by the initial length of the sample. Authors in [1] have reported setups to measure magnetostriction deformation based on the piezoelectric effect.

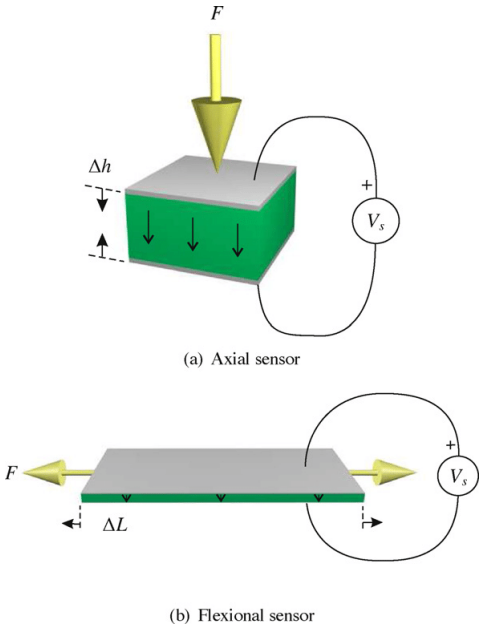

Figure 1.6.2: *A piezoelectric stack and plate strain sensor: (a) Axial sensor (b) flexional sensor [36].*

Nevertheless, the procedure of applying strain gauge or piezoelectric sensor is a delicate task and should be done by an experienced person, because it demands that the coating of the sample to be removed (to stick better to the sample) which may affect the reliability of magnetostriction measurements. Furthermore, at very low amplitude of magnetization, the accuracy is limited because of measurement noise [42]. To overcome these drawbacks of strain gauges and piezoelectric sensor, a non contact method based on interferometry principle can be a good alternative.

1.6.2 Non-contact techniques: optical means

The optical method is a non-contact measurement approach: no contact is required between the probe and the sample. Given the small magnetostriction strain (10^{-6}), optical application permits the measurements of magnetostriction in tiny sample with high accuracy.

Most of the existing optical methods are based on laser interferometers, being the basic part of a number of them [87, 97]. The general operating principal is based on

Michelson interferometer, figure 1.6.3. A coherent laser beam is split into two paths with a self-transparent mirror. The first goes to the reference arm and reflects from the reflector Z_1; the second goes to the measurement arm and reflects from the reflector Z_2. The reflected beams meet again on the detector. Because these beams come from the same and coherent source, they will interfere. When the moving reflector (Z_2) is being displaced, the frequency of the reflected beam in the measurement arm changes. The detector counts the frequency difference between reflected beams f_D (figure 1.6.3). The measured value of the displacement is obtained according to:

$$L = f_D \times \frac{\lambda}{2} \tag{1.6.3}$$

where λ is the light wavelength.

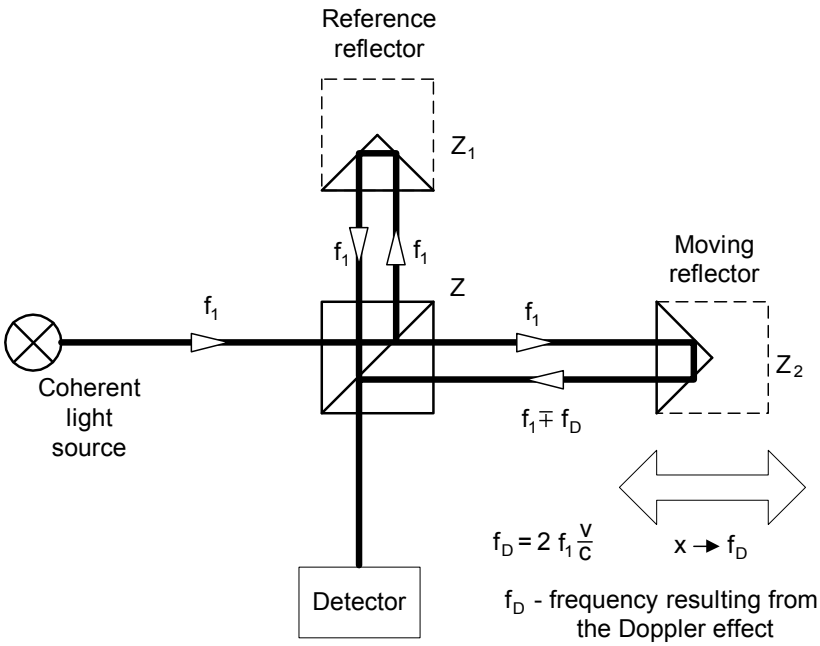

Figure 1.6.3: *Measuring principle of interferometer based on Michelson assembly.*

However Michelson interferometer does not determine the sign of the displacement of the moving object (positive or negative). To overcome this problem, other laser interferometers are used that allow to get also the direction of the movement. There are two methods depending on the number of light frequencies (wavelengths) used in the interferometer, the first is called homodyne method (one frequency) and the second heterodyne method (two frequencies). The optical technique used in this PhD work is based on the homodyne method, the principle will be discussed in chapter 2. Ghalamestani [42] has designed a new setup based on the second technique. The setup was made

to measure the magnetostriction strains of an uncoated sample using two tiny pieces of aluminum attached on it as mirrors. The laser beams are pointed at the mirrors, so when the magnetic field is applied, the difference between the velocity signals of the two mirrors delivers the relative change of the sample, corresponding to the magnetostriction strain. Figure 1.6.4 shows the general principal of this measurement method.

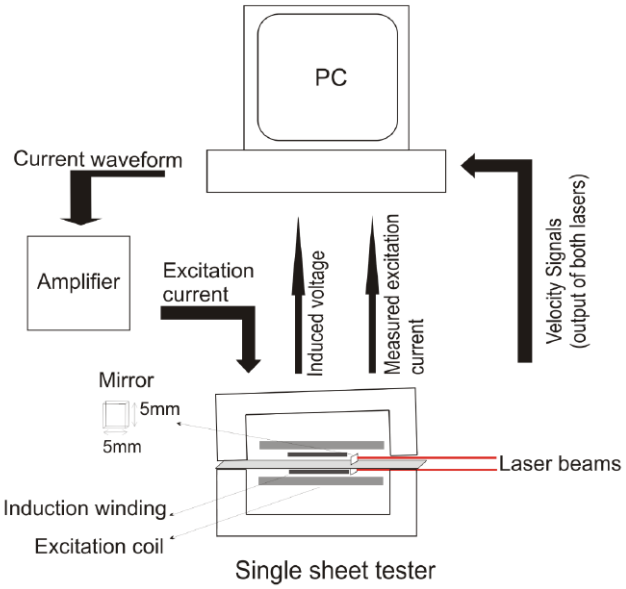

Figure 1.6.4: *General principal of the magnetostriction measurement setup using dual-laser heterodyne interferometer [42].*

Figure 1.6.5 represents a comparison between the strain gauge and the optical technique measurements (heterodyne interferometer). A very large noise can be observed in the strain gauge measurement. The amplitudes also differs a lot between the two methods. According to the authors, it can be due to coating removing when measuring with strain gauges.

It is clear that the laser setup has some advantages compared to the strain gauge :

- The measurements of magnetostrictive strain at very low amplitude with high accuracy.
- The sample preparation for the laser setup does not require any experience.
- The possibility to measure on surfaces that are difficult to access such as sheets in laminated structure where it is difficult to attach a strain gauge or a piezoelectric sensor.

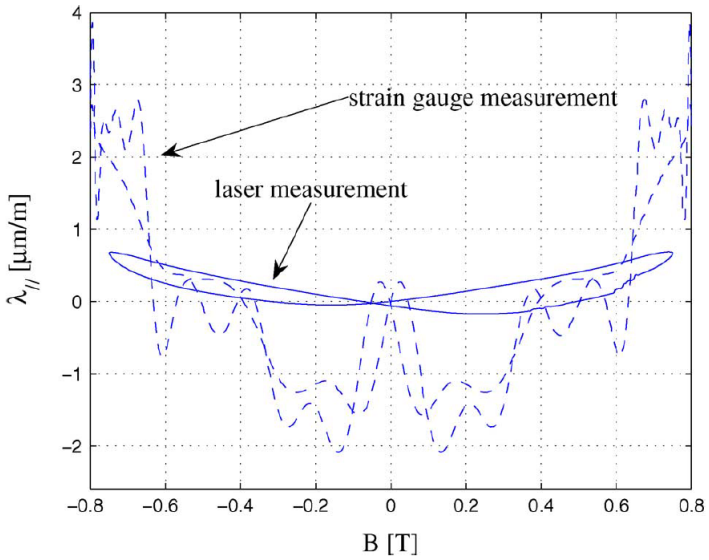

Figure 1.6.5: *Measurements of longitudinal magnetostriction strain in a non-oriented electrical steel (B=0.8T and f=50Hz) [42].*

However, repeatability of measurement by laser setup is low due to possible out of plane movement in case of SST measurements [43]. Also, the cost of such setup is expensive compared to other sensors.

We have seen some of the most common techniques for the measurements of the magnetostrictive deformation. These techniques are direct measurements. They are also indirect measurements techniques based on the Villari effect (Subsection 1.5.1), but they are not in the scope of the present work. More details about these indirect measurements techniques can be found in [32].

The present PhD work will only focus on direct techniques, particularly strain gauges and optical methods.

1.7 Magnetic forces

Magnetic or Maxwell forces are present when a magnetic flux passes through two medium of different permeabilities, figure 1.7.1. In rotating machines, they are particularly present at the interface between air gaps and stator teeth (they pull the rotor teeth towards the stator), figure 1.7.1a. In the case of a transformer, this phenomenon is essentially found in the joints since the assembly of magnetic core requires the presence of air gaps in these areas. As shown in figure 1.7.2, there are two potential sources of Maxwell forces: in plane forces due to the distributed air gap of the step lap arrangement and out of plane forces due to the air gap brought by sheet stack [118, 70]. The pref-

erence of the magnetic flux to flow in the plane or out of plane depends on the level of induction in the corners of the laminated structure and the configuration of the overlaps [52], as well as the anisotropy of used magnetic materials, figure 1.7.3.

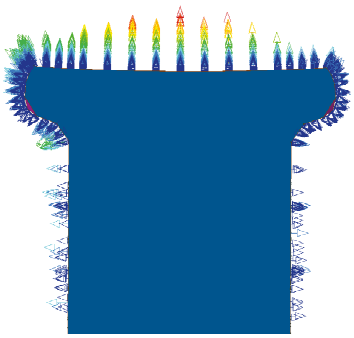

(a) *Maxwell forces exerted on a stator tooth [111].*

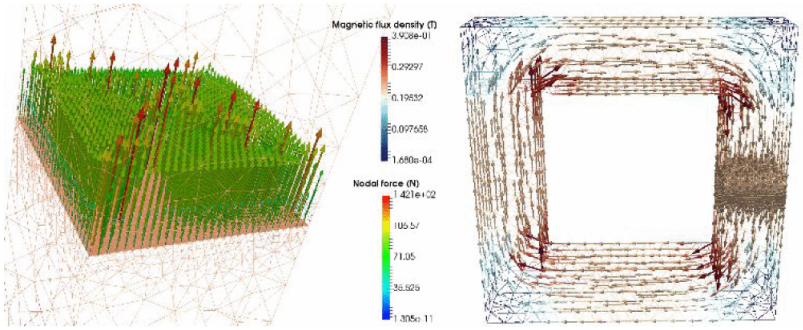

(b) *Maxwell forces on the contact surface of iron bodies (e.g. inductor) [103].*

Figure 1.7.1: *Maxwell forces illustrations: (a) rotating machine (b) inductor core.*

In order to estimate the Maxwell forces present in the air gap, many methods exists [5]. However, two methods are generally used to calculate Maxwell forces:

- Virtual Work method
- Maxwell's tensor method

1.7.1 Virtual Work method

This method presented by [99, 10] is based on the virtual work principle. The principle states that the variation of the electrical energy W_{el} due to a variation of the magnetic flux equilibrates with the variation of the stored magnetic energy W_{mag} and the work done by the magnetic force F_{mag} on a displacement of a system [122] :

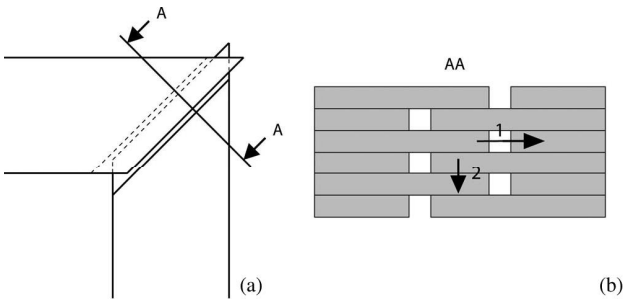

Figure 1.7.2: *In-plane and out of plane Maxwell forces [90].*

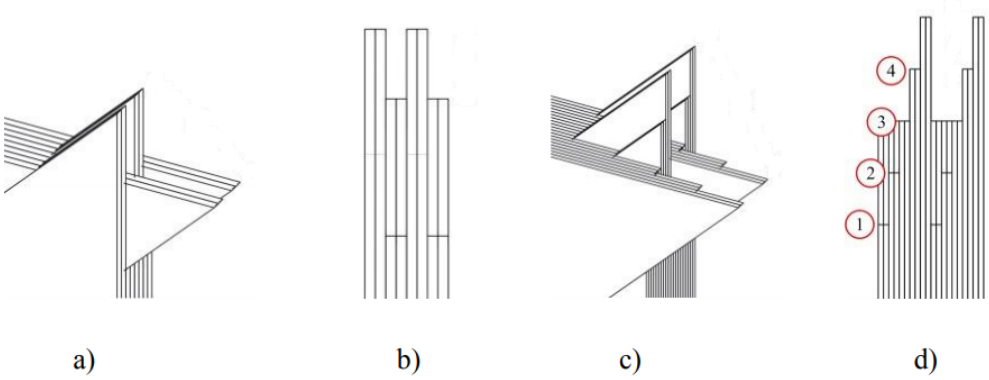

Figure 1.7.3: *Single step lap (a); Side view of single step lap with two laminations per step (b). Multi-step lap (c), Side view of multi-step lap with two laminations per step (d) [94].*

$$dW_{el} = dW_{mag} + F_{mag}du \tag{1.7.1}$$

with the electrical energy:

$$dW_{el} = IUdt = I(\frac{d\phi}{dt})dt = Id\phi \tag{1.7.2}$$

where I is the current, U is the voltage, ϕ is the magnetic flux and dt the time unit.

We can deduce that the magnetic force applied to a system is equal to the derivation of the magnetic energy W_{mag} with respect to the displacement u at constant flux :

$$F_{mag} = -\frac{\partial W_{mag}}{\partial u}_{\phi=Cste} \tag{1.7.3}$$

or by the derivation of the magnetic co-energy W^*_{mag} with respect to the displacement at constant current:

$$F_{mag} = \frac{\partial W^*_{mag}}{\partial u}_{I=Cste} \tag{1.7.4}$$

The equation linking energy to co-energy is written:

$$W_{mag} + W^*_{mag} = \phi I \tag{1.7.5}$$

1.7.2 Maxwell stress tensor method

This method uses Maxwell tensor divergence to obtain surface densities of the magnetic force:

$$\overrightarrow{F} = div(\overset{=Maxwell}{\sigma}) \tag{1.7.6}$$

It is worth mentioning that $\overset{=Maxwell}{\sigma}$ is not a stress tensor, but a tensor whose divergence (if it is not null) leads to the appearance of magnetic forces $\overrightarrow{F}$. For instance, in vacuum $\overset{=Maxwell}{\sigma} \neq 0$ however $div(\overset{=Maxwell}{\sigma}) = 0$, hence, no applied stress in vacuum.

The electromagnetic tensor is a function of the induction B and the magnetic field H, it is written in a general way in the form:

$$\overset{=Maxwell}{\sigma} = B \otimes H - \frac{1}{2}HB\overset{=}{I} = \frac{1}{\mu}(B \otimes B - \frac{B^2}{2}\overset{=}{I}) \tag{1.7.7}$$

which can be expressed as:

$$\overset{=Maxwell}{\sigma} = \frac{1}{\mu}\begin{pmatrix} B_x^2 - \frac{1}{2}B^2 & B_xB_y & B_xB_z \\ B_yB_x & B_y^2 - \frac{1}{2}B^2 & B_yB_z \\ B_zB_x & B_zB_y & -\frac{1}{2}B^2 \end{pmatrix} \tag{1.7.8}$$

Assuming that the magnetic permeability is constant and plane conditions of the flux density B (figure 1.7.4), the Maxwell tensor in the $(\vec{n},\vec{t})$ reference frame ($\vec{n}=\vec{x}$, $\vec{t}=\vec{y}$) can be written in the following form:

$$\overset{=Maxwell}{\sigma} = \frac{1}{\mu}\begin{pmatrix} B_nB_n-\frac{1}{2}B^2 & B_nB_t & 0 \\ B_tB_n & B_tB_t-\frac{1}{2}B^2 & 0 \\ 0 & 0 & -\frac{1}{2}B^2 \end{pmatrix} \tag{1.7.9}$$

with:

$$B^2 = B_n^2 + B_t^2 \tag{1.7.10}$$

B_n and B_t are the normal and tangential components of the magnetic flux density in the air-gap, unit Tesla (T).

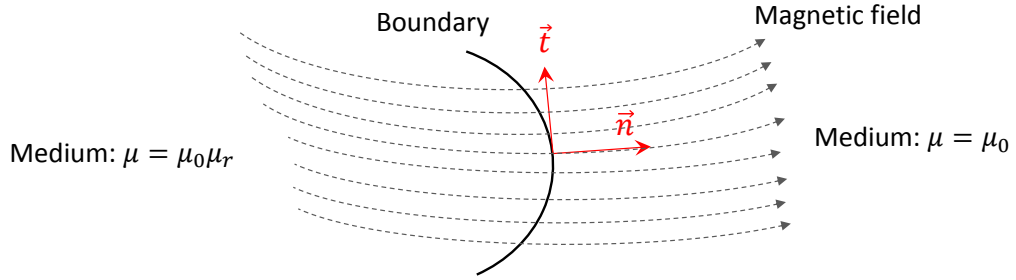

Figure 1.7.4: *Reference frame $(\vec{n},\vec{t})$ at the boundary of two different medium.*

Knowing that in the air gap, the permeability is equal to the vacuum permeability μ_0= $4\pi\times10^{-7}$H/m, and the normal and tangential stress expressions will be written:

$$\sigma_n^{Maxwell} = \overset{=Maxwell}{\sigma}.\vec{n} = \frac{(B_n^2-B_t^2)}{2\mu_0} \tag{1.7.11}$$

$$\sigma_t^{Maxwell} = \overset{=Maxwell}{\sigma}.\vec{t} = \frac{B_tB_n}{\mu_0} \tag{1.7.12}$$

$\sigma_n^{Maxwell}$ and $\sigma_t^{Maxwell}$ are expressed in N/m^2.

The Maxwell forces are the highest at the material-air gap surface due to lower magnetic permeability (μ_0 instead of $\mu_0\mu_r$) when flux lines are crossing perpendicularly the air gap, equation (1.7.11). As stated, these forces results in a magnetic pressure $\sigma_n^{Maxwell}$ along the flux lines direction, which act as a tensile/compressive stress on the limbs of the laminated core, generating vibration along the normal axis direction of the contact surface of iron bodies. Therefore, Maxwell stress can be an additional source of stress that can influence magnetic and magnetostrictive behavior among sources mentioned in subsection 1.5.4.

The magnetostrictive strain and Maxwell forces can act in the opposite directions along a magnetic flux path with air-gap, figure 1.7.5. Consequently, there might be an optimal air gap length or material to reduce vibrations by canceling the effects due to magnetostriction and Maxwell forces [100]. The geometry of the structure has to be considered because the distributions of these forces are in general not same.

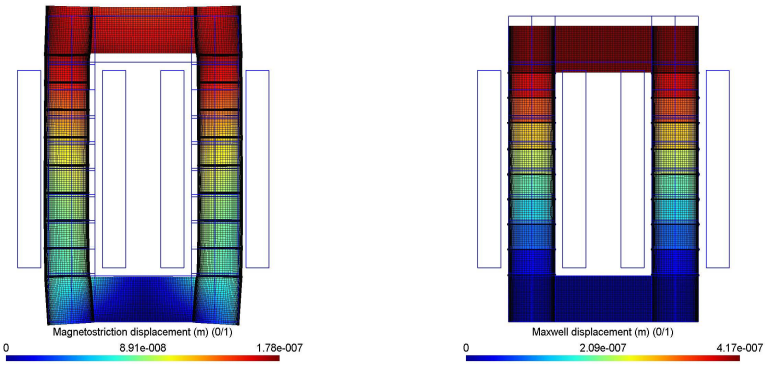

(a) (b)

Figure 1.7.5: *Displacement of an inductor due to: (a) magnetostriction (factor scale: 80000) and (b) Maxwell forces (factor scale: 30000) [100].*

1.8 Mechanical resonance induced by magnetostriction and Maxwell forces

Magnetostrictive strain and Maxwell forces cause the dimension of the core laminations to change and vibrate when the core is magnetized by an alternating field, which can lead to mechanical resonance [95, 78, 108, 69]. As these two phenomena are both quadratic functions of the flux density B, it is hard to quantify how much Maxwell forces are greater or lower than magnetostriction. In [100], it is shown that there is no general rule regarding the respective contribution of magnetostriction and the Maxwell forces, and that a structure (inductors in this case) can be excited by both phenomena. However, authors in [108], showed that only magnetostriction can induce resonance of a strip of non-oriented electrical steel. As it can be observed in figure 1.8.1, at magnetizing frequency of 2250 Hz, mechanical resonance due to the fundamental component of magnetostriction occurred at 4500 Hz (the mechanical frequency response is twice the electrical frequency excitation). The averaged value of peak-to-peak magnetostriction at

resonance (21.5 $\mu m/m$) is 14 times higher than that at 500 Hz. Moreover, they demonstrated that the magnetostriction due to pulse-width modulation voltage harmonics can excite a structural resonance.

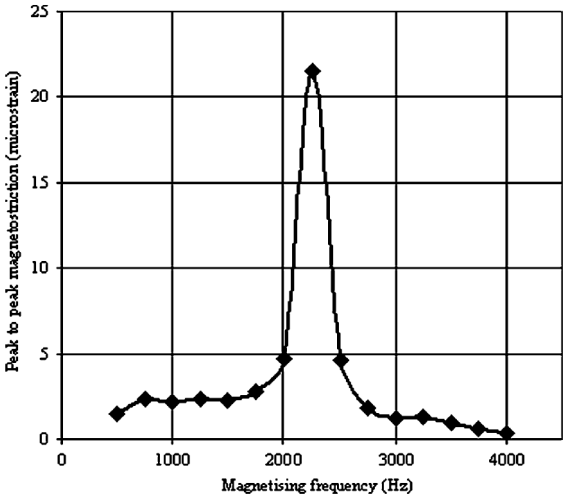

Figure 1.8.1: *Peak-to-peak magnetostriction as a function of magnetizing frequency at $B = 1T$ [108].*

On the other hand, the same authors have characterized the interaction between magnetostriction and mechanical resonance under pulse width modulation (PWM) excitation used in inverter-fed induction motors. In this case, the excitation waveform of flux density B contains high harmonics components that can lead to higher magnetostrictive deformation, up to 28% higher than that at sinusoidal excitation as shown in figure 1.8.2. Knowing that f_{sw} corresponds to the switching frequency and that m_i is the modulation index, it can be observed that peak-to-peak magnetostriction under PWM excitation are higher than those under sinusoidal excitation (the mechanical resonance occurs at 4500 Hz).

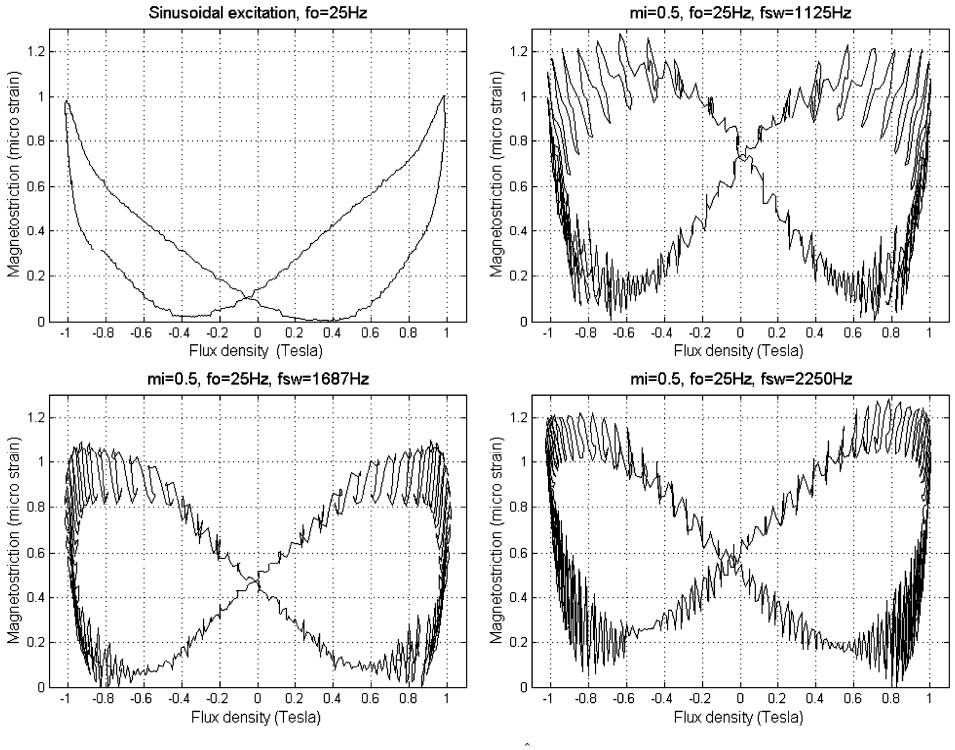

Figure 1.8.2: *Butterfly loops of magnetostriction deformation under sinusoidal and PWM excitation at B=1T, f_0=25 Hz.*

Despite these existing research on mechanical resonance induced by magnetostriction, there was no detailed investigation on a device similar to a transformer structure. In this thesis we will investigate in details the mechanical resonance and demonstrate that it can be induced by only magnetostrictive deformation in a laminated structure.

1.9 Magneto-elastic modeling strategies

The modeling of magneto-elastic coupling has been the focus of several authors. Many models have been proposed to describe the behavior of magnetic materials under stress. For the seek of simplicity, these models can be summarized into two categories depending on the scale observation and reversibility:

- Macroscopic modeling
- Multi-scale modeling

1.9.1 Macroscopic modeling

There are several macroscopic models to predict the magnetic and magnetostrictive behavior in magnetic materials. In this section, we will describe the most used and widely known models based on energy approach, taking into account the magneto-elastic coupling besides the magnetic behavior.

1.9.1.1 Jiles-Atherton model

Principal

Jiles Atherton's model [54, 56] uses energy approaches to describe the hysteretic behavior of a ferromagnetic material subjected to an external field. The total energy provided to the material can be written as the sum of a dissipated reversible energy and a stored one:

$$dE_{total} = dE_{dissipated} + dE_{stored} \tag{1.9.1}$$

The energy dissipated is due to the attachment to the defects (dislocation, inclusions) of the domains walls during the displacement. If the distribution of the defects is uniform, the energy dissipated due to the displacement of the walls will be proportional to the quantity of defects and therefore to the variation of the magnetization, hence :

$$dE_{dissipated} = \mu_0 k.dM \tag{1.9.2}$$

The k parameter characterizes the default density (energy dissipated by default). It influences the width of the hysteresis cycle. Likewise, the variation of the total and stored magnetic energy can be defined as:

$$dE_{stored} = \mu_0 M.dH \tag{1.9.3}$$

$$dE_{total} = \mu_0 M_{anh}.dH \tag{1.9.4}$$

In the case where the material presents no default (no hysteresis, therefore no dissipation), the stored energy corresponds totally to that supplied. This ideal material has an anhysteretic behavior law M_{anh} that can be modeled by the Langevin function usually used for paramagnetic materials :

$$M_{anh} = M_S \left(coth\left(\frac{H}{a}\right) - \frac{a}{H} \right) \tag{1.9.5}$$

where M_{anh} is the anhysteretic magnetization, and a is a fitting parameter, that can be written as:

$$a = \frac{k_b T}{\mu_0 m} \tag{1.9.6}$$

k_b is the Boltzmann constant, T is the temperature in Kelvin and m is the local magnetic moment.

Consequently, we can write the following expressions:

$$\begin{cases} dE_{dissipted} = & dE_{total} - dE_{stored} \\ \mu_0 k.dM = & \mu_0 M_{anh}.dH - \mu_0 M.dH \end{cases} \tag{1.9.7}$$

from equations in relation (1.9.7) we can deduce the following law of hysteretic behavior:

$$\frac{dM}{dH} = \frac{M_{anh} - M}{k} \tag{1.9.8}$$

For a more realistic description of the hysteresis behavior, Jiles considers a local magnetic field proportional to the magnetization representing interactions between domains. The result is an effective field H_e that derives from a thermodynamic potential, and is written as a function of H and M :

$$H_e = H + \alpha M \tag{1.9.9}$$

The parameter α characterizes the magnetic micro-structure. The field H_e is introduced in equation (1.9.5).

By combining the derivative with respect to the field H of the equation (1.9.9) and the relationship (1.9.8), we find in a general form the behavior law introduced by the model :

$$\frac{dM}{dH} = \frac{M_{anh} - M}{k - \alpha (M_{anh} - M)} \tag{1.9.10}$$

By introducing a reversible magnetization term which allows to take into account the reversible deformation of walls pinned on defects, magnetization M is defined as the sum of a reversible M_{rev} and irreversible M_{irr} components such as [54] :

$$\begin{cases} M = & M_{rev} + M_{irr} \\ M_{rev} = & c (M_{anh} - M_{irr}) \end{cases} \tag{1.9.11}$$

where c is a parameter representing the elasticity of magnetic wall.

From the relations (1.9.10) and (1.9.11), the total magnetization law can be written as follow :

$$\frac{dM}{dH} = \frac{M_{anh} - M_{irr}}{k\delta - \alpha (M_{anh} - M_{irr})} + c \left(\frac{dM_{anh} - dM_{irr}}{dH} \right) \tag{1.9.12}$$

where δ takes the values $+1$ or -1 respectively for an increasing ($\frac{dH}{dt} > 0$) or a decreasing ($\frac{dH}{dt} < 0$) magnetic field.

Thanks to this differential formulation (equation (1.9.12)) and after parameters identification, the Jiles-Atherton model can easily describe the hysteresis phenomenon (figure 1.9.1a). However, the dissipative term (equation (1.9.2)) takes into account only the interaction between the walls and the defects, which can limit the model to quasi-static regimes. Furthermore, the scalar formulation limits the model to one-dimensional problems.

Magneto-elastic modeling

The Jiles-Atherton model has been improved to take into account the effect of stress on magnetization by adding an equivalent magnetic field H_σ in the formulation of anhysteretic magnetization [101]:

$$H_e = H + \alpha M + H_\sigma \tag{1.9.13}$$

Based on the thermodynamic equilibrium, in the case of isotropic poly-crystalline materials, a scalar formula gives the expression of H_σ:

$$H_\sigma = \frac{3}{2}\frac{\sigma}{\mu_0}\left(\frac{d\lambda}{dM}\right)_\sigma \tag{1.9.14}$$

where σ represents the applied uniaxial stress and λ the magnetostrictive strain in the direction of applied field. Considering that the magnetostriction λ is an even function of the magnetization, we can write:

$$\lambda = \sum_{i=0}^{\infty} a_i M^{2i} \tag{1.9.15}$$

where a_i are the magnetostriction coefficients when $\sigma = 0$.

The use of the concept of equivalent field H_σ is, however, restrictive. In fact, the deformation values are measured in the absence of stress ($\sigma = 0$), which is contradictory with experience. This approach must therefore be limited to low stress amplitudes unless the magnetostriction coefficients a_i are a function of the stress (figure 1.9.1b).

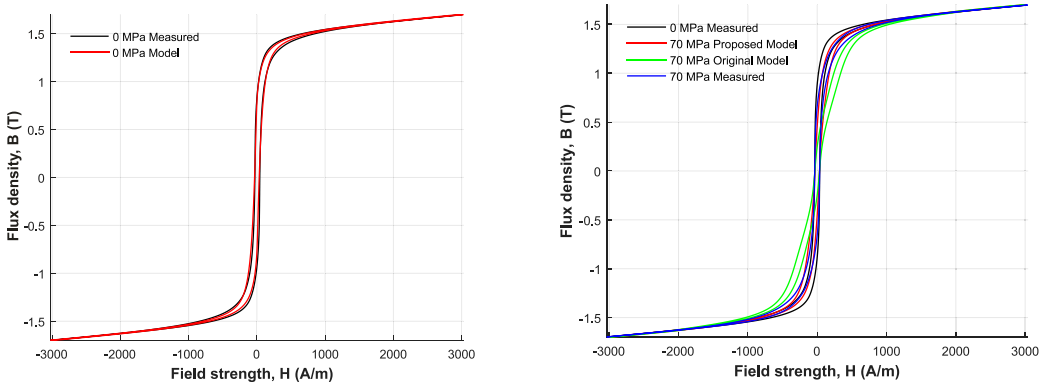

(a) $B(H)$ *loop at* $\sigma = 0$ *MPa.*

(b) $B(H)$ *loop at* $\sigma = 70$ *MPa.*

Figure 1.9.1: *Measured and modeled* $B(H)$ *loop by SJA model: (a)* $\sigma = 0$ *(b) Original model* (H_σ) *and proposed model* ($H_\sigma + a_i(\sigma)$) *[106].*

The Sablik-Jiles Atherton (SJA) model is a macroscopic model, even if it claims to describe microscopic behavior. The use of a Langevin function is not justified for the description of ferromagnetic systems. Besides, the identification of the model parameters is based on experimentation. Nevertheless, it allows modeling of the magnetic behavior of the ferromagnetic material taking into account of the stress effect (uniaxial stress).

1.9.1.2 Preisach model

Principal

The Preisach-type models constitute a family of macroscopic models that is widely used in the literature [96]. It is based, like the SJA model, on phenomenological approach. This approach considers an hysteretic material as an assembly of several elements that are independent of each others called hysterons $\gamma_{\alpha\beta}$. These hysterons have a bistable state behavior parameterized by (α, β) (equation (1.9.16)) and asymmetric with respect to the excitation (figure 1.9.2). In the case of a magnetic system, the asymmetry of the hysteron loop is explained by the existence of a magnetic field interaction between hysterons [107].

$$\gamma_{\alpha\beta} = \begin{cases} 1 \text{ for } H(t) \geq \alpha \\ -1 \text{ for } H(t) \leq \beta \\ h \text{ for } \beta \leq H(t) \leq \alpha \end{cases} \tag{1.9.16}$$

where t corresponds to time and h is defined as:

$$h = \begin{cases} 1 \text{ for } H(t^-) > \alpha \\ -1 \text{ for } H(t^-) < \beta \end{cases} \tag{1.9.17}$$

The history of the material is considered by the parameter h, t^-corresponds to the last instant for which $H(t) \notin [\alpha, \beta]$: previous value of $\gamma_{\alpha\beta}$.

Under an applied magnetic field $H(t)$, the macroscopic magnetization corresponds to the average of the hysterons $\gamma_{\alpha\beta}$ weighted by a distribution function $\mu(\alpha,\beta)$ in the Preisach plane (α,β):

$$M(t) = \iint \gamma_{\alpha\beta}(H(t))\mu(\alpha,\beta)\, d\alpha d\beta \tag{1.9.18}$$

The distribution function of Preisach $\mu(\alpha,\beta)$ characterizes the number of hysterons participating in the magnetization process. This distribution is defined on a triangle of surface S in the Preisach plane (figure 1.9.2b), divided into two domain $S^+$and S^- separated by a line $L(t)$. Depending on the evolution of the magnetic field, the line $L(t)$ also evolve and hence the magnetic state.

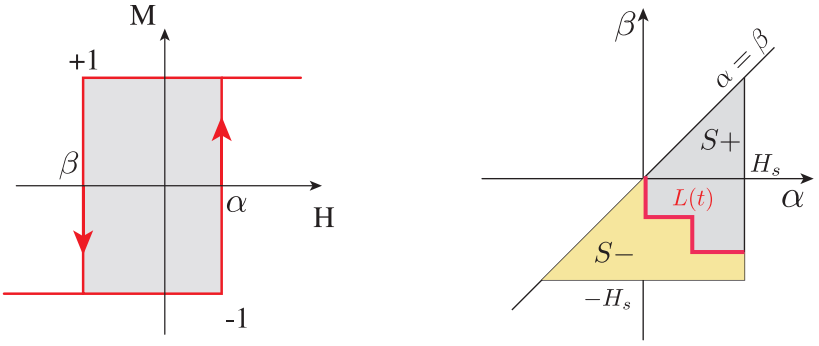

(a) *Hysteron cycle.* **(b)** *Preisach plan.*

Figure 1.9.2: *Preisach Hysteron [74].*

Magneto-elastic modeling

The effect of uniaxial stress σ on magnetization and magnetostriction deformation can be taken into account by the distribution function $\mu(\alpha,\beta,\sigma)$ shown in equation (1.9.19) [9] which is based on a Gaussian distribution, or by acting on the values of the operator $\gamma_{\alpha\beta}$ (equation (1.9.16)), [8]. Modeling the magneto-elastic coupling with this model seems possible, however, the proposed solutions require a great number of parameters identification under stress, which makes the modeling very difficult to achieve.

$$\mu(\alpha,\beta,\sigma)=\begin{cases}\exp(\frac{(\alpha-\beta-(c+g\sigma))^2}{10^{a+e\sigma}}-\frac{(\alpha+\beta-(d+h\sigma))^2}{10^{b+f\sigma}}) & \alpha+\beta\leq 0\\ \exp(\frac{(\alpha-\beta-(c+g\sigma))^2}{10^{a+e\sigma}}-\frac{(\alpha+\beta+(d+h\sigma))^2}{10^{b+f\sigma}}) & \alpha+\beta>0\end{cases} \tag{1.9.19}$$

where a, b, c, d, e, f, g and h are model parameters to be identified from experimental data.

1.9.1.3 Helmholtz energy based model (HE)

In this model, the constitutive equations to describe the magneto-elastic behavior of the material are derived from the Helmholtz free energy density named ψ [37, 38]. This energy density is defined as a function of two independent state variables which are the magnetic flux density $\overrightarrow{B}$ and the total strain tensor $\overline{\overline{\varepsilon}}$. The magnetization $\overrightarrow{M}$ and the magneto-elastic stress tensor $\overline{\overline{\sigma}}_{me}$ are expressed as partial derivatives of the Helmholtz free energy density ψ with respect to $\overrightarrow{B}$ and $\overline{\overline{\varepsilon}}$:

$$\overrightarrow{M}(\overrightarrow{B},\overline{\overline{\varepsilon}})=-\frac{\partial\psi(\overrightarrow{B},\overline{\overline{\varepsilon}})}{\partial\overrightarrow{B}} \tag{1.9.20}$$

$$\overline{\overline{\sigma}}_{me}(\overrightarrow{B},\overline{\overline{\varepsilon}})=\frac{\partial\psi(\overrightarrow{B},\overline{\overline{\varepsilon}})}{\partial\overline{\overline{\varepsilon}}} \tag{1.9.21}$$

The magnetic field strength is then obtained as $\overrightarrow{H}=\frac{\overrightarrow{B}}{\mu_0}-\overrightarrow{M}$. The magneto-elastic stress tensor $\overline{\overline{\sigma}}_{me}$ includes elastic and magnetostrictive stress contributions.

Considering an isotropic material, the Helmholtz free energy ψ can be expressed by the following six scalar invariants:

$$\begin{array}{lll}I_1=tr(\overline{\overline{\varepsilon}}) & I_2=\frac{1}{2}tr(\overline{\overline{\varepsilon}}^2) & I_3=det(\overline{\overline{\varepsilon}})\\ I_4=\overrightarrow{B}.\overrightarrow{B} & I_5=\overrightarrow{B}.(\underset{\sim}{\overline{\overline{\varepsilon}}}\overrightarrow{B}) & I_6=\overrightarrow{B}.(\underset{\sim}{\overline{\overline{\varepsilon}}}^2\overrightarrow{B})\end{array} \tag{1.9.22}$$

The first three invariants describe purely mechanical loading, whereas the fourth invariant I_4 describes anhysteretic magnetic behavior. Invariants I_5 and I_6 describe the magneto-elastic coupling , and are written using the deviatoric part of the strain in order to eliminate the effect of hydrostatic pressure on magnetic behavior in $I_5$and I_6:

$$\underset{\sim}{\overline{\overline{\varepsilon}}}=\overline{\overline{\varepsilon}}-\frac{1}{3}tr(\overline{\overline{\varepsilon}})\overline{\overline{I}} \tag{1.9.23}$$

The Helmholtz free energy density $\psi(I_1,I_2,I_3,I_4,I_5,I_6)$ is then written as:

$$\begin{array}{c}\psi=\frac{1}{2}\lambda I_1^2+2GI_2-\frac{1}{\mu_0}(\frac{I_4}{2}+\Sigma_{i=0}^{n_\alpha-1}\frac{\alpha_i}{i+1}I_4^{i+1}+...\\ \Sigma_{i=0}^{n_\beta-1}\frac{\beta_i}{i+1}I_5^{i+1}+\Sigma_{i=0}^{n_\gamma-1}\frac{\gamma_i}{i+1}I_6^{i+1})\end{array} \tag{1.9.24}$$

where λ and G are the Lamé constants of the material, μ_0 is the permeability of free space and α_i, β_i and γ_i are the fitting parameters to be determined from the measurements under uniaxial stress applied along the magnetization direction. Since in linear elasticity is assumed, ψ does not depend on I_3. The number of model parameters n_α, n_β and n_γ are material dependent. They are determined by fitting the model to uniaxial $B(H)$ curves using various numbers and choosing the best fitted case.

The first two terms in equation (1.9.24) yield Hooke's law and account for the purely mechanical behavior, whereas the last three terms account for the magneto-elastic coupling. The summation term in the middle (with $n_\alpha > 1$) accounts for the nonlinear $\vec{M}(\vec{B}, \overline{\overline{\varepsilon}})$ relation. Finally, the quadratic dependence of invariant I_6 on $\overline{\overline{\varepsilon}}$ allows modeling the decreasing permeability under both compressive and high tensile stresses.

Figure 1.9.3 shows the modeling results for the anhysteretic magnetization and magnetostriction curves obtained using the Helmholtz energy based model under four uniaxial stress levels. As can be seen, the model is able to take into account the non-monotonic dependency of the permeability on the stress. In addition, flipping of the magnetostriction curve with respect to the axis of abscissa at high tensile stress is also successfully modeled.

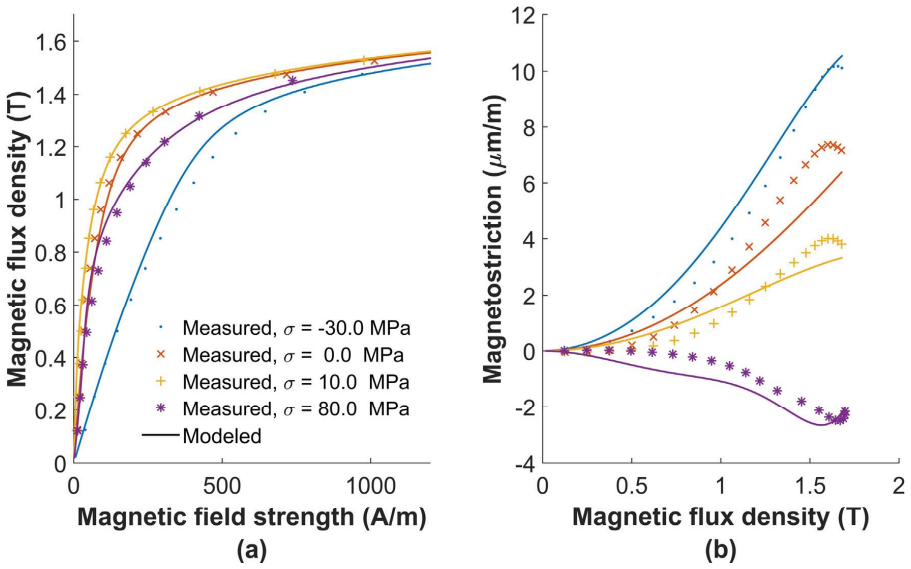

Figure 1.9.3: *Comparison of measured uniaxial stress dependent anhysteretic magnetization and magnetostriction on non-oriented (NO) Si-Fe electrical steel sheets with modeled results from HE model. (a) Anhysteretic magnetization and (b) anhysteretic magnetostriction results [4].*

1.9.1.4 Polynomial tensor model

This model is part of the so-called phenomenological approaches that describe the magnetostrictive phenomena based on experimental results at a macroscopic scale to deduce empirical laws of behavior. This model has been used to predict the magnetostrictive behavior of Terfenol-D [39], which is a material with a giant magnetostriction leading to a strong magneto-elastic coupling. It is often used with uniaxial compression prestressing in transduction applications.

From the experimental results on Terfenol-D presented in figure 1.9.4a, the author uses the following assumptions in order to simplify the model:

- Magnetostriction as a function of the flux density for a given stress has a parabolic shape ($\varepsilon^{\mu} \propto B^2$): this assumption is acceptable below saturation. Experiments on different Terfenol-D materials show that magnetostriction decreases for large inductions.
- The magnetostrictive behavior is isotropic: this hypothesis is not totally correct. In fact, the multi-directional magnetization measurements on Si-Fe samples made and presented in this work later on show that magnetostriction is very sensitive to the direction of magnetization.
- The magnetostrictive deformation seems to no longer depend on the stress from a prestressing level relatively low $\sigma^{ref} = -20\,\text{MPa}$, figure 1.9.4b: In case of materials with giant magnetostriction (high magneto-elastic coupling coefficients), the magnetostriction is very sensitive to the applied stress. However, this effect saturates very quickly, unlike conventional materials (Si-Fe for example).

This particular behavior of this type of material (Terfenol-D) allows the author to use the equivalent field approach to consider the effect of stress on magnetostrictive and magnetic behavior. This approach (field equivalent to an applied stress) used in [55] allows to deduce a magnetic field due to a stress thanks to the Maxwell[1] equalities relations and a set of magnetization curves at different stresses. Equation (1.9.25) is then obtained by linearization of the Maxwell equality (equation (1.9.26)).

$$H_i\left(\vec{B},\bar{\bar{\sigma}}\right) = H_i\left(\vec{B},\bar{\bar{\sigma}}^{ref}\right) - \underbrace{\frac{\partial \varepsilon_{kl}^{\mu}(B)}{\partial B_i}\overbrace{\left(\sigma_{kl}-\sigma_{kl}^{ref}\right)}^{\Delta\sigma}}_{equivalent\ field\ due\ to\ \Delta\sigma} \tag{1.9.25}$$

$$\left.\frac{\partial H_i}{\partial \sigma_{kl}}\right|_{\vec{B}} = \left.\frac{\partial \varepsilon_{kl}^{\mu}}{\partial B_i}\right|_{\bar{\bar{\sigma}}} \tag{1.9.26}$$

[1] Set of equations from thermodynamic potentials. They lead to the piezo-electric and magnetic coupling coefficients.

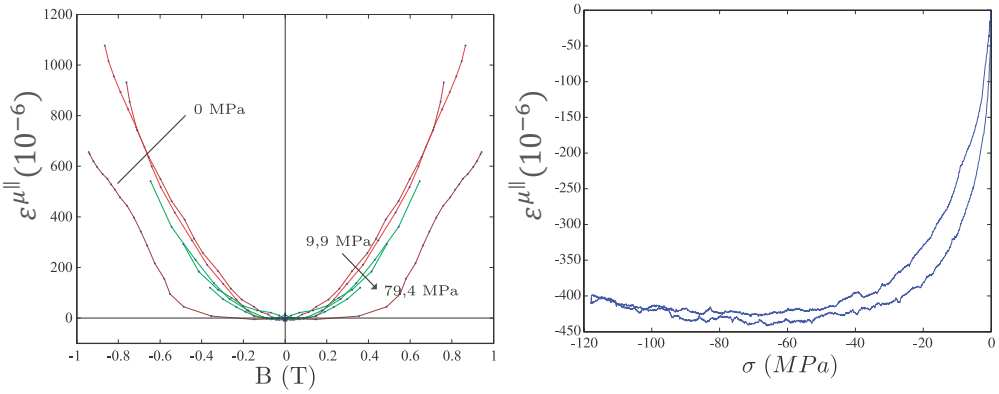

(a) *Magnetostriction of Terfenol-D rod under stress* $\varepsilon^{\mu}(B)$.

(b) ΔE *effect of Terfenol-D rod.*

Figure 1.9.4: *Magnetostrictive deformation measurements: (a) Anhysteretic magnetostriction of a Terfenol-D rod as a function of induction at different compression stresses, (b) magnetostriction (at zero field) due to compression of a Terfenol-D sample [39].*

Let $\overrightarrow{B}$ be the magnetic induction at a point of the material, then the magnetostrictive deformation tensor at this point with respect to the reference associated to $\overrightarrow{B}$ such that $\overrightarrow{B} = [\ B^{\parallel} \quad B_1^{\perp} \quad B_2^{\perp}\ ]^T$ is given by:

$$\begin{aligned} \overline{\overline{\varepsilon}}^{\mu} &= \begin{bmatrix} \varepsilon^{\mu\parallel} & 0 & 0 \\ 0 & \varepsilon_1^{\mu\perp} & 0 \\ 0 & 0 & \varepsilon_2^{\mu\perp} \end{bmatrix} \\ &= \sum_{n=0}^{N} \beta_n \| \overrightarrow{B} \|^{2(n+1)} \begin{bmatrix} 1 & 0 & 0 \\ 0 & -\frac{1}{2} & 0 \\ 0 & 0 & -\frac{1}{2} \end{bmatrix} \end{aligned} \tag{1.9.27}$$

Thanks to the Euler transformation, the magnetostrictive deformation tensor with respect to the reference of the material in which $\overrightarrow{B} = [\ B_1 \quad B_2 \quad B_3\ ]^T$ is given by:

$$\begin{aligned} \overline{\overline{\varepsilon}}^{\mu} &= \sum_{n=0}^{N} \beta_n \| \overrightarrow{B} \|^{2n} \begin{bmatrix} B_1^2 - \frac{B_2^2+B_3^2}{2} & \frac{3}{2}B_1B_2 & \frac{3}{2}B_1B_3 \\ \frac{3}{2}B_1B_2 & B_2^2 - \frac{B_1^2+B_3^2}{2} & \frac{3}{2}B_2B_3 \\ \frac{3}{2}B_1B_3 & \frac{3}{2}B_2B_3 & B_3^2 - \frac{B_2^2+B_1^2}{2} \end{bmatrix} \\ &= \frac{1}{2}\sum_{n=0}^{N} \beta_n \| \overrightarrow{B} \|^{2n} (3\overrightarrow{B} \otimes \overrightarrow{B} - \overrightarrow{B}.\overrightarrow{B}\overline{\overline{I}}) \end{aligned} \tag{1.9.28}$$

Magnetostriction parameters β_n can be calculated from the model and the experimental results by the least squares method [39]. This approach has the advantage of be-

ing simple, three-dimensional and easy to implement. However, the model is isotropic and the approach used to take into account stress limits the model to only Terfenol-D material. In this particular case, good matches with the experiments are observed (figure 1.9.5).

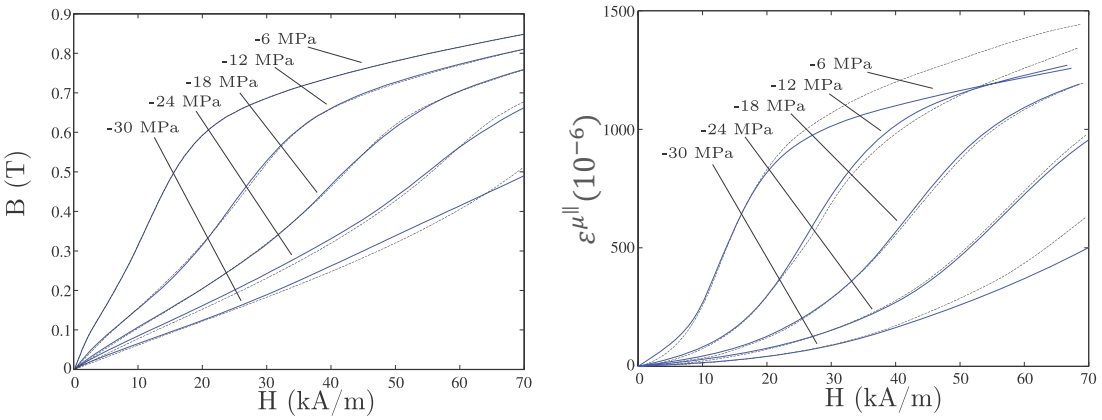

(a) *$B(H)$ curves.*

(b) *Magnetostriction curves $\varepsilon^{\mu\parallel}(H)$.*

Figure 1.9.5: *Comparison between measurements and simulation (dashed lines) of the flux density and magnetostriction under compressive stress of a Terfenol-D sample [39].*

1.9.1.5 Macroscopic model of magnetostriction based on energy minimization

Domain walls displacement and rotation of the magnetic moment in ferromagnetic sheets lead to a magnetization variation at a macroscopic scale. These processes results from the interaction between different energy terms [77] that we can discern at a mesoscopic scale:

- Exchange energy
- Magneto-crystalline anisotropy energy
- Magneto-elastic energy
- Magneto-static energy: Zeeman and demagnetizing field energy

This model aims to minimize the total energy composed by the energies quoted before, with respect to the magnetization. Nevertheless, during the interaction, the term of exchange energy is so big in ferromagnetic materials that leads to the alignment of the

magnetic moments of neighboring atoms inside domains. Although, this term is the same in all domains, and does not vary while magnetizing the sheet. Consequently, macroscopic magnetization depends on the domains volumes and the magnetization orientation insides domains. By considering isothermal process, and by choosing the demagnetized and unstressed state as the reference, the total energy of a ferromagnetic volume can be decomposed as follow [75]:

$$E_{total}(k,\theta) = E_z + E_d + E_{an} + E_\sigma \tag{1.9.29}$$

where:

- E_z: refers to the Zeeman energy.
- E_d: refers to the demagnetizing field energy.
- E_{an}: refers to the macroscopic anisotropy energy.
- E_σ: refers to the magneto-elastic energy.

The author assumes a planar magnetization giving the small thickness of the ferromagnetic sheet compared to other dimensions which favors a magnetic flux parallel to the sheet plane. Hence, the magnetization of the medium is described in polar coordinates by the couple (k,θ):

$$\vec{M} / \begin{cases} \|\vec{M}\| = k.M_S \text{ with } 0 \leq k \leq 1 \\ \left(\overrightarrow{\overrightarrow{RD},\vec{M}}\right) = \theta \text{ with } -\pi \leq \theta \leq \pi \end{cases} \tag{1.9.30}$$

M_s corresponds to the magnetization saturation and $\overrightarrow{RD}$ represents the rolling direction.

In the next chapter (chapter 2), the total energy terms will be presented in detail.

1.9.2 Multi-scale modeling

The multi scale model is part of the family of so-called medium-field or homogenization models [15]. It uses an energetic approach at the domains scale that relies on free energy to describe the macroscopic behavior (discussed in section 1.2). It involves changes of scale with localization operation (fields and stress at the local scale) and homogenization (averages). First, the microscopic behavior at the domain scale is found. Then, the behavior at the mono-crystal scale by homogenization is deduced. Finally, a last change of scale makes it possible to describe the behavior at the poly-crystal scale (figure 1.9.6).

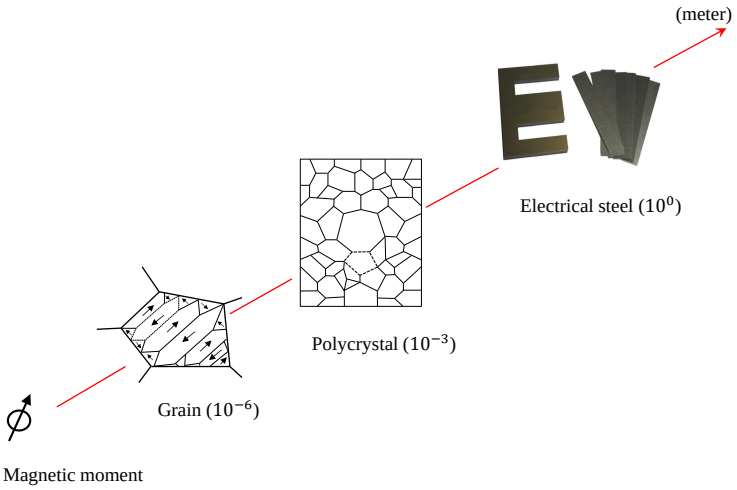

Figure 1.9.6: *Different modeling scale.*

1.9.2.1 Microscopic scale

The microscopic scale corresponds to the magnetic domains scale. In a magnetic domain named α, the magnetization inside $\overrightarrow{M_\alpha}$ is assumed to be uniform and directed in a direction $\overrightarrow{\gamma_\alpha}$ with respect to the crystallographic direction of the material. The magnetization and the magnetostriction deformation of the domain are defined by:

$$\overrightarrow{M_\alpha} = M_s \overrightarrow{\gamma_\alpha} = M_s{}^t [\gamma_\alpha^1 \gamma_\alpha^2 \gamma_\alpha^3] \tag{1.9.31}$$

$$\overline{\overline{\varepsilon_\alpha^\mu}} = \frac{3}{2} \begin{pmatrix} \lambda_{100}((\gamma_\alpha^1)^2 - \frac{1}{3}) & \lambda_{111}\gamma_\alpha^1\gamma_\alpha^2 & \lambda_{111}\gamma_\alpha^1\gamma_\alpha^3 \\ \lambda_{111}\gamma_\alpha^1\gamma_\alpha^2 & \lambda_{100}((\gamma_\alpha^2)^2 - \frac{1}{3}) & \lambda_{111}\gamma_\alpha^2\gamma_\alpha^3 \\ \lambda_{111}\gamma_\alpha^1\gamma_\alpha^3 & \lambda_{111}\gamma_\alpha^2\gamma_\alpha^3 & \lambda_{100}((\gamma_\alpha^3)^2 - \frac{1}{3}) \end{pmatrix}_{CR} \tag{1.9.32}$$

where γ_α^i are the direction cosines of the magnetization in the crystallographic reference frame CR, λ_{100} and λ_{111} are the saturation magnetostriction in the $< 100 >$ and $< 111 >$ directions respectively.

The energy of a magnetic material is the consequence of microscopic interactions within the material or with its external environment. These interactions can be of electrostatic origin (magneto-crystalline anisotropy energy related to the distribution of charges in the material) or magnetic (related to the presence of the magnetic moments of atoms). The free energy E_α of a domain α is assumed to be uniform and can be expressed as the sum of four energy contributions:

$$E_\alpha = E_\alpha^d + E_\alpha^{ani} + E_\alpha^\sigma + E_\alpha^{conf} \tag{1.9.33}$$

These energy terms have already been presented, we will recall their expression in the following.

The magneto-static or demagnetizing field energy E_α^d

In order to simplify the expression, we assume that the magnetic field is uniform in the domain and that it is equal to the magnetic field applied to the grain ($\overrightarrow{H}_\alpha = \overrightarrow{H}_g$). Under these conditions the magneto-static energy can be expressed as:

$$E_\alpha^d = -\mu_0 \overrightarrow{H}_g . \overrightarrow{M}_\alpha \tag{1.9.34}$$

where μ_0 is the vacuum permeability.

The anisotropy energy E_α^{ani}

$$E_{ani} = K_1((\gamma_\alpha^1\gamma_\alpha^2)^2 + (\gamma_\alpha^2\gamma_\alpha^3)^2 + (\gamma_\alpha^3\gamma_\alpha^1)^2) + K_2(\gamma_\alpha^1\gamma_\alpha^2\gamma_\alpha^3)^2 \tag{1.9.35}$$

where K_1 and K_2 correspond to the anisotropy constants of the material.

The magneto-elastic energy E_α^σ

With the hypothesis of homogeneous strain in the single crystal [26], it can be assumed that the magnetostriction deformation and stress are homogeneous. The magneto-elastic energy at the domain scale can be written as:

$$E_\alpha^\sigma = -\overline{\overline{\sigma}}_\alpha : \overline{\overline{\varepsilon}}_\alpha^\mu \tag{1.9.36}$$

σ_α and ε_α^μ are respectively the stress and the magnetostriction deformation tensors in the magnetic domain.

The configuration energy E_α^{conf}

The configuration effect was introduced to account for the anisotropy of the magnetostrictive behavior of rolled sheets as in the case of non oriented 3%Si-Fe, whose magnetostriction deformation in the rolling direction is different from that in the transverse direction (figure 1.9.7a). Without considering this effect, the model does not succeed in predicting the anisotropic behavior of the non-oriented grain (NO) material, figure 1.9.7b. In the case where this effect is integrated, there is a better match between measurements and simulations (figure 1.9.7c). In order to take this effect into account, a term called configuration energy is introduced.

In addition, this energy term is defined to take into account the possible non-randomness of initial domain configuration α, due for instance to plastic deformation [48] or to surface effect [49]. The chosen formulation corresponds to a magneto-mechanical form.

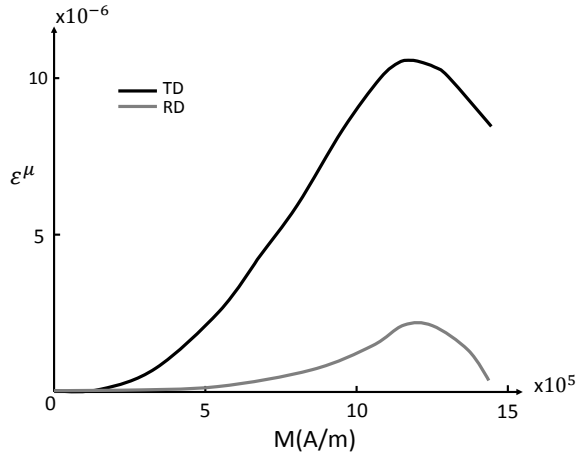

(a) *Measurements.*

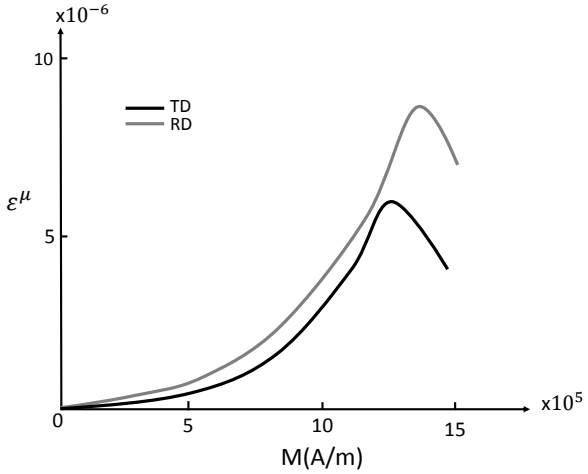

(b) *Model: without configuration effect.*

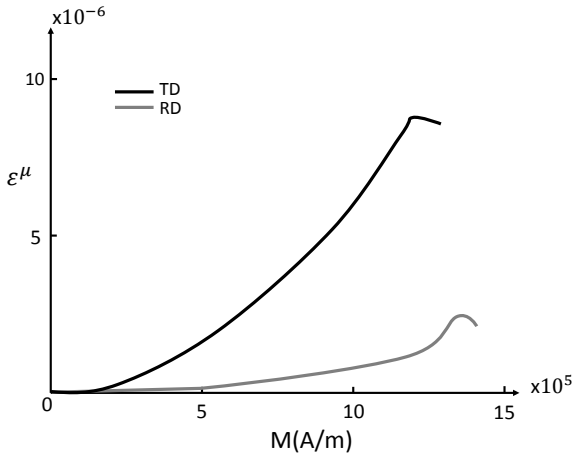

(c) *Model: With configuration effect.*

Figure 1.9.7: *Magnetostriction strain of NO 3%Si-Fe: Comparison between measurement and modeling results, with and without the consideration of the configuration effect [48].*

This configuration term can be considered as the effect of a residual stress uniform σ_c in the material. It is also equivalent to a demagnetizing energy [28], its expression is given by:

$$E_{\alpha}^{conf} = -\overline{\overline{\sigma}}_c : \overline{\overline{\varepsilon}}_{\alpha}^{\mu} \tag{1.9.37}$$

1.9.2.2 Single crystal scale

A single crystal is divided into several magnetic domains α. Each domain is characterized by an orientation of a uniform magnetization $\overrightarrow{M_{\alpha}}$. By knowing the direction $\overrightarrow{\gamma_{\alpha}}$ of the latter using the minimization of free energy (equation (1.9.33)), we can determine the magnetic state of the magnetic domain. This minimization is obtained by considering a large number of magnetic domains describing the best the behavior of the single crystal. There are two minimization approaches, a global minimization based on the Neel model (rigorous technique) and a second technique based on the Boltzmann function. For the sake of saving calculation time, we use an explicit formulation which is based on the Boltzmann function [15] to compute the volume fractions f_{α} of the magnetic domains:

$$f_{\alpha} = \frac{\exp(-A_s.E_{\alpha})}{\sum_{\alpha}\exp(-A_s.E_{\alpha})} \tag{1.9.38}$$

where A_s is a material parameter that can be written as a function of the initial susceptibility, the vacuum permeability and magnetization at saturation M_s [26]:

$$A_s = \frac{3\chi_0}{\mu_0 M_s^2} \tag{1.9.39}$$

Assuming that the elastic behavior of the mono-crystal is homogeneous and the magnetization (and the magnetostriction deformation) of the mono-crystal is equal to the average of the magnetizations (and the magnetostriction deformations) of the domains, then:

$$\overline{\overline{\varepsilon}}_g^{\mu} = <\overline{\overline{\varepsilon}}_{\alpha}^{\mu}> = \sum_{\alpha} f_{\alpha}\overline{\overline{\varepsilon}}_{\alpha}^{\mu} \tag{1.9.40}$$

$$\overrightarrow{M}_g = <\overrightarrow{M}_{\alpha}> = \sum_{\alpha} f_{\alpha}\overrightarrow{M}_{\alpha} \tag{1.9.41}$$

Finally, for a given loading (magnetic field $\overrightarrow{H}_g$ and stress $\overline{\overline{\sigma}}_g$), average magnetization and magnetostriction deformation of the crystal are computed.

1.9.2.3 Poly-crystal scale

In the case of a poly-crystal, the different crystallographic orientations between two neighboring grains causes heterogeneity of stresses and deformations. The distribution of the crystallographic orientations, called the texture, is then an important data to model these heterogeneity. In order to take into account the effects of the poly-crystalline structure, the multi-scale model presented here, consists of a succession of computation and change of scale (figure 1.9.8). Thus, from a given macroscopic loading, stress $\overline{\overline{\sigma}}$ and/or magnetic field $\overrightarrow{H}$, it makes it possible to calculate the macroscopic behavior of total deformation $\overline{\overline{\varepsilon^{\mu}}}$ and magnetization $\overrightarrow{M}$ of the sample.

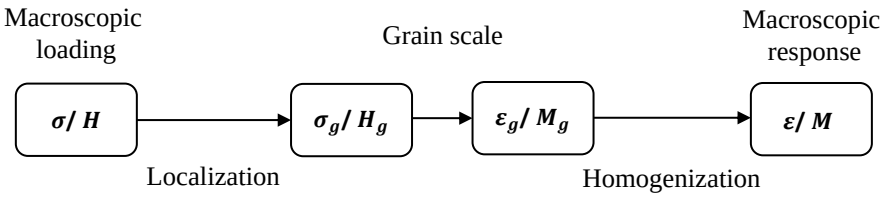

Figure 1.9.8: *Multi-scale modeling approach.*

A first so-called localization step, allows from a specific operators to pass from macroscopic loading to mono-crystal scale loading (equations (1.9.42) and (1.9.43)). Considering the mono-crystal (grain) as an ellipsoidal inclusion in a homogeneous medium and assuming that the mechanical and magnetic behaviors of the latter are isotropic, Eshelby shows that the deformation and stress of a mono-crystal are uniform. This hypothesis makes it possible to calculate the stress and the magnetic field seen by the mono-crystal (σ_g, H_g) from the macroscopic loading (σ, H) using the following equations:

$$\overline{\overline{\sigma_g}} = \overline{\overline{\overline{B_g}}} : \overline{\overline{\sigma}} + \overline{\overline{\overline{L_g}}} : (\overline{\overline{\varepsilon^{\mu}}} - \overline{\overline{\varepsilon_g^{\mu}}}) \tag{1.9.42}$$

$$\overrightarrow{H_g} = \overline{\overline{A_g}}.\overrightarrow{H} + \overline{\overline{M_g}}.(\overrightarrow{M} - \overrightarrow{M_g}) \tag{1.9.43}$$

$\overline{\overline{\overline{B_g}}}$ and $\overline{\overline{A_g}}$: are the elastic and magnetic localization operators.

$\overline{\overline{\overline{L_g}}}$ and $\overline{\overline{M_g}}$: are the elastic and magnetic incompatibility tensors.

Once the assumed uniform loading inside the single crystal is calculated in function of the external loading, the magnetization and the deformation of the mono-crystal correspond to the average of the magnetizations and deformations of the magnetic domains constituting it (equations (1.9.40) and (1.9.41)). By homogenization approach the poly-crystal response is calculated by averaging the response of the mono-crystals. Thus, we

obtain the macroscopic magnetization $\overrightarrow{M}$ and the magnetostriction deformation $\overline{\overline{\varepsilon^{\mu}}}$ of the poly-crystal:

$$\overrightarrow{M} = < \overline{\overline{{}^{t}A_g}}.\overrightarrow{M_g} > \tag{1.9.44}$$

$$\overline{\overline{\varepsilon^{\mu}}} = < \overline{\overline{\overline{{}^{t}B_g}}} : \overline{\overline{\varepsilon_g^{\mu}}} > \tag{1.9.45}$$

The multi-scale model simulates complex magnetic and mechanical loading across three scales (domain, mono-crystal and poly-crystal) while maintaining physical coherence. This distinction of the scales and the different rules of localization as well as the assumptions made, make it possible to simplify the calculations. It is able to take into account the effect of stress on the magnetic and magnetostrictive behavior of a material of different textures [27, 115]. But, in the case of NO Si-Fe, the effect of a tensile stress on the magnetization is not monotonous, something that the model with the current configuration of energies does not predict. To solve this problem, author in [98] proposed the addition of an energy term to the energy balance of a domain α. It will allow to take into account the evolution of the micro-structure in domains under stress. He called it energy of configuration demagnetizing field, it is defined by the following equation:

$$E_{\alpha}^{D} = -\mu_0 \overrightarrow{M_{\alpha}}.\overrightarrow{H_g}^{\sigma} \tag{1.9.46}$$

where $\overrightarrow{H}_g^{\sigma}$ is the configuration demagnetizing field (the magnetic field is assumed to be uniform in the grain: $\overrightarrow{H}_g^{\sigma} = \overrightarrow{H}_{\alpha}^{\sigma}$). It depends on the stress state, the following expression is proposed [28]:

$$\overrightarrow{H_g}^{\sigma} = -\overline{\overline{\mathrm{N}_g^{d}}}(\overline{\overline{\sigma_g}}).\overrightarrow{M}_g = \eta(N_g - \frac{1}{3}).\overrightarrow{M}_g \tag{1.9.47}$$

$\overline{\overline{\mathrm{N}_g^{d}}}$ is the demagnetizing effect tensor and η is a material parameter. $N_g$is the component of the tensor $\overline{\overline{\mathrm{N}_g^{d}}}$ in the same direction as the magnetization M:

$$N_g = \frac{1}{1 + 2\exp(-K\sigma_g^{eq})} \tag{1.9.48}$$

where K is a material parameter that is proportional to the initial slope of the unstressed anhysteretic magnetization curve and to the saturation magnetostriction in $<$ 100 $>$ direction (equation (1.9.49)). σ_g^{eq} is the equivalent stress for $\overline{\overline{\sigma_g}}$ [25], corresponding to the projection along the magnetic field direction of the deviatoric part of $\overline{\overline{\sigma_g}}$. The expression of the equivalent stress is given in equation (1.9.50), h is a unity vector corresponding to the direction of the magnetic field H_g. In case of uniaxial stress $\sigma_g^{eq} = \sigma_g$.

$$K = \frac{3}{5} A_s \lambda_{100} = \frac{3}{5} . (\frac{3\chi^0}{\mu_0 M_s^2}) . \lambda_{100} \tag{1.9.49}$$

$$\sigma_g^{eq} = \frac{3}{2} \overrightarrow{h} . (\sigma_g - \frac{1}{3} tr(\sigma_g) I) . \overrightarrow{h} \tag{1.9.50}$$

This new energy term modifies the distribution of domain fractions when the material is subjected to mechanical stress. The figure 1.9.9 shows the results of the magnetization curves of Si-Fe GO without and with the consideration of the configuration demagnetizing field term. It can be clearly seen that the modeling of the magnetization curves with this energy term takes into account non-monotonicity under high tensile stress.

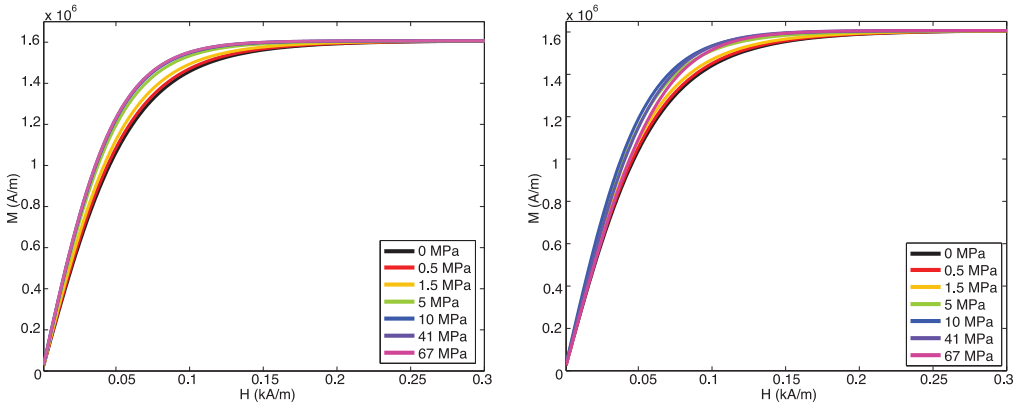

(a) *Without the configuration demagnetizing field.* **(b)** *With the configuration demagnetizing field.*

Figure 1.9.9: *Modeling of 3%Si-Fe behavior: Anhysteretic magnetization curves under tensile stress of a mono-crystal in* $< 011 >$ *direction [98].*

1.10 Conclusion

In this chapter different aspects of magnetic materials were discussed at different scales including the effect of stress on the magnetic and magnetostrictive properties: the magnetic and magnetostrictive behavior originate from the interactions between magnetic domains generated by an energy equilibrium. This equilibrium evolves under the application of a magnetic field or mechanical stress. It can be seen from the presented part that the magneto-elastic behavior in magnetic materials is complex and its improvement is still in progress.

As seen, many authors have tried (and still) to model the magneto-elastic coupling with different approaches of which the widely used are multi-scale and phenomenological modeling. The first approach is a physical approach based on a scale changes to

describe the macroscopic behavior, while the second relies more on the experimental measurements with easy incorporation in computation code and few parameter identification. Our model is based on the two approaches to fulfill a good compromise between the material physics and experimental behavior laws.

The next chapter will focus on magnetic and magnetostrictive measurements under uniaxial mechanical stresses. These experimentations are made on ten samples cut at different angles with respect to the rolling direction to study the anisotropy effect and stress dependency. Afterword, the in-house model is described and the contribution made in this thesis will be discussed.

CHAPTER 2

MAGNETO-ELASTIC BEHAVIOR: EXPERIMENTAL CHARACTERIZATION AND MODELING

2.1 Introduction

In this chapter, the magneto-elastic behavior of non-oriented electrical steel is characterized, then the measurements and modeling results are compared. First, the material under study is presented from a magnetic and mechanical point of view. Secondly, the measurement setup and instrumentation used are introduced. Next, the measurements under mechanical loading are performed and the results are discussed. These measurements are made on 10 samples cut in different directions with respect to the rolling direction. Based on the measurements results, the influence of the mechanical state on the magnetic and magnetostrictive behavior of non-oriented silicon iron alloys is analyzed, as well as the consequences of magneto-elastic coupling on the magnetic performances of these materials. The main purpose of these measurements is to build an extensive database of magnetic and magnetostrictive behaviors that will be useful for the identification and validation of the model.

The second part of this chapter will be dedicated to a presentation of the model studied in this thesis. We will then detail the contributions and modifications retained to account for the effect of mechanical stresses in addition to the effect of anisotropy, which consists of one of the expectations of this thesis. The modeling results are compared with the experimental results in terms of magnetic and magnetostrictive anhysteretic behaviors.

Experimental characterization

2.2 The studied material

Si-Fe non-oriented (NO) magnetic sheets are inexpensive soft magnetic materials, which make them largely used in applications of electrical engineering, such as rotating or static electrical machines (transformers), as well as certain actuators, sensors and inductors. These materials resulting from traditional metallurgy, become after rolling more or less textured (anisotropy) and alloyed in silicon according to the application requirements. The addition of silicon (Si) makes possible to improve the physical and mechanical characteristics of pure iron, to correct certain deficiencies (electrical resistivity, mechanical properties, etc.) and to propose a family of materials having different properties of use.

The studied material contains about 3% of silicon and other elements in very small shades summarized in table 2.1a to reduce the magnetic aging. It is a body centered cubic alloy (Fe-Si), it has a high and positive magneto-crystalline anisotropy constant K_1(table 2.1b). The direction of easy magnetization corresponds to $< 100 >$, difficult magnetization is along $< 111 >$ direction, which means that a strong energy is needed to go from one direction to another (36 kJ.m^{-3}). The other main property is the magnetostriction deformation, which is a consequence of the magneto-elastic coupling between the deformation of the material and its magnetization state, characterized by two constants λ_{100} and λ_{111} which are different in amplitude (table 2.1b).

The electrical sheets of the studied material belong to the family of so-called "fully processed" sheets. These sheets are usually used in rotating machines and low power transformers due to their low magnetic losses (table 2.1c). Particular care is taken to magnetically optimize the re-crystallization and the grain growth (figure 2.2.1), and also to electrically isolate the surface with a layer adapted in composition and thickness to the needs of the application. In tables 2.1c and 2.1d, the magnetic and mechanical characteristics of this material are shown. As it will be seen in the chapters that follow, these magnetic performances are strongly affected by the mechanical stress.

Non-oriented electrical steels have been among the steel products that benefit most from texture optimization for the improvement of magnetic properties. The texture is a population of crystallographic orientations whose individual components are linked to their location within the micro-structure. The ESBD (Electron Backscatter Diffraction) technique is used to determine the crystallographic information in non-oriented electrical steel sheets and other materials as well. The result of this technique is named pole figure (figure 2.2.2). On the right of figure 2.2.2 is illustrated pole figure of GO Si-Fe texture (so-called Goss texture). A strong anisotropy can be observed between the rolling (RD) and transverse direction (TD) explained by a higher probability of magnetic domains to be oriented along RD. Compared to GO Si-Fe, NO Si-Fe has a more

Shades	Si	Mn	C	S	P
wt%	3	0.1	0.005	0.003	0.01

(a) *The chemical composition of 3%Si-Fe NO [98].*

Constants	Value	Unit
K_1	36	kJ.m^{-3}
λ_{100}	23	µm/m
λ_{111}	5	µm/m

(b) *Anisotropy and magnetostriction constants.*

Properties	Value	Unit
Specific total loss at 50 Hz - 1.5T	2.25	W/kg
Magnetic induction at H=2500 A/m	1.53	T
Relative permeability at 1.5 T	610	H/m
Coercivity	35	A/m
Anisotropy of loss	10	%

(c) *Magnetic properties.*

Properties	Value	Unit
Density	7600	kg/m^3
Resistivity	59	$\mu\Omega cm$
Young's Modulus RD	185	GPa
Young's Modulus TD	200	GPa
Poisson coefficient	0.27	-
Yield strength	460	MPa
Tensile strength	580	MPa

(d) *Mechanical properties.*

Table 2.1: *Magnetic and mechanical characteristics of Si-Fe 3% NO of thickness 0.35 mm (Source: Cogent Power Ltd).*

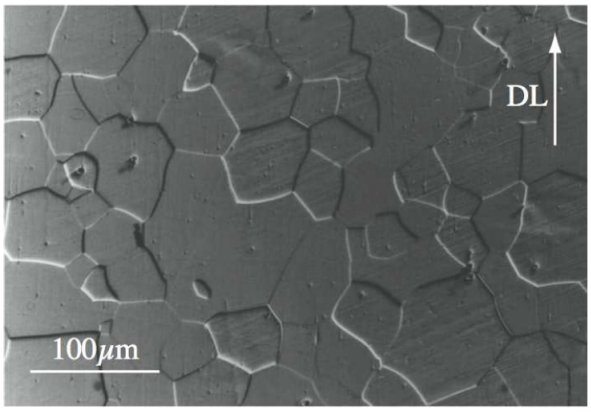

Figure 2.2.1: *A typical micro-structure of a fully processed and non-oriented electrical steel sheet : 3%Si-Fe NO [98].*

complex texture characterized by random cube texture where each grain has the [100] plane in the sheet plane, leading to isotropic properties. However, looking to the pole figure of NO Si-Fe material (figure 2.2.2 on the left) still some degree of anisotropy exists with a Goss $110 < 001 >$ component, but not with the same magnitude as GO Si-Fe.

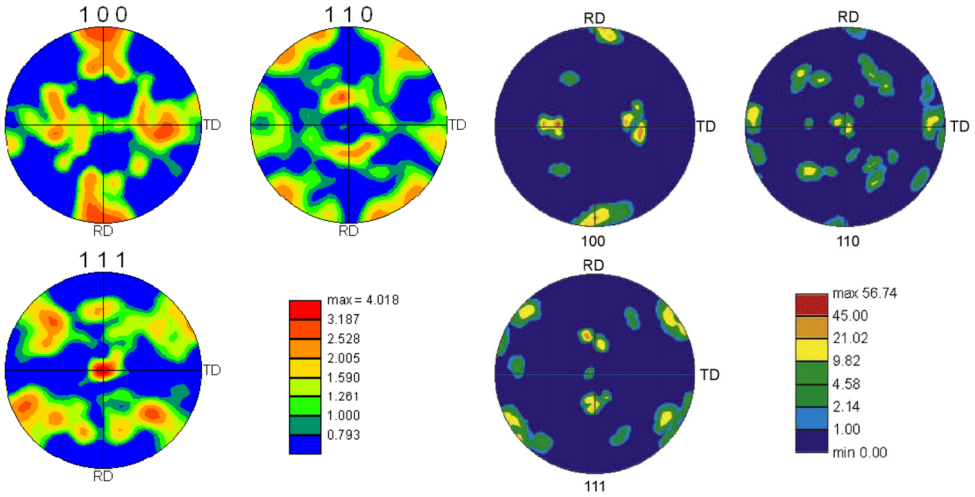

(a) *NO 3% Si-Fe* **(b)** *GO 3% Si-Fe*

Figure 2.2.2: *Pole figures obtained from electron back scattered diffraction (EBSD).*

2.2.0.1 Electrical sheets sampling: motivations

In order to highlight the effect of anisotropy and stress on the magnetic and magnetostrictive properties of the studied material (3%Si-Fe NO), a number of samples were cut in different directions with respect to the rolling direction as shown in figure 2.2.3. Thereby, 10 samples of 150 mm long, 30 mm wide and 0.35 mm thick are obtained. The chosen dimensions of the sample favor a uniform magnetization along its length [3, 35]. This choice makes it possible to validate the assumption of a unidirectional magnetization to identify parameters of the model. Moreover, characterizing samples of the same size minimizes the form effect. Hence, any variation of behavior (magnetic or magnetostrictive) from a sample to another, is purely the anisotropy effect of the material. Finally, the rectangular shape of the sample ensures a uniform stress when it is subjected to a tensile or compressive stress. Despite all this precautions, some difficulties related to buckling persisted when measuring magnetostrictive deformation under compressive stress. A detailed description of this issue will be given in the following section.

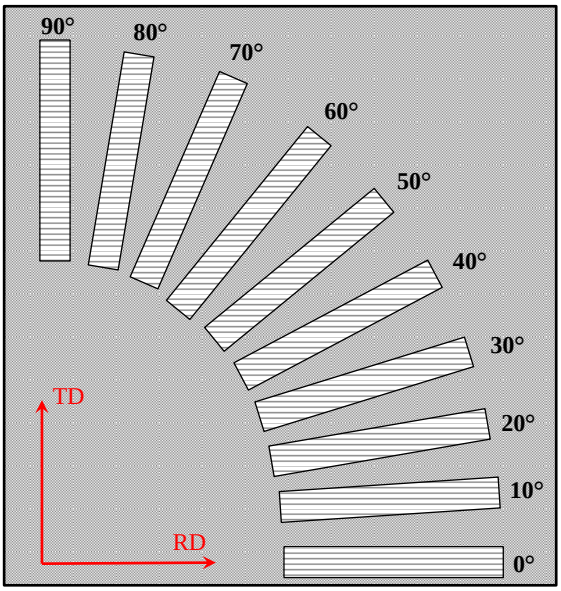

Figure 2.2.3: *10 steel sheets samples cut along different directions with respect to the rolling direction by water jet cutting machine.*

2.3 Magnetic and magnetostrictive behavior characterization under mechanical stress

2.3.1 Description of the set-up

2.3.1.1 Single Sheets Tester (SST)

The characterization of magnetic steel sheets is usually done by two methods: the Epstein frame and the single sheets tester. The Epstein method requires the sample to be cut into the shape of strips, the mandatory multiple of 4 standard dimensions are then trimmed, weighed and annealed according to specific standards. These strips are then stacked inside the solenoids so as to form joints in the double overlap angles. However, these operations involve a long and tedious manipulation. Moreover, the overlaps of the strips at the "corners" can be a source of other deformations than magnetostriction (e.g. magnetic forces).

In order to avoid these problems and for the sake of simplicity, we will use an adapted SST characterization method (figure 2.3.1). It ensures a better homogeneity of the magnetic field all along the sample. The SST is equipped with a special mechanism of yoke in order to insert and remove the tested steel sheets easily and to ensure the magnetic flux closure. The simplicity of the method can be however, a source of dispersion of the measurements due to the change of sample or instrumentation (strain gauge and gauge gluing).

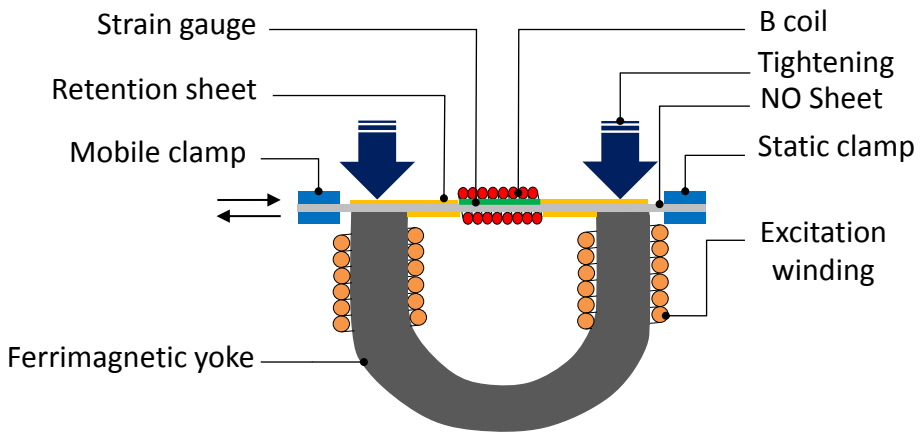

Figure 2.3.1: *Device used for magnetic and magnetostrictive measurements on steel sheets samples (SST).*

Figure 2.3.1 gives a detailed description of the characterization SST device. The ferromagnetic yoke in Silicon Iron allows the magnetic flux closure created by the exci-

tation winding (two windings in series, 70 turns each). The yoke has a magnetic mean path of 250 mm, a section of 30×30 mm^2 and an end-to-end length of 125 mm. The B-coil allows the measurement of the magnetic flux flowing in the sample. This flux is estimated by integration of the voltage across the B-coil. The magnetic field H created around the sample can be evaluated in first approximation by Ampere's theorem. Whereas, the magnetostriction deformation measurements are made using strain gauge disposed on the top of the specimen. The strain gauge measures only longitudinal magnetostriction deformation ε^{μ} (parallel to the direction of the applied field H) as shown in figure 2.3.2. All elements are arranged in a stress application device (figure 2.3.3) for imposing a mechanical loading in addition to the magnetic loading. To avoid buckling during measurements when a compressive stress is applied, retention plates were placed on the steel sheet surface on both sides (figure 2.3.1). To minimize the damping effect on magnetostriction, the retention plates were oiled before put in place. Leaving the sample free to move generates a variation of the air gap that can cause magnetic forces of Maxwell type to appear. A suitable tightening is applied to avoid air gaps and therefore, reduce the effect of these magnetic forces.

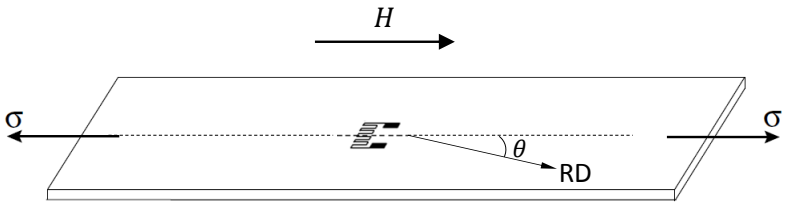

Figure 2.3.2: *Direction of applied stress and magnetic field for samples cut at* $\theta = (0°, 10°...90°)$ *with respect to the rolling direction.*

Figure 2.3.3 shows the mechanism used for applying in-plane uniaxial stress. It offers the possibility to exert both tensile and compressive stress up to ±50 MPa for a 30 x 0.35 mm cross-sectioned SST sample. To apply the required force, a manual locking screw system is used (clamping crank in figure 2.3.3). Also, to better control the stress levels, a compression spring is considered. Thus, a stress resolution of 0.1 MPa can be achieved. Furthermore, clamps with a grinded surface are used to ensure proper gripping of the SST sample. Guide rails passing through the lower part of the clamps and fixed to the rigid back wall, ensure the in-plane application force. Finally, all the components of the stressing mechanism are made of non-magnetic stainless steel to avoid any flux leakage path.

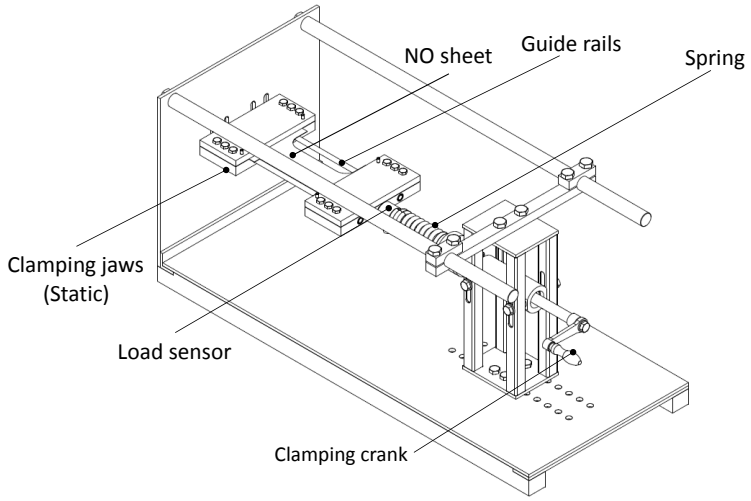

Figure 2.3.3: *Description of the stressing mechanism [106].*

2.3.1.2 Excitation system

Since the relationship between the flux density B and the magnetic field H is nonlinear, the induced magnetic flux density in the sample differs from the one generated initially by the excitation. If we assume sinusoidal magnetization waveform of the excitation, the measured flux density B has a different waveform in amplitude and shape (figure 2.3.4). In order to overcome this issue and obtain a sinusoidal magnetic flux density B in the SST sample, a programmable power source controlled by an algorithm is set up to iteratively correct the magnetic flux density B. The schematic diagram of the excitation control system is shown in figure 2.3.5.

The excitation control system was developed in Aalto university [106]. A programmable power source (AMETEK CSW 5550VA) and a data acquisition system (DAQ-NI USB-6251 BNC) with analog output are operated by a PC to control the magnitude and the waveform of the supply voltage so as to obtain a sinusoidal flux density in the SST sample. Then, an algorithm programmed using MATLAB/DAQ toolbox control the feedback of the excitation voltage. Low-noise/high-gain signal amplifiers are also used to amplify the signal obtained from the B-coil. In addition, a high sampling rate DAQ system (DEWETRON 50 khz) controlled by PC/DEWE software is used to retrieve the measured signal for the flux density. The complete process to magnetize the sample and iteratively feedback control can be described as follows:

1. **Excitation:** Start from a sinusoidal voltage shape with amplitude depending on the magnetic flux density level and excitation frequency.

2. Induced voltage in the search coil may not be sinusoidal when the sample saturates i.e. at higher amplitudes of the flux density (figure 2.3.4).

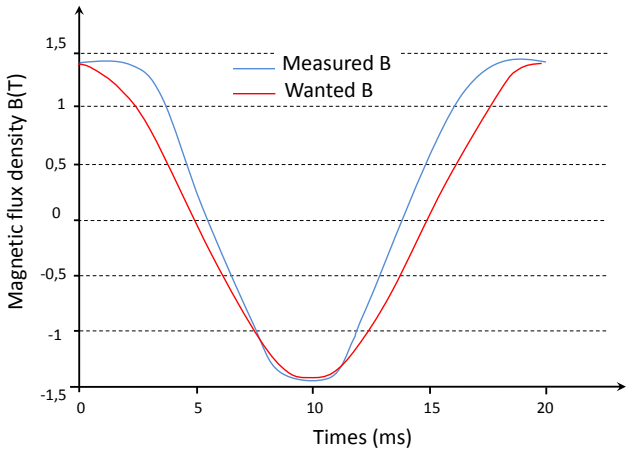

Figure 2.3.4: *The curve of one period of the measured B (blue line) and wanted B (red line) signals.*

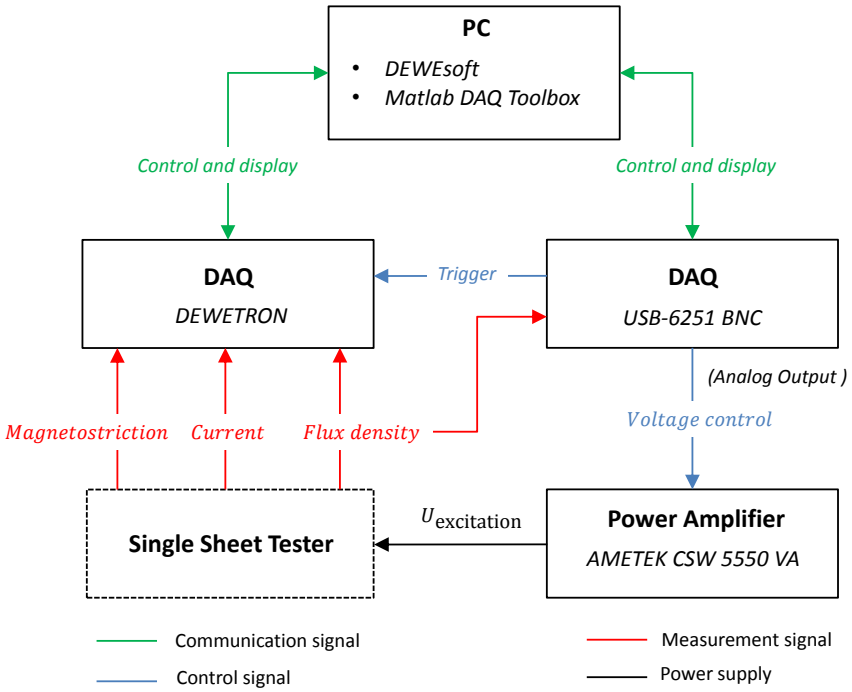

Figure 2.3.5: *Schematic representation of the magnetizing and control system.*

3. **Amplitude Control**: The amplitude correction, within the user-defined tolerance, is done by acting on the input signal to the power amplifier and based on the amplitude error (ε_{amp}) between the measured and the wanted magnetic flux density ($B_{measured}$ and B_{wanted}).

4. **Waveform Control**: Second the waveform control is done. However, during the waveform control if the error in amplitude exceeds the user defined tolerance, the amplitude and waveform control will be done again.

5. **Termination Criteria**: Both the controls are iterated until the convergence criteria in equation (2.3.1) are met.

$$error_{relative} = \frac{||B_{measured} - B_{wanted}||}{||B_{wanted}||} \leqslant \text{user specified tolerance} \tag{2.3.1}$$

Further details on the sequence control can be found in [106]. The general view of the experimental device for the magnetic and magnetostrictive measurements under stress is shown figure 2.3.6.

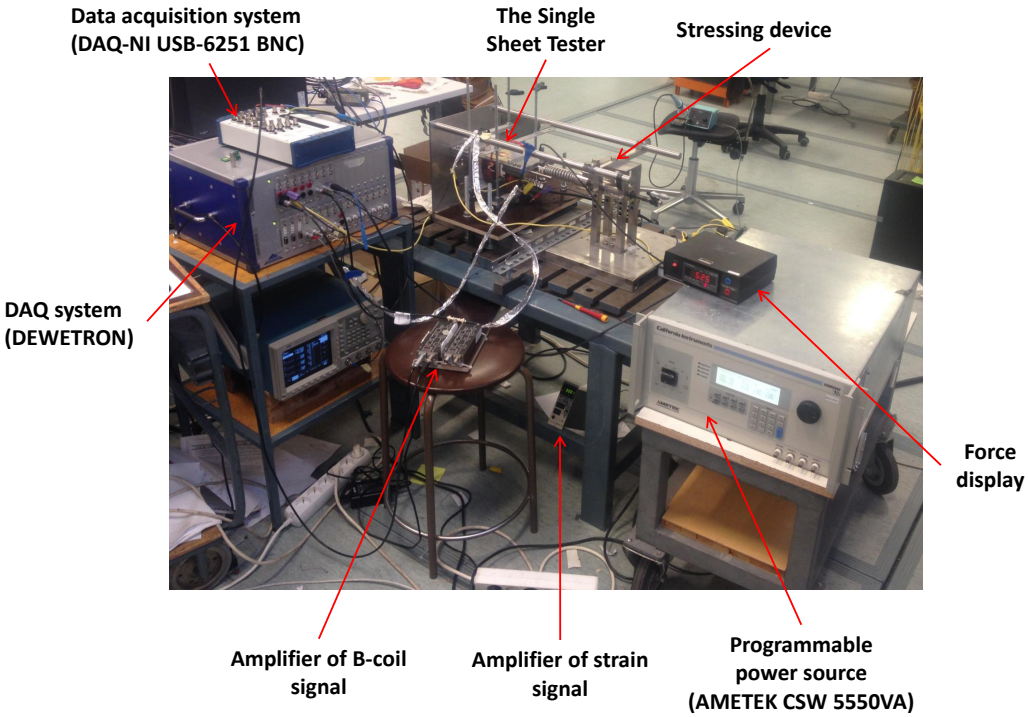

Figure 2.3.6: *General view of the experimental set-up.*

2.3.2 Magnetic measurements

2.3.2.1 Magnetic flux density measurements

The search coil or B-coil sensor method is a common approach to measure the magnetic flux density B induced in a magnetic steel sheet (figure 2.3.7). The search coil should feel the same flux as the sample, that is why it is wound directly around it to avoid measurement errors. The induced voltage in the coil sensor V_{bcoil} is proportional to the magnetic flux variation passing through the coil ($\frac{d\phi_{bcoil}(t)}{dt}$) and the number of turns of the coil sensor N_{bcoil} according to Faraday's law:

$$V_{bcoil}(t) = -N_{bcoil}.\frac{d\phi_{bcoil}(t)}{dt} \tag{2.3.2}$$

The integration of the induced voltage V_{bcoil} at the B-coil terminals allows to determine the magnetic flux density B:

$$B = \frac{-1}{N_{bcoil}S}\int V_{bcoil}dt - \mu_0\frac{S_{bcoil}-S}{S}H \tag{2.3.3}$$

where S and S_{bcoil} correspond respectively to the sample and B-coil sensor cross section. The second term of equation (2.3.3) considers the magnetic flux between the B-coil sensor and the sample. Given its small value for our experiments, it will be neglected and only the first term is used to calculate B.

2.3.2.2 Magnetic field measurement

The magnetic field H is measured either directly or indirectly. With the direct method, an H-coil sensor is used to measure locally the magnetic field at the top surface of the sample (figure 2.3.7), assuming that the tangential component of the magnetic field is continuous across the sample. The second approach is the indirect magnetic field measurement that calculate the magnetic field by knowing the magnetization current. According to Ampere's law, if a current I is going through a magnetization winding made of N_{win} turns in a closed magnetic circuit of a magnetic mean path of l_m, the magnetic field can be calculated by the following formula:

$$H = \frac{N_{win}I(t)}{l_m} \tag{2.3.4}$$

To obtain a satisfactory result by this technique, the magnetic path should be clear and well defined, and the potential drop should be completely on the sample. The uncertainty in the determination of l_m in the ferromagnetic frame decreases the accuracy of this method, since l_m can vary with the peak magnetic flux density, excitation frequency, shape of the excitation waveform - whether it is sinusoidal or not - and the material anisotropy [72]. The advantage of the current method (I) is that the measured

signal is relatively large and almost free of distortion compared with signal obtained by the direct method (H-coil sensor). Nevertheless, this method is not recommended in rotational core magnetization where the magnetic flux path is not well known.

Before using the two sensors (H-coil and B-coil) for magnetic properties measurements, a calibration was carried out to estimate their sections, the details of this study can be found in the appendix **A**. A comparison between H-coil sensor method and Ampere's law method showed that the latter gives better and accurate measurements (appendix A.2). Hence, this method will be used for magnetic field measurements.

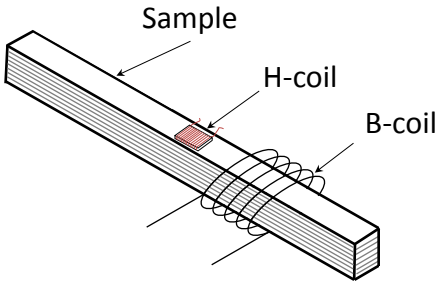

Figure 2.3.7: *Examples of B-coil and H-coil sensors.*

2.3.3 Magnetostriction measurements

The magnetostrictive strain was measured by means of two methods: strain gauges and laser vibrometer. The setup of each methods will be described. However, measurements of magnetostriction strain on single sheets samples were exclusively done by the strain gauge method because of the complexity of setting up the laser vibrometer method. But for the laminated structure, both methods were used and compared (chapter 3).

Strain gauge

The strain gauge has become a common technique because of the simplicity of strain measurement. After the insulation coating has been removed to prepare the surface for a better contact with the sample, the strain gauge is bonded to the sample surface using an epoxy resin on the top surface and in the middle of the samples to locally measures the longitudinal magnetostrictive deformation parallel to the magnetization direction. Then, the output wires of the gauge are soldered to the gauge terminals. Then, the strain gauge is connected with an electronic circuit (DPM-900/950) in a quarter bridge configuration (figure 2.3.8) to amplify and filter the noise signal. The main characteristics of the strain gauge used in this PhD work are summarized in Table 2.2.

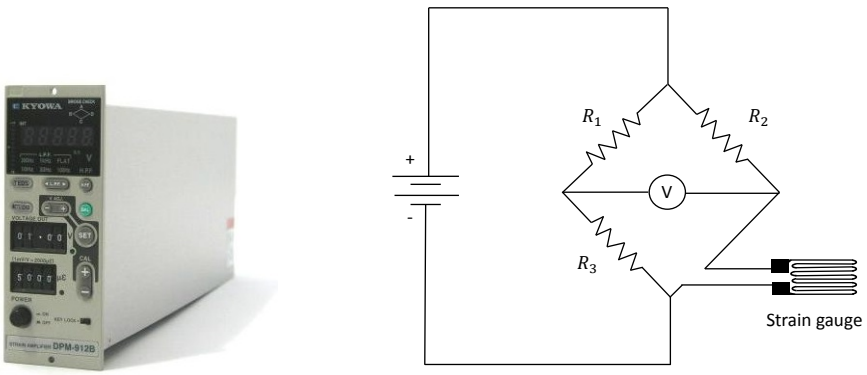

(a) *Electronic amplifier DPM-900/950.*

(b) *Wheatstone bridge in quarter bridge configuration.*

Figure 2.3.8: *Electronic amplifier and bridge configuration for strain gauge.*

Gauge reference	KFN-2-350-C9-11
Gauge factor	1.93 ± 2.0 %
Gauge length (mm)	2 mm
Gauge width (mm)	3 mm
Gauge resistance (Ω)	350 ± 1.8

Table 2.2: *Characteristics of used strain gauge.*

Despite the numerous advantages of the strain gauges (repeatability, accuracy, simplicity ... etc), this method has some disadvantages. Measurements at low amplitudes are very noisy and even by filtering, the signals obtained remain unusable. Also, the fact of removing the coating introduces another source of variability that can influence the measurement of magnetostriction deformation. Moreover, measurements by strain gauges are very local. For geometries where the field is parallel to the strain measurement, this raises no problem, however, for structures such as the transformer core, a global measurement is more appropriate because of the presence of rotating field in the corners for example. To overcome these limitations, a non-contact strain measurement approach based on laser interferometry is proposed. SIOS SP-S vibrometer sensor was chosen for our new magnetostrictive strain measurement setup, which will be explained in details further on in chapter 3.

2.3.4 Demagnetizing process

For the reliability of the magnetic and magnetostrictive measurements results, a demagnetization process is carried out on the electrical steel samples before starting any magnetic and magnetostrictive measurements. The demagnetization principle works with a controlled alternating magnetic field, passing through a maximum value and then reduced to zero. Besides, this demagnetization curve guarantees the elimination of any residual magnetic field. The working principle of this process is illustrated in figure 2.3.9.

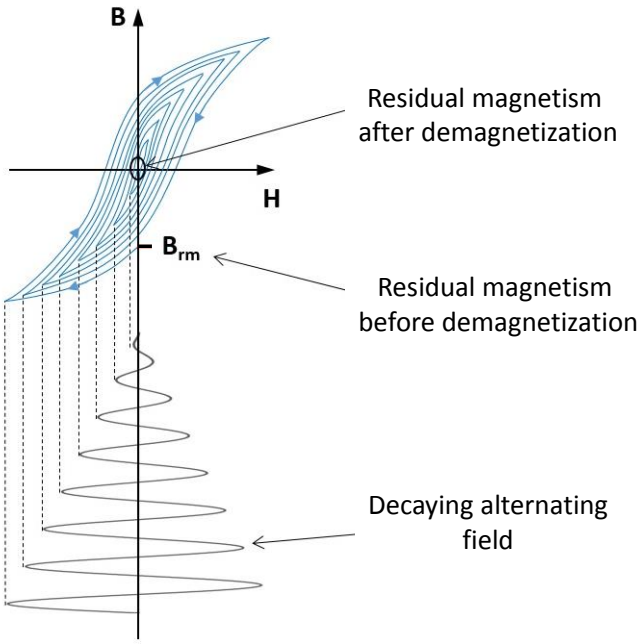

Figure 2.3.9: *Description of demagnetization process.*

First, to overcome the coercive force and reverse the polarity of the magnetic moments in the material, we need a high intensity. Moreover, in order to reduce the induced currents and help the magnetic field penetration, a low frequency is required. Second, the high number of the demagnetizing pulse oscillations make it possible to reach all magnetic moments. Finally, a good result is then obtained only if the pulse stops practically with a zero current. Otherwise, a sudden interruption of the magnetic flux leads to a measurable residual magnetism.

2.3.5 Average or anhysteretic magnetic and magnetostrictive curves extraction

After applying the mechanical stress σ to the electrical steel sample, an elastic deformation ε^e and a magnetostrictive deformation ε^μ appear according to the following equation:

$$\sigma = E.\varepsilon^{'} = E.(\varepsilon^e + \varepsilon^\mu) \tag{2.3.5}$$

Before starting the magnetostrictive and magnetic measurements, the deformation $\varepsilon^{'}$ signal is set to zero thanks to the electronic circuit (figure 2.3.8a). Furthermore, resetting the Wheatstone bridge to zero before the cyclic measurement maintains a high measurement sensitivity of the magnetostrictive deformation and measures only magnetostrictive changes at zero magnetization.

We are particularly interested in anhysteretic curves because of their relevance. They will also be used to characterize the model parameters offering an easy comparison with the anhysteretic model results. The measured signals are first filtered with low pass filter (7 harmonics) to reduce noise and averaging is performed over 10 periods. Then, the obtained branches of magnetostrictive deformation or magnetic cycles are averaged point by point to result in anhysteretic or averaged curves. Figure 2.3.10 shows the signal conditioning applied for extracting the anhysteretic magnetic and magnetostriction curves.

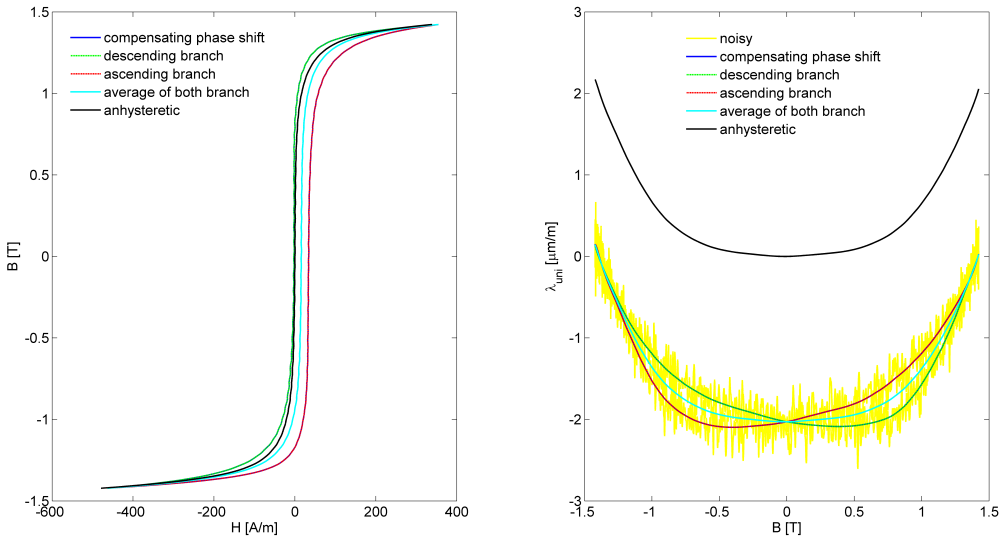

Figure 2.3.10: *Signal conditioning applied to obtain anhysteretic magnetic and magnetostrictive curves.*

2.4 Results: multi-directional measurements under uniaxial stress

As previously mentioned, to illustrate the magnetic and magnetostrictive behavior under stress, we have considered the median curve between the branches of the hysteresis cycle (averaged over several periods) as the anhysteretic curve. After removing the strain corresponding to the elastic deformation, the magnetostriction curves have been extracted following the same process, by calculating the median curve of the butterfly loops. This procedure of calculating the median curve can be used for low frequency measurements, which is the case in the present work [41].

2.4.1 Magnetic measurements

Magnetic measurements were carried out under various mechanical loading from -15 MPa (compression) to 50 MPa (tension), with a sinusoidal flux density and a frequency of 6 Hz. It is worth noticing that the measurements were done on a non-oriented steel sheets (3% Si-Fe alloy) for many directions with respect to the rolling direction $\theta = (0°, 10°...90°)$ as it will be discussed afterwards.

Figures 2.4.1 and 2.4.2 show the $B(H)$ curves of the NO Fe-Si samples under tensile and compressive stresses from the rolling to the transverse direction with 10° step. In general trends, the magnetization curves reveal that the permeability increases under tensile stress and decreases under compressive stress. Similar behavior has also been observed in [98, 4, 93, 92] for NO electrical steel under uniaxial stress in the rolling direction. However, the measurements carried out show a different behavior for the other directions particularly under tensile stress (figures 2.4.1 and 2.4.2). These figures indicate that the sample is more sensitive to the effect of tensile stress as the direction go from 0° to 90° direction with respect to the rolling direction, whereas, compressive stress decreases the permeability for all samples cut in different direction. For sample in 0° direction (rolling), the curves at 0 and 10 MPa are superimposed, which reveals that the permeability has improved in this interval; beyond 10 MPa the permeability decreases, while for 10° direction, it decreases starting from 10 MPa stress. Samples cut at 20° and 30° direction have their permeabilities improved by tensile stress up to 30 MPa, beyond that, it starts decreasing. For 40° and 50° direction samples, the same behavior as 10° direction sample is observed. The permeability start to increase again for 60° direction sample, a significant amelioration is noticed at 10 MPa. The same observation is noticed for 70° direction sample but less striking. Similar trends are found for 80° and 90° direction samples, the permeability improves up to 30 MPa this time. Independently of the magnetization direction, the compressive stress deteriorates the permeability even at low magnitude (-5 MPa).

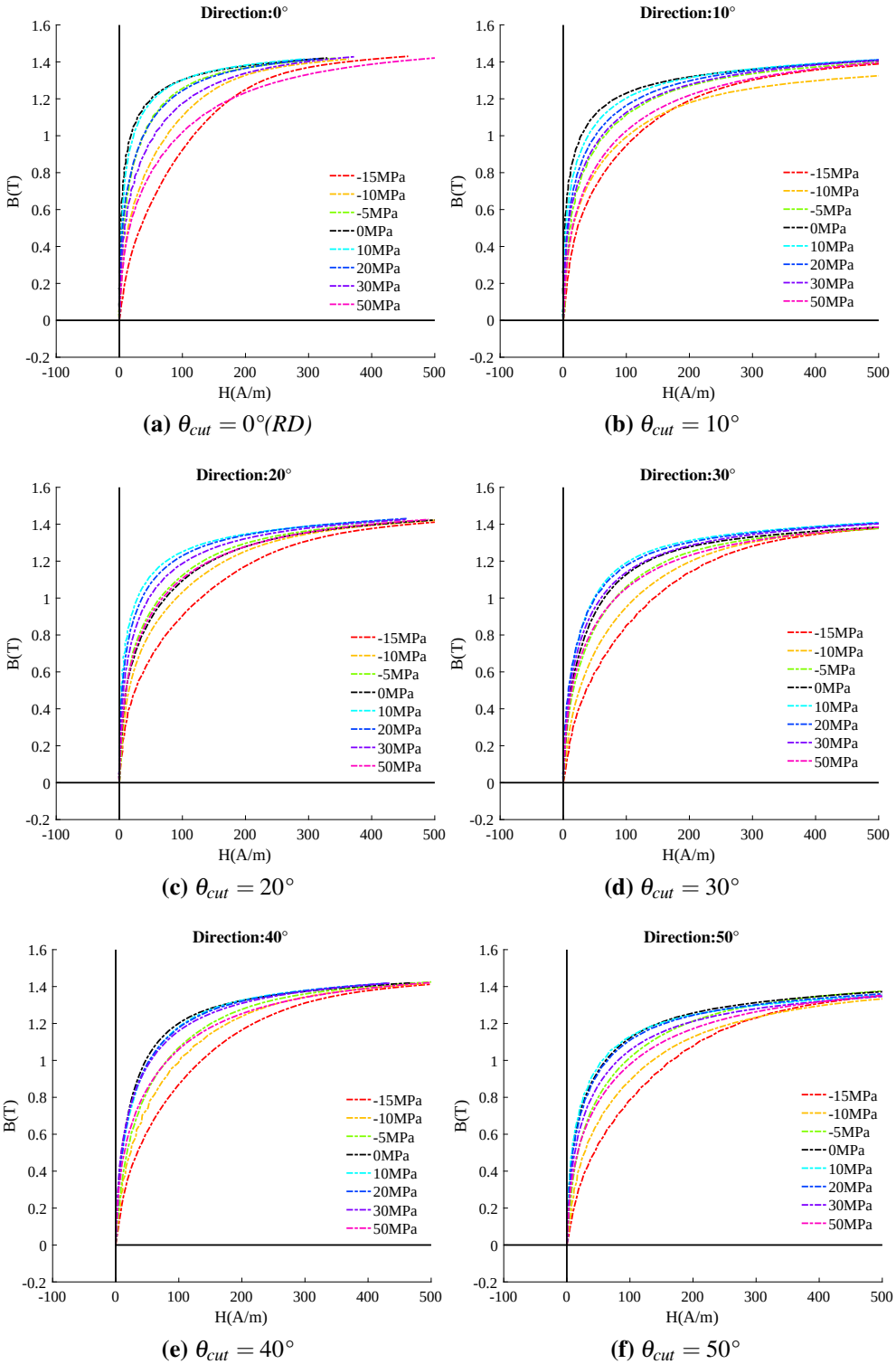

(a) $\theta_{cut} = 0°$*(RD)* **(b)** $\theta_{cut} = 10°$

(c) $\theta_{cut} = 20°$ **(d)** $\theta_{cut} = 30°$

(e) $\theta_{cut} = 40°$ **(f)** $\theta_{cut} = 50°$

Figure 2.4.1: *Anhysteretic magnetic behavior under stress in different direction with respect to the rolling direction (1.4 T, 6Hz):* $\theta = (0°...50°)$.

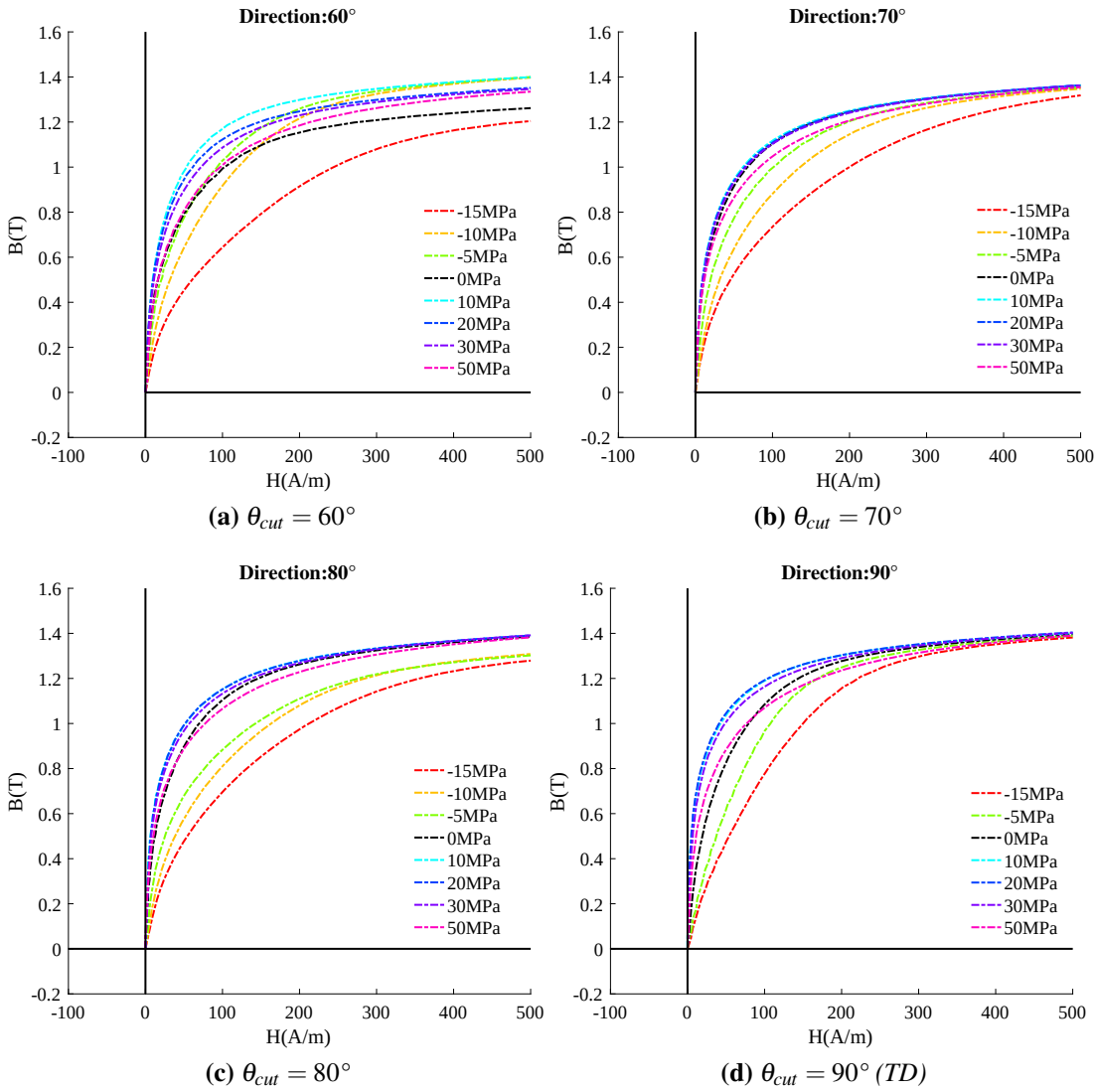

(a) $\theta_{cut} = 60°$ **(b)** $\theta_{cut} = 70°$

(c) $\theta_{cut} = 80°$ **(d)** $\theta_{cut} = 90°$ *(TD)*

Figure 2.4.2: *Anhysteretic magnetic behavior under stress in different direction with respect to the rolling direction (1.4 T, 6Hz):* $\theta = (60°...90°)$.

This variation of permeability with the sample direction with respect to RD can be explained by the anisotropy effect. In fact, it is known that a tensile stress favors magnetization along easy axis which is close to the applied stress direction. Besides, at unstressed state, the electrical sheet steel exhibits some magnetic anisotropy and it is non monotonic with the magnetization direction [50, 77]. Regarding the rolling and transverse direction; the magnetization is higher in the rolling direction because of the fabrication process; also most of the grains are oriented in this direction leading to a small improvement in the magnetization at small tension. Whereas in the transverse

direction, the easy axis is total perpendicular to the magnetization direction. When applying a tensile stress, it improves the magnetization since less energy is needed to orientate the magnetic domains. Consequently, a close connection is pointed between stress and magnetization at different directions of cut, referred commonly to magneto-elastic effect.

Looking to the figure 2.4.1 ((a) and (b) for instance), some curves cross each others at particular field magnitudes; they correspond to what is called Villari effect [31, 88]. This effect can be analyzed by considering the cross derivative equality based on Maxwell relations and defined by:

$$\left(\frac{\partial \lambda}{\partial H}\right)_{\sigma} = \left(\frac{\partial B}{\partial \sigma}\right)_{H} \tag{2.4.1}$$

for a small stress σ, equation (2.4.1) can be written as:

$$\delta B = \left(\frac{\partial \lambda}{\partial H}\right)_{\sigma=0} \times \sigma \tag{2.4.2}$$

Where B is the flux density, λ is the magnetostrictive strain; σ corresponds to the applied stress and H to the magnetic field. The subscripts σ and H mean that the derivative is made at constant values of these quantities, i.e., when a mechanical stress is applied at a particular field strength, there is an increase or a decrease in the magnetic flux density in the sample. In the case of Si-Fe sample, saturation magnetostriction λ_s is positive, thus, when the product $\left(\frac{\partial \lambda}{\partial H}\right)_0 \times \sigma$ is positive (tensile stress), the flux density B increases. At compressive stress, $\left(\frac{\partial \lambda}{\partial H}\right)_0 \times \sigma$ is negative and the flux density B decreases.

Figure 2.4.3 shows the relative permeability curves for NO samples cut in different direction with respect to RD and under uniaxial stress. In addition to the explanation given above and taking the unstressed state as reference (σ=0 MPa), relative permeability decreases rapidly with compressive stress as well for all studied directions. This might be due to the domains wall movement that is prevented because of stressing, which makes it more difficult to magnetize the samples. On one hand, it is observed that for each cutting direction, the relative permeability does not evolve in a monotonous way with applied stress. On the other hand, starting from an easy magnetization direction (RD) to the transverse direction, the relative permeability curves have a non-monotonic behavior over the whole stress range (curves crossing). When a tensile stress is applied, for samples cut at 30°, 50° and 70° the magnetization increases slightly up to σ=10 MPa before decreasing again. Moreover, for 90° direction, the relative permeability increases from σ=0 MPa to σ=20 MPa and starts decreasing after. For 0° and 10° direction samples, going from σ=0 MPa to σ=10 MPa, relative permeability decreases. However, if we had a finer discretization step, we should see an improvement of the magnetization at smaller values of tensile stress [42].

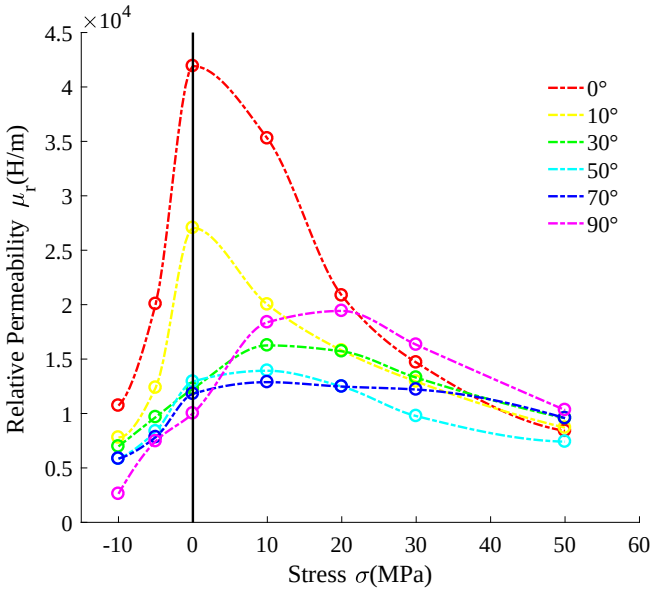

Figure 2.4.3: *Stress sensitivity of permeability in NO Fe-3%Si samples, when magnetized at 1T, 6Hz (RD, 10°,30°, 50°,70° and 90°).*

The saturation magnetostriction in a cubic crystal in a direction defined by the direction cosines $\beta_1, \beta_2, \beta_3$ relative to the crystal axes, when it changes from the demagnetized state to saturation in a direction defined by the direction cosines $\alpha_1, \alpha_2, \alpha_3$ is given by:

$$\begin{aligned}\lambda = \tfrac{3}{2}\lambda_{100}(\alpha_1^2\beta_1^2 + \alpha_2^2\beta_2^2 + \alpha_3^2\beta_3^2 - \tfrac{1}{3}) + \\ 3\lambda_{111}(\alpha_1\alpha_2\beta_1\beta_2 + \alpha_2\alpha_3\beta_2\beta_3 + \alpha_3\alpha_1\beta_3\beta_1)\end{aligned} \tag{2.4.3}$$

where λ_{100} and λ_{111} are saturation magnetostriction when crystal is magnetized, and the strain is measured, in the directions $< 100 >$ and $< 111 >$, respectively. Since the magnetostrictive strain is measured in the same direction as the magnetization ($\beta_1 = \beta_2 = 0, \beta_3 = 1$), the equation (2.4.3) is reduced to:

$$\lambda = \frac{3}{2}\lambda_{100}(\cos^2(\theta) - \frac{1}{3}) \tag{2.4.4}$$

where θ is the angle between the saturation magnetostriction λ_{100} and the magnetic field direction.

To determine the effect of stress on magnetic behavior, we assume an isotropic magnetostriction ($\lambda_{100} = \lambda_{111} = \lambda_s$). Hence, in the case of uniaxial stress σ acting upon a single magnetic domain, the magneto-elastic energy E_σ can be written as follow [13]:

$$E_\sigma = -\sigma\lambda = -\frac{3}{2}\lambda_s\sigma\cos^2(\theta_s) \tag{2.4.5}$$

Where λ_s is magnetostriction at saturation and θ_s is the angle between the saturation magnetization M_s and the stress direction. For iron (Fe), λ_s and σ are both positive, which lead to a minimum energy when tension is aligned with the saturation magnetization ($\theta_s = 0$, $E_\sigma = -\frac{3}{2}\lambda_s\sigma$). We note that the way in which a material responds to stress depends only on the sign of the product of λ_s and σ. The application of a small tensile stress to the demagnetized specimen, will cause domain walls to move in such a way as to decrease the volume of domains magnetized at right angles to the stress axis (closure or 90° domains), because such domains have a high magneto-elastic energy. These domains are totally eliminated by some higher value of the stress. Consequently, the volume of domains magnetized parallel to stress axis increases making the magnetization improved by small tensile stress (sample cut at 30° and beyond). When σ is negative, the process is reversed and the magnetization decreases whatever the angle of magnetization.

2.4.2 Magnetostrictive strain measurements

As one would expect, the stress has also an important influence on the magnetostriction strain. Figures 2.4.4 and 2.4.5 show 3D curves of the longitudinal magnetostrictive deformation as a function of the flux density B and stress σ for 10 directions of cut with respect to the rolling direction θ=(0°, 10°...90°). The curves were obtained by interpolation based on 9 experimental measurement (9 stress levels). As general trends, it can be seen that for all direction of cut, compressive stress increases the magnetostriction strain while tensile stress tends to decrease it, and even turn it negative for high tensile stress. We also observe that a high tensile stress tends to saturate magnetostriction rapidly because we reduce considerably 90° domain walls that are responsible of magnetostriction. These observations were confirmed as well by authors in [2, 98]. A close look to the figures 2.4.4 and 2.4.5 show that the shape of the measured deformation under stress is different from one direction to another. Considering the magnetic domain structure under stress of each direction of cut, we can assume the following: The application of a small tensile stress to the demagnetized sample leads to a decrease of 90° domain volume (figure 2.4.6, $H = 0$) because they have high magneto-elastic energy (equation (2.4.5)). These domains can completely be eliminated at higher value of tensile stress. However, this value of tensile stress depends also on the direction of cut of the sample. In these conditions, only a small applied field is required to saturate the sample because the magnetization process is accomplished mainly by 180° domain walls (figure 2.4.6, $H \neq 0$). Nevertheless, for compressive stress, the structure (iron based) is strongly affected because we favor 90° domains walls that are stress sensitive as illustrated in figure 2.4.6. This explains the high magnetostriction deformation for all direction when a magnetic field is applied (figure 2.4.6, $H \neq 0$).

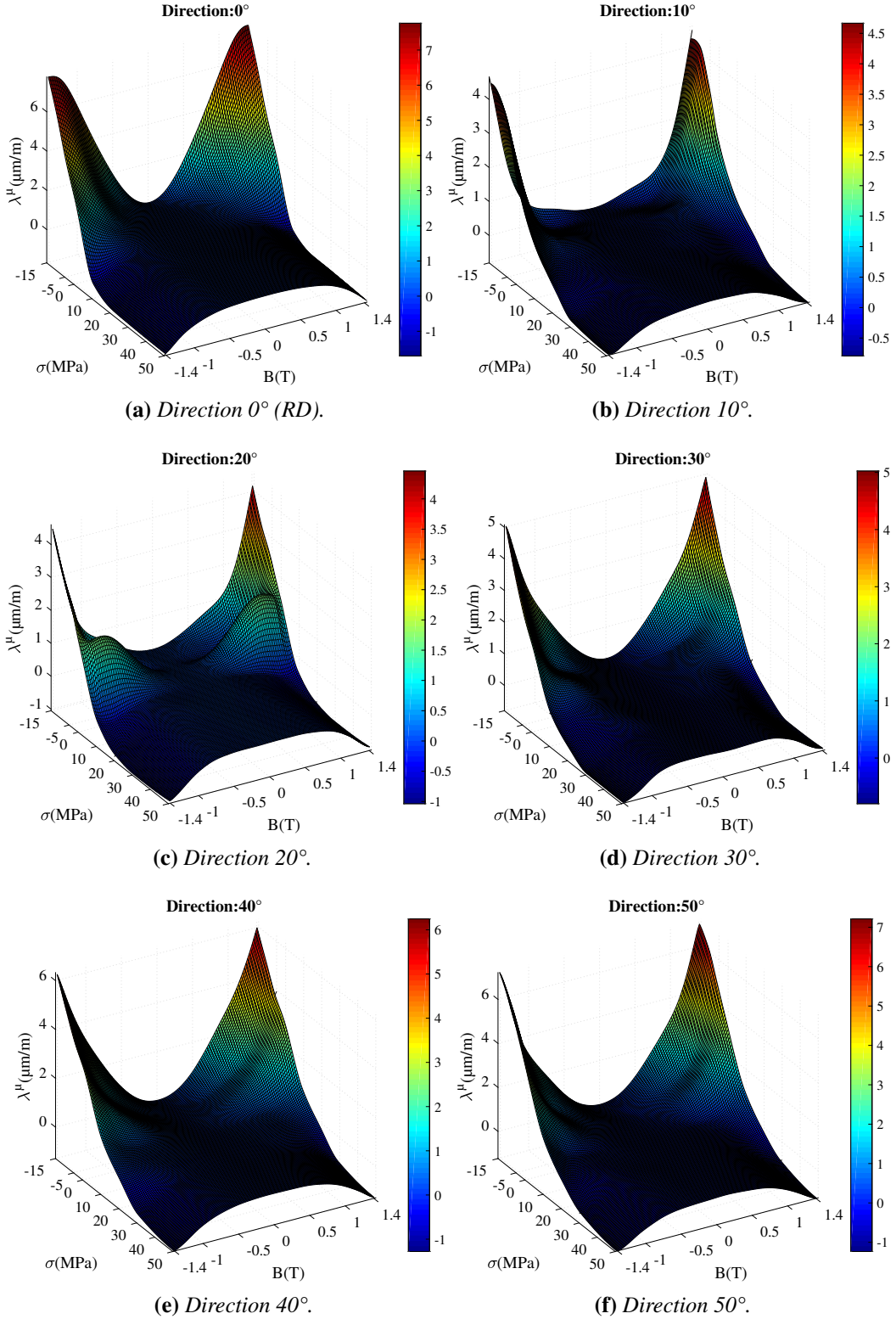

(a) *Direction 0° (RD).* **(b)** *Direction 10°.*

(c) *Direction 20°.* **(d)** *Direction 30°.*

(e) *Direction 40°.* **(f)** *Direction 50°.*

Figure 2.4.4: *Anhysteretic magnetostrictive behavior under stress in different direction with respect to the rolling direction (1.4 T, 6Hz):* $\theta = (0°...50°)$.

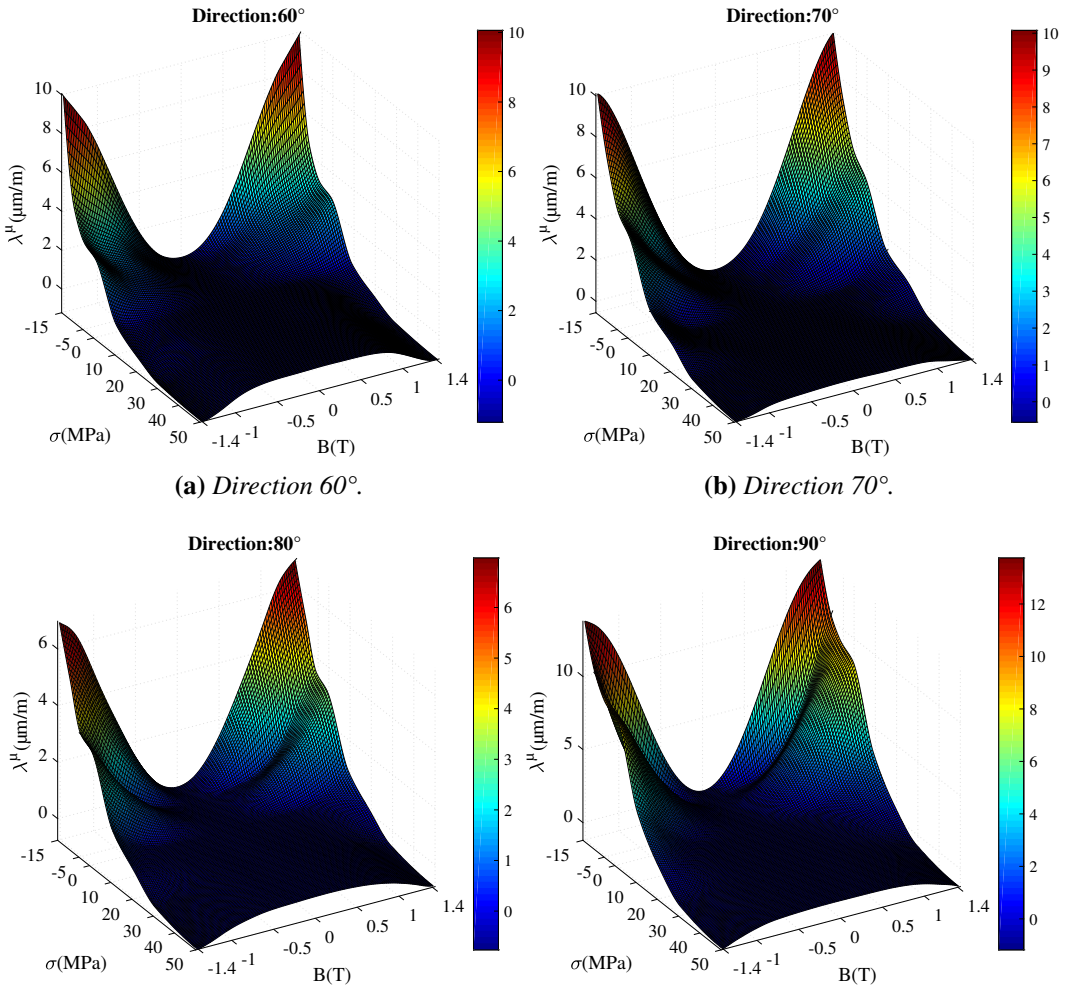

(a) *Direction 60°.* **(b)** *Direction 70°.*

(c) *Direction 80°.* **(d)** *Direction 90°(TD)*

Figure 2.4.5: *Anhysteretic magnetostrictive behavior under stress in different direction with respect to the rolling direction (1.4 T, 6Hz):* $\theta = (60°...90°)$.

To further investigate the influence of stress on magnetostriction strain, the variation of maximum magnetostriction with the direction of cut (0°...90°) and with the applied stress is plotted in figure 2.4.7. The results confirm the previous observations for all directions. A compressive stress increases the magnetostriction strain, while tensile stress decreases it and make it even negative for high value of tensile stress. Furthermore, the magnitude of magnetostriction under stress has a non-monotonous variation with angle with respect to RD of the samples between RD (0°) and TD (90°) due to crystallographic anisotropy. This anisotropic behavior was observed as well in previous work under unstressed conditions (σ= 0 MPa) in [50, 77] (figure 2.4.8). Similarly, we notice that the anisotropic behavior remains valid under uniaxial stress conditions.

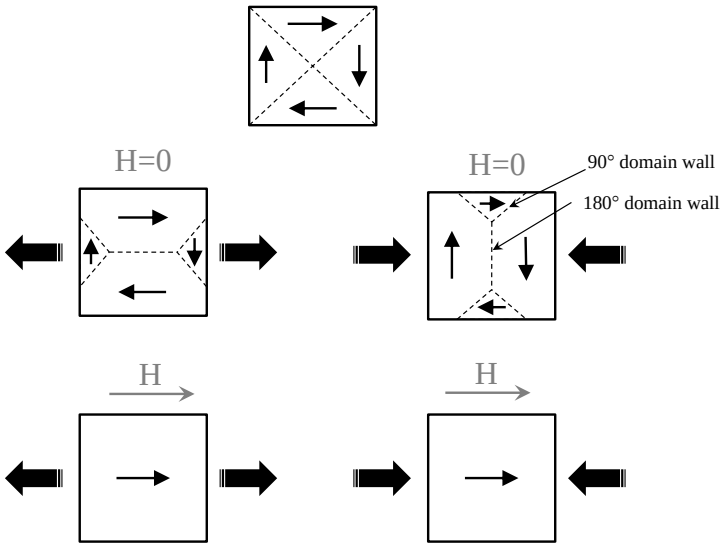

(a) Tension (b) Compression

Figure 2.4.6: *The stress induced domain reorientation and 90°-180° domain walls illustration.*

We can clearly see from figure 2.4.7 that the non-monotonous behavior is still present for medium stresses (σ = 20 MPa and σ= -10 MPa) and starts to become less striking for high tensile stresses. This proves that the relative effect of crystallographic texture (compared to unstressed state) is strongly decreased at high stress amplitudes for all the directions. Thus, at σ= 50 MPa we start achieving the saturation state of magnetostriction deformation and the crystal anisotropy is nearly zero. In this state, most of the closure domains (90° domains) are removed (figure 2.4.6). Under compressive stress, the highest magnitude of magnetostriction is found for the transverse direction and the lowest at 20°. Furthermore, at 10 MPa, magnetostriction at 90° direction is three times larger than magnetostriction at 20° direction.

Let figure 2.4.6 represents a small portion of the sample containing four domains. Under applied stress, the growth of the domains either parallel to the tensile stress or perpendicular to the compressive stress induces the additional magnetostriction ($\triangle\varepsilon_{\mu}^{\parallel}$) to the elastic strain. Providing constant volume of magnetostrictive deformation, we can write:

$$\varepsilon_{\mu}^{\parallel} = \lambda v^{\parallel} - \frac{\lambda}{2} v^{\perp} \tag{2.4.6}$$

where $v^{\parallel}$ and $v^{\perp}$ are relative volumes of the small portion of the sample linked by the

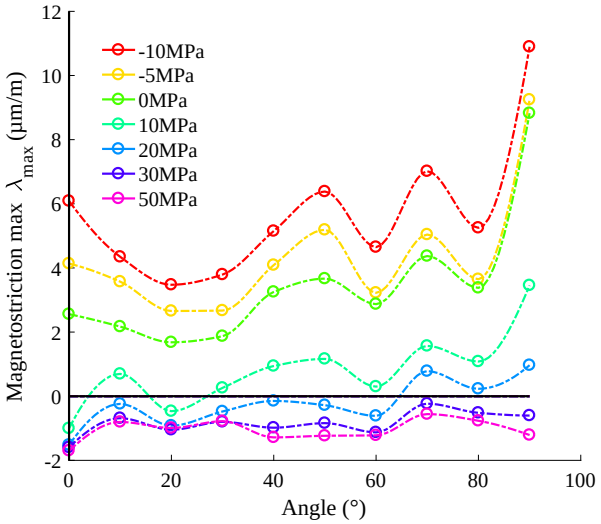

Figure 2.4.7: *Variation of peak magnetostriction with angle of cut in NO Fe-3%Si for applied compressive and tensile stresses* σ*= [-15, -10, -5, 0, 10, 30, 50] MPa, when magnetized at 1.4 T, 6 Hz.*

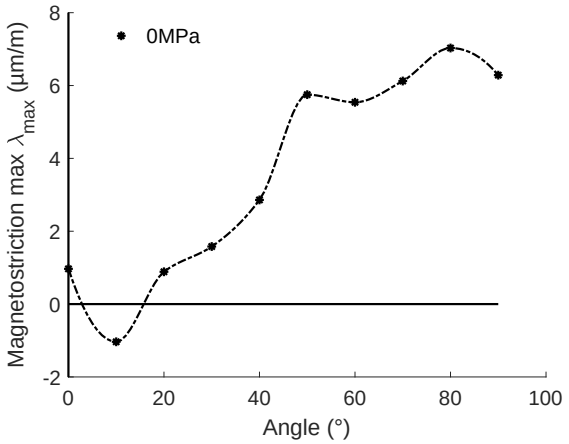

Figure 2.4.8: *Variation of peak magnetostriction with angle of cut in NO Fe-3%Si at* $\sigma = 0$ *MPa, when magnetized at 1.4T [50].*

relation: $v^{\perp}$=1-$v^{\parallel}$. Hence, the equation (2.4.6) can be expressed as:

$$\varepsilon_{\mu}^{\parallel} = \frac{3}{2}\lambda(v^{\parallel} - \frac{1}{3}) \tag{2.4.7}$$

Under an applied field H, the induced variation of deformation is written as:

$$\triangle\varepsilon_{\mu}^{\parallel} = \frac{3}{2}\lambda\triangle v^{\parallel} \tag{2.4.8}$$

Consequently:

$$\begin{cases} \text{Under tensile stress :} & \triangle v^{\parallel} \sim 0 \rightarrow \quad \text{small } \triangle\varepsilon_{\mu}^{\parallel} \\ \text{Under compressive stress:} & \triangle v^{\parallel} \sim 1 \rightarrow \quad \text{large } \triangle\varepsilon_{\mu}^{\parallel} \end{cases} \tag{2.4.9}$$

When the sample is magnetized, magnetostriction occurs as a result of the motion of the 90° domain walls. Thereby, if the sample is magnetized parallel to the stress direction as in the present measurements the maximum magnetostriction decreases with tensile stress (few 90° domain walls) and increases with compressive stress (increase of 90° domain walls). As shown in figure 2.4.7, the effect of compressive stress is more pronounced for sample cut in RD (0°) because we create more 90° domain [85]. However, for all 10 samples, magnetostrictive strain saturation is reached rapidly when a tensile stress is applied.

2.4.3 ΔE effect

The measurements of ΔE effect are obtained from magnetostrictive measurements under stress. The procedure is based on an assumption of magnetic saturation of magnetostriction: Whatever the uniaxial stress level, magnetostriction at saturation is the same (same domain configuration at saturation). First, a stress value is applied resulting in an elastic strain $\varepsilon^{e}(\sigma)$ and a magnetostrictive strain $\varepsilon^{\mu}(M=0,\sigma)$ according to equation (2.4.10):

$$\varepsilon^{'}(M=0,\sigma) = \varepsilon^{e}(M=0,\sigma) + \varepsilon^{\mu}(M=0,\sigma) \tag{2.4.10}$$

However, after demagnetization, the magnetostrictive strain $\varepsilon^{\mu}(M=0,\sigma)$ is very difficult to measure as it is much lower than the elastic one. Hence, the deformation $\varepsilon^{'}$ is put to zero (initialization). Next, we proceed to magnetostriction measurements under quasi-static conditions corresponding to a variation of deformation $\varepsilon^{"}$ due to magnetization at constant stress (equation (2.4.11)). Because the elastic strain is the same ($\varepsilon^{e}(M,\sigma) = \varepsilon^{e}(M=0,\sigma)$), the measurements agree now to the following equation:

$$\begin{aligned} \varepsilon^{"}(M,\sigma) &= \varepsilon^{'}(M,\sigma) - \varepsilon^{'}(M=0,\sigma) \\ &= \varepsilon^{\mu}(M,\sigma) - \varepsilon^{\mu}(M=0,\sigma) \end{aligned} \tag{2.4.11}$$

From equation (2.4.11), we can deduce that $\varepsilon^{"}(M=0,\sigma)$ is always zero whatever the stress level. If we assume that the magnetization saturation M_s is reached at high field, then the domain configuration and hence the magnetostriction strain is the same regardless of the stress level. Which means that $\varepsilon^{"}(M_s,0)=\varepsilon^{\mu}(M_s,0)$. Consequently, $\varepsilon^{\mu}(M_s,0)$ is considered the reference point that all strains $\varepsilon^{"}(M,\sigma)$ must reach (magnetic saturation of magnetostriction). By proceeding to a shift between $\varepsilon^{"}(M_s,0)$ and $\varepsilon^{"}(M,\sigma)$ as illustrated in figure 2.4.9 we obtain the magnetostriction at zero magnetic field corresponding to a point of ΔE effect curve.

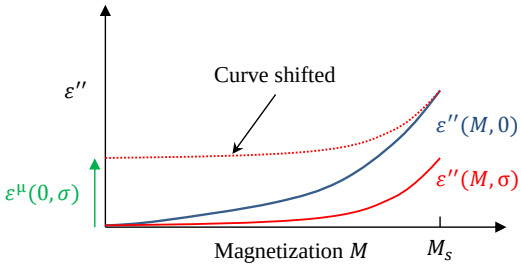

Figure 2.4.9: *Schematic extraction procedure of $\varepsilon^{"}(0,\sigma)$ (ΔE effect).*

From the two figures 2.4.4 and 2.4.5, the evolution of magnetostrictive deformation with zero magnetization, so-called ΔE effect, can be plotted. Looking at the ΔE effect curves (figure 2.4.10a), we observe that they depend on the direction of cut, moreover, the evolution from one direction of cut to another is non monotonic.

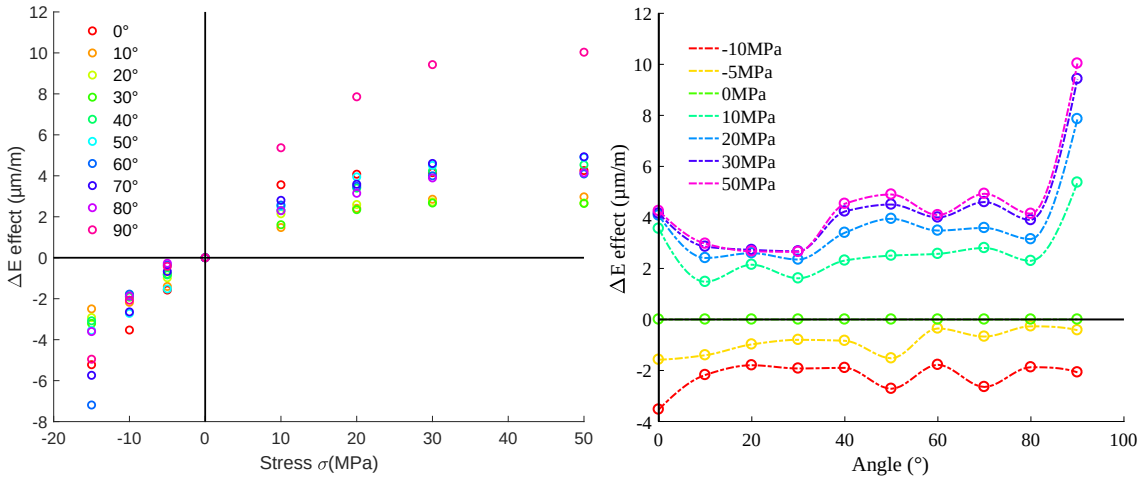

(a) *Longitudinal ΔE effect.* **(b)** *Longitudinal ΔE effect.*

Figure 2.4.10: *ΔE effect: influence of stress on longitudinal magnetostriction at different directions with respect to RD.*

To further investigate the ΔE effect, we represented differently the ΔE curve (figure 2.4.10b). We notice as general trends that for tensile stress ΔE effect is positive and negative for compressive stress. For tensile stress, magnetostrictive deformation tends to saturate and maintain the same amplitude at around σ= 30 MPa. For compressive stress, it seems that the saturation state have not been reached yet at -10 MPa (buckling problem beyond). However, we expect a saturation state beyond -10 MPa as found in [98, 24]. Under compression, a higher magnitude of ΔE effect (than tensile stress) is observed at saturation for all directions, because at σ= -10 MPa we have already reached the order of magnitude of saturation state corresponding to a tensile stress of σ=50 MPa.

The saturation of ΔE effect under tensile stress is not the same for all directions of cut. The lowest value was obtained for 20° and 30° samples and the highest for 90° sample. As explained before, this non monotonous behavior can be related to domain reorientation under stress.

2.4.4 Frequency influence on magnetostriction under stress

Figure 2.4.11 shows a bar graph describing the variation of the maximum magnetostriction strain with the applied stress and with the frequency for many angles of cut with respect to RD. All samples were magnetized at 1,4 T and two frequencies f = 6 and 50 Hz.

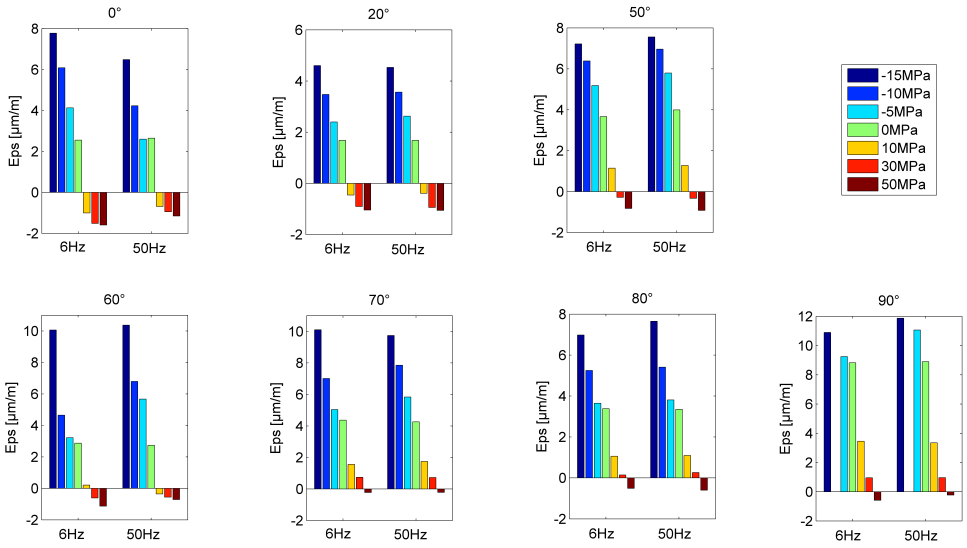

Figure 2.4.11: *Peak magnetostriction of stressed samples cut at different directions and magnetized at 6 and 50 Hz (B=1.4T).*

It is worth mentioning that magnetostriction measurements are highly sensitive to the

different disturbances that may impact the measurement results because of the small deformations involved. The fact that some variations (measurements uncertainty, sample to sample variations...) may interfere with the measurements is not totally excluded, however, this variation cannot be attributed mainly to the sheet dispersion or the uncertainties given that a consistent trends in the studied direction is observed.

We first note that at $\sigma = 0$ MPa, the effect of frequency is almost invisible and no significant variation of magnetostriction is observed for all samples cut in different direction. A higher variation in frequency (frequency gap) is needed to observe changes at unstressed state [86]. However, when $\sigma \neq 0$ MPa the magnetostriction behavior changes with frequency. In the rolling direction (0°), a compressive or tensile stress seems to increase the effect of frequency. Furthermore, for the same direction, when we increase the frequency from 6 to 50 Hz, the magnetostriction strain decreases. Nevertheless, for 20°, 50°, 60° and 70° samples, the trend is reversed. A compressive stress induces a slighter increase of magnetostriction strain, while a smaller magnetostriction variation is observed when a tensile stress is applied. For 80° sample, the magnetostriction strain at 50 Hz is greater than the one at 6 Hz for a certain applied stress, but the difference of magnetostriction strain between the two frequencies becomes smaller and stabilizes. Finally, for 90° sample, the magnetostriction strain is greater at 50 Hz than at 6 Hz when a compressive stress is applied. Whatever the frequency (6 or 50 Hz), as we evolve from 0° to 90° direction, a greater tensile stress is needed to make the magnetostriction negative, because of the domains orientation under stress as mentioned before (figure 2.4.6). Besides, the variation of magnetostriction with frequency of stressed sample has a non-monotonous behavior. Since no effect of frequency on magnetostriction strain was observed for unstressed samples, the reasons of magnetostriction strain variation with frequency under stress can be assumed to be the combination of the skin effect (at high frequency domains closer to the surfaces will be more greatly activated and a large volume of material remains demagnetized) and domain reorientation (due to stress). In addition, as mentioned in [86], under free stress state and depending on the sample thickness, when the frequency increases, the domains closer to the surface will be more activated and a large volume of material remains demagnetized (skin effect). However, this process (skin effect) seems to be more pronounced when applying stress on the sample as illustrated in figure 2.4.11, even with low variation of frequency (6 to 50 Hz). As noted in [104], other effects can be involved in this process like surface effects and domain walls bowing. However, further studies with larger gap in frequency and under mechanical loading are still needed to confirm these observations.

Magnetostriction modeling

2.5 Magnetostriction model: Macroscopic and anhysteretic energy based model

The magnetostriction model presented in this section is based on Serigne Mbengue's thesis work [77]. The model has been developed in the present thesis to take into account the effect of mechanical stress (compression and traction) keeping the consideration of the magnetic and magnetostrictive anisotropic behavior, which is the strongest point of the model. First a brief description of the model is detailed and the energy terms are described. Later on, we explain the procedure of stress effect integration to the model and the modifications made on energy terms affected by stress loading. Then, modeling results are compared to measurements made on samples cut in many directions with respect to the rolling direction (magnetic and magnetostrictive anisotropy). Finally, the limitations of the model with its new configuration are discussed.

2.5.1 Model description

Since ferromagnetic sheets are characterized by a small thickness, the magnetic flux circulates mainly in the plane. Thus, the proposed model considers a plane magnetization. Moreover, in order to consider a homogeneous magnetization in the sheet, the magnetization process is described at the macroscopic scale. Finally, the demagnetized and unstressed state will be taken as the reference state. Under these conditions, the total energy that governs the magnetic equilibrium of the ferromagnetic material can be written as the sum of the following energetic terms:

$$E_{total}(k,\theta) = E_z + E_d + E_{an} + E_\sigma \tag{2.5.1}$$

where:

- E_z: refers to the Zeeman energy.
- E_d: refers to the demagnetizing field energy.
- E_{an}: refers to the macroscopic anisotropy energy.
- E_σ: refers to the magneto-elastic energy.

The magnetization of the medium is described in polar coordinates by the couple (k,θ):

$$\vec{M} / \begin{cases} \|\vec{M}\| = k.M_S \text{ with } 0 \leq k \leq 1 \\ \left(\overrightarrow{RD},\overrightarrow{M}\right) = \theta \text{ with } -\pi \leq \theta \leq \pi \end{cases} \tag{2.5.2}$$

M_s corresponds to the magnetization saturation and $\overrightarrow{RD}$ represents the rolling direction.

Zeeman energy

The definition of the Zeeman energy was presented in chapter 1. We remind here the expression:

$$E_z = -\mu_0.\overrightarrow{M}.\overrightarrow{H} \tag{2.5.3}$$

μ_0 refers to the vacuum permeability.

Demagnetizing field energy

We have seen in chapter 1 that the demagnetizing field $\overrightarrow{H}_d$ is linked to the magnetization $\overrightarrow{M}$ by the following equation:

$$\overrightarrow{H}_d = -N_d.\overrightarrow{M} \tag{2.5.4}$$

where N_d is a demagnetizing factor. In fact, because of the difference in behavior between the neighboring crystals and magnetic domains, a local magnetic field appears and creates some heterogeneity in the total magnetization. This effect is rather important in the beginning of the magnetization as the difference in local behavior is big and starts to decrease rapidly as the magnetization increases. The expression of the demagnetizing factor depending on the magnetization variable k and the initial susceptibility $\chi_i(\theta)$ (depends on direction of cut θ) is given by:

$$N_d = \frac{1}{\chi_i(\theta).(1-k^2)} \tag{2.5.5}$$

In general, the magnetization M can be written as a function of the internal field H_i and the susceptibility χ by the following equation:

$$M = \chi(H_i).H_i \tag{2.5.6}$$

The internal field H_i results from the field due to the free currents H_0 (external field) and that due to the magnetization of the material itself $-N_d.M$:

$$H_i = H_0 - N_d.M \tag{2.5.7}$$

The equations (2.5.6) and (2.5.7) allow us to write the magnetization as a function of the external magnetic field:

$$M = \frac{\chi(H_i)}{1+N_d.\chi(H_i)}.H_0 \tag{2.5.8}$$

Due to the very high initial anhysteretic susceptibility (theoretically in finite for weak H_i) of soft ferromagnetic materials, we can write for the quasi-linear part of the magnetization:

$$M_{\chi\to\infty} \to \frac{1}{N_d}.H_0 \tag{2.5.9}$$

On the other hand, we introduce an amplitude susceptibility (commonly known as secant susceptibility) $\chi_a = \frac{M}{H_0}$ (figure 2.5.1). In the case of anhysteretic magnetization, the susceptibility χ_a for a given field direction can be estimated by the initial susceptibility and the magnetization variable k:

$$\chi_a = \chi_i.(1-k^2) \tag{2.5.10}$$

This expression of the susceptibility χ_a is not unique, it can take a more complex form.

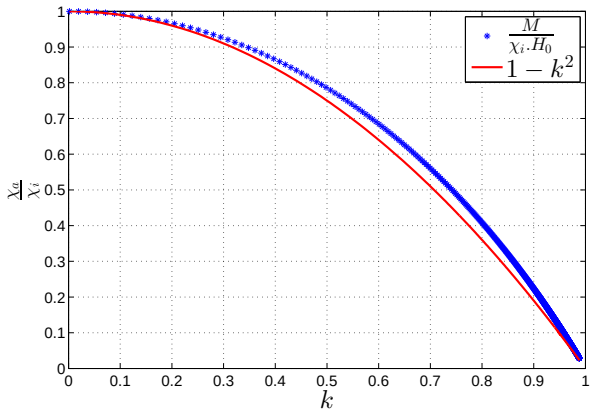

Figure 2.5.1: *Normalized amplitude susceptibility χ_a (deduced from dotted measurements [50] and modeled in solid lines) for a given magnetic field direction.*

Thus for a given external field direction, the demagnetizing field factor is given by $N_d = \frac{1}{\chi_i.(1-k^2)}$. This demagnetizing factor N_d is valid for low field levels (equation (2.5.9)) and allows the magnetization curve to be influenced before the "bend".

The energy associated with this demagnetizing effect becomes:

$$E_d = \frac{1}{2}.\mu_0.N_d.\|\vec{M}\|^2 \tag{2.5.11}$$

Macroscopic anisotropy energy

The magnetocrystaline anisotropy energy is caused by the magnetic moments which are not aligned along the crystallographic easy direction ($< 001 >$ for a cubic crystal lattice of iron), figure 2.5.2a. Whereas the macroscopic anisotropy energy E_{an} takes into account the preference of the material to be magnetized according to certain directions at macroscopic scale. As illustrated in figure 2.5.2b, the ferromagnetic poly-crystal NO Si-Fe exhibits macroscopic anisotropy due to the material texture (rolling operation) [19, 109].

Assuming that the influence of the anisotropy on the magnetization rotation is π-periodic and even, then the associated energy can be decomposed into a modulated Fourier series by an increasing exponential function according to the magnetization (equation (2.5.12)). This exponential function (adjusted by the variable α) is introduced to influence the magnetization for high magnetic fields (above the bend of the magnetization curve).

To model the described behavior of the anisotropy energy the following expression has been adopted:

$$E_{an} = \left[\exp\left(k^{\alpha}\right) - 1\right]\left[\sum_{n=0}^{\infty} A_n.\cos\left(n.\theta\right)\right] \tag{2.5.12}$$

where:

(k,θ): represent model variables

α: fitting variable at high magnetic field

n: pair index

A_n: model parameters to be identified (describe the macroscopic magnetic anisotropy due to texture).

The significant number of anisotropy parameters A_n varies from one texture to another. For example, if we consider the obtaining conditions of figure 2.5.2b, then for a strongly textured sheet of type SiFe GO the significant A_n are more important than for non-oriented grain sheet (figure 2.5.3). The identification of A_n parameters is detailed in [76].

The anisotropy described in equation (2.5.12) increases with k and reaches its minimum for $k = 0$.

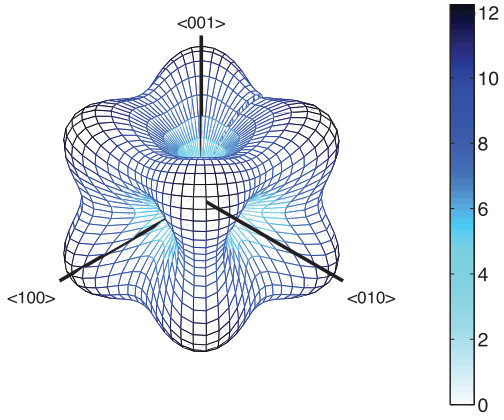

(a) *Spatial distribution of the magnetocrystaline anisotropy energy [98].*

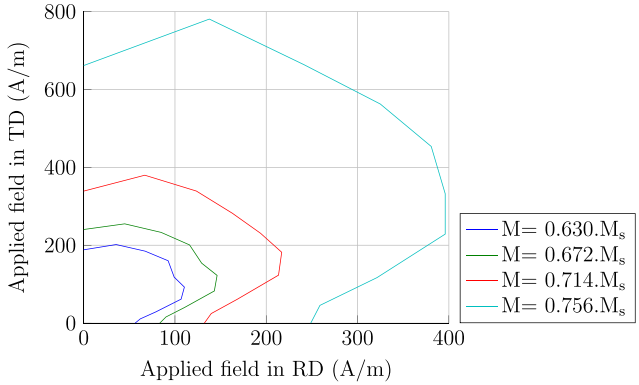

(b) *Polar representation of the magnetic field at 4 magnetization levels (NO (non-oriented) 3%Si-Fe) [76].*

Figure 2.5.2: *Magnetocrystaline and macroscopic anisotropy of Si-Fe material.*

Magneto-elastic energy

When an external stress is applied to a magnetic material, it induces a change in the domain structure, leading to a variation in the total magnetization. This coupling effect between the magnetic and the mechanical phenomena is named magneto-elastic coupling and the associated energy is written as:

$$E_\sigma = -\overline{\overline{\sigma}} : \overline{\overline{\varepsilon}}^{\mu} \tag{2.5.13}$$

$\overline{\overline{\sigma}}$ and $\overline{\overline{\varepsilon}}^{\mu}$ refer respectively to the applied stress and magnetostrictive strain tensors in the materiel reference frame $\left(\overrightarrow{RD}, \overrightarrow{TD}\right)$.

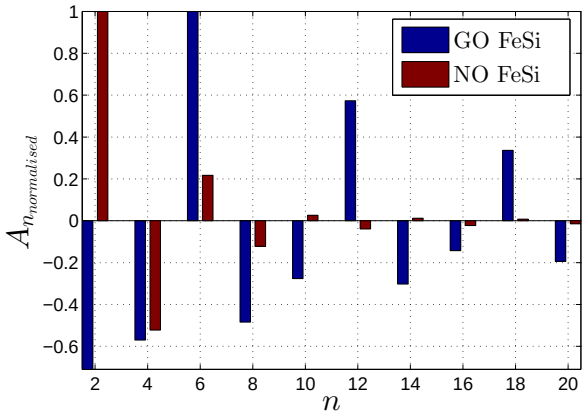

Figure 2.5.3: *Macroscopic anisotropy parameters A_n for two sheets (GO and NO) from the data in figure 2.5.2b.*

$$\overline{\overline{\sigma}} = \begin{bmatrix} \sigma_{RD} & \sigma_{RTD} \\ \sigma_{RTD} & \sigma_{TD} \end{bmatrix} \tag{2.5.14}$$

From the isochoric assumption, the anisotropic magnetostriction strain tensor in the reference frame of magnetization $\overrightarrow{M}$ is written as:

$$\overline{\overline{\varepsilon}}^{\mu}_{\overrightarrow{M}} = g(k^{2n},\theta).\begin{bmatrix} 1 & 0 \\ 0 & -\frac{1}{2} \end{bmatrix} \tag{2.5.15}$$

where $g(k^{2n})$ is an anisotropic function representing magnetostriction at saturation ($k \to 1$) that can have the following form:

$$g(k^{2n},\lambda_i(\theta)) = \lambda_1(\theta).k^2 + \lambda_2(\theta).k^4 + \lambda_3(\theta).k^6 + \lambda_4(\theta).k^8 \tag{2.5.16}$$

$\lambda_1(\theta)...\lambda_4(\theta)$ are model parameters, which can be identified from unidirectional measurements on samples cut on different angle θ with respect to the rolling direction.

Magnetostrictive deformation is anisotropic and depends on the orientation of the magnetization [23]. In other words, its saturation value ($k \to 1$), which is an intrinsic property of the material, changes and is a function of θ. Thus, the functions $\lambda_1(\theta)...\lambda_4(\theta)$ are expressed thanks to the deformation measurements following different directions and a simple identification of polynomial coefficients from equation (2.5.18). In fact, the measured deformation (supposed magnetostrictive) in a direction β is given by:

$$\lambda^{\mu}_{\beta} = \frac{\Delta l}{l}\rfloor_{\beta} = \sum_{i,j} \varepsilon^{\mu}_{ij}\beta_i\beta_j \tag{2.5.17}$$

Thus, assuming that $\beta \approx \theta$ for low fields, the measured magnetostriction is given by the equation (2.5.18). This hypothesis ($\beta \approx \theta$) is true if the longitudinal magnetostriction is measured on a rectangular sample whose length is greater than the width (type SST device). In this type of device, the effect of the sample shape favors a magnetization close to the longitudinal direction.

$$\lambda_{\beta}^{\mu} = \frac{\Delta l}{l}\rfloor_{\beta=\theta} = \lambda_1(\theta).k^2 + \lambda_2(\theta).k^4 + \lambda_3(\theta).k^6 + \lambda_4(\theta).k^8 \tag{2.5.18}$$

Using the transformation matrix R from the reference frame of magnetization $\overrightarrow{M}$ to the material frame reference $\left(\overrightarrow{RD}, \overrightarrow{TD}\right)$:

$$\overline{\overline{\varepsilon}}^{\mu} = R.\overline{\overline{\varepsilon}}_{\overrightarrow{M}}^{\mu}.R^{-1} \tag{2.5.19}$$

with:

$$R = \begin{bmatrix} \cos\theta & -\sin\theta \\ \sin\theta & \cos\theta \end{bmatrix} \tag{2.5.20}$$

The parameters used in the macroscopic model are summarized in table 2.3. They are evaluated experimentally whatever the angle θ from magnetic $M(H)$ and magnetostrictive $\lambda^{\mu}(M)$ curves at different direction ($\theta = 0°...90°$, 10 angles). Based on figure 2.5.3 and given that the studied material is a non-oriented grain SiFe, a maximum index of $n = 12$ was chosen for the A_n parameters because it seems representative of the anisotropic behavior of the material. For $\lambda_i.k^{2n}$ parameters, a maximum numbers of $i = 4$ and $n = 4$ were chosen because a polynomial of order 8 is enough to obtain a magnetostriction curve similar to that obtained by measurement. The corresponding identification procedure is described in [77].

Parameter	number	Description
$\chi_i(\theta)$	1	Initial susceptibility
α	1	Dimensionless material parameter
$A_n(\theta)$	12	Anisotropy coefficients
$\lambda_n(\theta)$	4	Magnetostriction coefficients
M_s	-	Saturation magnetization

Table 2.3: *Parameters of the macroscopic model.*

By definition [107], the anhysteretic magnetization curve represents a succession of states or configurations, each of which corresponds to the lowest energy for a given

excitation. Hence, the reconstitution of the anhysteretic behavior (magnetization, indirectly the magnetostriction) can be presented as a problem of global minimum search of the total energy (equation (2.5.1)) with a given excitation (figure 2.5.4):

$$\min\left(E_{total}\left(k,\theta\right)\right) / \begin{cases} k \in & [0,1] \\ \theta \in & [-\pi,\pi] \end{cases} \tag{2.5.21}$$

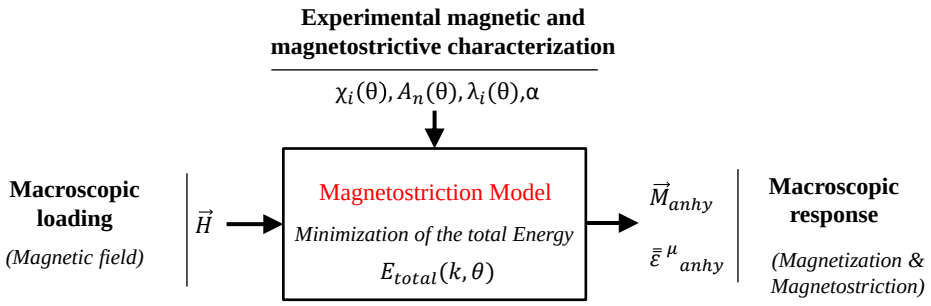

Figure 2.5.4: *The computation process of the magnetization and magnetostriction deformation.*

2.5.2 Application of the macroscopic model without mechanical loading

The proposed anisotropic model is based on an energy approach, allowing it to best represent the physics that governs the magnetic and magnetostrictive properties of magnetic materials. However, this model is macroscopic unlike the multi-scale approach that is based on the interactions between three different scales, starting from the domain scale to the grain scale, and using homogenization to describe the material behavior. On the other hand, the proposed model emphasizes the influence of the magnetic and magnetostrictive anisotropy, which according to experimental studies on electric motor and transformer [118, 80] is a source of vibration in these structures.

Figures 2.5.5 to 2.5.8 show a comparison between the measurement and the modeling results of magnetic and magnetostrictive behavior of a non-oriented grain Si-Fe material in different magnetization directions (with respect to the rolling direction). Measurements and model are in good agreement. We observe that the model respects the trends related to the effect of magnetic anisotropy with a maximal error not exceeding 5.6%. With regard to the magnetostrictive behavior, the effect of a non-monotonic anisotropy according to the magnetization direction is well restored.

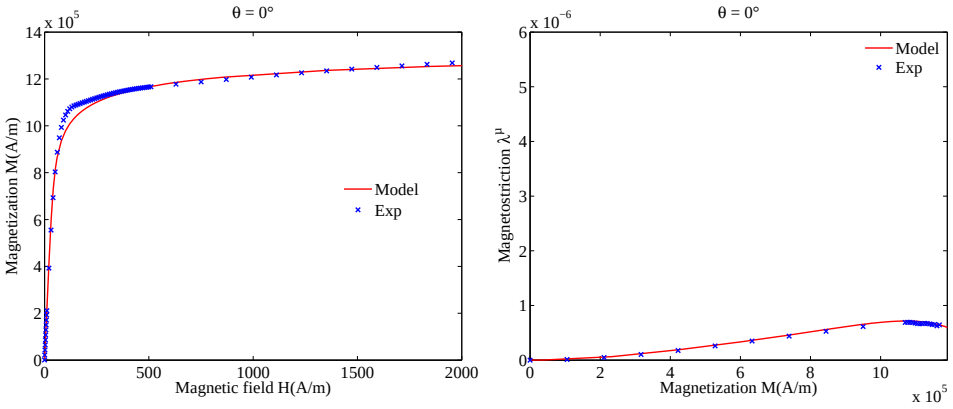

(a) *The rolling direction (RD).*

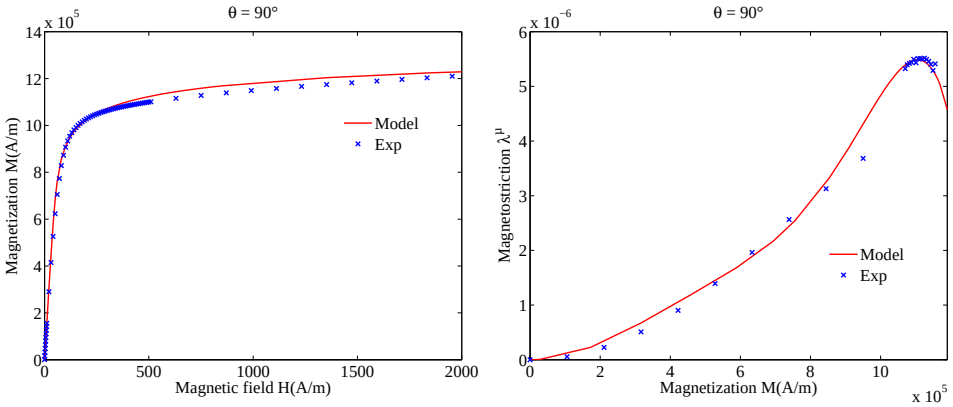

(b) *The transverse direction (TD).*

Figure 2.5.5: *Comparison between measurements and modeling results: $M(H)$ on the left, $\lambda^{\mu}(M)$ on the right.*

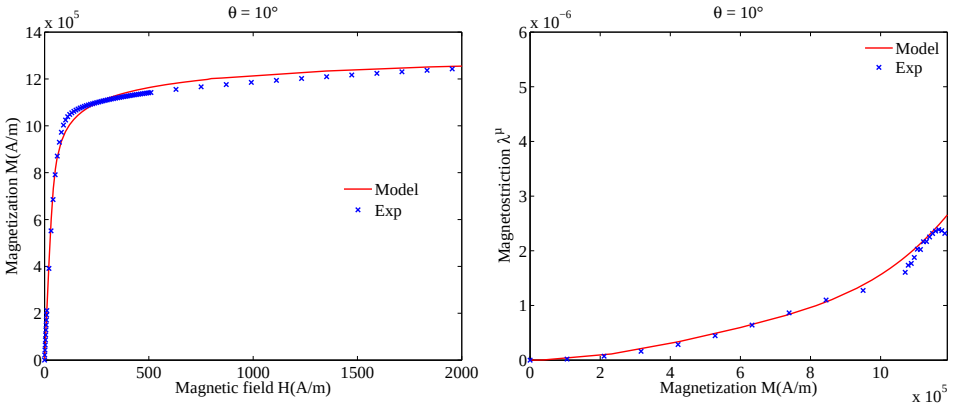

(a) *10° with respect to RD.*

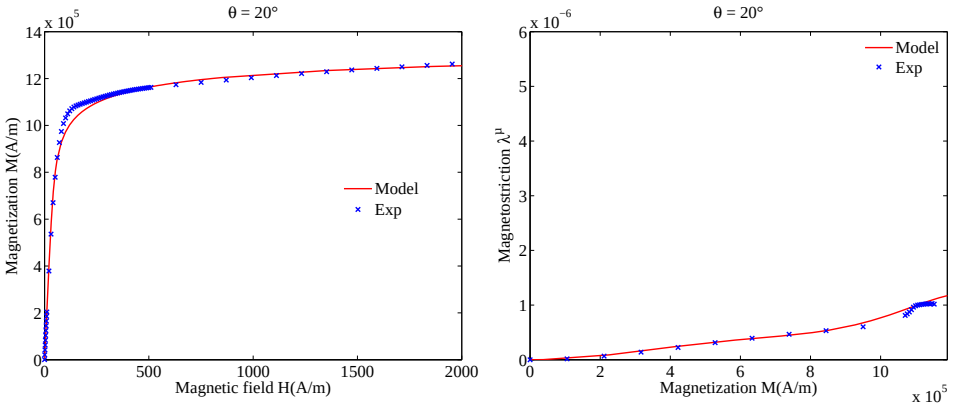

(b) *20° with respect to RD.*

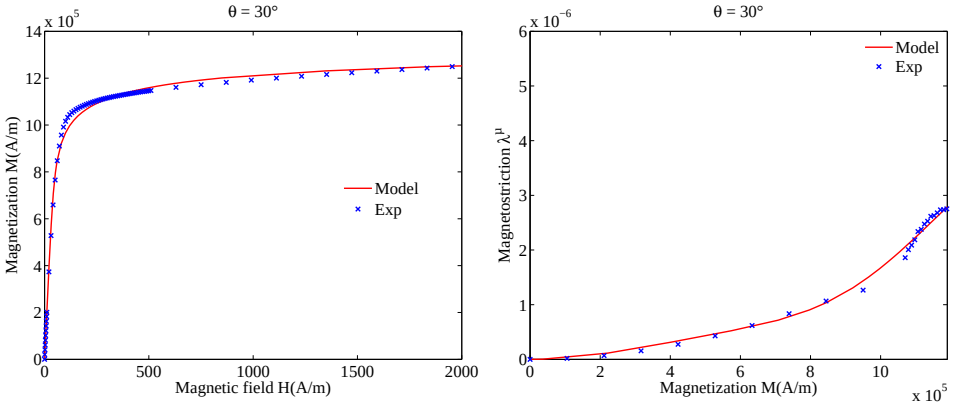

(c) *30° with respect to RD.*

Figure 2.5.6: *Comparison between measurements and modeling results: $M(H)$ on the left, $\lambda^{\mu}(M)$ on the right.*

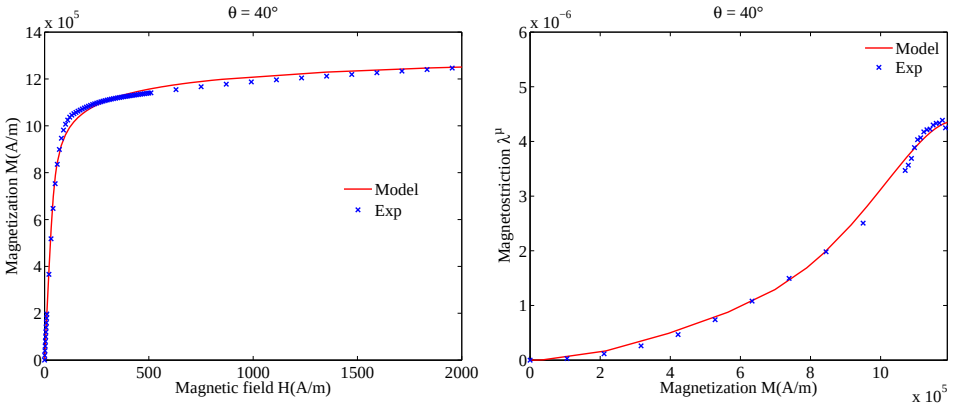

(a) *40° with respect to RD.*

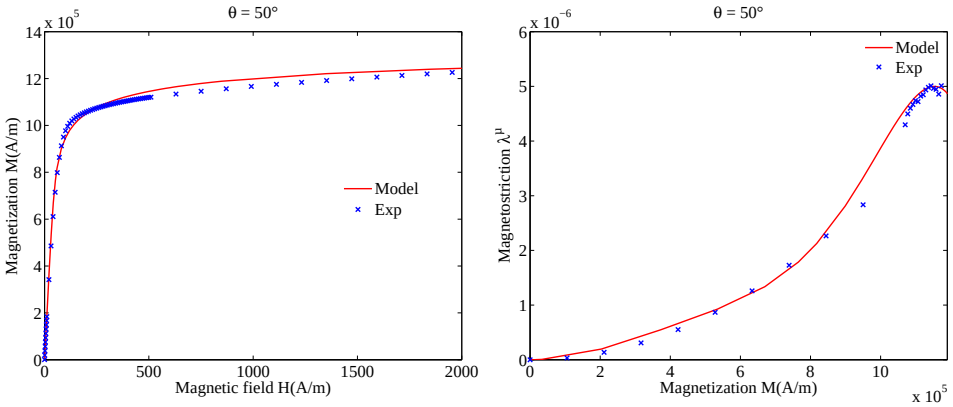

(b) *50° with respect to RD.*

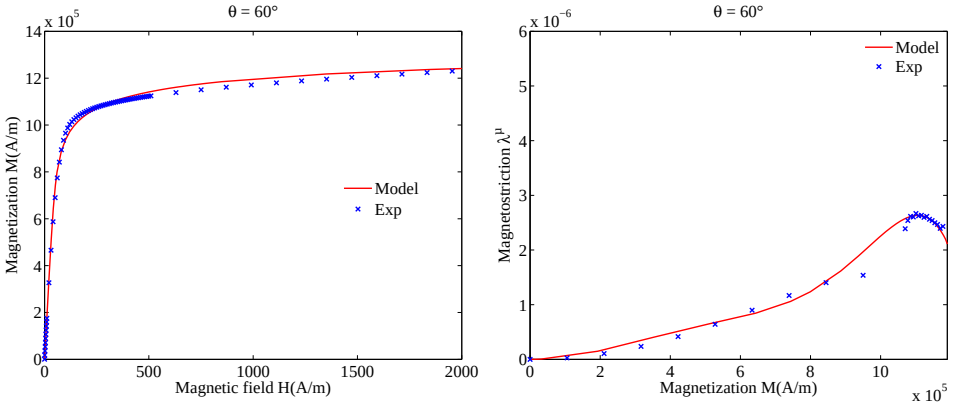

(c) *60° with respect to RD.*

Figure 2.5.7: *Comparison between measurements and modeling results: $M(H)$ on the left, $\lambda^{\mu}(M)$ on the right.*

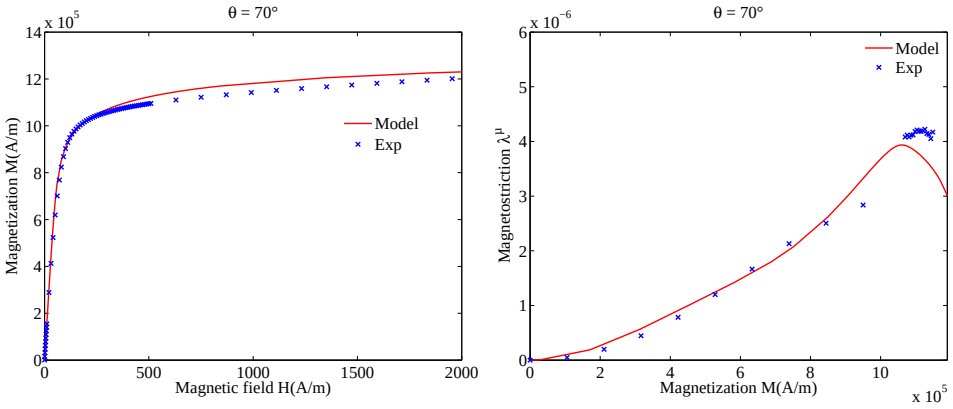

(a) *70° with respect to RD.*

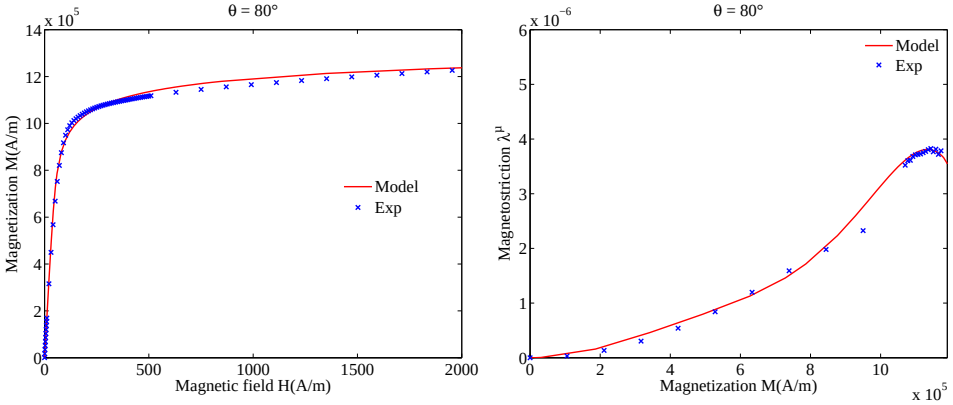

(b) *80° with respect to RD.*

Figure 2.5.8: *Comparison between measurements and modeling results: $M(H)$ on the left, $\lambda^{\mu}(M)$ on the right.*

We describe in the following the main modifications that have been made to the model during this thesis.

2.5.3 Modeling the magneto-elastic effect

We initially had a version of the anhysteretic anisotropic model corresponding to the detailed description in section 2.5.1. Nevertheless, the proposed approach did not take into account the influence of mechanical loading on the magnetic and magnetostrictive behavior of the studied material. Accordingly, we propose a modified version of the energy based model by making changes to certain energy terms that are directly or indirectly related to this magneto-elastic coupling.

In fact, many studies have highlighted the existence of a strong coupling between magnetostrictive and magnetic properties on one hand, and the application of mechan-

ical stress on the other hand [4, 28]. In the case of the material which is studied (NO 3% Si-Fe), a general trend is observed: for an applied compressive stress, an increase of the magnetostriction deformation and a degradation of the magnetic permeability and this, whatever the amplitude. On the other hand, when a tensile stress is applied, the magnetostriction decreases and reaches saturation quickly. Besides, the permeability is improved for small amplitudes of tensile stress but deteriorated in the case of large amplitudes [69]. Despite the existence of these works, the modeling of magnetostriction under stress was limited to the rolling direction [4, 28]. The anisotropy effect of both the magnetization and the magnetostriction was not taken into consideration in the modeling. Aware of this weakness we propose a more complete modeling, describing more accurately the anisotropic behavior of non-oriented materials as well as the magneto-elastic effect.

2.5.3.1 Proposed magneto-elastic energy term E_σ

As detailed previously the magneto-elastic energy term takes into account the effect of mechanical stress on the magnetostriction deformation and the magnetic properties of the ferromagnetic material. To integrate the influence of stress, a function $h(\sigma)$ will be added to scale $g(k^{2n}, \lambda_i(\theta))$ (equation (2.5.16)) depending on the stress level and nature (compression or traction). Hence, the magnetostriction strain in the reference frame will be written as follows :

$$\overset{=\mu}{\varepsilon}_{\vec{M}} = g(k^{2n}, \lambda_i(\theta,\sigma)).h(\sigma).\begin{bmatrix} 1 & 0 \\ 0 & -\frac{1}{2} \end{bmatrix} \tag{2.5.22}$$

$\lambda_i(\theta,\sigma)$ are know identified depending on angle of magnetization θ and applied stress σ as well. $h(\sigma)$ corresponds to the stress dependence function and is given by:

$$h(\sigma) = \frac{a - \exp(b\sigma)}{c + 2\exp(b\sigma)} + d \tag{2.5.23}$$

a, b, c, d are fitting parameter which can be identified from unidirectional measurements under compressive and tensile stress for each magnetization direction θ with respect to the rolling direction. The function $h(\sigma)$ scales $g(k^{2n}, \lambda_i(\theta,\sigma))$ depending on the stress σ. It was obtained by observation of the variation of maximum magnetostriction with respect to stress, the expression in equation (2.5.23) is similar to the hyperbolic tangent function which has the same evolution as the measurements. Figure 2.5.9 shows the fitted and measured magnetostriction deformation at maximum flux density ($k \to 1$) for different values of stress along RD (0°), TD (90°) and 50°, others angles are reported in appendix B. It can be seen that the function $h(\sigma)$ fits best our measurements for all directions of magnetization with respect to the rolling direction (0°....90°).

In the expression of function g describing the magnetostriction strain, the functions λ_i were originally dependent only on θ, the angle of magnetization with respect to the

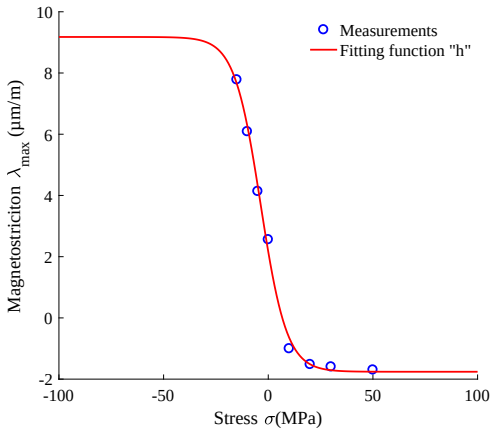

(a) *The rolling direction* $(0°)$.

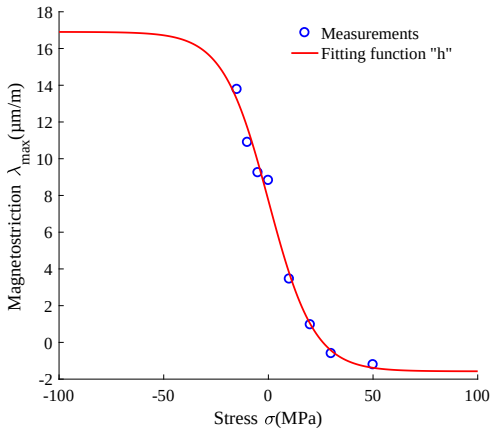

(b) *Transverse direction* $(90°)$.

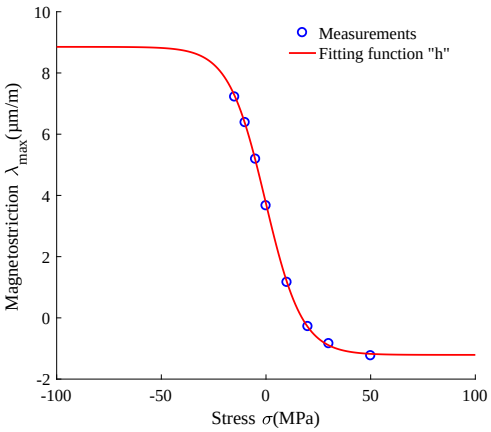

(c) *50° with respect to RD.*

Figure 2.5.9: *Fitted* $(h(\sigma))$ *and measured maximum magnetostriction* $\lambda_{max}(\sigma)$ *at different mechanical stress in the rolling direction.*

rolling direction. Now they depend also on the applied stress σ. Since our model is anisotropic and to best fit the experimental curves, we suggest three fitting functions instead of only one: a first function for compressive stress, a second function for tensile stress and a last function for 0 MPa. In these conditions, the general expression of function g can be written as follow:

$$g(k^{2n},\lambda_i(\theta,\sigma)) = \frac{1}{2}\left[g_{\sigma<0}.(sign(\sigma)-1).sign(\sigma) + g_{\sigma>0}.(sign(\sigma)+1).sign(\sigma) \right. \\ \left. -2.g_{\sigma=0}.(sign(\sigma)-1).(sign(\sigma)+1)\right] \tag{2.5.24}$$

The identification of the functions λ_i is done depending on θ and the nature of stress σ:

$$at \begin{cases} \sigma = -10MPa & \\ \sigma = 50MPa & \text{for } g_{\sigma>0} \\ \sigma = 0MPa & g_{\sigma=0} \end{cases} \tag{2.5.25}$$

2.5.3.2 Proposed macroscopic anisotropy energy term E_{an}

We have seen in paragraph 2.5.1 that the macroscopic anisotropy energy without mechanical loading can be written:

$$E_{an} = (\exp(k^{\alpha}) - 1)\left(\sum_{n=0}^{\infty} A_n.\cos(n.\theta)\right) \tag{2.5.26}$$

Nevertheless, it is well known that the applied stress introduces a supplementary anisotropy to the material [23]. To describe the effect of stress on the macroscopic anisotropy, a small modification will be made on the first term of the equation (2.5.26) to make the anisotropy energy high or low depending on the stress and the magnetization direction with respect to the rolling direction. In order to extend this expression to higher number of angles with respect to the rolling direction, it has been adapted to take two formulations depending on the angle by introducing a function $L(\theta)$:

$$E_{an} = (\exp(k^{\alpha}) + L(\theta))\left(\sum_{n=0}^{\infty} A_n.\cos(n.\theta)\right) \tag{2.5.27}$$

where the function $L(\theta)$ is introduced to consider the influence of the anisotropy effect depending on the angle θ with respect to the rolling direction. It takes two values 1 or -1 depending on the angle θ:

$$L(\theta) = \begin{cases} 1 & \text{for} \quad \theta = 0...30° \\ -1 & \text{for} \quad \theta = 40...90° \end{cases} \tag{2.5.28}$$

hence,

$$\begin{cases} \text{for angles} = 0...30^\circ & E_{an} = (\exp(k^\alpha) + 1)\,(\sum_{n=0}^{\infty} A_n.\cos(n.\theta)) \\ \text{for angles} = 40^\circ...90^\circ & E_{an} = (\exp(k^\alpha) - 1)\,(\sum_{n=0}^{\infty} A_n.\cos(n.\theta)) \end{cases} \tag{2.5.29}$$

2.5.3.3 Proposed demagnetizing factor energy

As explained in paragraph 2.5.1, the demagnetizing energy can be written as:

$$E_d = \frac{\mu_0}{2} N_d \parallel \overrightarrow{M} \parallel^2 \tag{2.5.30}$$

$$N_d = \frac{1}{\chi_i(\theta).(1-k^2)} \tag{2.5.31}$$

N_d is named demagnetizing factor and it was established for unstressed state. To describe the effect of stress (especially at compressive stress) on the initial domain structure, a configuration demagnetizing field H_d^σ has been introduced by [98], to be added to the initial field H with a new demagnetizing factor:

$$\overrightarrow{H}_d^\sigma = \eta.(N_d^\sigma - \frac{1}{3}).\overrightarrow{M} \tag{2.5.32}$$

where η is a material parameter, $\overrightarrow{M}$ is the magnetization and N_d^σ is the stress demagnetizing effect.

In the case of uniaxial stress σ applied in the same direction as the magnetic field H, N_d^σ can be written as follows:

$$N_d^\sigma = \frac{1}{1 + 2 \times \exp(-K\sigma)} \tag{2.5.33}$$

K is a material parameter that is defined by other modeling parameters [28]:

$$K = \frac{3}{2} A_s \lambda_{100} = \frac{9.\chi_i(\theta).\lambda_{100}}{\mu_0 M_s^2} \tag{2.5.34}$$

$\chi_i(\theta)$: is the initial susceptibility as a function of magnetization angle θ.
λ_{100}: is the saturation magnetostriction in the $< 100 >$ cubic axis.
μ_0: is the vacuum permeability.
M_s : is the saturation magnetization.

As the stress demagnetizing field is now defined, it will be integrated to the demagnetizing energy by the expression of magneto-static energy that can be divided into two contributions (Zeeman and demagnetizing field energy):

$$\begin{aligned} E_{ms} &= E_z + E_d = -\mu_0.\vec{M}.\vec{H} - \mu_0.\vec{M}.\vec{H}_d \\ E_{ms} &= -\mu_0.\vec{M}.\vec{H} + \tfrac{1}{2}\mu_0(N_d - 2\eta.(N_d^\sigma - \tfrac{1}{3}))\parallel \vec{M} \parallel^2 \end{aligned} \tag{2.5.35}$$

If a single crystal ferromagnetic material with no applied field is considered, the magneto-static energy (E_{ms}) will be equal to the energy of the demagnetization field (E_d).

The demagnetizing field energy is then defined as:

$$E_d = \frac{\mu_0}{2}(N_d - 2\eta.(N_d^\sigma - \frac{1}{3}))\parallel \vec{M} \parallel^2 \tag{2.5.36}$$

To take only the effect of compressive stress, the expression in equation (2.5.36) becomes:

$$E_d = \frac{\mu_0}{2}(N_d + \eta.(sign(\sigma) - 1).(N_d^\sigma - \frac{1}{3}))\parallel \vec{M} \parallel^2 \tag{2.5.37}$$

The equation (2.5.37) corresponds to the expression of the demagnetizing field energy under mechanical stress. This expression is reduced to equation (2.5.30), when there is no applied stress ($N_d^\sigma = \frac{1}{3}$) or under tensile stress ($(sign(\sigma) - 1) = 0$ for $\sigma > 0$). However, the non-monotonic behavior at very high tensile stress is not considered.

2.5.4 The model parameters

The model parameters are identified from anhysteretic magnetic and magnetostrictive measurements under uniaxial stress. The identification has been done for non-oriented (NO) electrical steel in 10 directions of cut with respect to the rolling direction. The samples were loaded by uniaxial stresses varying from -10 MPa to 50 MPa. In order to identify the model parameters, the measured anhysteretic magnetization curves under free stress are used to describe the macroscopic anisotropy. Whereas, the anhysteretic magnetostriction curves under uniaxial stress levels of -10 MPa, 0 MPa and 50 MPa are used to reproduce the magnetostriction behavior. The parameters retained resulting from the identification are grouped in the table 2.4.

Parameter	M_s	λ_{100}	η	α
Value	$1{,}3.10^6$	23.10^6	1.10^{-4}	20
Unit	A/m	-	-	-

Table 2.4: *Model parameters.*

The parameters presented in the table 2.4 were simply chosen to reproduce accurately the unidirectional experimental results obtained under stress on samples cut in different

directions. To these parameters is added those of $h(\sigma)$ function a, b, c, d which can be identified from unidirectional measurements under compressive and tensile stress for each magnetization direction θ.

The coefficients A_n (anisotropy coefficients), the anisotropic functions λ_i (magnetostriction constants at saturation), as well as the initial susceptibility $\chi_i(\theta)$ are identified respectively from experimental characterization thanks to the following equations:

$$\sum_{n=0}^{\infty} A_n.\cos(n.\theta) = \mu_0.\underbrace{\left(\frac{1}{\exp(1^{\alpha})-1}\right)}_{k_{exp}\approx 0.6\ \forall\alpha}.M_S.\sqrt{H_{0_{RDexp}}^2 + H_{0_{TDexp}}^2} = E_{an_{exp}}(\theta)$$
$$\begin{cases} A_0 &= \left\langle E_{an_{exp_j}} \right\rangle \\ &= \frac{1}{N}\sum_{j=0}^{N-1} E_{an_{exp_j}} \\ A_n &= \frac{2}{N}\sum_{j=0}^{N-1} E_{an_{exp_j}} \cos\left(n.\theta_{exp_j}\right) \end{cases} \tag{2.5.38}$$

where N and θ_{exp_j} are respectively the number and the measurement angles.

$$\chi_i = \frac{dM}{dH} \tag{2.5.39}$$

$$\lambda_i = \frac{1}{2}\left[\frac{d^2\lambda^{\mu}(k)}{dk^{2i}}\right]_{k=0} \tag{2.5.40}$$

λ^{μ}corresponds to the measured magnetostriction deformation: $\lambda^{\mu} = \lambda_1 k^2 + \lambda_2 k^4 + \lambda_3 k^6 + \lambda_4 k^8$.

In order to integrate these functions in a minimization algorithm, we need to generalize them to ensure their continuity whatever the angle of cut θ. By considering these functions π-periodic and even, we obtain the generalized version shown in figure 2.5.10 for each function. Considering the red vertical line as the symmetry axis, the results on the right were obtained by symmetry based on the measurements results on the left. It is worth noticing that the functions λ_i in figure 2.5.10c were plotted under -10 MPa and 50 MPa in addition to $\sigma = 0$ MPa.

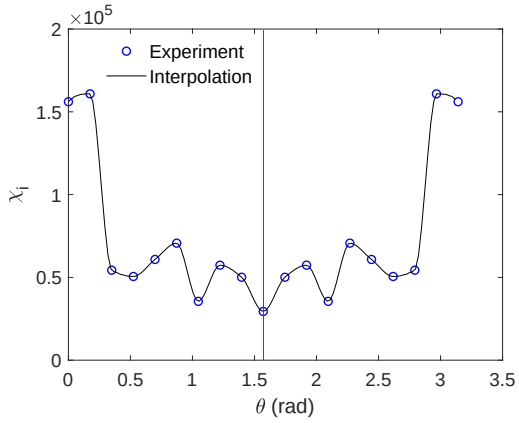

(a) *Initial susceptibility evolution.*

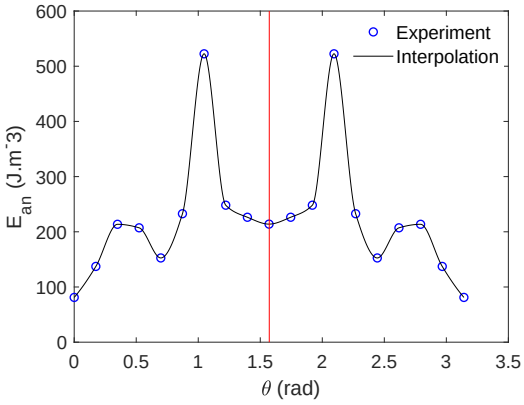

(b) *Anisotropy energy for a magnetization* $M = 0,6.M_s$.

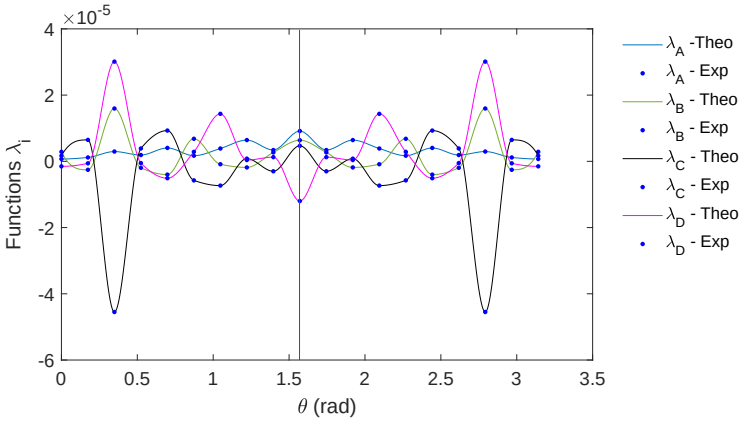

(c) *Magnetostriction functions* λ_i *at saturation.*

Figure 2.5.10: *Evaluation of model parameters in different direction of cut at* $\sigma = 0$ *MPa.*

The modeling process is described in figure 2.5.11. Given that the anhysteretic magnetization curve represents a succession of states which each one corresponds to the lowest energy for a given load (magnetic field and/or stress), the reconstitution of anhysteretic behavior (magnetization and magnetostriction deformation) may be represented as a problem of global minimum search for total energy (equation (2.5.1)).

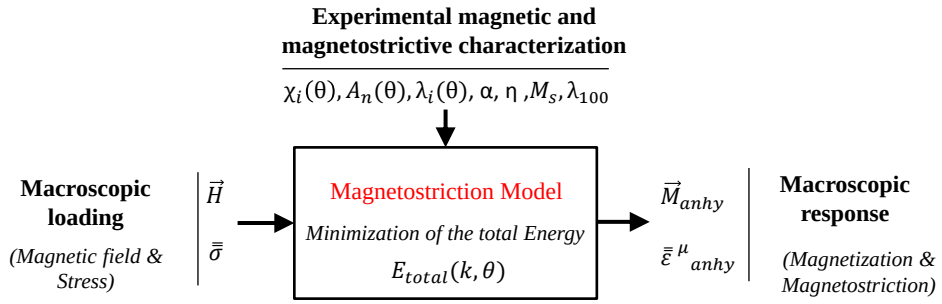

Figure 2.5.11: *The computation process of the magnetization and magnetostriction deformation under stress.*

2.6 Results of modeling and comparison to measurements

This section describes the modeling results that will to be compared to experimental measurements. The material parameters used for the modeling were presented in the previous paragraph (subsection 2.5.4). It is reminded that the direction of uniaxial mechanical loading is parallel to the magnetic and magnetostrictive measurements. The magnetization and magnetostriction evolution are modeled under stress with σ ranging from -10 MPa to 50 MPa. In order to better observe the anisotropy of the magnetic and magnetostrictive behavior, the measurements are shown for a maximal external magnetic field value of 500 A/m.

2.6.1 Magnetic behavior

The figures 2.6.1, 2.6.2 and 2.6.3 describe the experimental and modeled magnetization curves for samples cut in different direction with respect to the rolling direction. For each sample, the experimental curve is on the left (dashed line) and the modeled is on the right (continuous line). As a general trends, the modeled effect of tensile stress on the magnetic behavior is well restored and reasonably accurate for the studied directions. However, the prediction of the behavior under compressive stress is not sufficiently accurate. In addition, a compressive stress leads to a very significant drop in the magnetic permeability, whereas a tensile stress has a much slighter effect. This evolution of magnetic properties with the stress nature is in agreement with the measurements. In some directions, the tensile stress leads to an improvement of the magnetic permeability as it is the case for 90° direction sample (figure 2.6.3a). Also, the model is able to take into account the non-monotonic dependency of the permeability on the stress at low and medium tensile stress for certain directions but not for all (figure 2.6.1). This problem

could probably be overcome by involving the expression of the demagnetizing field factor (N_d^σ) for tensile stresses (not considered for tensile stress in the equation (2.5.37)). But this may increase the relative error between the experimental and the modeled results. In all directions, at compression, a bowing of the anhysteretic curve of magnetization is observed (figure 2.6.1a). Phenomenologically, this could be explained by the increase of 90° domains under compressive stress as discussed in section 2.4.1.

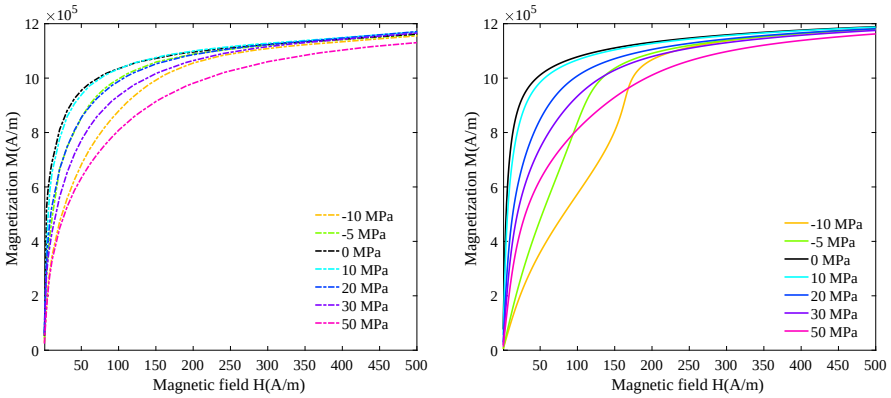

(a) *Rolling direction: 0°*

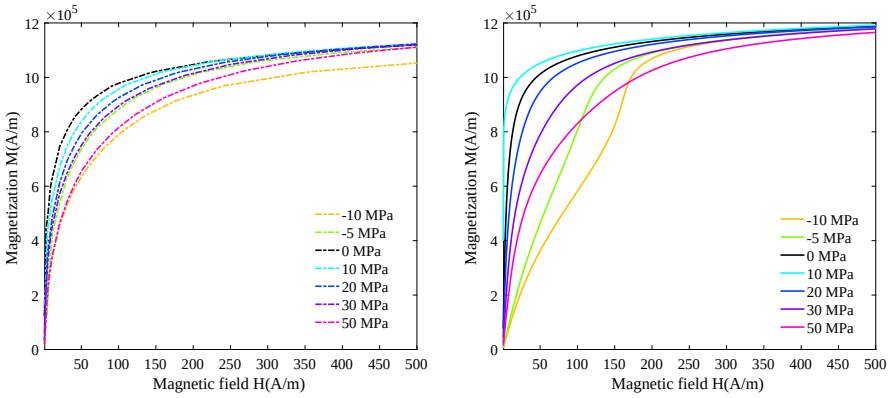

(b) *10° with respect to RD*

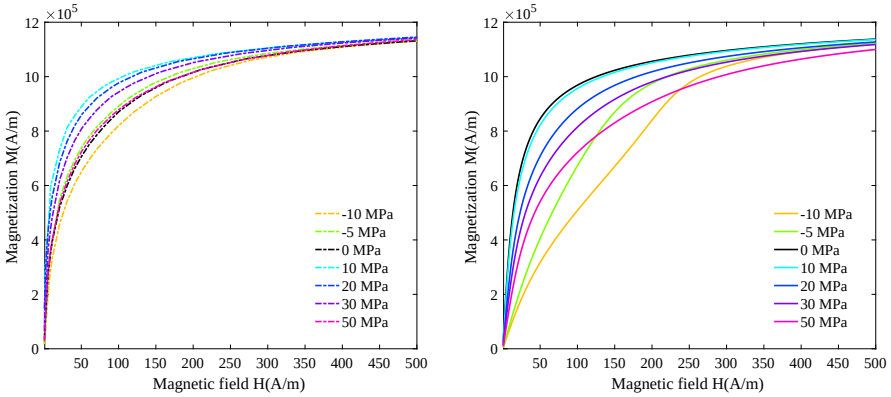

(c) *20° with respect to RD*

Figure 2.6.1: *Anhysteretic $M(H)$ behavior of the NO steel along different direction of magnetization and under uniaxial stress $\theta = (0°, 10°, 20°)$: Experimental results (left), modeling results (right).*

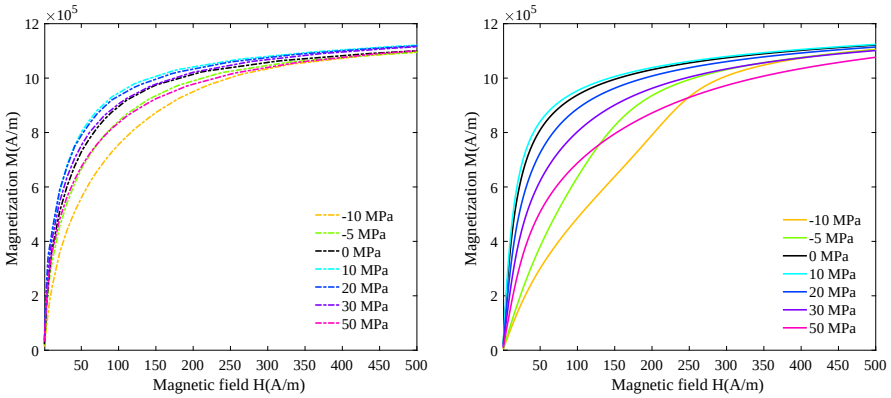

(a) *30° with respect to RD*

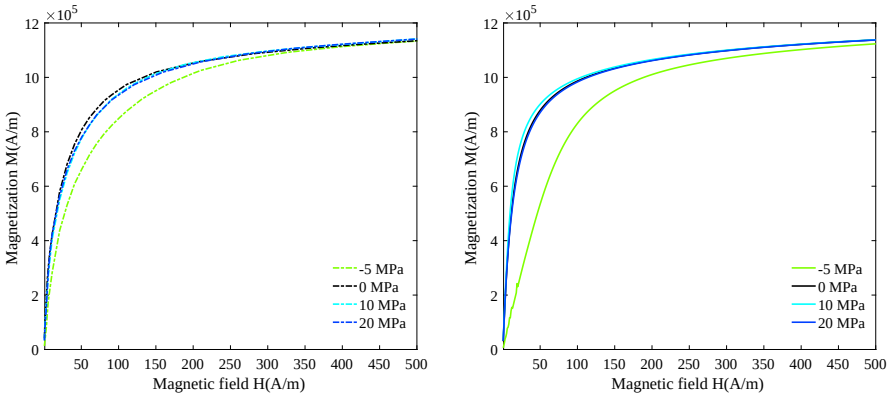

(b) *40° with respect to RD*

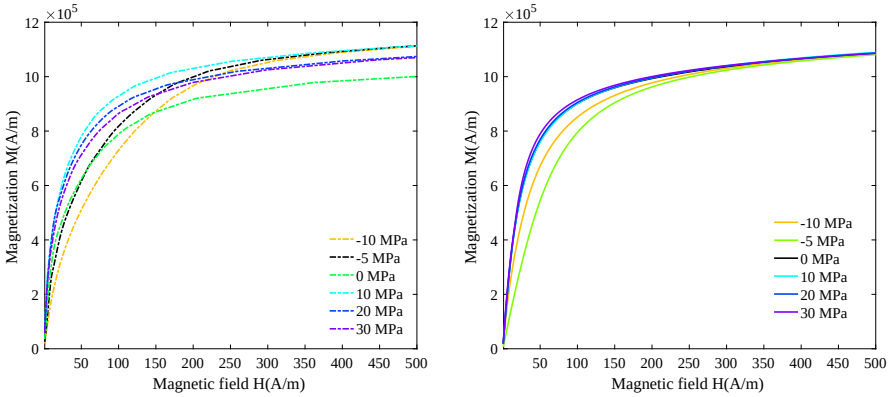

(c) *60° with respect to RD*

Figure 2.6.2: *Anhysteretic $M(H)$ behavior of the NO steel along different direction of magnetization and under uniaxial stress $\theta = (30°, 40°, 60°)$: Experimental results (left), modeling results (right).*

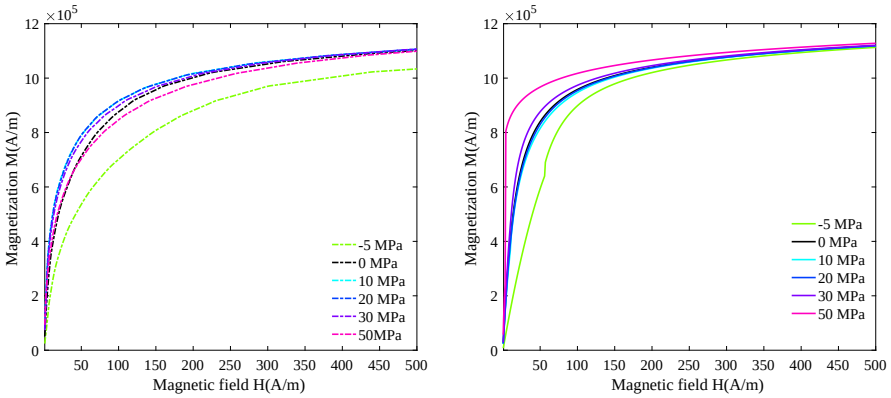

(a) *80° with respect to RD*

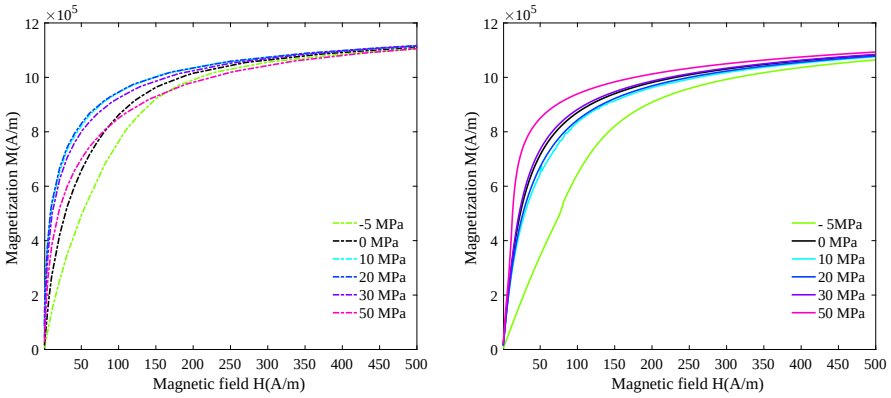

(b) *The transverse direction: 90°*

Figure 2.6.3: *Anhysteretic $M(H)$ behavior of the NO steel along different direction of magnetization and under uniaxial stress $\theta = (80°, 90°)$: Experimental results (left), modeling results (right).*

2.6.2 Magnetostrictive behavior

The comparison between modeled and experimental results is shown in figures 2.6.4 and 2.6.5. The figures have been plotted so that all the curves start from zero. It appears first of all that the pace and the general trends of the magnetostrictive curves are correctly represented by the model. The model, however, tends to overestimate the magnetostrictive behavior in certain directions. Furthermore, we observe that the model reproduces well the effect of macroscopic and stress anisotropy. Hence, the trends correspond to the experimental observations. While under compression magnetostriction increases, magnetostriction decreases for tensile stress and a reversal is observed from positive to

negative when high tensile stress is applied. On the other hand, the inversion of the direction of magnetostrictive deformation variation reproduced by the model for certain directions of magnetization (figure 2.6.4a) corresponds to a stage where the magnetic state becomes essentially driven by the rotation of the magnetization in the domains. This reversal of the direction of variation also occurs experimentally if measurements are made for more intense magnetic fields.

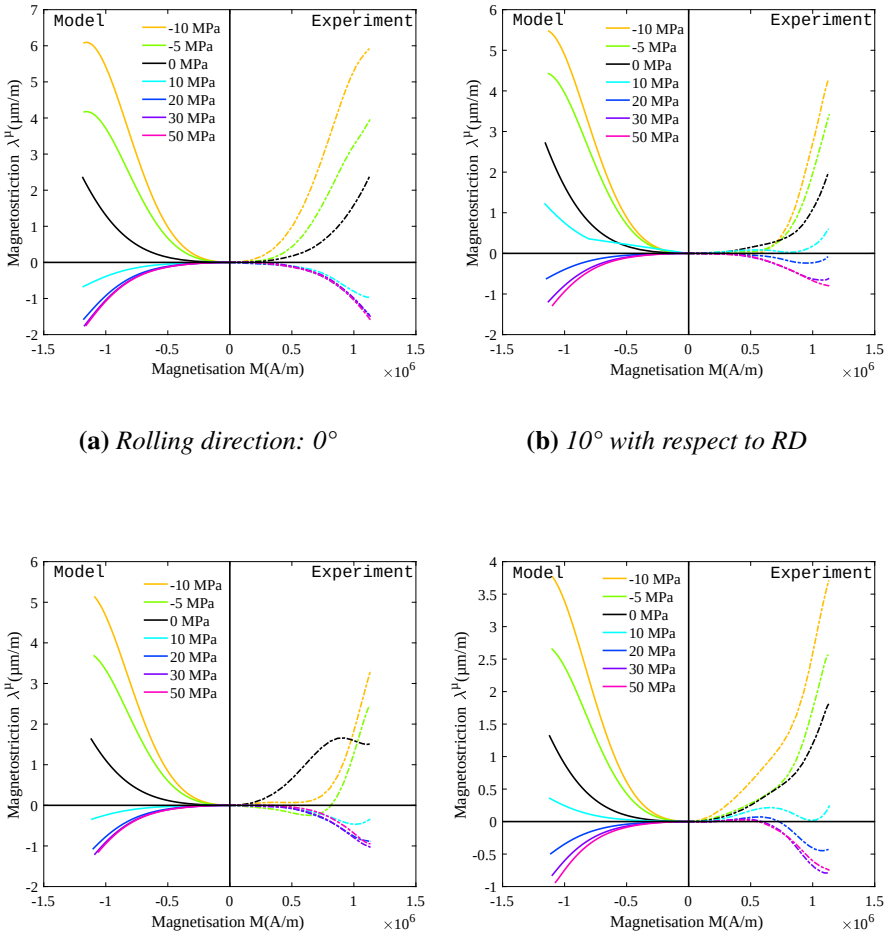

(a) *Rolling direction: 0°*

(b) *10° with respect to RD*

(c) *20° with respect to RD*

(d) *30° with respect to RD*

Figure 2.6.4: *Anhysteretic magnetostrictive behavior $\lambda^{\mu}(M)$ of NO steel different directions of magnetization and under uniaxial stress: Modeling and experimental results $\theta = (0°...30°)$.*

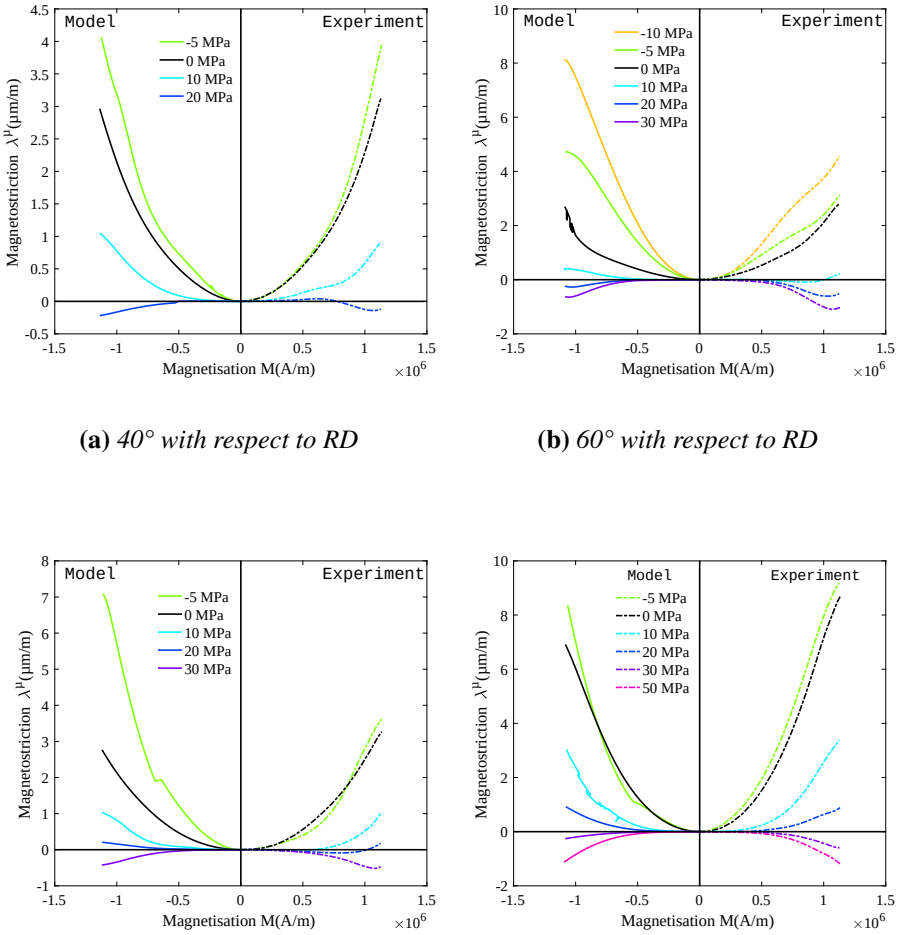

(a) *40° with respect to RD*

(b) *60° with respect to RD*

(c) *80° with respect to RD*

(d) *Transverse direction: 90°*

Figure 2.6.5: *Anhysteretic magnetostrictive behavior $\lambda^{\mu}(M)$ of NO steel different directions of magnetization and under uniaxial stress: Modeling and experimental results $\theta = (40°, 60°, 80°, 90°)$.*

These comparisons between model and measurements allow us to conclude that the modeling is capable of representing correctly the anhysteretic magneto-elastic coupling and anisotropy effects for different directions of cut. Comparisons reveal some gaps and limitations, such as the difficulties to reproduce behaviors under high compression stress, as well as, the non-monotonic behavior under high tensile stress for certain directions of cut with respect to the rolling direction.

2.7 Conclusion

Measurements were carried out on a non-oriented grain iron alloy with 3% of silicon. The magnetic and magnetostrictive behaviors were characterized under mechanical stresses for samples cut in different directions with respect to the rolling direction. This constitute the originality brought by our measurements. The results of magnetic and magnetostrictive behavior on the samples showed that the anisotropy effect remains dominant under low and medium stresses but tends to disappear for very high stresses. On the other hand, a strong link has been established between permeability, magnetostrictive deformation and stress. In some particular configuration of stresses, one can have improvements in the magnetic properties and the decrease of the magnetostriction deformation, as is the case for the transverse direction under tensile stress.

The second part was devoted to present the recent developments which allowed the improvement of the model. These improvements concern in particular the accounts of the effect of the stress on the magnetic and magnetostrictive properties. Comparisons between experimental and modeling results show a qualitative agreements. However, more adjustment are needed to achieve a quantitative comparison. The advances compared to the old version of the model are certain, but the modeling remains imperfect. Considering the stress effect coupled with the macroscopic anisotropy (due to texture) seems to be difficult to predict for all angles of cut in the present configuration of the model, other expressions are to be added and some energy terms are to be modified in future work. Besides, the model requires high number of material parameters (around 21), a reduction of the number of parameters seems necessary for easier use and exploitation.

“One never notices what has been done; one can only see what remains to be done.”

(Marie Skłodowska-Curie)

CHAPTER 3

FROM SINGLE SHEET TO LAMINATED STRUCTURES

3.1 Introduction

Since the aim of this PhD work is to extend the work from material to a transformer-type device, the present chapter deals with the magnetic and magnetostrictive behavior of laminated structures.

In this chapter the measurement results obtained on two types of structure will be presented and compared to results obtained with a finite element approach. First, the results of magnetic and magnetostrictive behavior of the laminated structure without air gap under two different magnetization conditions are presented depending on the voltage or current magnetization mode. Also, a comparison is made between the strain gauge method and the laser vibrometer setup in term of magnetostriction measurements, then, the contribution of each method is discussed. Next, measurement results under uniaxial compressive stress will be described and the magneto-elastic coupling highlighted. Next, an overview of the 2D FE method for the computation of the deformation of the structure due to magnetostriction will be detailed. For the computation of magnetostrictive deformation, the energy based model presented in chapter 2 is used. After that, the FE results will be compared to measurement results. The second part of the chapter will be devoted to study the structure with air gaps to investigate the interaction between magnetostriction and the Maxwell forces. For the FE computation, in addition to the magnetostrictive deformation, Maxwell forces are calculated by the Maxwell stress tensor. An analytical approach is also established to make a comparison with the FE calculation. Later on, the FE and measurements results will be compared and discussed in details. Based on these results, the effect of the air gap material hardness on the total displacement will be discussed.

3.2 Description of the laminated structures under study

The ferromagnetic structure under study can be assimilated to a single phase transformer core of dimension 250×250 mm and 15 mm width leg. The core consists of 40 impregnated iron sheets with a total thickness of 15 mm where each sheet is 0.35 mm thick.

In a first place, to study only magnetostrictive deformation, a simple ferromagnetic frame assembly has been considered, figure 3.2.1a. This choice of cutting (frame shape) allows, in addition to the elimination of air gaps, the possibility of studying the magnetostriction in the direction of rolling and transverse for the same magnetic flux and the same structure. In a second place, a laminated structure made of U and I cores shape was assembled with the same dimensions as the previous one. The introduction of two air gaps in the flux path helps in the production of large magnetic forces, figure 3.2.1b. Materials with different mechanical properties and width are inserted in the air gap to evaluate their effect on the magnetostrictive deformation.

In the air gaps, the magnetic flux lines are mainly perpendicular to the air gaps surface resulting in a perpendicular magnetic stress pressure. Therefore, magnetic forces result only in tensile/compressive stress in the legs where the air gaps are present.

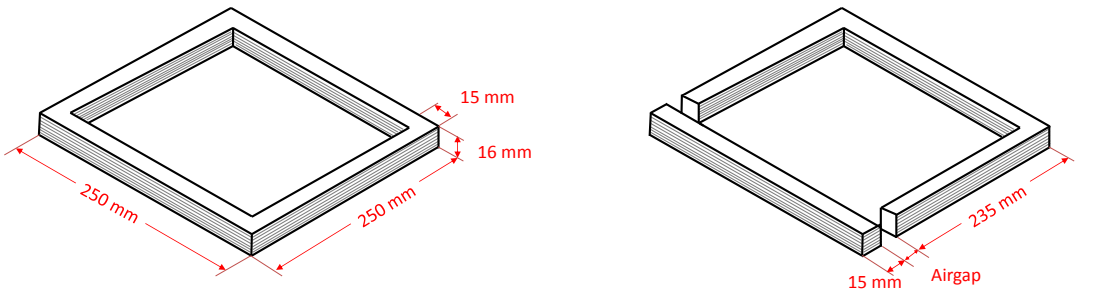

(a) *The laminated structure without air gaps* **(b)** *The laminated structure with air gaps*

Figure 3.2.1: *The laminated structures under study: without air gaps (a), with air gaps (b).*

3.3 Magnetic and magnetostrictive measurements conditions

In the framework of this work the magnetic and magnetostrictive measurements on the laminated structure are performed under unidirectional excitation. It means that the

magnetic field is always unidirectional along the legs of the laminated structures where the measurements are made, figure 3.3.1a. The excitation winding creates the magnetic field in the laminated structure, magnetostrictive deformation occurs and is measured by a strain gauge. Thereafter, the magnetic field and the magnetic flux density are retrieved by coil sensors ($H-coil$, $B-coil$). Each measurement was carried out five times to evaluate the repeatability error using Student Law and the average was kept. The confidence level of the measured values is 95%. Figure 3.3.1b shows a picture of the studied structure with the measurements and excitation elements.

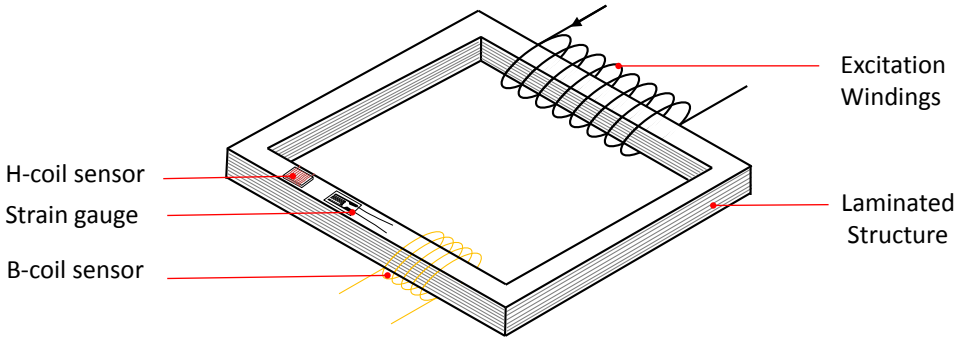

(a) *Excitation and measurements elements on the laminated structure*

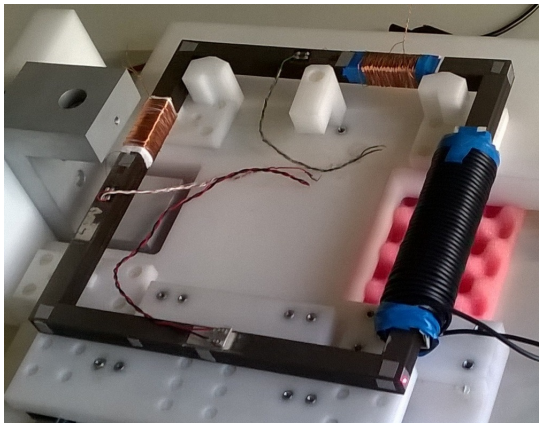

(b) *Picture of the laminated structure without air gaps*

Figure 3.3.1: *The laminated structure with all elements for sensing magnetic flux density and magnetostriction strain*

Considering the limitations of the strain gauge measurements method due to the contact with the sample, an non-intrusive approach using a laser Doppler vibrometer has been used in addition to strain gauges. This technique overcome the drawbacks of the strain gauge since no contact with the sample is required.

3.3.1 SIOS SP-S laser interferometric vibrometer

Laser interferometric vibrometers are used to measure precisely and without contact the change of position over time of an object or surface of any degree of roughness. The SP-S[1] laser vibrometer was chosen for more precise magnetostriction measurements. It belongs to the family of single-point vibrometer with a fixed focal length as it allows to measure an object's vibrations in the direction of the laser beam (figure 3.3.3a). The working principle is based on Laser Doppler Vibrometry (LDV). This method offers better displacement and velocity resolution compared to the strain gauge technique and is used in many fields of basic science. The technology is based on the Doppler effect (figure 3.3.2); sensing the frequency shift of back scattered light from a moving object. If the object under investigation is moving with the speed V_{object} in the measurement axis of the interferometer, then the maximum oscillation frequency $f_{doppler}$ of the measurement signal can be calculated using the Doppler effect:

$$f_{doppler} = 2.\frac{V_{object}}{\lambda_{He-Ne}} \tag{3.3.1}$$

where λ_{He-Ne} is the wavelength of He-Ne laser (632.8 nm).

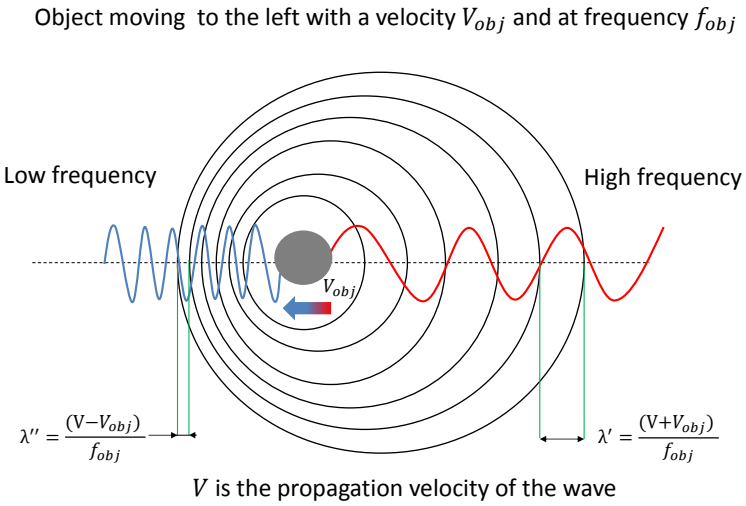

Figure 3.3.2: *Doppler effect: frequency shift phenomenon that occurs whenever a wave source and an observer are moving with respect to one another.*

All optical parts of the laser vibrometer are located within the sensor head and balanced (figure 3.3.3b). First, The beam of a helium-neon laser is split by a beam splitter

[1] SP-S: Single Point-Serie

BS-I into a reference beam and a measurement beam. After passing through a second beam splitter BS-II, the measurement beam is focused onto the vibrating object, which reflects it. This reflected beam is now deflected downwards by BS-II, is then merged with the reference beam by the third beam splitter BS-III and is then directed onto the detector.

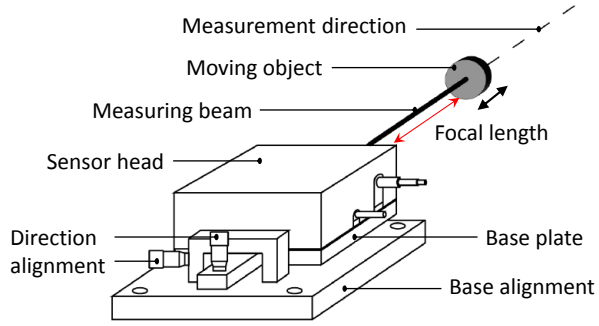

(a) *Sensor head pointing to the object to be measured*

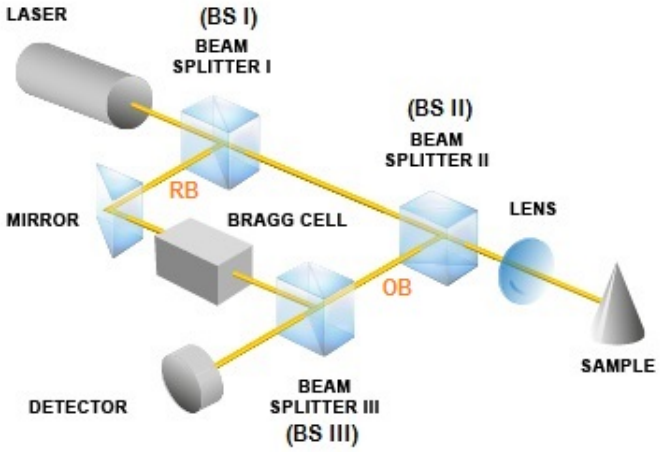

(b) *Schematic description of the arrangement of sensor head.*

Figure 3.3.3: *SP-S vibrometer sensor head.*

As the path length of the reference beam (RB) is constant over time (with the exception of negligible thermal effects on the interferometer RB = C^{ste}), a movement of the object under investigation (OB[2] = OB(t)) generates a dark and bright pattern typical of

[2]OB: Object Beam

interferometry on the detector (fringe). One complete dark bright cycle on the detector corresponds to an object displacement of exactly half of the wavelength of the light used. In the case of the helium-neon laser used almost exclusively for vibrometers, this corresponds to a displacement of 316 nm.

Changing the optical path length per unit of time manifests itself as the Doppler frequency shift of the measurement beam. This means that the modulation frequency of the interferometer pattern determined is directly proportional to the velocity of the object (equation (3.3.1)). As object movement away from the interferometer generates the same interference pattern (and frequency shift) as object movement towards the interferometer, this setup cannot determine the direction the object is moving in. For this purpose, an acoustic-optic modulator (Bragg cell) is placed in the reference beam, which shifts the light frequency by 40 MHz (by comparison, the frequency of the laser light is 4.74×10^{14}Hz). This generates a modulation frequency of the fringe pattern of 40 MHz when the object is at rest. If the object then moves towards the interferometer, this modulation frequency is reduced and if it moves away from the vibrometer, the detector receives a frequency higher than 40 MHz. This means that it is now possible not only to detect the amplitude of movement but also to clearly define the direction of movement. Nevertheless, the direction information depends on the laser head and software used for measurements acquisition.

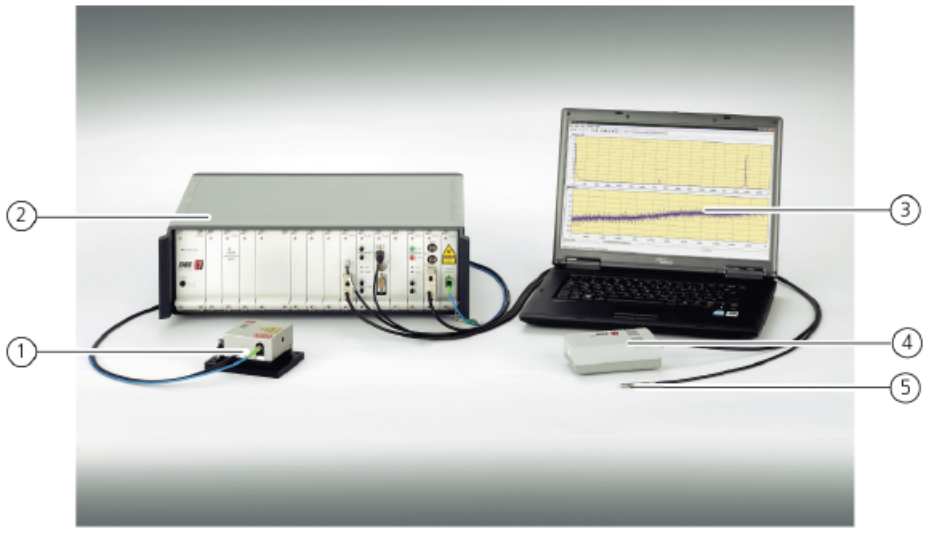

1 Sensor head with alignment base
2 Supply and evaluation unit (SEU)
3 Computer
4 Sensor box
5 Temperature sensor

Figure 3.3.4: *Overall view of SP-S series vibrometer.*

The SP-S laser interferometric vibrometer consists of three basic components (fig-

ure 3.3.4):

- The compact, fiber optic coupled sensor head.
- The modular Supply and Evaluation Unit (SEU) with an integrated He-Ne laser.
- The personal computer with control software INFAS Vibro.

The main characteristics of the SP-S vibrometer are summarized in table 3.1.

Property	Value
Focal distance	240 mm
Laser spot diameter	100 µm
Resolution	0.1 nm
Frequency range	0...500 kHz
Sampling frequency range	1...1000 kHz
Measurement range	$\leq \pm 20$ mm

Table 3.1: *Technical data of the vibrometer SP-S.*

3.3.2 Excitation system

To create a sinusoidal voltage or sinusoidal current waveforms, two setups were used depending on the quantities imposed (current or voltage), hereafter named as voltage magnetization and current magnetization. Since a proportional relationship exists between the magnetostrictive deformation and the magnetization waveform ($\lambda = f(M)$=$\lambda_0 + \lambda_2.M^2$), the aim of the excitation systems is to generate different magnetic induction waveforms B in the structure and observe the effect on the magnetostrictive deformation waveforms.

3.3.2.1 Voltage magnetization

The excitation setup for voltage magnetization and electrical quantities are shown in figure 3.3.5 and figure 3.3.6 respectively. Since the setup is fully controlled manually, the signal amplitude can be adjusted using an auto-transformer. First, the voltage coming from the grid (the default frequency is 50 Hz) is reduced and then, the voltage signal is sent to the magnetization coil of the laminated structure thanks to an auto-transformer. Later on, the magnetic induction B, the magnetic field H and the magnetostriction strain signals are then measured. Afterwards, all the measured signals are sent to the oscilloscope and saved. All the signal calculations, post-processing and the visualization of the signals are further processed in the MATLAB software.

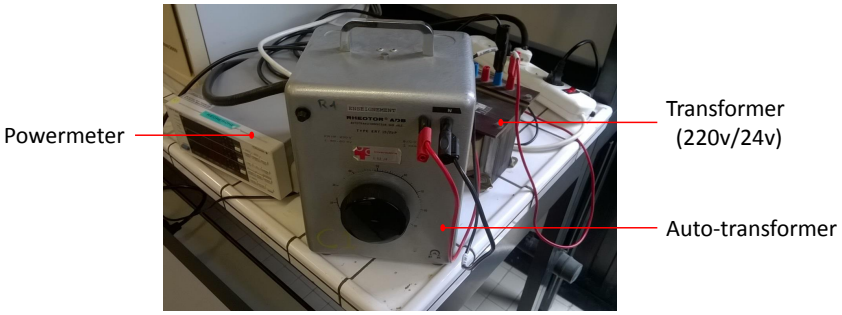

Figure 3.3.5: *Voltage magnetization set-up.*

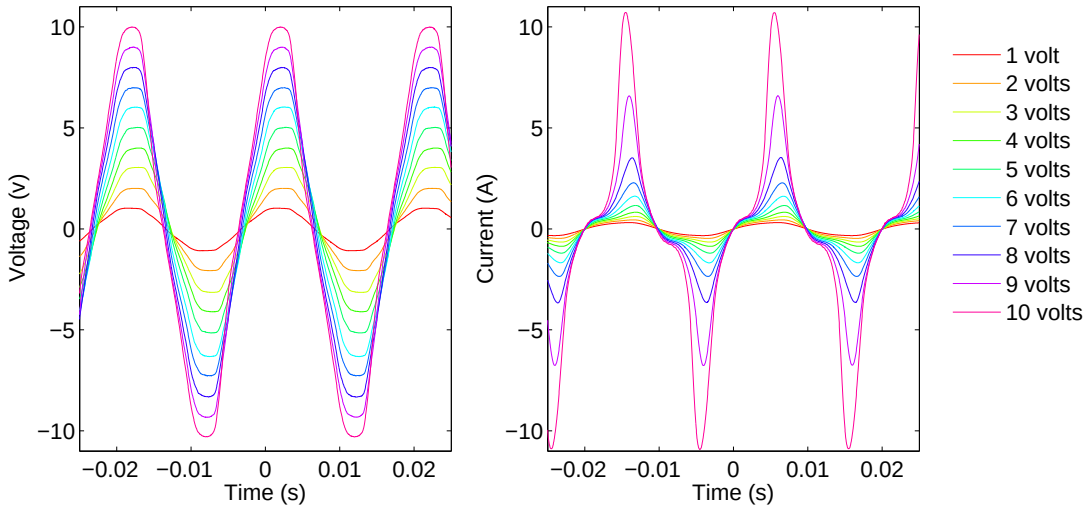

Figure 3.3.6: *Voltage magnetization: voltage and current waveforms.*

3.3.2.2 Current magnetization

The set-up composition for current magnetization and the electrical quantities are illustrated in figure 3.3.7 and figure 3.3.8 respectively. A signal generator generates a sinusoidal wave $u(V)$ with a variable amplitude and frequency $f(Hz)$, then, the signal is sent to a power amplifier. Next, the output current $i(A)$ is sent to the excitation winding ($N = 80$ turns) surrounding the laminated structure. Hence, a magnetic field H is established in the ferromagnetic structure. This excitation system is equipped with a filter with adjustable cutting frequency and a signal amplifier of $B-coil$ and $H-coil$ sensors.

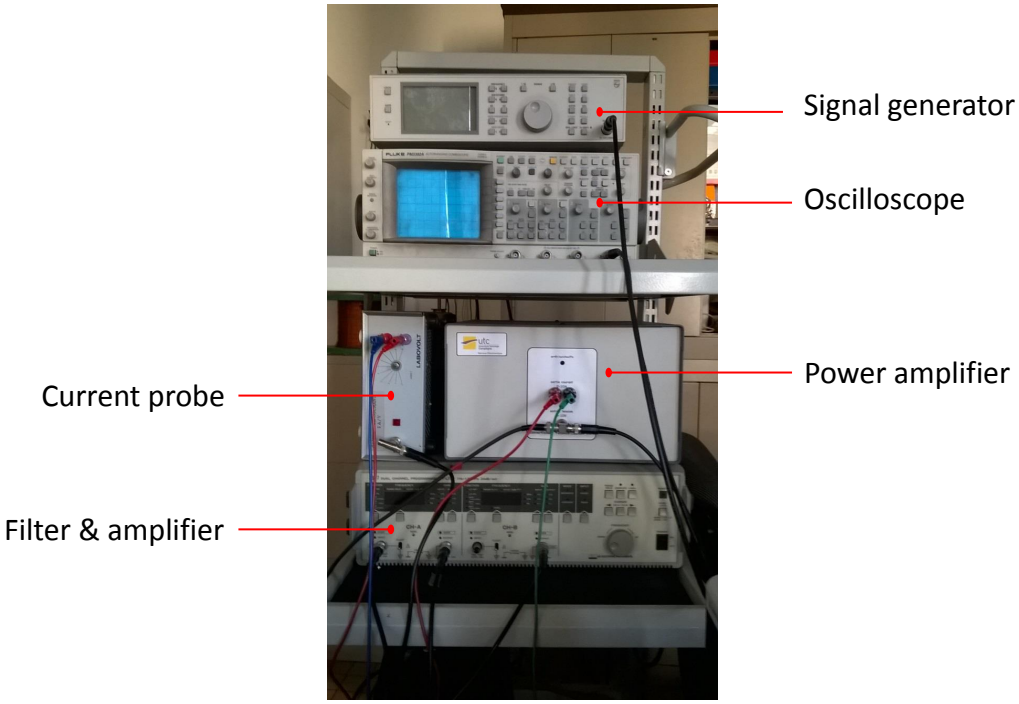

Figure 3.3.7: *Current magnetization set-up.*

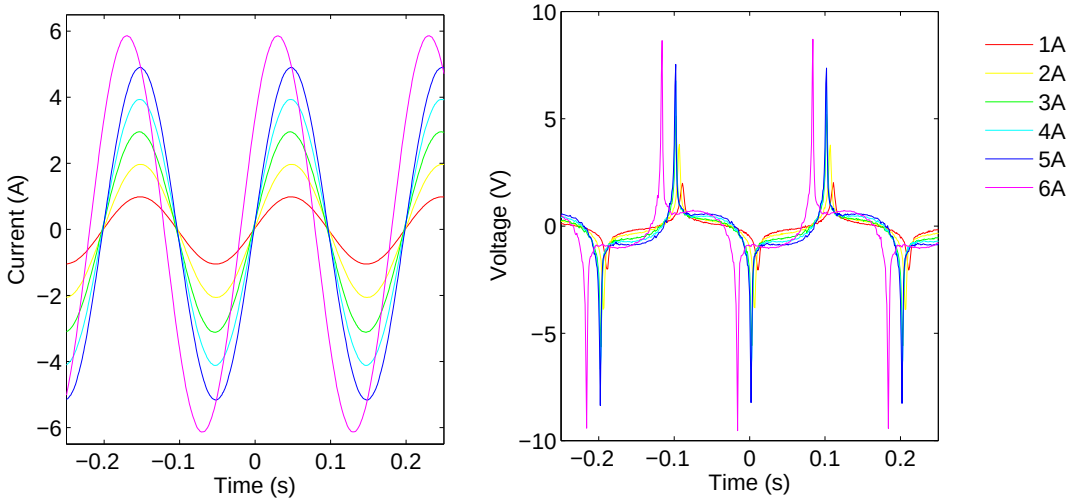

Figure 3.3.8: *Current magnetization: current and voltage waveforms.*

3.3.3 Stressing device for the laminated structure

In order to study the effect of compressive stress on the magnetostrictive strain (like in transformer assembly), the laminated structure is stressed in lamination direction by means of a clamping vise shown in figure 3.3.9, a description on the clamping vise is reported in appendix C. The use of rigid polymer parts (equivalent in size to the section of the structure leg) make it possible to apply the force uniformly to the structure leg. The variation of the magnetostrictive deformation in the structure is retrieved by means of a strain gauge. Due to accessibility issues the laser vibrometer could not be used when the structure is under stress. In fact, the setting up of the vise prevents the laser beam from reaching the surface of the bar under compressive stress. All the parts which constitutes the device for applying stress are non-magnetic so as not to alter the magnetic field circulating in the ferromagnetic structure.

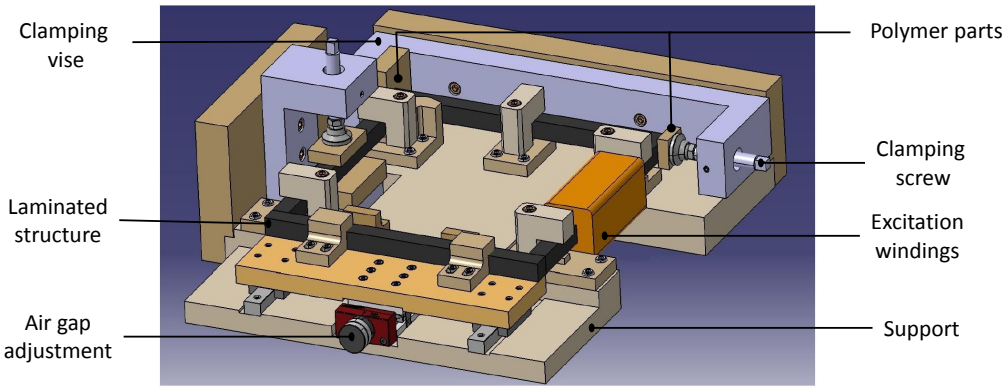

Figure 3.3.9: *General view of the clamping device.*

In order to apply a precise effort through the vise, torque wrenches are used to control the tightening torque (figure 3.3.10). The work done by the tightening torque C after one turn is written as follows:

$$W_{torque} = C.\theta = C.2\pi \tag{3.3.2}$$

On the other hand, the work done by a screw can be written as:

$$W_{screw} = F_s.p \tag{3.3.3}$$

where F_s is the stressing force and p the pitch of the screw.

If we make the assumption of a negligible friction (difficult to establish), the work of the torque should be equal to the work done by the screw, hence, we obtain the equation (3.3.4) to make the connection between the torque applied, the screw of the

vice and the stressing force applied to the laminated structure:

$$F_s = \frac{2\pi C}{p} \tag{3.3.4}$$

where F_s is the stressing force, C is the applied torque on the torque wrench and p corresponds to the trapezoidal pitch of the screw (p=3 in this case).

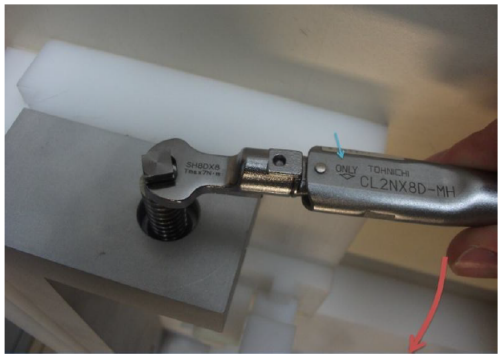

Figure 3.3.10: *Tightening the screw with the torque wrench.*

Two torque wrenches (CL2NX8D and CL5NX8D) provide a tightening torque ranging from 0.4 N.m to 5 N.m with a precision step of 0.05 N.m. Since the surface under pressure of the structure leg is small ($s = 2.25 \times 10^{-4}$m), we can reach interesting compressive stress levels with the presented stressing device up to $\sigma = -50$MPa. Furthermore, the risk of buckling is very small as the leg has a bigger section compared to the single sheet. Unfortunately, this stressing device does not allow the application of a tensile stress, despite the fact that tensile stress has a small effect on magnetic and magnetostrictive behavior of non-oriented electrical steel as it has been discussed in the chapter 2.

3.4 Study of the laminated structure without air gaps

3.4.1 Measurement results without mechanical loading

3.4.1.1 Strain gauge results

Figure 3.4.1 shows the selected points for the longitudinal magnetostrictive strain measurements. Only RD and TD directions can be present in the laminated structure in the measurement locations (A and B). Besides, the assembly of the structure was done randomly, independently of the cutting direction (RD or TD) in order to validate the

anisotropic assumption of the non-oriented grain material. This being said, it is assumed from the obtained results that TD sheets are predominant in location B and RD sheets are predominant in location A.

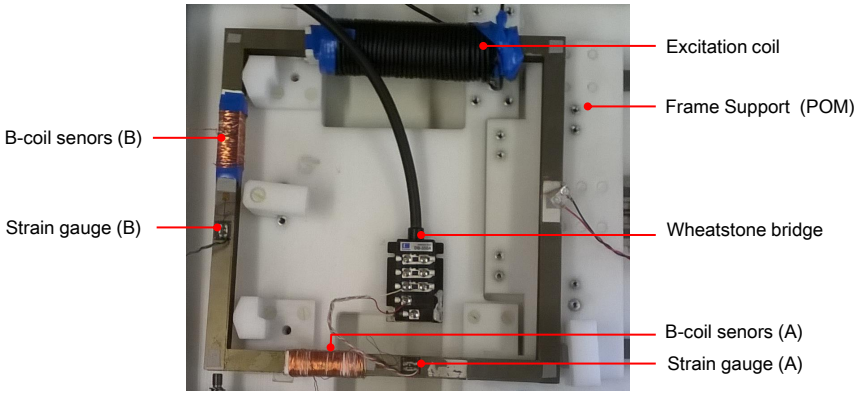

Figure 3.4.1: *Selected points for local magnetostrictive strain measurements.*

Voltage magnetization at 50 Hz

Figure 3.4.2 shows the hysteretic magnetic behavior ($B(H)$ loops) retrieved from the laminated structure at point B and the corresponding waveform of the magnetic field H and the magnetic flux density B at several magnitude of excitation.

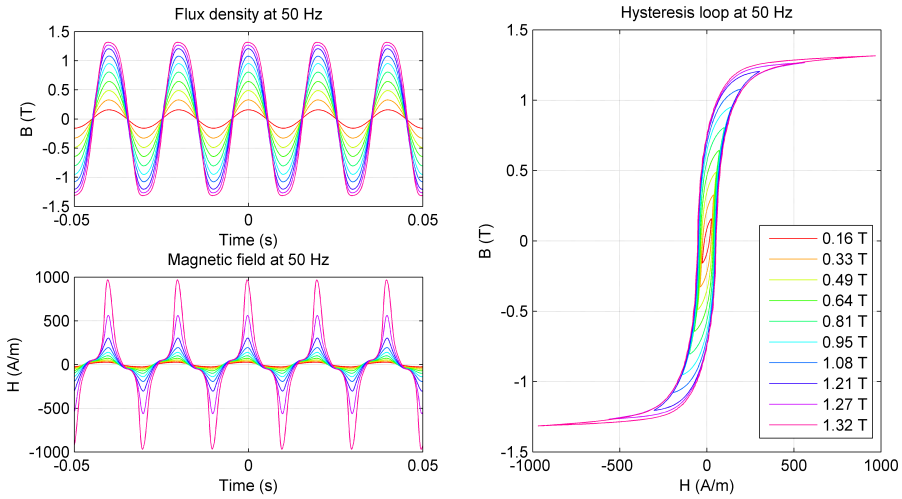

Figure 3.4.2: *Waveforms of magnetic field H and magnetic flux density B (left), and the $B(H)$ loops (right).*

The $B(H)$ loops measurements of the laminated structure are performed under a magnetization with peak magnetic field of 1000 A/m and a frequency of 50 Hz. The results illustrated in figure 3.4.3 show a small anisotropy of the magnetic behavior due to the cutting angle of the samples with respect to the rolling direction (RD or TD) but the difference seems negligible. If we assume isotropic behavior for non-oriented material, the ferromagnetic structure assembly should have almost the same magnetic characteristics in every direction including RD and TD (locations A and B). However, we notice a small magnetic anisotropy that can be due to the random assembly of the structure (mixture of RD and TD sheets), or due to a small magnetic flux leakage given the position of the B-coil sensors at point A and B respectiveley (figure 3.4.1).

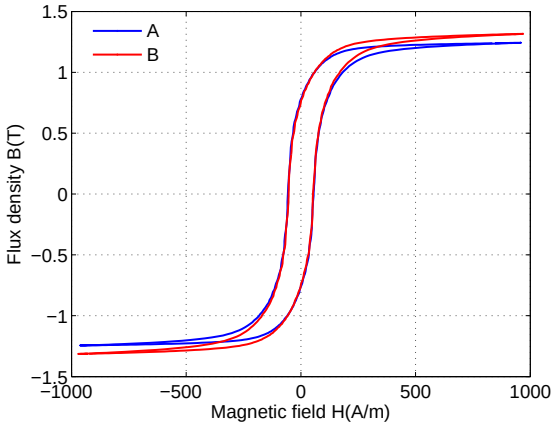

Figure 3.4.3: *Comparison of $B(H)$ curves at points A and B of the laminated structure.*

The local magnetostriction strain obtained on the laminated structure is shown in figure 3.4.4. The longitudinal strain at the two measured locations (A and B) is positive which was expected as the studied material is Si-Fe. Moreover, the magnetostrictive behavior is non-linear and hysteretic. At saturation, we notice that the magnetostrictive strain at location B $\varepsilon_B^{||} = 5.8 \times 10^{-6}$ is higher than the strain measured at location A, $\varepsilon_A^{||} = 4.23 \times 10^{-6}$.

According to the material behavior measured on single sheet (Chapter 2), the magnetostrictive strain along RD is smaller than the magnetostrictive strain along TD. However, on the laminated structure the magnetostrictive strain at location A (more RD sheets than TD) is greater than the one at RD on the single sheet. While the magnetostrictive strain at location B (more TD sheets than RD) is of the same magnitude as the one found on the single sheets in TD. The increase of strain magnitude at location A can be explained by the presence of some TD sheets as the laminated structure was randomly assembled. In fact, as we observed in Chapter 2, the magnetostrictive defor-

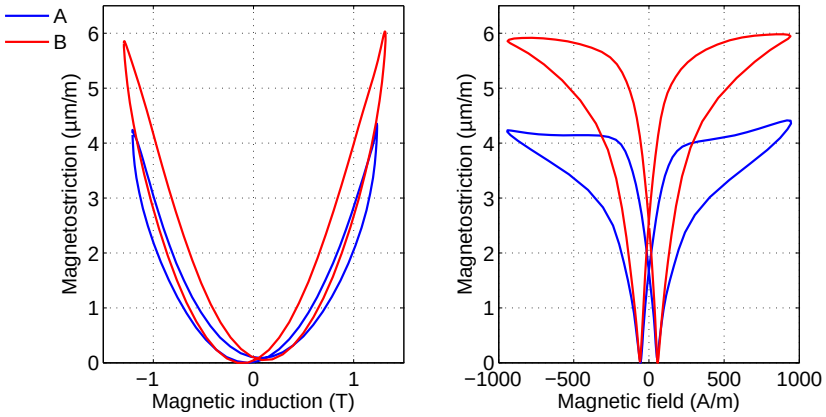

Figure 3.4.4: *Hysteretic behavior: Local magnetostrictive strain of the laminated structure at 50 Hz.*

mation in TD is greater than the one in RD direction. As explained, this is due to the predominant presence of 90° domains in TD than in RD when magnetizing along the length of the sample. In the case of our structure, the presence of small proportion of TD sheets among the RD sheets, causes an increase of the total deformation in the bar inducing an increase of the strain in location A compared to only RD sheets. Of course, since the deformation of the RD sheets is lower than the TD sheets, the deformation in location B (where TD sheets are predominant) is mainly driven by TD sheets.

This findings confirm the anisotropic behavior of non-oriented grain steel and that considering it isotropic in assembled structure like transformer or electrical machine may lead to more deformation and as a consequence to more vibrations.

Since the behavior at the two locations is similar in terms of magnetic and magnetostrictive behavior, only location B is considered for further discussion.

Comparison between voltage and current magnetization

The longitudinal magnetostrictive deformation and the $\mathrm{B}(\mathrm{H})$ loops have been measured in location B for both excitation systems. Figure 3.4.5 and 3.4.6 show the results averaged over five measurements, current magnetization results (denoted c) are shown on the left and the voltage magnetization results (denoted v) on the right. Due to excitation device limitation, saturation could not be achieved for the current magnetization. Nevertheless, a comparison can still be made at magnetic induction around $\mathrm{B} = 1\mathrm{T}$. Assuming that the frequency effect is negligible [86] (10 to 50 Hz), the magnetic behavior between the two magnetization is very similar: at $\mathrm{B} = 1\mathrm{T}$, the maximum field achieved for current magnetization and voltage magnetization is $\mathrm{H}^{\mathrm{c}}_{\mathrm{max}} = 168\,\mathrm{A/m}$ and $\mathrm{H}^{\mathrm{v}}_{\mathrm{max}} = 169\,\mathrm{A/m}$ respectively. The same observation for the coercive field $H_c^c = 46 A/m$

and $H_c^v = 48\,A/m$. As the magnetic behavior, the magnetostrictive behavior versus the magnetic induction B and the magnetic field H is non linear. Furthermore, at $B = 1T$ the amplitudes of magnetostrictive strain are very close: $\varepsilon_B^c = 3.9 \times 10^{-6}$(current magnetization) and $\varepsilon_B^v = 4.05 \times 10^{-6}$. Looking at the waveform of $\varepsilon_B^c(H)$ and $\varepsilon_B^v(H)$ for current and voltage magnetization, they are slightly different, which was expected given the different waveforms of excitation modes. We can observe in figure 3.4.6c some measurement noise of magnetostriction curves at low frequency excitation.

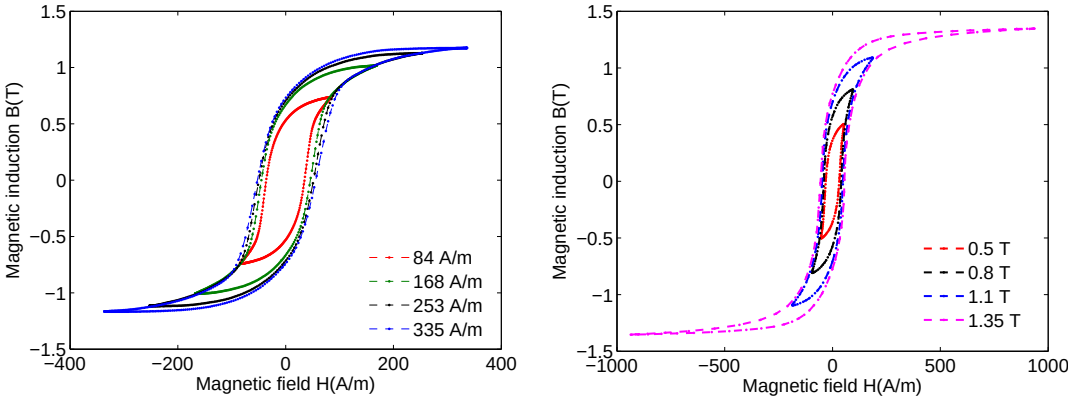

(a) *Current magnetization: B(H) loops.* **(b)** *Voltage magnetization: B(H) loops.*

Figure 3.4.5: *Hysteretic behavior: B(H) loops at point B.*

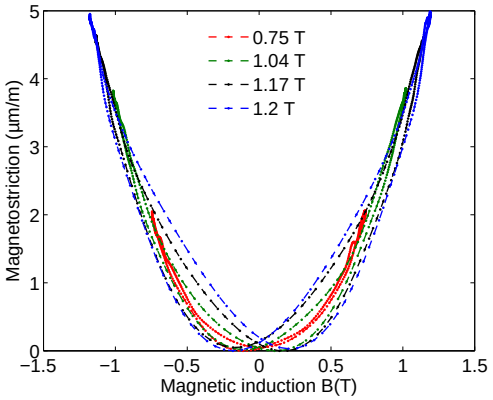

(a) *Current magnetization:* $\varepsilon^{\parallel}(B)$.

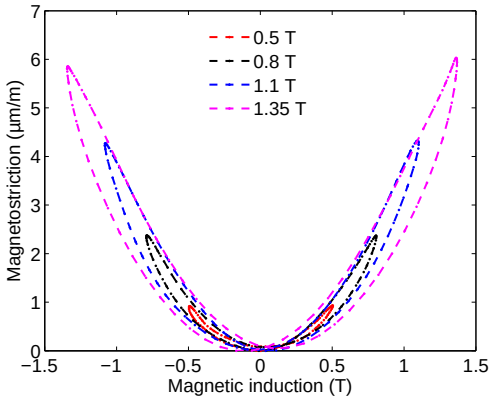

(b) *Voltage magnetization:* $\varepsilon^{\parallel}(B)$.

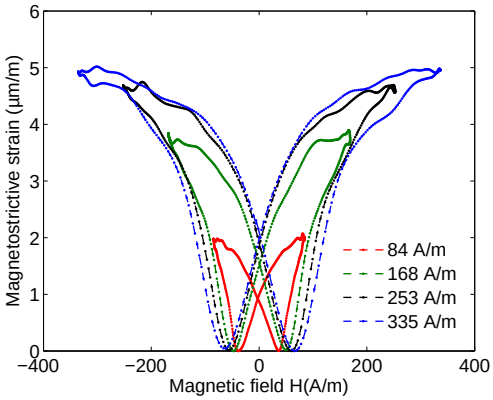

(c) *Current magnetization:* $\varepsilon^{\parallel}(H)$.

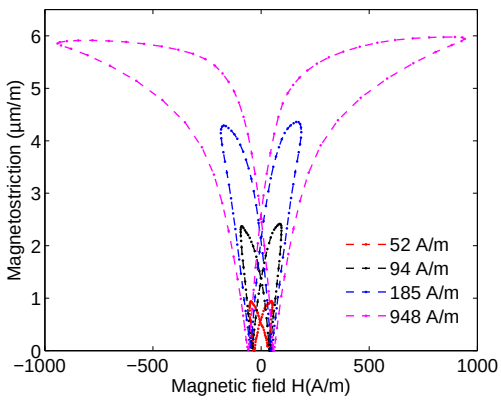

(d) *Voltage magnetization:* $\varepsilon^{\parallel}(H)$.

Figure 3.4.6: *Hysteretic behavior: longitudinal magnetostrictive strain at point B.*

Although we obtained different waveforms of magnetostrictive deformation depending on the magnetization mode, the magnetostrictive deformation amplitude remains almost unchanged. It can be concluded that the magnetization mode has a small effect on the magnetostrictive deformation amplitude. However, further studies are still needed for understanding in details the influence of the magnetization mode on magnetostrictive deformation amplitude.

3.4.1.2 Frequency dependence on magnetostriction

To investigate the frequency effect on the magnetostrictive strain, the laminated structure was excited with two different frequencies (10 and 50 Hz). To avoid any influence related to B and H waveforms, the same excitation system is used for both frequencies (current magnetization, figure 3.3.7). Figure 3.4.7 illustrates the effect of frequency

on the magnetic and the magnetostrictive behavior. At higher frequency, the hysteretic behavior is larger. Despite the fact that the frequency gap is not large, magnetostriction at 50 Hz shows less deformation than magnetostriction at 10 Hz, which indicates that the magnetostriction decreases as the frequency increases. Of course, more the frequency gap is significant, the larger is the impact on magnetostriction as observed in *Moses* work [86].

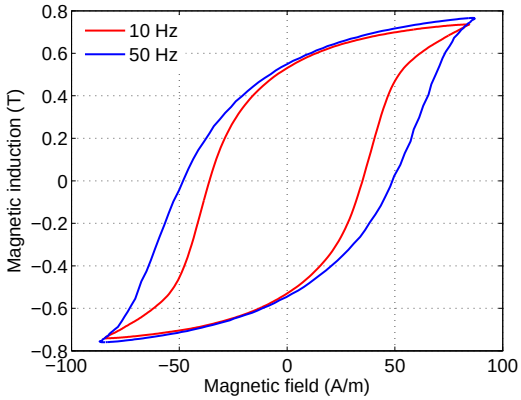

(a) $B(H)$

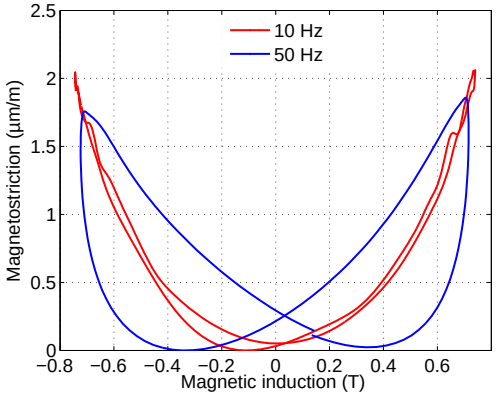

(b) $\varepsilon_B^{||}(B)$

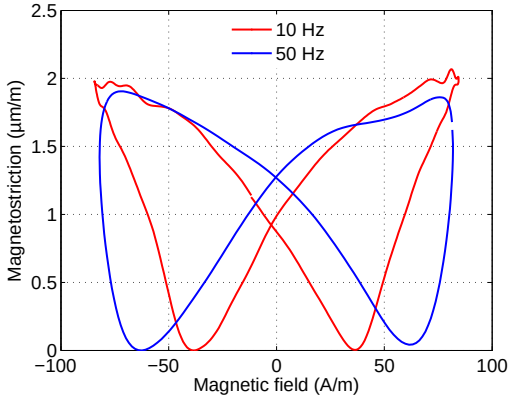

(c) $\varepsilon_B^{||}(H)$

Figure 3.4.7: *Point B: Magnetostrictive strain and hysteresis at two different frequencies.*

Figure 3.4.8 shows the hysteresis loops at several excitation frequencies of the ferromagnetic structure at point B. The maximum magnetic field that could be achieved was $\mathrm{H} = 25\mathrm{A/m}$ (limitation of excitation system). The results demonstrate that as the frequency increases, the hysteresis cycles tilt and the magnetic induction level decreases. These loops are called Rayleigh cycles, they appear at low magnetic field and they occur

because of magnetic domain walls displacements (reversible behavior).

Given the low amplitude of magnetic field, the magnetostrictive strain measurements were highly influenced by noise and thus the results were inaccurate to draw any discussion.

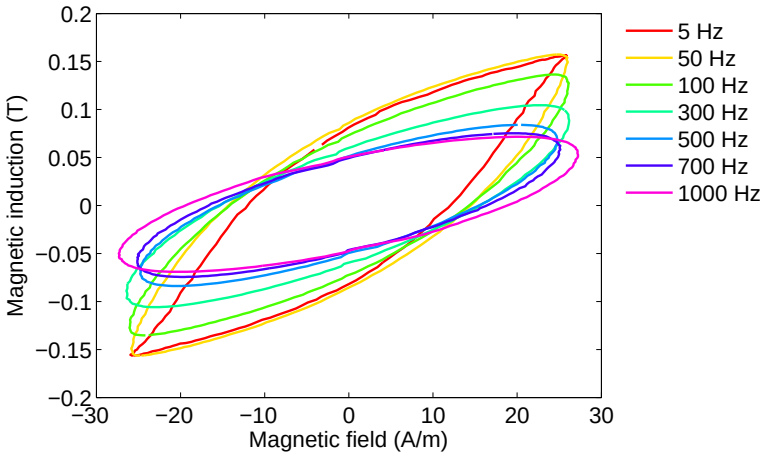

Figure 3.4.8: *Frequency dependence of the hysteresis cycles (*$\mathrm{H_{max}} = 25\mathrm{A/m}$*).*

3.4.1.3 Laser vibrometer results

Considering the noise issue of magnetostrictive strain measurements obtained by strain gauge especially at low magnetic field amplitude, a high resolution measurements method was needed to confirm the obtained measurements. Besides, given the architecture of the laminated structure, the strain gauge setup could not afford deformation information along the lamination height. Consequently, a single point laser vibrometer is used to perform magnetostriction strain. The principle of such a vibrometer has been presented in section 3.3.1.

A general schematic view of the magnetostriction deformation measurements setup using the laser vibrometer is shown in figure 3.4.9. In contrast to the strain gauge setup, only voltage magnetization was used ($f = 50Hz$). The displacement due to magnetostrictive strain is measured in addition to the magnetic induction B and the magnetic field H. The laser head point a laser beam on one leg (where point B is positioned) of the structure at three different location along the height as shown in figure 3.4.10. The motivations for such measurements is to analyze the global deformation of several layers along the lamination surface.

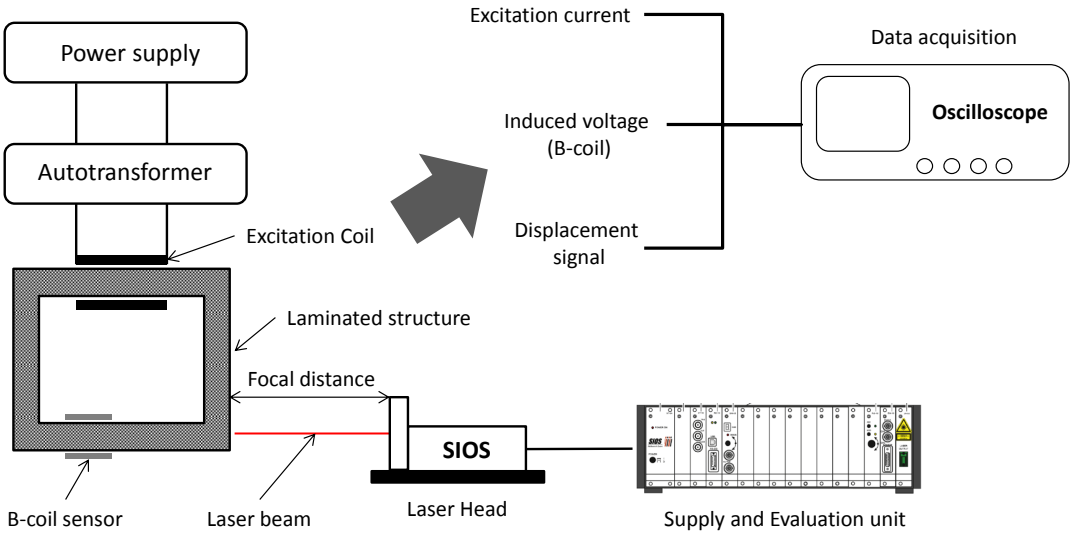

Figure 3.4.9: *A schematic view of the magnetostrictive strain measurements setup based on the interferometric laser vibrometer technique.*

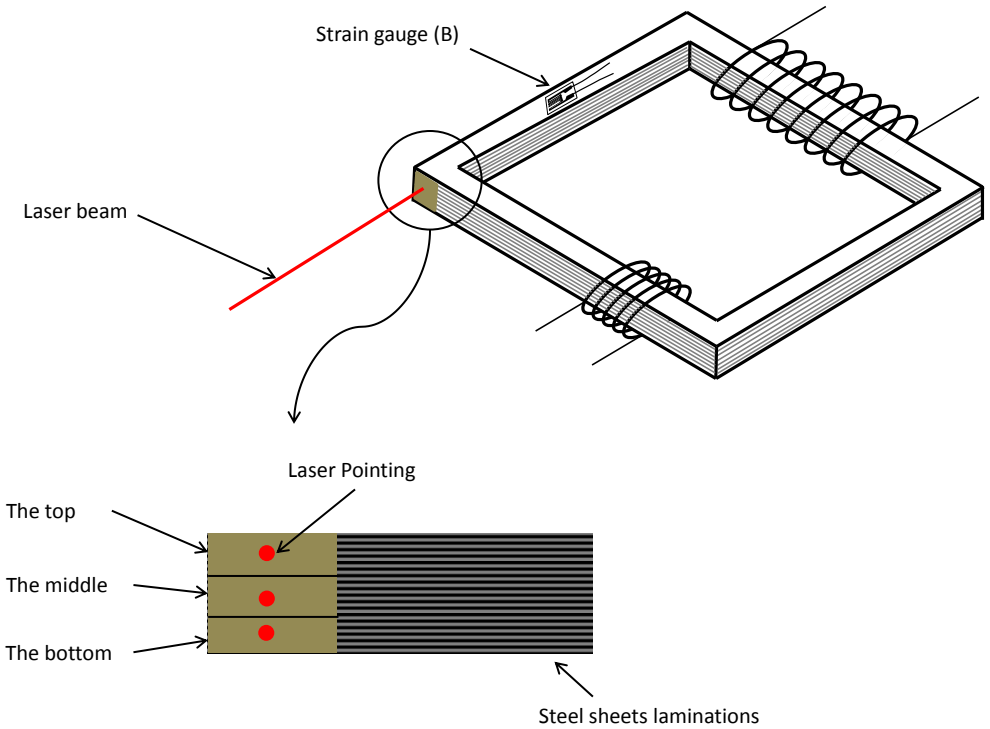

Figure 3.4.10: *Measurement locations on the laminated structure.*

The results of the magnetostrictive behavior of the structure at the defined locations and under different levels of magnetic induction is shown in figure 3.4.11. Since we are interested in the deformation, the displacement obtained is divided by the length of the leg ($L = 0.25m$):

$$\varepsilon = \frac{\Delta L}{L} \tag{3.4.1}$$

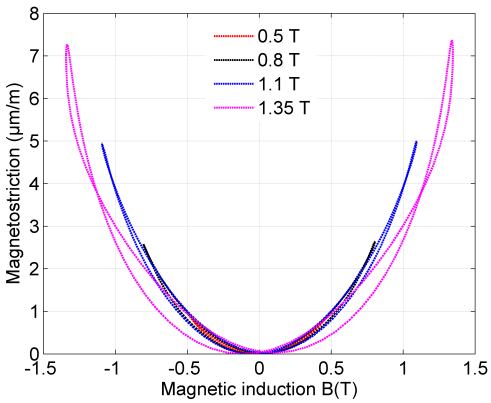

(a) *The top.*

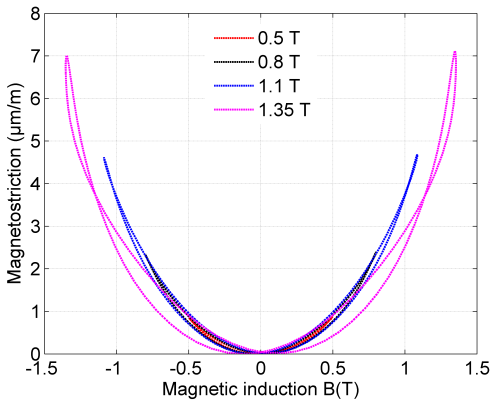

(b) *The middle.*

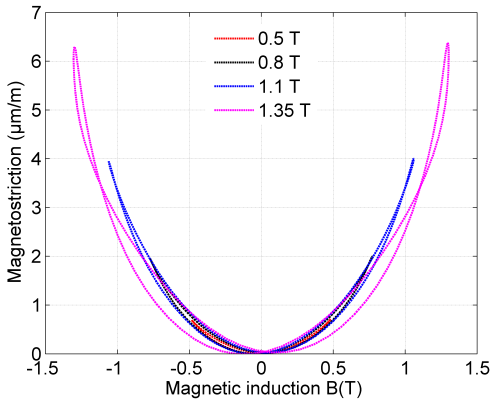

(c) *The bottom.*

Figure 3.4.11: *Magnetostriction measurements by laser vibrometer at three locations along the lamination surface ($f = 50Hz$).*

The measurement results at the top of the leg lamination (figure 3.4.11a) show that the magnetostrictive deformations obtained by laser vibrometer are close to those obtained by the strain gauge in terms of amplitudes for all magnetic induction levels but not exactly the same. On one hand, this is because the measurements by laser vibrometer are global (ends of the lag) and those of strain gauge are local (middle of the leg).

on the other hand, the measurements point on the top is located at the corner of the structure where the magnetic field turns (rotational field), which can lead to additional deformation compared to parallel field (strain gauge). In contrast to the measurements of the strain gauges influenced by noise, the magnetostrictive deformation curves obtained by laser vibrometer show a high accuracy and a smooth behavior even at low peak amplitudes. Regarding the other locations (the middle and the bottom), the magnetostrictive deformation decreases by $1\,\mu m/m$ as the measured point moves from the top to the bottom. This variation might be originated from the random assembling of the structure (mixture of RD and TD sheets). As previously confirmed, non-oriented steel sheets shows some magnetostrictive anisotropy (figure 3.4.4). Hence, when assembling non-oriented randomly, inhomogeneous displacement along the lamination may appear.

The results clearly demonstrate that the laser vibrometer allows to reveal information that the strain gauge can not with high accuracy. However, the first measured quantity is displacement, which can affect the accuracy of the magnetostriction deformation value compared to the strain gauge (direct measurements). Furthermore, adjustments (laser head re-installation, calibration) are needed at every measurements which makes the measurements tedious and very time consuming.

3.4.2 Measurements results under mechanical loading

As observed in chapter 2, the application of an external stress modifies the magnetic and magnetostrictive properties of electrical steel sheets. The aim of this section is to study the influence of stress on a laminated structure constituted of impregnated single sheet (frame shaped).

3.4.2.1 Setup scheme

The general principle of the magnetostriction measurements setup under stress is shown in figure 3.4.12. Once a stress level is applied by a clamping device and the elastic deformation removed by initializing the Wheatstone bridge of the strain gauges, a magnetization waveform (voltage magnetization) is generated by the power source and sent to the magnetization coil in the laminated structure. Then, the magnetic induction B, the magnetic field H and the magnetostrictive strain ε are measured. After acquisition, all signals are processed under MATLAB software.

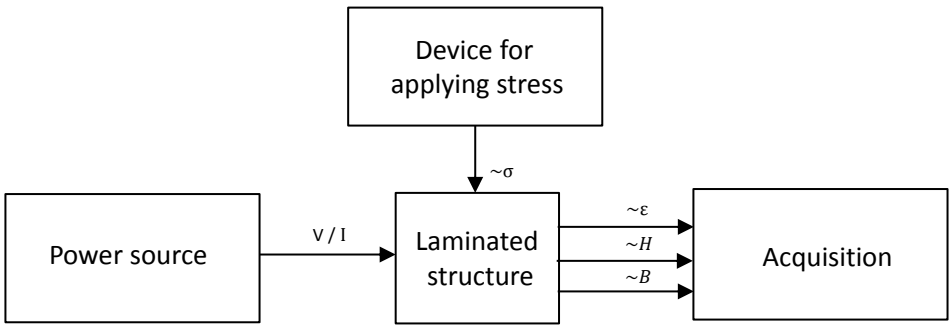

Figure 3.4.12: *Schematic description of the magnetostriction measurement under stress.*

3.4.2.2 Validation of the clamping device by simulation

As one would expect, applying clamping stress on one side of the laminated structure could be influenced by the free part of the latter (figure 3.4.13). For this reason, the aim here is to validate by simulation the clamping device in terms of stress transmission and absence of buckling for the studied range of applied stress. Besides, for the seek of simplicity and to save computation time, we consider the continuity of the displacements at the interfaces between the laminated structure and the clamping screw (figure 3.4.13).

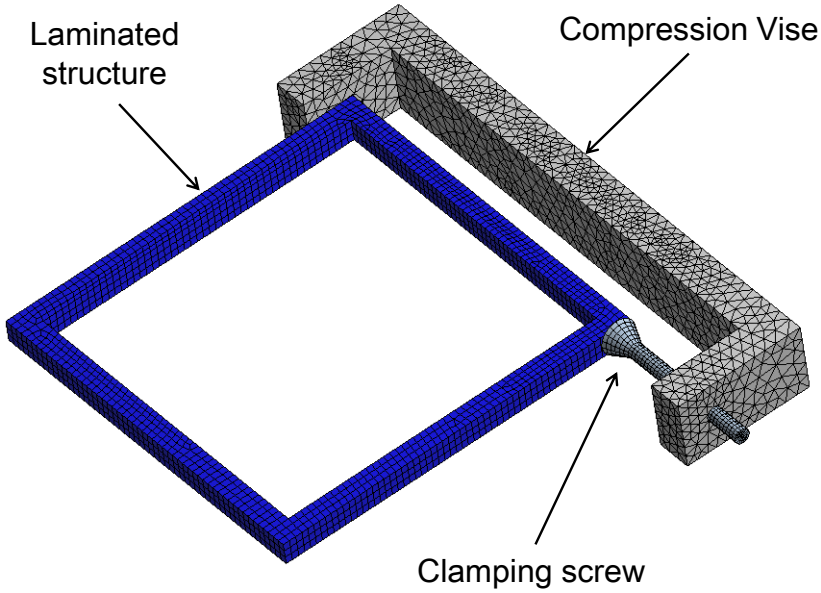

Figure 3.4.13: *Models of clamping device and the laminated structure.*

Figure 3.4.14 shows the simulation results of the isolated ferromagnetic structure under stress computed in Ansys workbench. It can be observed that the maximum compressive stress in the column is located at the contact zone with the clamping device (surrounded zone in figure 3.4.14). This stress concentration will not disturb the stress distribution in the measurement zone where the uniformity of the mechanical stresses is ensured over almost the entire column under stress (figure 3.4.14). A small in-plane buckling effect is observed, it will have a negligible effect on magnetostrictive measurements since the strain gauge measures the longitudinal component of the magnetostriction.

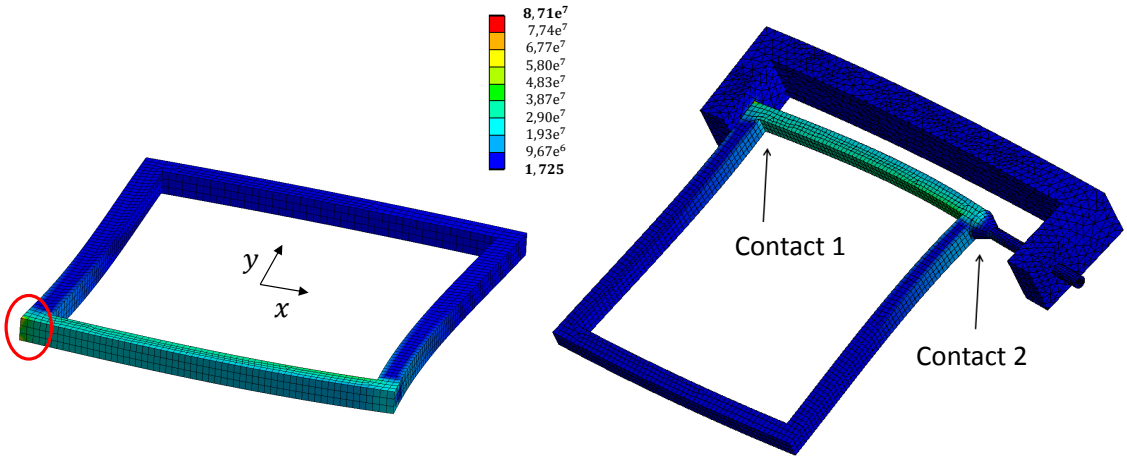

Figure 3.4.14: *Von-Mises stress distribution (Pa) in the laminated structure for an applied force $F = 5.6\,kN$.*

Assuming that the stress σ can be expressed as a function of the stressing force F_s and the column section S_c :

$$\sigma = \frac{F_s}{S_c} \tag{3.4.2}$$

For a stressing force $F_s = 5600\,\mathrm{N}$ and a section of $S_c = 2.24 \times 10^{-4}\,\mathrm{m}$, the applied compressive stress is estimated to:

$$\sigma = \frac{5600}{2.24 \times 10^{-4}} = 25\,\mathrm{MPa} \tag{3.4.3}$$

which correspond to the stress value found by simulation. Hence, the stressing force applied to the screw thanks to the torque wrench can be assumed to be totally transmitted to the column structure.

The maximum stress level that could be reached by this clamping device is $\sigma = -50$MPa. Furthermore, for each experience, five measurements were performed and the average data have been considered for discussion.

3.4.2.3 Results of magnetic and magnetostrictive behavior under compressive stress

Voltage magnetization at $f = 50$Hz

Figure 3.4.15 shows the measurement results of the hysteresis cycles under compressive stress at locations A and B respectively. First, we make the clamping on the leg where point A is located, once the measurements are made, we dismount the vise, then the leg where the point B is located is clamped and the measurements are made. Unlike the unstressed situation where only one point was discussed (location B), this time the two measurement locations (A and B) are described. This "on purpose" redundancy makes it possible to confirm the tendency found under mechanical compressive stress.

Hysteresis curves under stress represented in figure 3.4.15 show that a compressive stress decreases slightly the permeability in a monotonous way until $\sigma = -50$MPa. Besides, at maximum value of magnetic field ($H_{max} = 1000$ A/m), the difference in magnetic flux density between hysteresis curves at $\sigma = 0$MPa and $\sigma = -50$MPa corresponds to the Villari effect. In this respect, the change in flux density is proportional to the level of the applied stress. We also notice that the coercive field H_c does not change with the compressive stress.

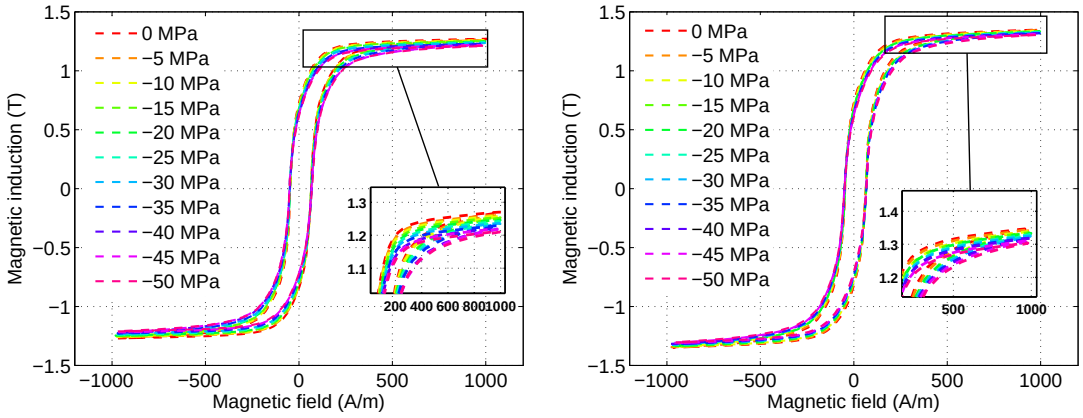

(a) *Hysteresis cycle $B(H)$ at point A.*

(b) *Hysteresis cycle $B(H)$ at point B.*

Figure 3.4.15: *Voltage magnetization: hysteresis cycles under compressive stress at $H_{max} = 1000$ A/m.*

Figure 3.4.16 shows the measurement results of the longitudinal magnetostrictive

strain (parallel to the magnetic field H) at point A and B. For comparison, the magnetostrictive strain at free stress state ($\sigma = 0\,\text{MPa}$) is shown in red. We observe that the magnetostrictive strain increases significantly with increasing compressive stress at point A location as well as at point B location. At $\sigma = -50\,\text{MPa}$, the magnetostrictive strain has increased of about 2.5 µm/m at location A and increased of 3.5µm/m at location B compared to the unstressed state. The magnetostrictive deformation at location B shows around 30% more deformation increase, which confirms that at this location, among the 40 sheets constituting the laminated structure, there is more TD than RD sheets. Actually, as we have observed in chapter 2 for single sheet under stress, sample cut in RD are more sensitive to compressive stress than sample cut in TD. The reason behind seems to be the creation of more 90° domain walls leading to an increase of magnetostrictive strain. It can be seen also from the figure 3.4.16 that when achieving a compressive stress of $\sigma = -30\,\text{MPa}$ (in blue) and beyond, the magnetostriction curves begin to get closer to each other, indicating that magnetostrictive saturation is being reached.

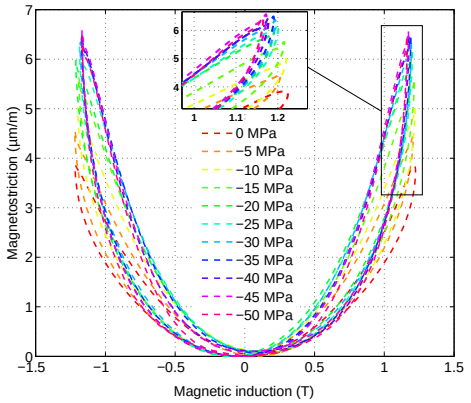

(a) *Magnetostrictive deformation at point A:* $\varepsilon_A^{||}(B)$

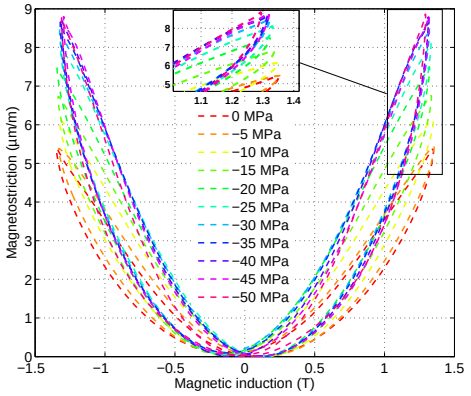

(b) *Magnetostrictive deformation at point B:* $\varepsilon_B^{||}(B)$

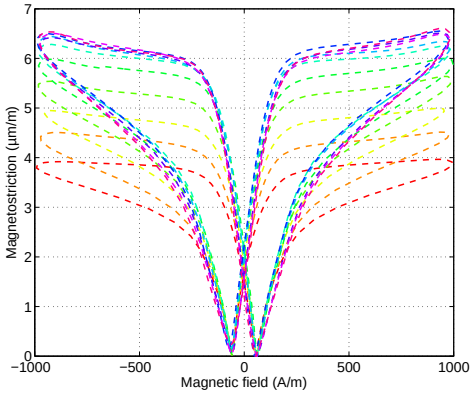

(c) *Magnetostrictive deformation at point A:* $\varepsilon_A^{||}(H)$

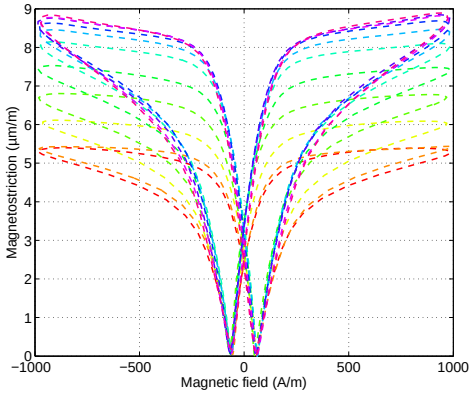

(d) *Magnetostrictive deformation at point B:* $\varepsilon_B^{||}(H)$

Figure 3.4.16: *Voltage magnetization: magnetostriction deformation under compressive stress at* $H_{max} = 1000\text{A/m}$.

Current magnetization at $f = 10\,\text{Hz}$

Figure 3.4.17 shows the hysteresis cycles at 10 Hz under several magnitude of compressive stress, respectively at point A and at point B of the laminated structure. The measurements were carried out at a maximum magnetic field of $H_{max} = 275$ A/m. The results clearly show that compressive stress decreases the permeability since it prevents the process of magnetization. Whereas, the coercive field seems not to be influenced by the stress and remains the same for all applied stress.

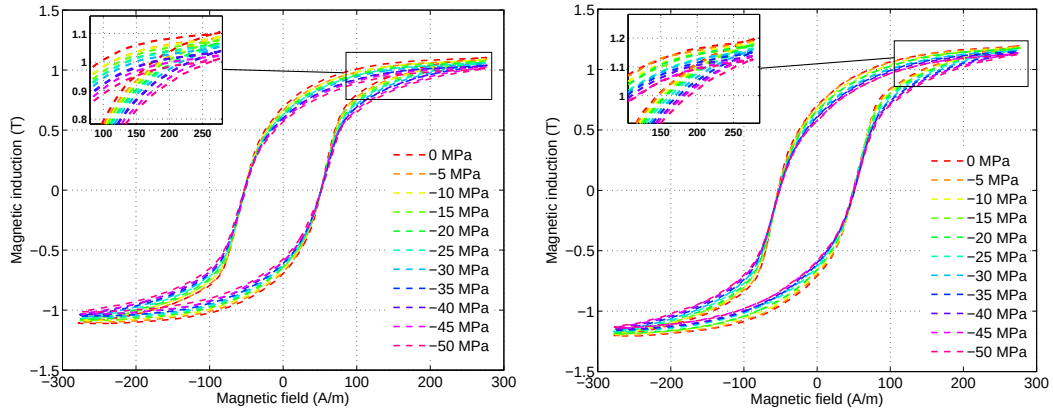

(a) *Hysteresis cycle at point A: $B(H)$*

(b) *Hysteresis cycle at point B: $B(H)$*

Figure 3.4.17: *Current magnetization: hysteresis cycle under compressive stress at $H_{max} = 275$ A/m.*

Figure 3.4.18 represents the longitudinal magnetostrictive strain behavior under compressive stress. We observe that the evolution of the magnetostrictive strain is monotonic. Also, the magnetostriction function $\varepsilon^{||}{}_{A,B}(B)$ has a parabolic shape. In addition, a close look shows that the curves get closer as the compressive stress increases due to saturation of magnetostriction mechanism at high compressive stress (around $\sigma = -30$MPa). Moreover, the slight decrease of magnetic permeability as a function of the compressive stress is followed by a decrease in the magnetic induction peak (figure 3.4.17). This process is also well noticed in the evolution of the magnetostriction as a function of the magnetic induction (see the zoomed area of figure 3.4.18a and figure 3.4.18b). Moreover, due to compressive stress $\sigma = -50$MPa the magnetostrictive deformation shows an increase around 36% at location A and around 44% at location B. As for the voltage magnetization, magnetostriction variation due to compressive stress is larger at point B.

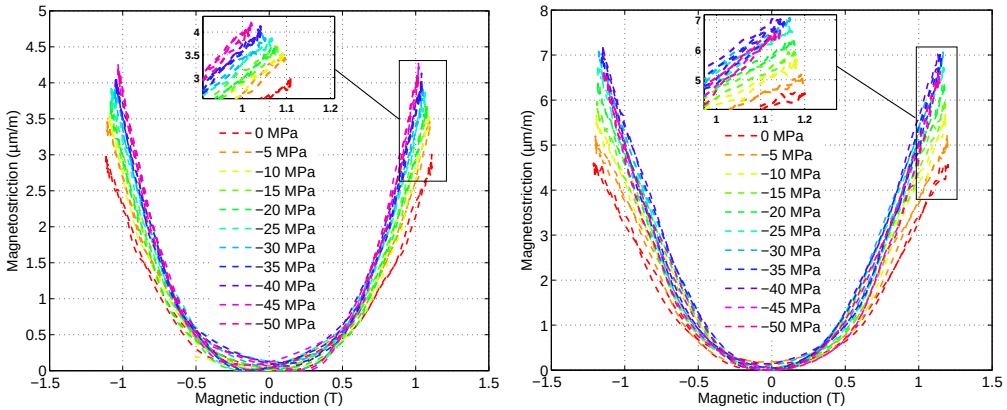

(a) *Magnetostrictive deformation at point A:* $\varepsilon_A^{||}(B)$ **(b)** *Magnetostrictive deformation at point B:* $\varepsilon_B^{||}(B)$

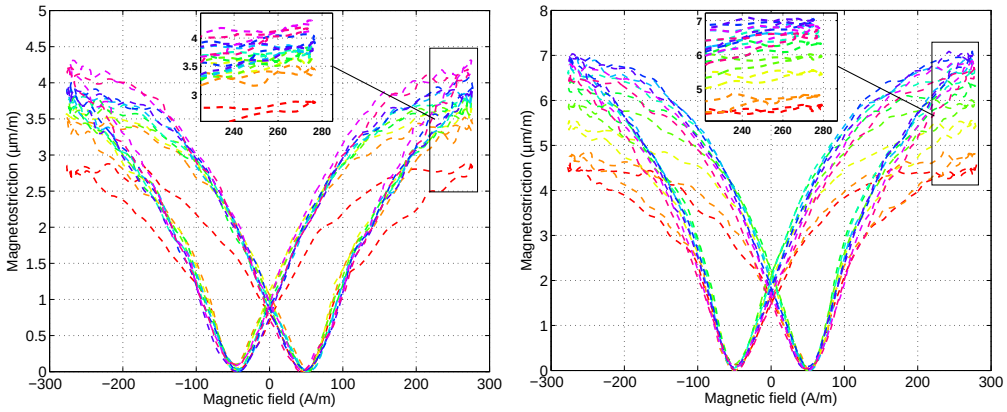

(c) *Magnetostrictive deformation at point A:* $\varepsilon_A^{||}(H)$ **(d)** *Magnetostrictive deformation at point B:* $\varepsilon_B^{||}(H)$

Figure 3.4.18: *Current magnetization: magnetostriction deformation under compressive stress at* $H_{max} = 275\mathrm{A/m}$.

Longitudinal ΔE effect

The extraction method of the ΔE effect has been presented in Chapter 2. The same procedure has been followed for the laminated structure. Figure 3.4.19 shows the ΔE effect of the longitudinal deformation parallel to the magnetic field H. The ΔE effect was obtained from the magnetostriction curves under a maximum compressive stress of $\sigma = -50\,\mathrm{MPa}$. It can be observed that the ΔE effect at location B is greater than the one at location A of approximately $1\mu\mathrm{m/m}$. Besides the magnetostriction strains $\varepsilon^{||}{}_{A,B}(\sigma)$ exhibit a non-linear behavior and tend to saturate at high compressive stress.

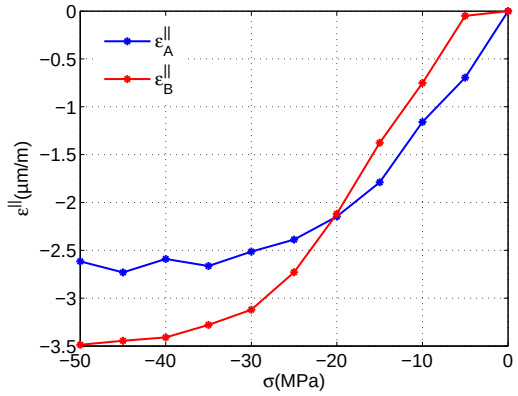

Figure 3.4.19: ΔE *effect:* $\varepsilon^{||}(\sigma)$ *at location A and B of the laminated structure.*

To conclude, we can say that once a laminated structure is magnetized, the magnetostrictive strain depends only on the magnitude of the excitation field and not on the excitation mode (voltage or current mode). Although non-oriented electrical steel are globally isotropic compared with the grain-oriented materials, still some degree of anisotropy exists in the magnetostrictive properties of these materials. Magnetostriction measurements by laser vibrometer have shown higher accuracy compared to the strain gauge setup. The laser setup provides some achievement that could not be reached by strain gauge, like measurements along the height of the lamination. Next, measurements under compressive stress confirmed that non-oriented materials are stress sensitive and may lead to more vibration due to an increase of magnetostrictive deformation under compressive stress. In the following, from these experimental measurements and based on the magnetostriction model (chapter 2), a FE tool has been developed that reproduces as accurately as possible the obtained measurements by considering the anisotropy effect related to magnetic and magnetostrictive behavior. Nevertheless, the stress effect is not considered.

3.4.3 FE modeling

3.4.3.1 Description of the ferromagnetic structure modeling

To model the structure, we have made 2D hypothesis in the same way as our developed model which is based on plane magnetization assumption (chapter 2). Next, the structure was modeled as four glued columns, figure 3.4.20. It is worth mentioning that the finite elements results are not influenced by the gluing configuration of the columns. Unlike the real structure where the assembly of the sheets is random, the model contains long RD sheets in one bar and only TD sheets in the other (without mixing). From a

magnetic point of view, the software (ANSYS) does not allow to take into account both anisotropy and non-linearity of the magnetic behavior. Thus, for a more realistic simulation, we chose four magnetically isotropic columns with different non-linear behavior (figure 3.4.21). From a mechanical point of view, the four columns are isotropic and have the same elastic behavior (same Young modulus E and Poisson ratio ν).

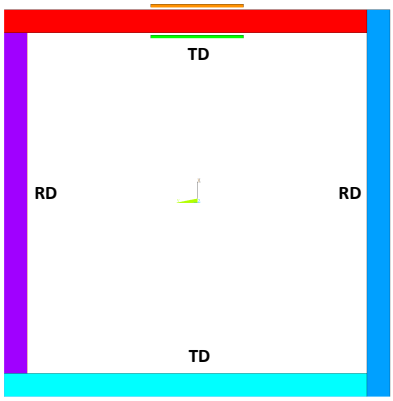

Figure 3.4.20: *2D model of the ferromagnetic structure with the excitation coil and RD/TD directions (no air gaps).*

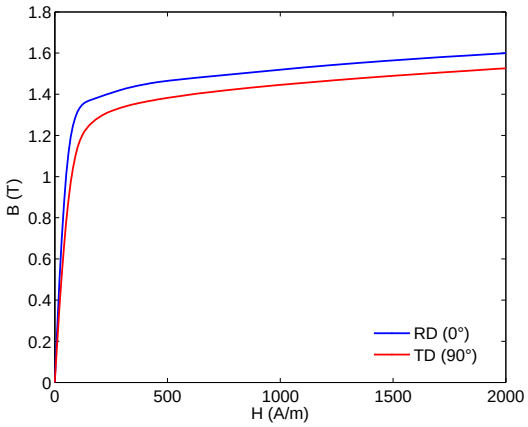

Figure 3.4.21: *Magnetic behavior law for magnetic simulation.*

The software used for magnetic and mechanical simulations has the advantage of being multi-physical since it provides elements that can be used in coupled physics

simulation (electromagnetic and mechanic). Consequently, we were able to maintain the same mesh for both magnetic and mechanical calculations avoiding meshing problems related to the change of physics. In this thesis work, the element "PLANE13" allowing to make magnetic and mechanical simulations is used (figure 3.4.22). It also gives the possibility to include magnetic forces: Lorentz and Maxwell forces.

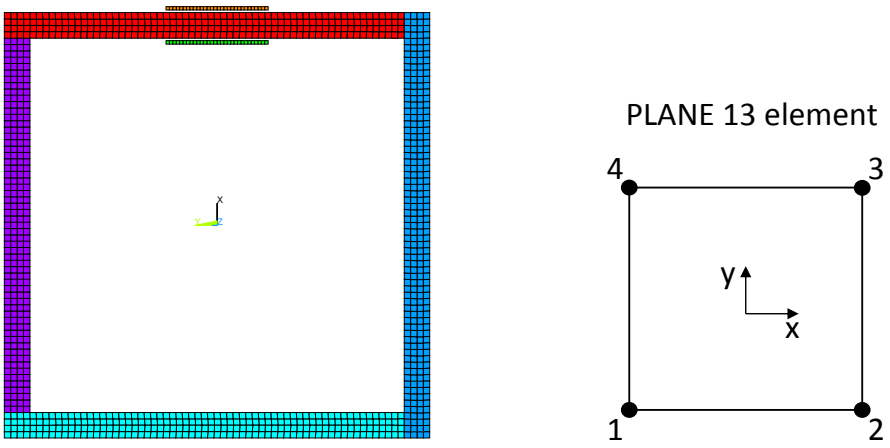

Figure 3.4.22: *Model mesh: PLANE13 element.*

3.4.3.2 Magnetic resolution

The aim of magnetic simulation is to calculate the distribution of magnetic field and magnetic flux density in the ferromagnetic structure. That is to say, it will calculate the average of magnetic field of each element of the modeled ferromagnetic structure. To do so, we impose a current density j_s calculated from the measured current I_{mes} and the section of excitation winding S_{copper} (j_s=$\frac{I_{mes}}{S_{copper}}$). Knowing that the magnetostriction is even and our model is anhysteretic, a quarter period of the current is simulated for magnetic and magnetostrictive distribution at maximum current, figure 3.4.23. However, for comparison with measurements the entire period is simulated. The magnetic characteristics of the electrical steel sheets in the rolling and transverse direction are injected figure 3.4.21, and parallel magnetic flow conditions are adopted.

Due to relatively low frequency usually used in applications like rotating machines and transformers (50 Hz), the approximation of magneto-static regime is adopted (magnetic scalar potential formulation). This leads to the resolution of the following equations:

$$\vec{\nabla} \times \vec{H} = \vec{J} \tag{3.4.4}$$

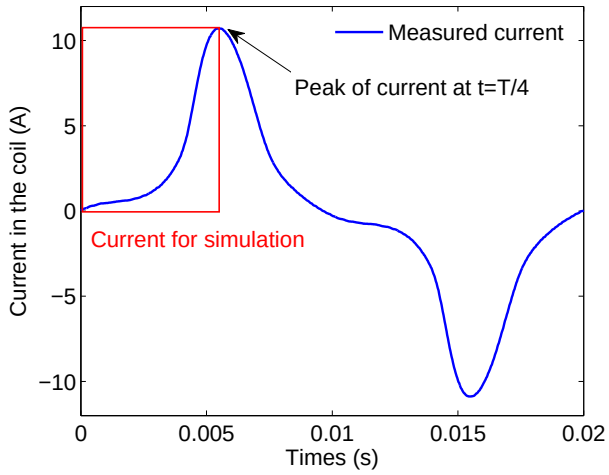

Figure 3.4.23: *Simulation: current injected in the ferromagnetic structure.*

$$\overrightarrow{\nabla}.\overrightarrow{B} = 0 \tag{3.4.5}$$

The results of magnetic field distribution (average field of the elements) will be used to calculate the equivalent nodal forces.

3.4.3.3 Nodal magnetostrictive forces computation

Equivalent nodal forces is an approach often used to solve magneto-mechanical coupling problems in finite element [81, 46, 53, 40]. The general principle of this method is to calculate the equivalent forces (fictive forces) in a mechanical analysis (section 3.4.3.4) in order to reproduce the deformations and displacements (due to magnetostriction or Maxwell forces...). These nodal forces are function, inter alia of magnetic quantities such as the distribution of calculated magnetic field (section 3.4.3.2). In general, the computation of the nodal forces is fulfilled in two stages: computation and assembly of the elementary forces [75].

Elementary forces computation

It is inherent to the Finite Element Method that nodes are shared by multiple elements. However, unassembled nodal forces obviously belong to a single element instead of them being a sum of contributions from multiple elements (figure 3.4.24). Thus, these nodal force components constituting an element form an elementary force vector denoted $\overrightarrow{F_e^{\mu}}$ (equation (3.4.6)). In our case, our structure has been meshed thanks to the

"PLANE 13" elements (figure 3.4.22). Each element has 4 nodes, each with 2 DOFs[3]. Hence, the vector of elementary force $\overrightarrow{F_e^{\mu}}$ will have the following form:

$$\overrightarrow{F_e^{\mu}} = \left[\begin{array}{cccccccc} F_{n1x}^{\mu} & F_{n1y}^{\mu} & F_{n2x}^{\mu} & F_{n2y}^{\mu} & F_{n3x}^{\mu} & F_{n3y}^{\mu} & F_{n4x}^{\mu} & F_{n4y}^{\mu} \end{array} \right]^T \tag{3.4.6}$$

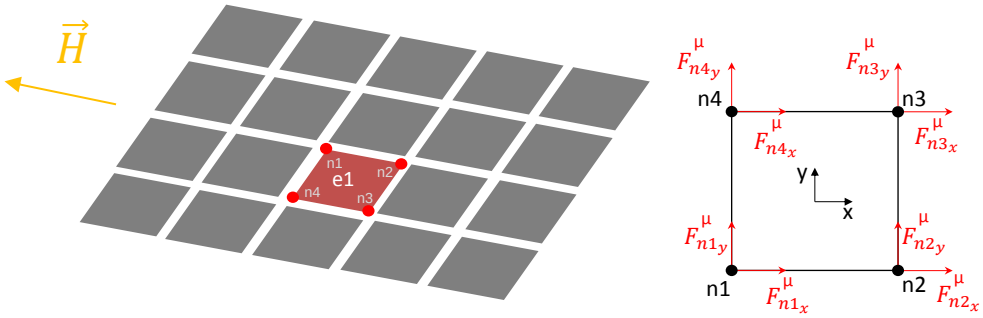

Figure 3.4.24: *Illustration of nodal forces before assembling.*

According to [16, 21], the elementary forces is defined as:

$$\overrightarrow{F_e^{\mu}} = -\int_{Ve} [N]^T \overrightarrow{f_V^{\mu}} dV \tag{3.4.7}$$

- Ve denotes the element volume.
- $[N]$ denotes the shape matrix.
- $\overrightarrow{f_V^{\mu}}$ denotes the volume force equivalent to magnetostriction.

The calculation of the elementary forces from equation (3.4.7) requires knowledge of the shape matrix $[N]$ and $\overrightarrow{f_V^{\mu}}$. The shape matrix depends on the used element type and contains N_i shape functions (interpolation functions). In the case of PLANE13 element consisting of 4 nodes 2 DOFs each ($i = 1..4$) , the matrix $[N]$ is written:

$$[N] = \left[\begin{array}{cccccccc} N_1 & 0 & N_2 & 0 & N_3 & 0 & N_4 & 0 \\ 0 & N_1 & 0 & N_2 & 0 & N_3 & 0 & N_4 \end{array} \right] \tag{3.4.8}$$

The volume force $\overrightarrow{f_V^{\mu}}$ can be deduced from the fundamental relationship of dynamics defined by:

$$\overrightarrow{\nabla} . \overline{\overline{\sigma^{\mu}}} + \overrightarrow{f_V^{\mu}} = \rho_m \frac{\partial^2 \overrightarrow{u}}{\partial t^2} \tag{3.4.9}$$

[3] Degree of Freedom

where $\overline{\overline{\sigma^{\mu}}}$is the 2^{nd} order of stress tensor induced by magnetostrictive deformation, ρ_m is the mass density, and $\overrightarrow{u}$ is the displacement field.

Given the assumption of magneto-static regime (low frequency) to predict magnetostriction in our model, the equation (3.4.9) is reduced to :

$$\overrightarrow{\nabla}.\overline{\overline{\sigma^{\mu}}} + \overrightarrow{f_V^{\mu}} = \overrightarrow{0} \tag{3.4.10}$$

Since the model is a two dimension system with two degrees of freedom, the expression of the volume force can be written as follows:

$$\overrightarrow{f_V^{\mu}} = -[\partial] : \overline{\overline{\sigma^{\mu}}} = -\begin{bmatrix} \frac{\partial}{\partial x} & 0 & \frac{\partial}{\partial y} \\ 0 & \frac{\partial}{\partial y} & \frac{\partial}{\partial x} \end{bmatrix} \begin{bmatrix} \sigma_{xx}^{\mu} \\ \sigma_{yy}^{\mu} \\ \sigma_{xy}^{\mu} \end{bmatrix} \tag{3.4.11}$$

Consequently, the combination of equation (3.4.7) and (3.4.11) leads to the elementary forces that can be expressed in the following form:

$$\overrightarrow{F_e^{\mu}} = \int_{Ve} [N]^T [\partial] : \overline{\overline{\sigma^{\mu}}} dV = \int_{Ve} [B]^T : \overline{\overline{\sigma^{\mu}}} dV \tag{3.4.12}$$

where $[B]$ is a matrix containing the derivative of shape functions:

$$[B] = [\partial]^T [N] = \begin{bmatrix} N_{1,x} & 0 & N_{2,x} & 0 & N_{3,x} & 0 & N_{4,x} & 0 \\ 0 & N_{1,y} & 0 & N_{2,y} & 0 & N_{3,y} & 0 & N_{4,y} \\ N_{1,y} & N_{1,x} & N_{2,y} & N_{2,x} & N_{3,y} & N_{3,x} & N_{4,y} & N_{4,x} \end{bmatrix} \tag{3.4.13}$$

Hence, the magnetostrictive deformation $\overline{\overline{\varepsilon^{\mu}}}$ can be deduced from the general expression (3.4.14):

$$\overline{\overline{\sigma^{\mu}}} = \overline{\overline{C}} : \overline{\overline{\varepsilon^{\mu}}} \tag{3.4.14}$$

where $\overline{\overline{C}}$ is a forth-order stiffness tensor as a function of Young modulus and Poisson ratio.

Elementary forces assembling

After calculating the elementary forces, the elements are reassembled and connected to each other to calculate the nodal forces for mechanical resolution. The reassembling process implies the sum of all elementary forces associated to the node as detailed in equation (3.4.15). As illustrated in figure 3.4.25, the nodal force $\overrightarrow{F_{n1}^{\mu}}$ is the contribution of the four elements ($e1$, $e2$, $e3$, $e4$).

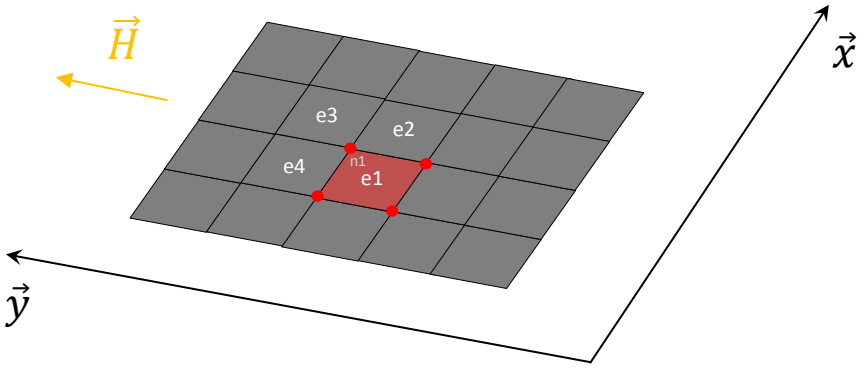

Figure 3.4.25: *The element assembly process for nodal force calculation.*

$$\overrightarrow{F_{n1}^{\mu}} = \begin{bmatrix} F_{e1_x}^{\mu} + F_{e2_x}^{\mu} + F_{e3_x}^{\mu} + F_{e4_x}^{\mu} \\ F_{e1_y}^{\mu} + F_{e2_y}^{\mu} + F_{e3_y}^{\mu} + F_{e4}^{\mu} \end{bmatrix} = \begin{bmatrix} F_{n1_x}^{\mu} \\ F_{n1_y}^{\mu} \end{bmatrix} \tag{3.4.15}$$

Once the nodal forces equivalent to the magnetostrictive deformation are calculated for all nodes of the structure, they are used as a loading for the mechanical resolution.

3.4.3.4 Mechanical resolution

The mechanical resolution was done under ANSYS as the magnetic resolution. Given the small values of magnetostrictive deformation (10^{-6} for Si-Fe), the mechanical behavior of the structure is considered elastic. However, in contrary to the magnetic resolution where the behavior is assumed anisotropic ($B(H)_{RD} \neq B(H)_{TD}$), the elastic behavior is supposed isotropic (same Young modulus E and Poisson ratio ν) due to the lack of detailed information from the electrical steel supplier: Young modulus and Poisson ratio evolution the with angle of cut in the sheet plane is missing.

There are two types of formulations that can be used to solve 2D elastic problem: plane stress or plane strain formulations. Since the studied model is a 2D problem and given the geometry of the electrical steel (small thickness), the loading is mainly in the plane of the sheets, thus, the plane stress formulation is more suitable.

3.4.3.5 FE model results

In the following, the distribution of magnetic (H and B) and mechanical quantities (σ^{μ} and ε^{μ}) will be presented. In order to make a comparison, the numerical simulation are carried out under the same condition as the experimental ones. Besides, figure 3.4.27 shows the selected evaluation lines where the magnetostrictive deformation results are drawn. To avoid rigid body movement during simulation (z-axis rotation

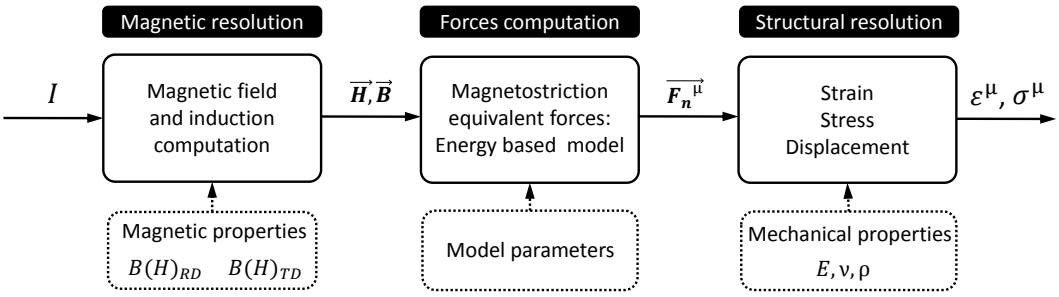

Figure 3.4.26: *The global simulation strategy.*

of the structure, translation following x and y), boundary conditions are applied to the structure while leaving the structure free to deform under magnetostrictive deformation (figure 3.4.27).

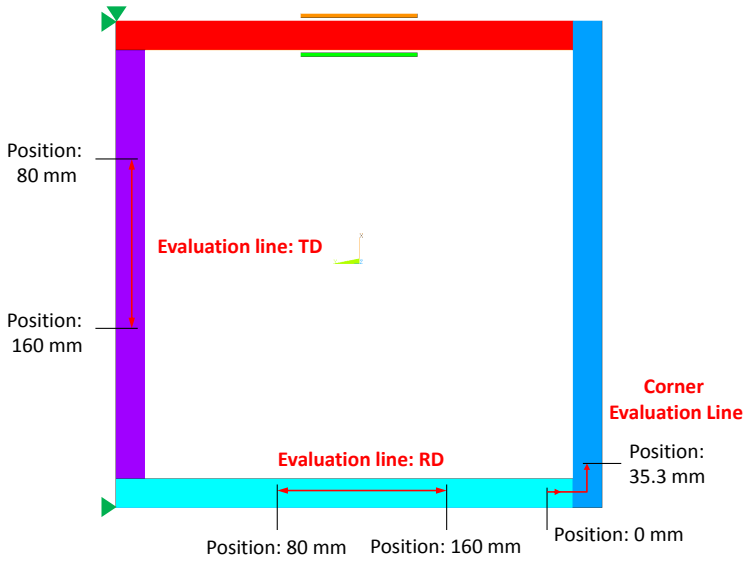

Figure 3.4.27: *2D model: the mechanical boundary conditions and evaluation lines along RD, TD and the corner for simulation results.*

Magnetic results

Figure 3.4.28 shows the magnetic induction and the magnetic field distribution at peak current amplitude (figure 3.4.23). The magnetic induction is almost uniform in the ferromagnetic structure except in the corners where there is a gradient decrease towards the

outside of the corners, this is due to the concentration of the field lines in the inner side of the corner, this would explain the rounded shape at the corners of some transformers. There is also an intense localized induction level due to the presence of the coil in the upper horizontal column. The induction level obtained in the evaluation line (RD and TD) is around B = 1,5T. The same observations were noticed for the magnetic field. The maximum magnetic field obtained is H = 1500 A/m (excitation coil location).

Figure 3.4.29a shows an homogeneous distribution of the magnetic field along the columns. Besides the magnetic anisotropy behavior is well reproduced ($H_{RD} = 1100\,A/m$ and $H_{TD} = 500\,A/m$ for $B = 1.5T$). Figure 3.4.29b shows the leakage magnetic field lines.

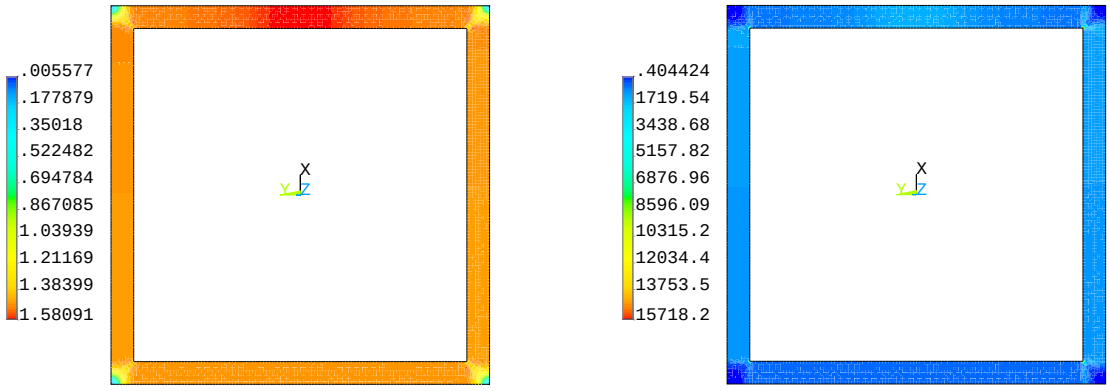

(a) *Magnetic induction B(T).* **(b)** *Magnetic field H(A/m)*

Figure 3.4.28: *Magnetic behavior in the ferromagnetic structure at a peak of current (t = $\frac{T}{4}$).*

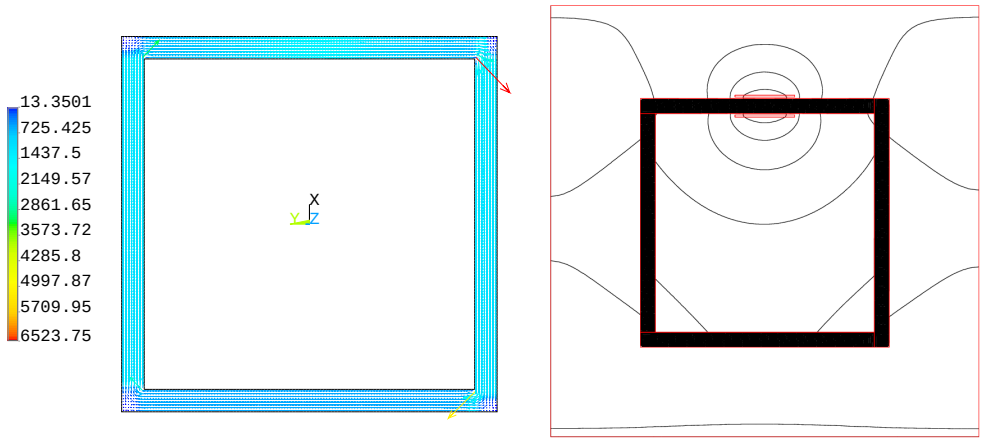

(a) *Magnetic field distribution at peak of current.* **(b)** *Leakage flux lines.*

Figure 3.4.29: *Magnetic field distribution: maximum magnetic field distribution and the flux line leakage (t=$\frac{T}{4}$).*

Magnetostrictive deformation and induced stress results

The longitudinal components ε^{μ}_{xx}, ε^{μ}_{yy} and ε^{μ}_{xy} of the magnetostrictive deformation generated in the structure for a maximum magnetic induction (B = 1.47T) are shown in figure 3.4.30 on the left. We observe a larger deformation in the transverse direction $\varepsilon^{\mu}_{xx} = 4.92 \times 10^{-6}$ compared to the rolling direction $\varepsilon^{\mu}_{yy} = 0.65 \times 10^{-6}$. The anisotropic effect is well reproduced by the simulation, the deformation along TD is 6 times larger than RD. Besides, the shear deformation is particularly high at the internal corner of the structure $\varepsilon^{\mu}_{xy} = 3.47 \times 10^{-6}$. This is due to the fact that the magnetic field sweeps all angles as it switches from RD column to TD column (or vice versa). Also, given the positive magnetostrictive deformation of Si-Fe, the extension of the two legs (RD and TD) creates at the corner a high shear deformation.

Stress components ${\sigma^{\mu}}_{xx}$, σ^{μ}_{yy} and ${\sigma^{\mu}}_{xy}$ induced in the structure for a maximum magnetic induction (B = 1.47T) are shown in figure 3.4.30 on the right. The stress level - given at instant $t = \frac{T}{4}$ - varies depending on regions (RD or TD). Firstly, the stress distribution is uniform along the length of the legs. Next, the stress generated in the x-direction corresponds to the transverse direction $\sigma_{xx} = 0.92$MPa, and in the y-direction corresponds to the rolling direction $\sigma_{yy} = 0.12$MPa. This stress difference is due to the difference in magneto-elastic behavior between TD and RD. On the other hand, shear stress is particularly significant in the corner of the structure ($\sigma_{xy} = \pm 0.26$MPa).

Figure 3.4.31 represents the magnetostriction deformation as a function of the magnetic induction at the different evaluation lines (figure 3.4.27). These results show that the deformation is homogeneous in the middle of the RD and TD columns (figure 3.4.31a and 3.4.31b). It is observed that the maximum magnetostriction does not

correspond necessarily to a peak of magnetic induction ($\varepsilon^{RD} = 0.72 \times 10^{-6}$ and $\varepsilon^{TD} = 5.5 \times 10^{-6}$ at $B = 1.4T$). In addition, the magnetostrictive anisotropy effect is very well predicted since each column contains only sheets with a single cutting direction RD or TD (figure 3.4.31c). However, the comparison of simulation results with experimental measurements can not be easily made. Indeed, the laminated structure is composed of several square-shaped sheets randomly assembled, hence the increase observed on the point A (presence of TD sheets). In this case, an homogenized model would be more appropriate and close to the real behavior of the structure.

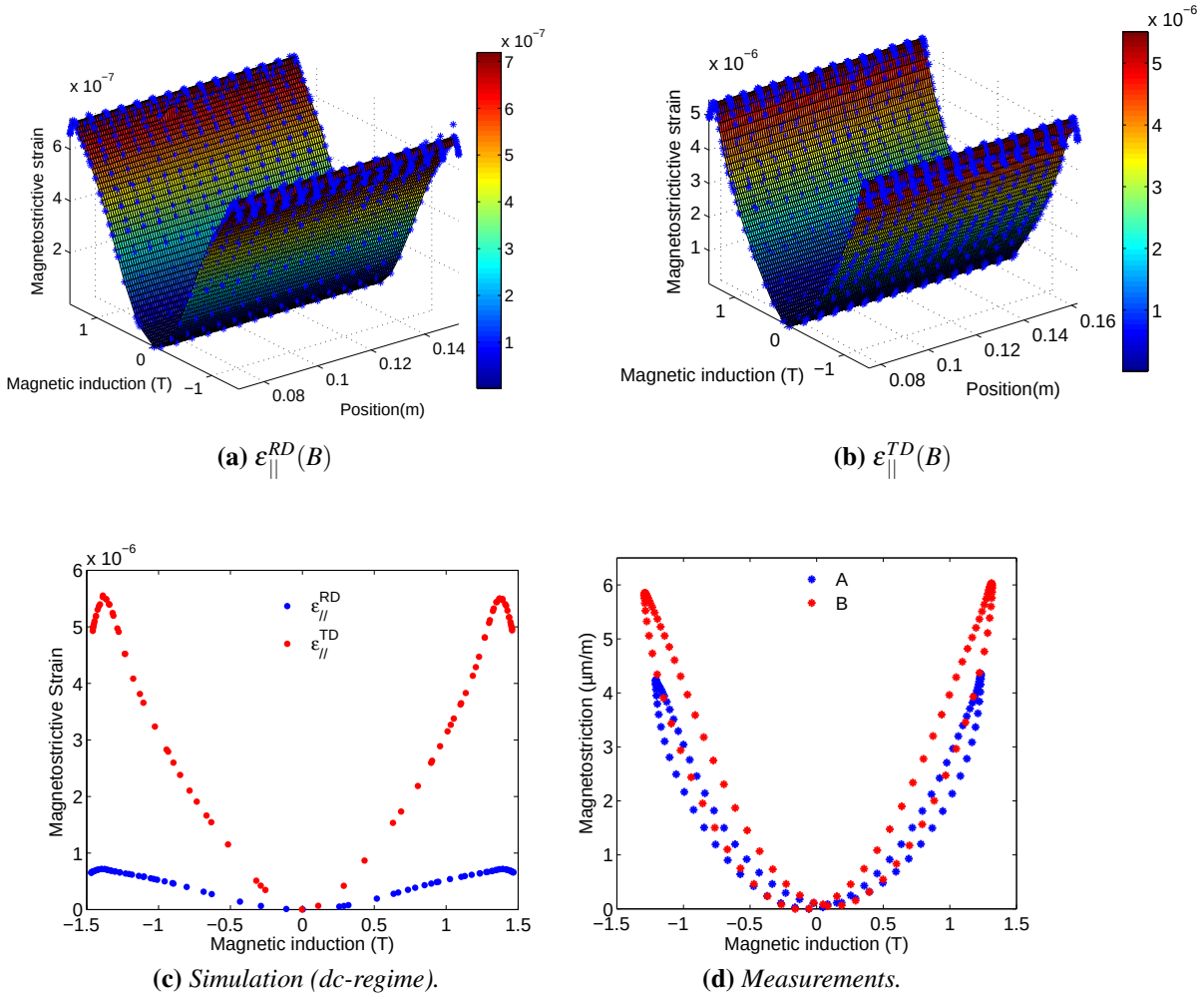

(a) $\varepsilon_{||}^{RD}(B)$ **(b)** $\varepsilon_{||}^{TD}(B)$

(c) *Simulation (dc-regime).* **(d)** *Measurements.*

Figure 3.4.31: *Longitudinal magnetostrictive strain in the structure.*

In order to test the robustness of the model and its ability to reproduce the magnetostrictive behavior on a structure at different angles between RD and TD, a rep-

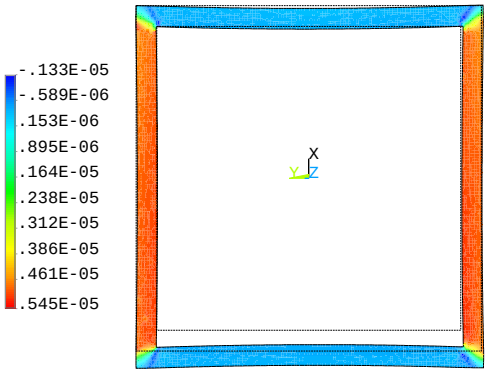

(a) ε_{xx}^{μ}

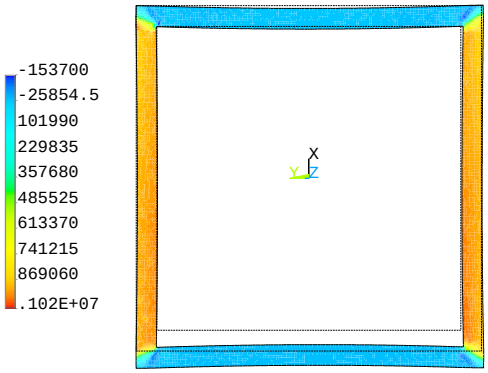

(b) σ_{xx}^{μ}

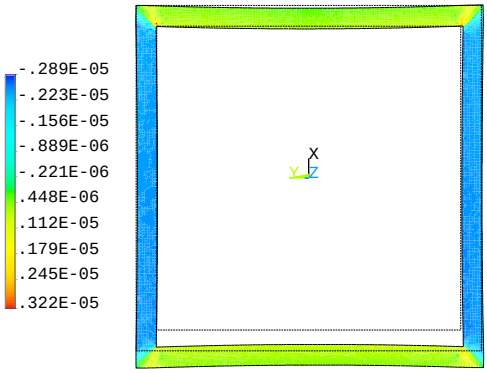

(c) ε_{yy}^{μ}

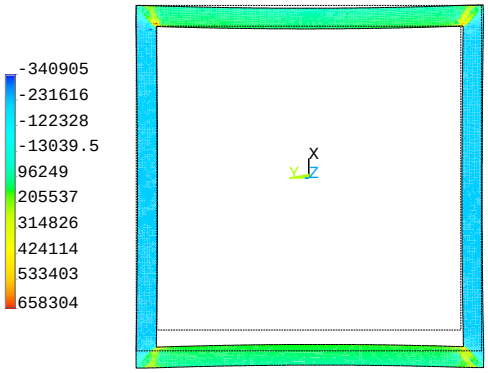

(d) σ_{yy}^{μ}

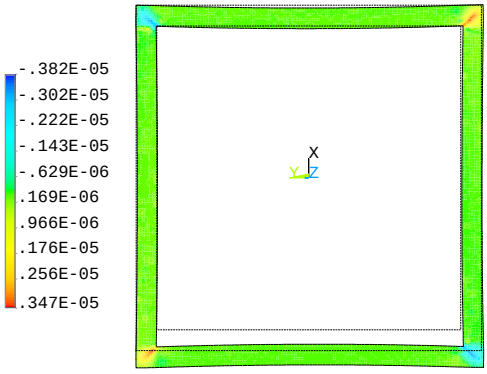

(e) ε_{xy}^{μ}

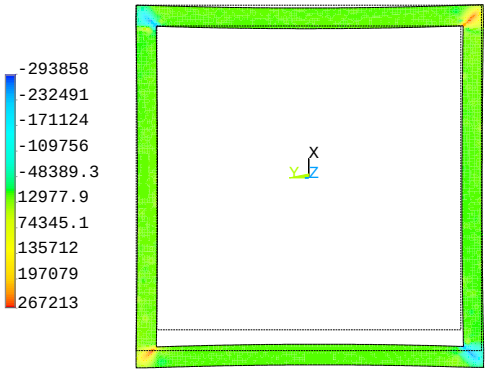

(f) σ_{xy}^{μ}

Figure 3.4.30: *Induced magnetostrictive strain and stress in the structure at peak of current ($t = \frac{T}{4}$).*

resentation of the magnetostrictive strain in the corner of the structure seems to be a suitable area. In fact, in the corner the magnetic flux sweeps all directions with respect to RD, which will give us a magnetostrictive behavior that evolves depending on the angle between magnetization and RD. Figure 3.4.32 shows the result of the equivalent magnetostrictive deformation $\varepsilon_{eqv}^{corner}$ in the corner of the modeled structure along the evaluation line and as a function of the flux density B. It can be seen that the model reproduces the magnetostrictive anisotropy between RD and TD, the evolution of the magnetostrictive strain $\varepsilon_{eqv}^{corner}$ seems to be continuous when the magnetic flux sweeps the angles between RD and TD at the corner.

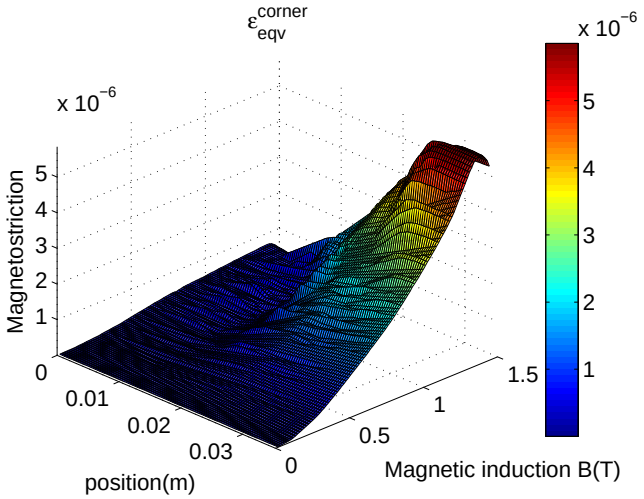

Figure 3.4.32: *The equivalent magnetostrictive strain $\varepsilon_{eqv}^{corner}$ in the corner (from RD to TD).*

3.5 Study of the laminated structure with air gaps

Transformer core are build from a stack of electrical steel sheets shaped in different forms (E-I core, U-I core...), creating necessarily involuntary small air gaps. Nevertheless, these air gaps can be voluntary created as in the case of inductors (chokes). When the magnetic field meets the air gaps, magnetic forces (Maxwell forces) appears generating noise and vibration besides the magnetostriction. However, unlike magnetostriction that occurs in the magnetic core, Maxwell forces act mainly at the interfaces between materials with different permeabilities (iron-air) inducing additional displacement of the structure. The present study focuses on the magnetic forces generated in the plane of

the electrical steel of a U-I shaped core and their contribution with the magnetostrictive deformation to the total displacement.

3.5.1 Structure and procedure description

Whether it is a transformer or an inductor, air gaps exist; in the case of transformers, the small air gaps are involuntary replaced by a non-magnetic medium like air or resin, but in the case of inductor, these air gaps are created on purpose filled by some materials immune to saturation to allow higher levels of magnetic flux. Unfortunately, these air gaps are a source of magnetic forces besides magnetostriction generating noise and vibration.

In order to study the effect of the magnetic forces in addition to the magnetostrictive deformation on the total displacement, a second ferromagnetic structure including air gap has been developed, figure 3.5.1. The structure assembly consists of U-I stacked core of non-oriented material (3%Si-Fe) without any lap joint assembly (no attractive inter-laminar forces). Hence, only attractive forces in the plane of the structure exist. The introduction of two air gaps in the flux path helps in the production of these magnetic forces, figure 3.5.1. These air gaps are parallel to the rolling direction (RD). Furthermore, materials with different mechanical properties and thickness are inserted in the air gap to evaluate their effect on the total displacement. The typical mechanical properties of the chosen air gap materials are described in table 3.2.

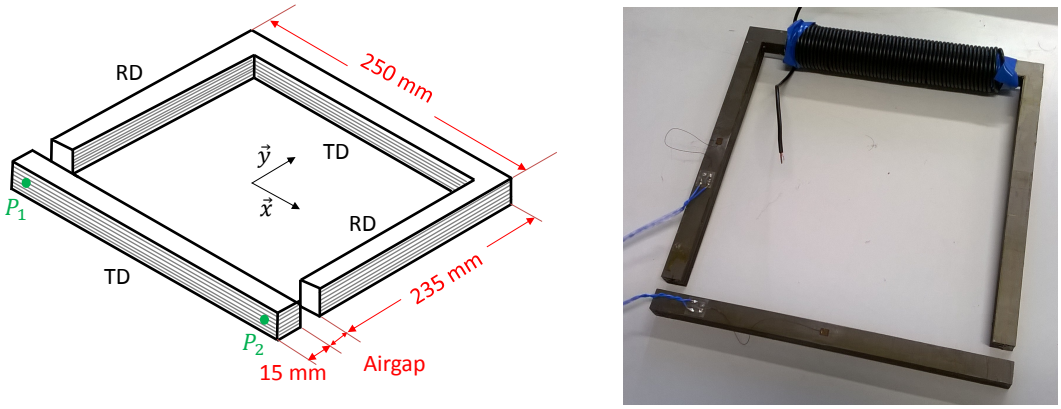

(a) *Schematic view: dimensions and measurements points.*

(b) *A picture of the studied structure.*

Figure 3.5.1: *Laminated structure with air gaps.*

Material type	Width (mm)	color	Young Modulus (GPa)	Poisson ratio	Density (Kg/m^3)
Glass mat	1	White	10	0.38	1800
AEM elastomer	1.9	Black	0.013	0.5	1266

Table 3.2: *Mechanical properties and width of the tested air gap materials.*

The structure is excited by a voltage magnetization system used previously (figure 3.3.5). A current $I_{max} = 10.5\,A$ at $f = 50Hz$ is then imposed to the feeding winding of 110 turns creating a magnetic field. Accordingly, a displacement due to magnetostriction and magnetic forces takes place. Like magnetostrictive strain, Maxwell forces occur at a fundamental frequency twice the excitation one. Several air gap materials are tested to study their influence on the total displacement. Given the small displacement magnitude in operation and for the seek for accuracy, the displacement measurements are obtained using the laser vibrometer. The displacement is measured at two key points on the I-shaped core (P_1, P_2) in the direction $\overrightarrow{y}$ (figure 3.5.1a).

To maintain the assembly of the magnetic circuit (I-U stacked sheets), a mechanical clamping is applied on each column of the core (figure 3.5.2). The clamping pressure is carefully chosen to keep together the different parts (U-shaped sheets, I-shaped sheets and the air gap material) without inducing a significant stress that can change the magneto-elastic behavior of the structure.

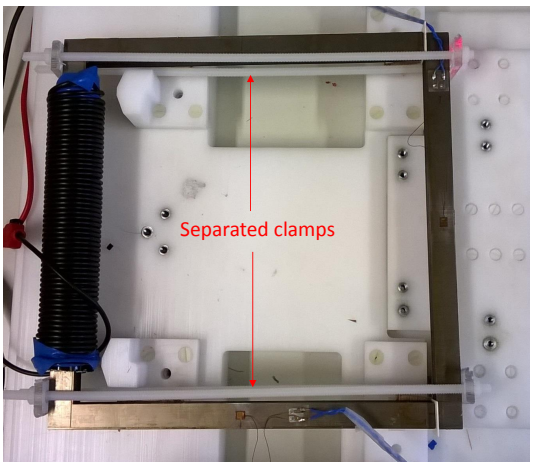

Figure 3.5.2: *The U-I stacked core with clamps.*

3.5.2 Finite Element Simulation

3.5.2.1 Consideration of Maxwell forces in the air gap

To calculate the magnetic forces applied to the structure, several mathematical expressions of electromagnetic tensors exist including the Maxwell tensor (Minkowski, Einstein & Laud...). The Finite Element software ANSYS calculates the magnetic forces at the air-iron interface by the Maxwell stress tensor approach. Then, these forces are used as loads in the structural analysis in addition to the magnetostriction forces. In the following we remind the expression of the Maxwell tensor and some simplifying assumptions.

Maxwell stress tensor method

The electromagnetic tensor is a function of the induction B and the magnetic field H, it is written in a general way in the form:

$$\overline{\overline{T}} = B \otimes H - \frac{1}{2} HB\bar{\bar{I}} \tag{3.5.1}$$

$\bar{\bar{I}}$ corresponds to the identity tensor.
The surface forces density is then defined as the product:

$$\vec{f_s} = [\overline{\overline{T}}] . \vec{n} \tag{3.5.2}$$

where $\vec{n}$ is the normal vector on the surface (figure 3.5.3).

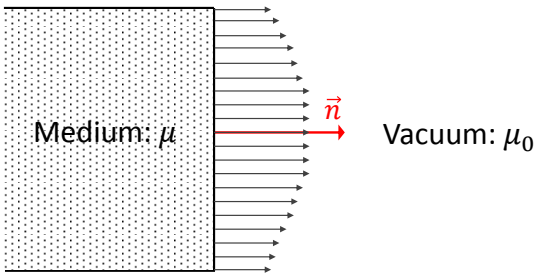

Figure 3.5.3: *Illustration of magnetic forces at a separation surface between two medium of different permeabilities.*

The classical expression of the Maxwell tensor for a magneto-static conducting medium corresponds to the expression of the tensor in a non-magnetic medium (vacuum or material of negligible susceptibility):

$$\overline{\overline{T}}^{Maxwell} = \frac{B \otimes B}{\mu_0} - \frac{1}{2}\frac{B^2}{\mu_0}\overline{\overline{I}} \tag{3.5.3}$$

Thus, in case of normal interface to the magnetic induction ($\vec{B} = B\vec{e}_x$ and $\vec{n} = \vec{e}_x$), there is no variation of Maxwell tensor $\overline{\overline{T}}^{Maxwell}$ at the transition from an interface normal to the induction, so no force. However, if we consider an interface between vacuum and a medium of high permeability (assumed infinite), $\vec{n}$ being oriented to the vacuum, we obtain:

$$\vec{f}_s \simeq -\frac{B^2}{2\mu_0}\vec{e}_x \tag{3.5.4}$$

If the medium is magnetic ($\mu_{medium} >> \mu_0$), the estimation of the pressure by the Maxwell stress tensor is of the order of MPa.

Simulation strategy

The global simulation strategy including air gaps is summarized in figure 3.5.4. First, once the magnetic forces are obtained by the Maxwell stress tensor, they are added to the magnetostrictive equivalent force calculated by the energy based model in a second step. Then, as detailed in section 3.4.3.3, these forces are transformed to nodal forces concentrated on the nodes of the mesh, and are used as a loading to be applied to the structure for the mechanical resolution. Nevertheless, the obtained deformation ε^{tot}, induced stress σ^{tot} and displacement U depend on one hand on the air gap width (magnetic forces magnitude) and on the mechanical properties of the material inside the air gap (soft or hard material).

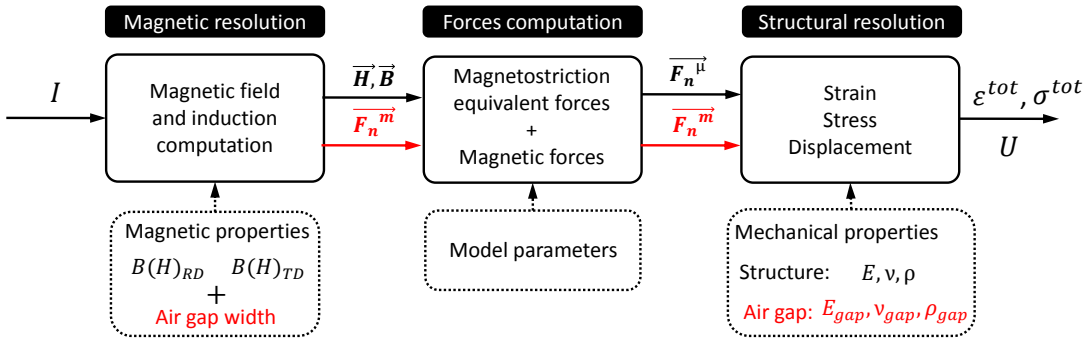

Figure 3.5.4: *The global simulation strategy including air gaps (magnetic forces).*

3.5.3 Estimation of displacement due to Maxwell forces and magnetostriction by analytical approach

Figure 3.5.5 gives a schematic view of the U-I shaped core and air gap material of thickness e subjected to a stress σ corresponding to a compressive stress due to Maxwell forces. Providing uniaxial conditions of stress, the components of stress tensor $\overline{\overline{\sigma}}$ and strain tensor $\overline{\overline{\varepsilon}}$ in the structure reference frame $(\overrightarrow{x}, \overrightarrow{y})$ can be written as:

$$\overline{\overline{\sigma}} = \begin{bmatrix} 0 & 0 \\ 0 & -\sigma \end{bmatrix}; \quad \overline{\overline{\varepsilon}} = \frac{\sigma}{E} \begin{bmatrix} \nu & 0 \\ 0 & -1 \end{bmatrix} \tag{3.5.5}$$

where E is the Young modulus and ν is the Poisson ratio of the air gap material. The elongation of the air gap material of thickness e in the $\overrightarrow{y}$ direction can be written as:

$$\varepsilon_{yy} = \frac{-\sigma}{E} = \frac{\Delta e}{e} \tag{3.5.6}$$

From equation (3.5.6) and considering e as the thickness of the air gap, the displacement can be estimated by equation:

$$\Delta e = \frac{-\sigma \times e}{E} \tag{3.5.7}$$

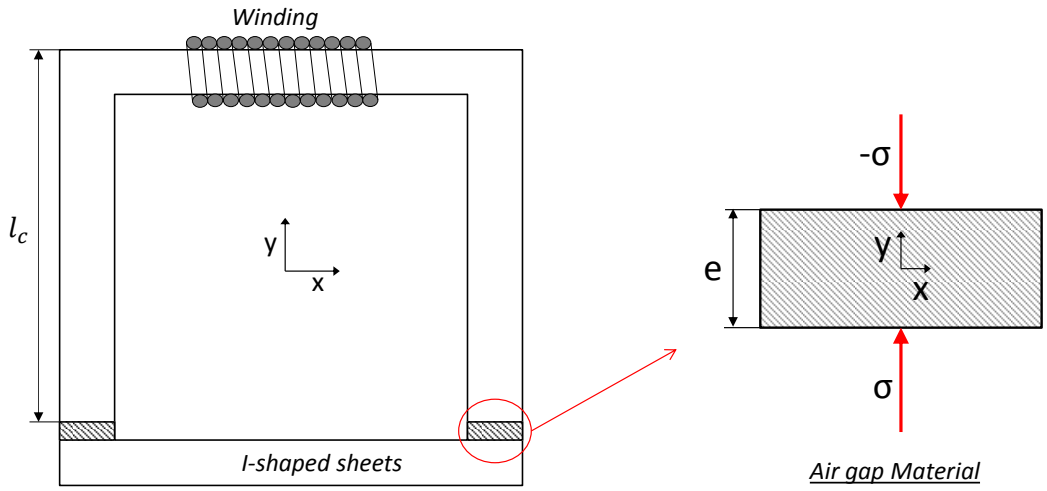

Figure 3.5.5: *Schematic view of the U-I shaped structure and equilibrium of air gap material under a stress σ.*

In our study the stress $\sigma = \sigma_{Maxwell}$ corresponds to the Maxwell forces interacting in the air gap between the I-shaped sheets and U-shaped sheets. It can be expressed by

equation (3.5.4):

$$\sigma_{Maxwell} = \frac{B^2}{2\mu_0} \tag{3.5.8}$$

where B corresponds to the air gap magnetic induction and μ_0 is the vacuum permeability.

Consequently, the equation (3.5.7) becomes:

$$\Delta y_{air\,gap}^{Maxwell} = \frac{B^2}{2\mu_0 E_{air\,gap}} e\,\overrightarrow{y} \tag{3.5.9}$$

Similarly, Assuming that the magnetostrictive deformation takes place only in the magnetic core, the displacement due to magnetostriction in a column of length l_c (figure 3.5.5) can be written:

$$\Delta y^{magnetostriction} = -\lambda_{long}^{\mu}(B) l_c\,\overrightarrow{y} \tag{3.5.10}$$

where $\lambda_{long}^{\mu}(B)$ is the longitudinal magnetostrictive strain as a function of the magnetic induction B. The sign $(-)$ means that the displacement is in the opposite direction of the $\overrightarrow{y}$ axis.

Thus, the total displacement can be expressed as the sum of equations (3.5.9) and (3.5.10), [100]:

$$\Delta y = -\lambda_{long}^{\mu}(B) l_c + \frac{B^2}{2\mu_0 E_{air\,gap}} e \tag{3.5.11}$$

Similarly, the flux density B can be estimated analytically. Figure 3.5.6 illustrates the U-I stacked core and the equivalent magnetic circuit. This procedure is known as the mean path approximation and according to Hopkinson's law it can be represented by the equation (3.5.12):

$$NI = (\Re_{UI\,core} + \Re_{airgap})\phi \tag{3.5.12}$$

where $\Re_{UI\,core}$ and $\Re_{airgap}$ are respectively the reluctance of the UI core and the air gaps, while ϕ corresponds to the magnetic flux :

$$\begin{cases} \Re_{UI\,core} = \frac{l_{UI\,core}}{\mu S_{UI\,core}} \\ \Re_{airgap} = \frac{2e}{\mu_0 S_{airgap}} \\ \phi = BS \end{cases} \tag{3.5.13}$$

Given that the air gap thickness is usually smaller than 5% of the length of the magnetic circuit, the air gap simplification $S_{airgap} = S_{UI\,core}$ can be made. In this case, the magnetic induction can be obtained by the equation :

$$B = NI\frac{\mu_0\mu_r}{2\mu_r e + l_{UI\,core}} \tag{3.5.14}$$

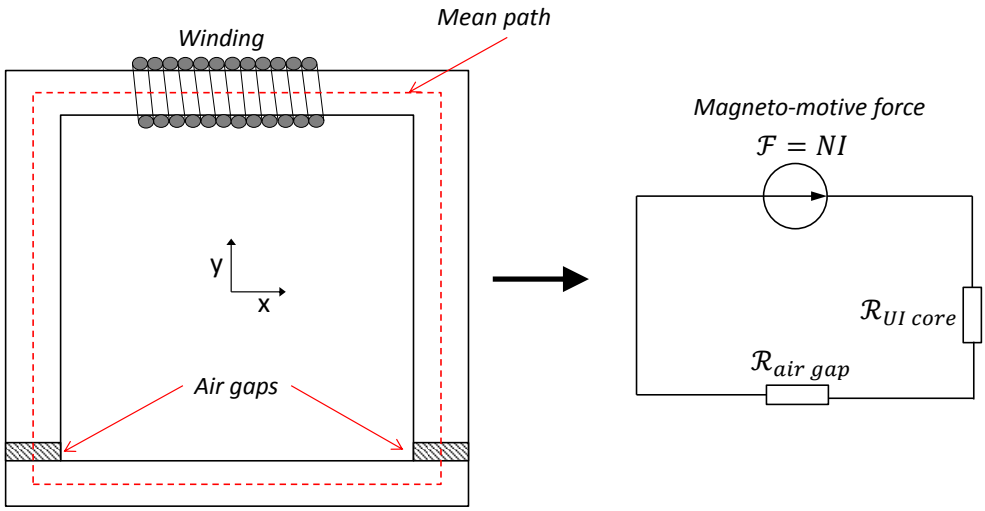

Figure 3.5.6: *A magnetic equivalent circuit representing the U-I core.*

Description	value
Turn number (N)	110
Vacuum permeability (μ_0)	$4\pi 10^{-7}$
Relative permeability (μ_r)	20000
Air gap thickness (e)	1-1.9 mm
Core length U+I ($l_{UI\,core}$)	0.94 m
column height (l_c)	0.235 m
Section of core U+I ($S_{UI\,core}$)	$2.25.10^{-4}$

Table 3.3: *Geometry and material properties*

3.5.4 Discussion of finite element, analytical and experimental results

3.5.4.1 FE computation Results

To investigate the deformation and displacement generated in the U-I shaped core because of magnetostriction and Maxwell forces in the air gap, two key points were chosen on the structure where the results have been extracted (figure 3.5.7). Given the structure symmetry, only the left leg of the structure will be discussed, the right leg has shown the same behavior. As the real structure, the rolling direction is along the vertical legs and hence the magnetization, while the top and bottom leg are along the transverse direction. To observe the contribution of each phenomena, the simulation results are shown when the deformation and the displacement are only due to magnetostriction, only due to Maxwell forces and due to the sum of both phenomena. Contrary to real samples (two air gap materials), three types of air gap materials were computed on the structure, from a relatively hard material equivalent to "glass mat" (Young modulus E = 10 GPa) to a soft material equivalent to a rubber (Young modulus E = 13 MPa). Between the two, a material of Young modulus E = 0.5 GPa (Teflon PTFE) is also computed.

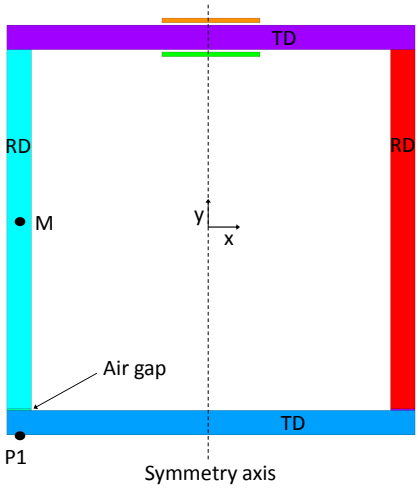

Figure 3.5.7: *Evaluation location: magnetostriction and displacement.*

Magnetic results

Figure 3.5.8 shows the distribution of the flux density B and the Maxwell forces for 1 mm air gap thickness at I_{max}=10.5 A. The flux density is nearly uniform in the structure and the average value in the left leg is 0.84 T. The average of flux density obtained analytically by equation (3.5.14) is around 0.75 T, which is rather very close. The flux density at the air gap is around 0.7 T. The Maxwell forces in the air gaps produce uniformly

distributed compressive stress applied on both side of the iron sheet (figure 3.5.8b). For the 1.9 mm air gap, the tendency is the same between simulated and analytical approach but in lower magnitude (0.55 T and 0.4 T respectively), whereas, the magnetic induction at the air gap is around 0.38 T.

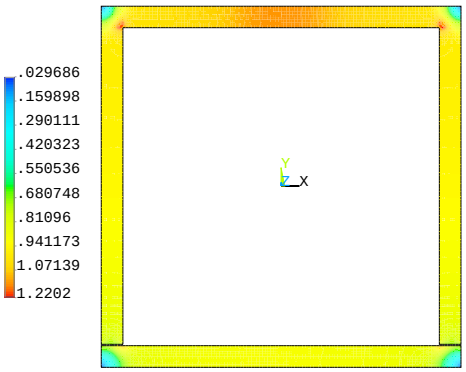

(a) *Magnetic flux density distribution (T).*

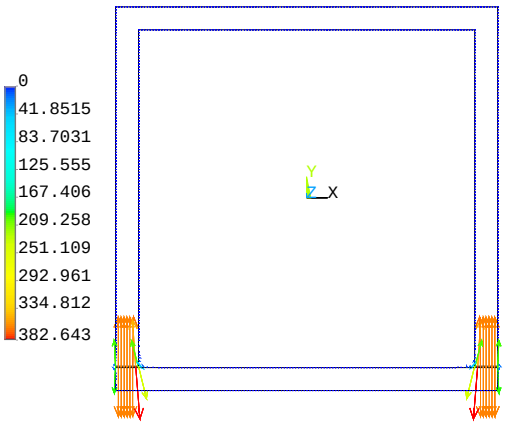

(b) *Maxwell nodal forces in the air gap (N/m), equivalent to a pressure of* $\sigma = 0.2\,\text{MPa}$.

Figure 3.5.8: *Magnetic flux density and Maxwell forces in the air gap (1mm air gap).*

Displacements results

Figure 3.5.9 shows the computed total displacements at point P1 due to magnetostriction, Maxwell forces and the sum of both of them over one period of current and for three different air gap materials. The results are shown for two air gaps thickness (1mm and 1.9 mm), nevertheless, the tendencies are the same. Hence, the discussion will focus

on only the 1 mm air gap.

In general, in all three figures (figures 3.5.9 a, c and e) and whatever the air gap material, the displacement due to magnetostrictive strain is the same and has a negative sign. In fact, whatever the hardness of the air gap material, the magnetostrictive deformation is transmitted from one side of the air gap material to the other side and hence, to the free leg (I-shaped sheets). As the I-shaped leg is free to move, nothing prevent the expansion of magnetostrictive deformation (in one direction). The negative sign means that the displacement takes place in the opposite side of y-axis. Looking at the displacement due to Maxwell forces, the amplitudes decreases progressively with the increase of the air gap material Young modulus. Furthermore, unlike the displacement due to magnetostriction, displacement due to Maxwell forces is positive (attractive forces). Which means that the two phenomenon act in the opposite direction along the air gap thickness. This is more visible on the displacement due to both magnetostriction and Maxwell forces. The harder is the air gap material (Young modulus increase), the less it compresses under the effect of Maxwell forces and therefore the associated displacement is decreased (figure 3.5.9 a, c and e). Since the displacement due to Maxwell forces acts in the opposite direction to that of magnetostriction, the total displacement will depend mainly on the Young modulus of the air gap material. Thus, with an appropriate and optimal Young's modulus value (for a fixed air gap thickness), it is possible to compensate both phenomena and nearly cancel the total displacement.

As it can be seen from figure 3.5.9, the total displacement changes sign when moving from $E = 0.5\,GPa$ to $E = 10\,GPa$, Thus, the optimal value is situated in this interval. In the same excitation conditions, this value is estimated to an air gap material of $E = 1.49\,GPa$ for 1 mm air gap and $E = 1.68\,GPa$ for 1.9 mm air gap.

3.5.4.2 Analytical approach results and comparison with FE computation results

The FE simulation results were compared with the results obtained with an analytical approach using the relation described in equation (3.5.11). Similarly, in analytical calculation the two phenomena were estimated separately then the sum of both estimated too. The comparison results are summarized in figure 3.5.10. Except some qualitative differences, the results obtained by the analytical approach are very satisfactory and close to those obtained by FE simulation. In this respect, the results have the same order of magnitude and follow the same tendency. Going from a hard Young modulus to a soft one, the influence of magnetostriction decreases in favor of magnetic forces (Maxwell forces) and this for the two air gaps thickness. Furthermore, this comparison confirms that the FE model reproduces accurately the structural behavior of the structure including magnetostriction and magnetic forces phenomena.

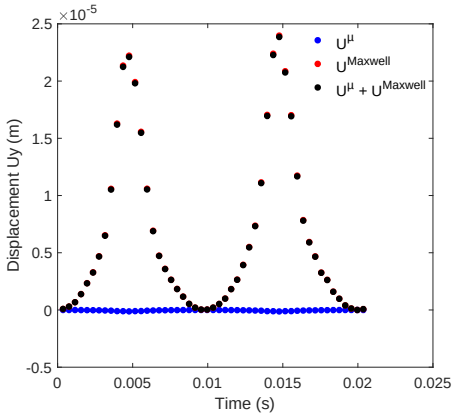

(a) *1mm air gap:*E = 13MPa *(AEM).*

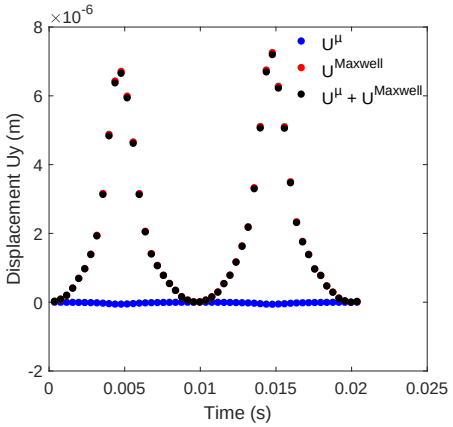

(b) *1.9mm air gap:*E = 13MPa *(AEM).*

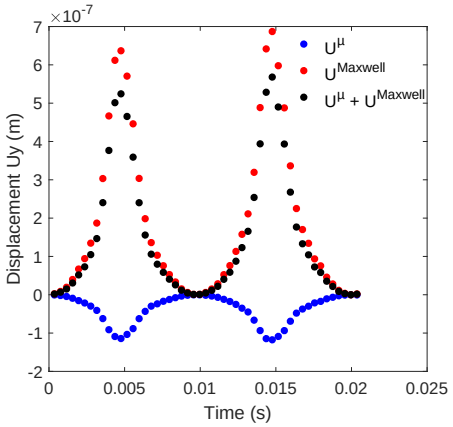

(c) *1mm air gap:*E = 0.5GPa *(Teflon).*

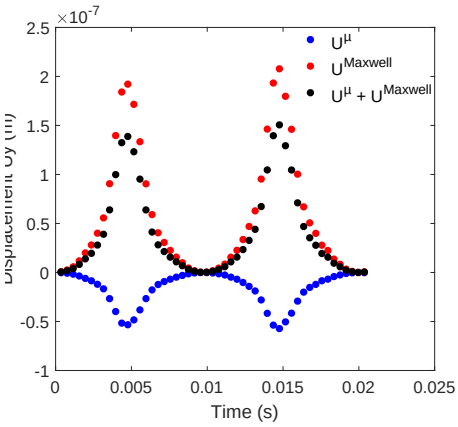

(d) *1.9mm air gap:*E = 0.5GPa *(Teflon).*

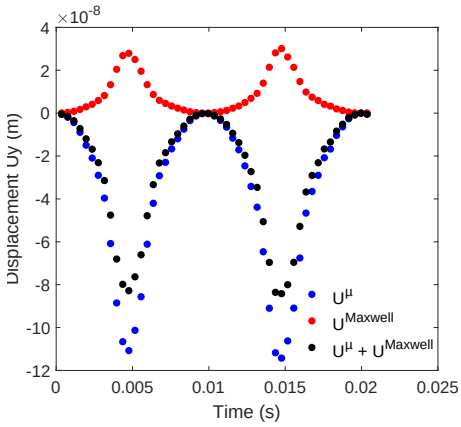

(e) *1mm air gap:*E = 10GPa *(Glass mat).*

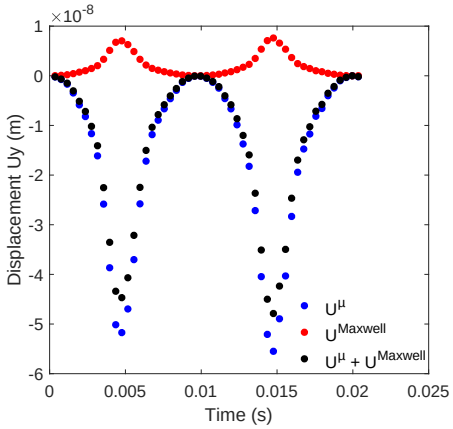

(f) *1.9mm air gap:*E = 10GPa *(Glass mat).*

Figure 3.5.9: *Total displacements of I-shaped sheets at point P1 over one period of excitation current: 1mm air gap (left), 1.9 mm air gap (right).*

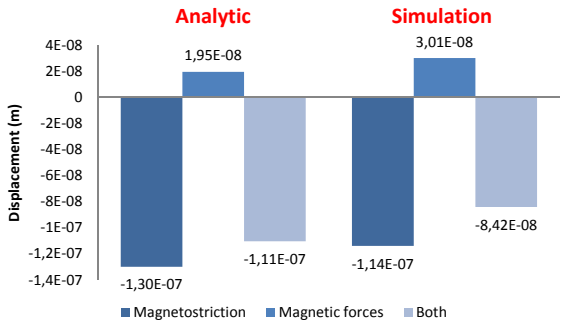

(a) *1mm air gap:*E = 10GPa *(Glass mat).*

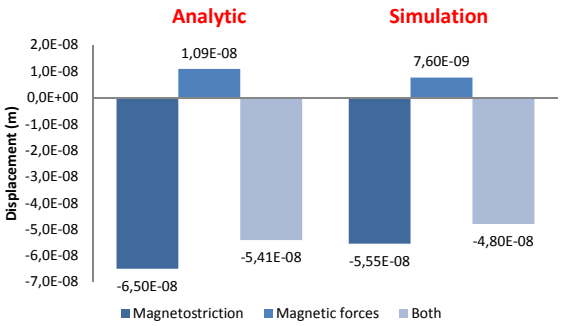

(b) *1.9mm air gap:*E = 10GPa *(Glass mat).*

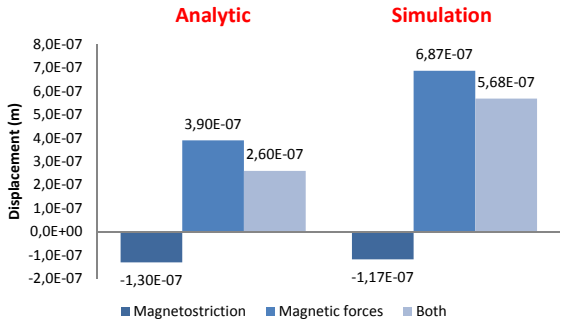

(c) *1mm air gap:*E = 0.5GPa *(Teflon).*

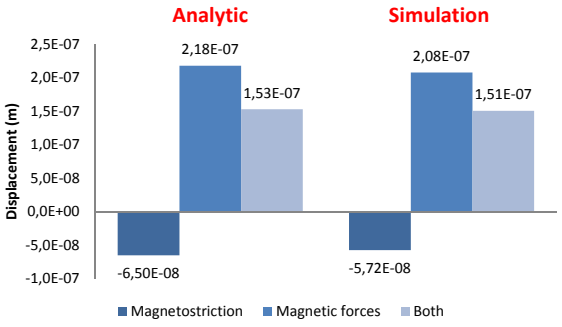

(d) *1.9mm air gap:*E = 0.5GPa *(Teflon).*

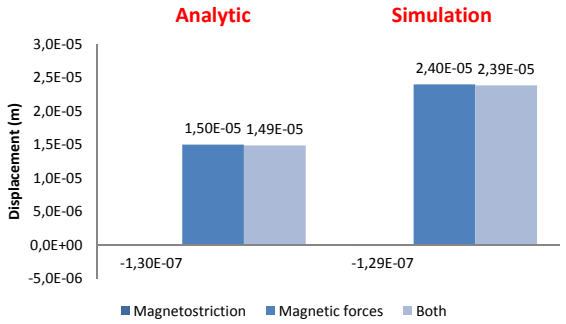

(e) *1mm air gap:*E = 13MPa *(AEM).*

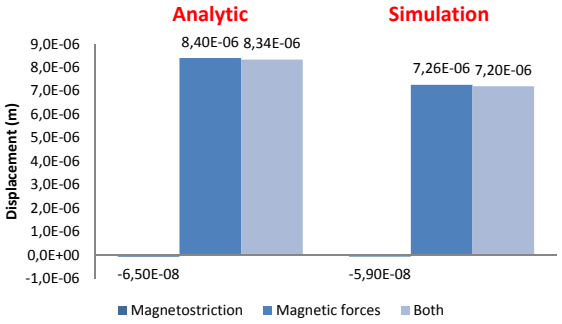

(f) *1.9mm air gap:*E = 13MPa *(AEM).*

Figure 3.5.10: *Comparison of total displacements between analytical and computational approach at point P1: 1mm air gap (on the left), 1.9 mm air gap on the right).*

3.5.4.3 Measurements results and comparison

Figure 3.5.11a shows the displacement results of the structure with an air gap thickness of 1.9 mm (AEM). Theoretically, according to symmetry, point P_1 and P_2 should present almost the same displacement. However, it can be observed that the displacement at P_1 is larger than displacement at P_2. This may come from the unbalanced clamping. In fact, the two side of the structure are clamped separately by two clamps (figure 3.5.11b), which can create unbalanced clamping. The same experience repeated and made this time on purpose by clamping more on one side than the other confirmed the same observations.

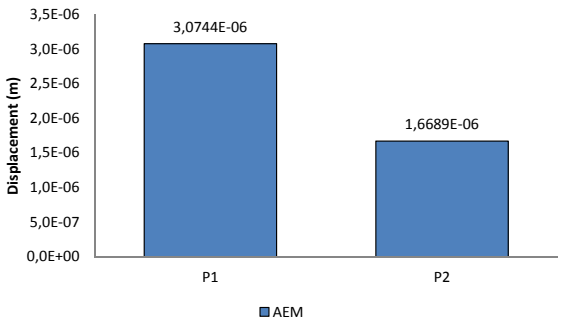

(a) *Peak to peak displacement of points* P_1 *and* P_2.

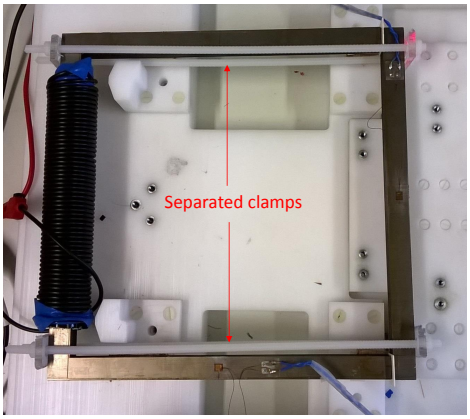

(b) *Picture of the structure clamped with two separate clamps.*

Figure 3.5.11: *Displacement at two measuring points of the U-I structure (clamps).*

To reduce the effect of unbalanced clamping, a second solution of clamping is adopted. As shown in figure 3.5.12a, thanks to a linear slide, the air gap value can be adjusted with an accuracy of 0.01 mm over the entire length of the I-shaped core, leading to a more uniform clamping. The displacement results obtained by the second solution of clamping are shown figure 3.5.12b, the difference between the two point is less striking. On second thoughts, there would be probably some magnetic field leakage leading to unbalanced magnetic forces and hence, different displacements. Besides, because of the imperfection of the single sheet assembly (inaccuracy of process tolerance), the contact of the U-shaped core, the air gap material and the I-shaped core is not perfect as it can be seen on figure 3.5.13.

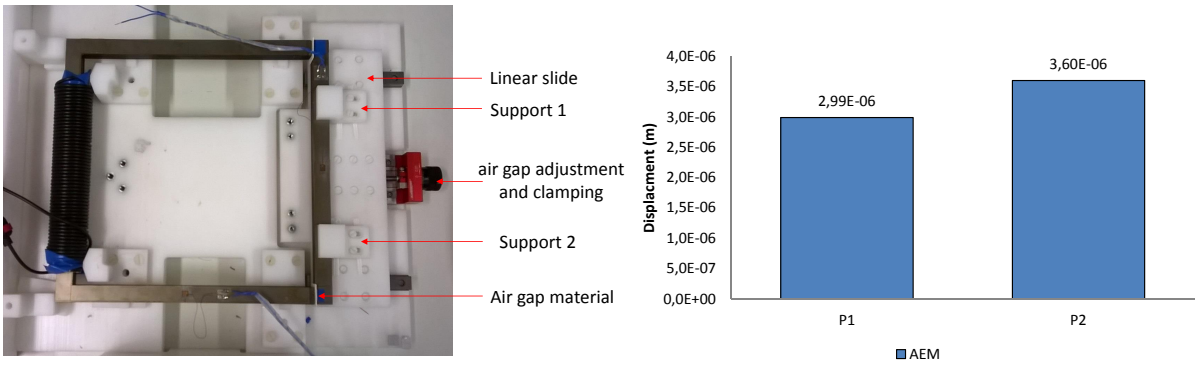

(a) *Second solution of clamping the structure.* **(b)** *Peak to peak displacement of points* P_1 *and* P_2.

Figure 3.5.12: *Displacement at two measuring points of the U-I structure (linear slide).*

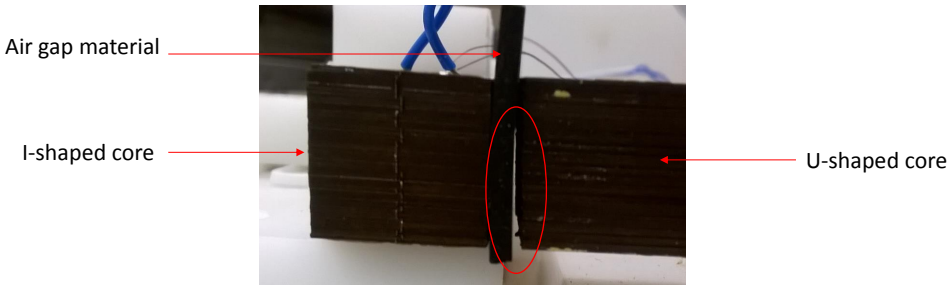

Figure 3.5.13: *Misalignment at the air gap.*

This solution will be retained for the upcoming displacements measurements. It is reminded that the air gap materials samples are: 1.9 mm (AEM) and 1 mm (glass mat). Figure 3.5.14 represents the comparison of measurements results with the FE simulation and the analytical calculation results for these two materials at point P1. It is observed that for the AEM materials ($E = 13\,MPa$), the measurement results are consistent with the simulation and the analytical calculation despite a small difference. On the other hand, for the glass mat ($E = 10\,GPa$), the measurement results are much higher than those obtained by simulation or by analytical calculations. This difference can be explained by two main reasons. The first reason is the true Young modulus. Indeed, the true value of the latter was not provided by the manufacturer and its value was estimated, which can induce errors regarding the material hardness. The second is the misalignment observed during the contact of the air gap material with the U-I shaped core. The absence of a perfect contact coupled with the magnitude of the Maxwell effort which is 2 times greater than that of 1.9 mm air gap can cause displacements increase. To some extent, the contact misalignment between I and U core in the case of the hard air gap material (10 GPa), creates a pivot behavior which can explain the higher displacements.

In the case of a soft material (13 MPa), this pivot behavior due to the misalignment is "absorbed".

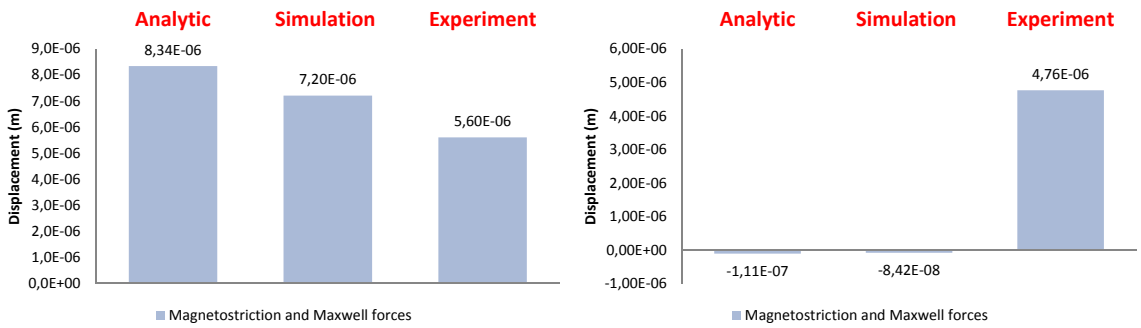

(a) *1.9 mm air gap: E=13MPa.* **(b)** *1 mm air gap: E=10GPa.*

Figure 3.5.14: *Displacement due to magnetic forces and magnetostriction for two air gap materials.*

On the basis of these measurements, the following observations are pointed out:

- The total displacement of the structure depends greatly on the tightening performed.
- A separate clamping can lead to unbalanced displacement of the structure, which can be a source of additional vibration. To avoid this issue, an uniform clamping is advised.
- The assembly precision of a U-I core structure, can have a great impact on the total displacement of the latter during its operation (e.g. misalignment at the air gap).
- Under optimal conditions of assembly and tightening, an optimal choice of air gap materials can significantly reduce the displacement of the structure and consequently its vibration.

3.6 Conclusion

Magnetic and magnetostrictive characterization of a laminated structure made of non-oriented electrical steel using strain gauges and laser vibrometer have been presented. A comparison between two types of magnetization (current and voltage) shows similar amplitudes of magnetostrictive deformation, nevertheless the current or voltage waveform of the excitation were different. Moreover, magnetostrictive deformation results

measured by strain gauges have shown acceptable agreement with laser vibrometer results. The laser vibrometer setup afford some advantages that strain gauges method can't, like measurements along the height of the lamination and accurate measurements under low magnetization. Besides, magnetic and magnetostrictive behavior under compressive stress were measured and showed similar trends to the single sheet results.

Next, a two dimensional FE computation method to predict magnetostrictive deformation in a frame structure was presented. This method considers the magnetic and magnetostrictive anisotropy of the studied material and requires the energy based model presented in chapter 2. The Finite Element results were compared to measurement results obtained previously on a laminated structure. The results have shown good agreement on the transverse direction, however, due to the random assembly of the laminated structure, the comparison on the rolling direction did not give satisfactory agreement. Nevertheless, the magnetostrictive measurement results obtained on the laminated structure show larger deformation compared to single sheet (RD). This reveals that the isotropic hypothesis for non-oriented materials during a sheet assembly can lead to an increase in the overall deformation of the structure: Because of the presence of some sheets in TD among the RD sheets, even if the percentage is small, their influence remains significant.

A second laminated structure including air gaps inducing magnetic forces in addition to the magnetostrictive deformation is presented. The aim of this study was to investigate the interaction between magnetostriction and magnetic forces by acting on the hardness of the air gap material. Displacements measurements using laser vibrometer were obtained for different materials and compared to FE and analytical results. First, the FE method calculation was developed to include Maxwell forces in addition to magnetostriction. Then, a validation is performed by analytical approach. The FE method showed similar results to the analytical method in terms of displacement. However, when compared to the measurement results, a good agreement was found for only one material. An improvement of the experimental setup or of the model still needed to achieve better matching.

To conclude, going from a simple single sheet to a simple assembled structure like a transformer core is not obvious. This complexity lies in several parameters: assembly precision, resin, magnetostriction and magnetic forces interaction, stress.... All these mechanisms may influence the vibration of the structure. In the next chapter, we will investigate the interaction between magnetostriction and mechanical resonance of the structure.

CHAPTER 4

INVESTIGATION ON MECHANICAL RESONANCE INDUCED BY MAGNETOSTRICTIVE DEFORMATION

4.1 Introduction

This chapter deals with the investigation of mechanical resonance induced by magnetostrictive deformation in a laminated structure. First, the background of the study and a short description of the modal analysis will be given. Then, the estimation of the magnetostriction strain and Maxwell forces contributions to the total displacement of the structure is presented. For the computation of the eigenfrequencies and eigenmodes, a mechanical model of the structure is developed. This model includes the friction contact interactions between the neighboring laminated sheets. After that, the finite element calculations will be compared to the experimental modal analysis results. Based on these results, the following section will detail the development of a numerical model based on analytical and numerical homogenization to better approach the real dynamic behavior of the structure. In the last section, the magnetization at resonance procedure will be presented and the magnetostriction strain induced resonance results will be described and discussed in details.

4.2 A general overview

4.2.1 Background

The most typical noise component of transformers and rotating machines is the noise coming from electromagnetic sources. Besides the contribution of Laplace forces in

conductors (e.g. coils), electromagnetic noise in these electrical devices is caused mainly by magnetostriction (e.g. ferromagnetic core) and Maxwell forces (e.g. air gap). As a consequence, noise and vibration are inherent characteristics of electrical devices and can not be completely eliminated. According to authors in [80], magnetostriction could be responsible for up to 50% of the total electromagnetic forces. That's why it remains a preoccupying source of noise in rotating machines and transformers as shown in these studies [7, 82, 84]. Due to magnetostriction, structure lamination like transformer and rotating machine can resonate under magnetization, increasing the vibration and the acoustic noise. Despite that, there are few works that deal with the interaction of magnetostriction with the structure vibration of electrical devices [60, 108, 78].

4.2.2 Modal analysis

The fundamental notion that usually intervenes in vibration problem is the notion of natural frequency. As a matter of fact, when a structure (rotating machines, transformers, etc.) with low damping is excited by a periodic forces of frequency f, it may undergoes resonance vibrations if the excitation frequency matches one of the eigenfrequencies of the structure (mode at frequency f). Modal analysis provides information on the dynamic characteristics of structural elements at resonances, and thus helps in understanding of their dynamic behavior. Each vibration mode is linked to a natural frequency, the modal representation in mathematical terms consists of using the basis of the eigenfrequencies and the eigenforms of the structure vibration. The dynamic behavior of a multiple degree of freedom system can be represented by a linear second-order differential equation with constants coefficients matrices $[M]$, $[C]$ and $[K]$ which can be written as:

$$[M]\{\ddot{x}\} + [C]\{\dot{x}\} + [K]\{x\} = \{F\} \tag{4.2.1}$$

where:
$[M]$ is the mass matrix
$[C]$ is the damping matrix
$[K]$ is the stiffness matrix
$\{F\}$ is the exciting force vector
$\{x\}, \{\dot{x}\}, \{\ddot{x}\}$: the displacement vector, and its first and second derivatives with respect to time, $(\cdot) \equiv \frac{d}{dt}$.

For the calculation of the FE technique, an undamped system is usually considered. Hence, The equation (4.2.1) consists only of mass M and stiffness K. The equation of free vibration will be written as:

$$[M]\{\ddot{x}\} + [K]\{x\} = 0 \tag{4.2.2}$$

Assuming a solution type in the following form:

$$\{x\} = \{X\}\exp(j\omega t) \tag{4.2.3}$$

and inserting the solution (4.2.3) into equation (4.2.2) yields:

$$([K] - \omega^2[M]).\{X\}\exp(j\omega t) = 0 \tag{4.2.4}$$

Which is an eigenvalue problem. The solution to this problem is the eigenvalues (eigenfrequencies $f_i = 2\pi\omega_i$) and the corresponding eigenvectors (eigenforms ϕ_i for $i = 1, 2, ..., N$). The relationships between the natural frequencies and the modes shapes can be represented by the equation:

$$([K] - \omega_i^2[M])\{\phi_i\} = 0 \tag{4.2.5}$$

The above eigenvalue problem shows that the problem of determining natural frequencies and mode shapes could be solved if one had a way to measure the mass and stiffness matrices. Such measurements are, however, difficult to accomplish. Instead, one can measure transfer functions in the frequency domain which hold enough information to extract the modal properties. Such measurements will be described in subsection 4.4.2.

4.2.3 Mechanical resonance

To understand the basis principle of mechanical resonance, we consider the example of an embedded-free bending beam (figure 4.2.1). The equation of bending motion of the beam is expressed in equation (4.2.6) as a function of the eigenpulses ω_n (or eigenfrequencies) that represent the temporal dependence, and the eigenmodes ϕ_n representing the spatial dependence:

$$w(x,t) = \sum_{n=1}^{\infty}(A_n sin(\omega_n t) + B_n cos(\omega_n t))\phi_n(x) \tag{4.2.6}$$

where:
$w(x,t)$ is the transverse displacement (magnitude of deflection)
x,t represent the spatial and temporal dependence
n is an integer representing the mode number
A_n, B_n are two constants that depend on the initial conditions
$\phi_n(x)$ is the deformed eigenmodes of mode n

For instance, if the beam is submitted to a traction-compression loading at a frequency close to the flexion mode natural frequency it will not induce a flexion resonance. Because, resonance is possible only if the excitation forces are capable of inducing a deformation close to the eigenmode shape: modal appropriation. Hence, the dynamic behavior of the mechanical structure assumes that a resonance occurs if and only if both of the following conditions are fulfilled:

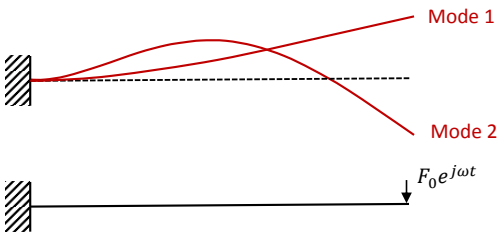

Figure 4.2.1: *The first two bending modes of the fixed-free beam (on the top) and the beam subjected to periodic force (on the bottom).*

- A matching between both the spatial order of the force wave and the mode number of the structure.
- A matching between the force frequency of the wave and the structure mode natural frequency.

Magnetostriction induced resonance in NO steels has been studied in [95, 108], however the sample they worked on seems to have a simple geometry and far from a laminated transformer core. As demonstrated by authors in [73], structure laminations may have a strong influence on the vibrational behavior of the structure, which is also true if the excitation force is coming from magnetostriction deformation [53]. Similarly, other authors make the finding of mechanical resonance but do not detail the reasons (magnetostriction, Maxwell forces or both) with certainty [123, 70]. Despite these existing research on mechanical resonance induced by magnetostriction, there was no detailed investigation on a device similar to a transformer structure.

4.3 Magnetostriction and Maxwell forces

4.3.1 Structure under study: Brief description

Figure 4.3.1 shows the ferromagnetic structure under study. The structure was already described in details in the previous chapter (chapter 3). We remind that to study only magnetostrictive deformation, a simple assembly of electrical sheets of frame shape without any lap joint has been considered. In fact, a lap joint assembly, overlapping the laminations in the corner, is often used as it allows the flux to always circulate in the rolling direction of the material. However, the flux lines that go from one lamination to another pass through small inter-laminar air gaps which create magnetic attractive forces. Therefore, in addition to vibrations due to magnetostriction, vibrations due to magnetic forces of the joint regions of the laminated can be generated as well [117, 118]. Consequently, the ferromagnetic structure laminations were cut out of one piece,

so that there would be no air gap or overlaps along the flux path (representing only the magnetostrictive vibration). The structure is set in horizontal position as shown in figure 4.3.1. An excitation winding in black was set on one leg to magnetize the ferromagnetic structure.

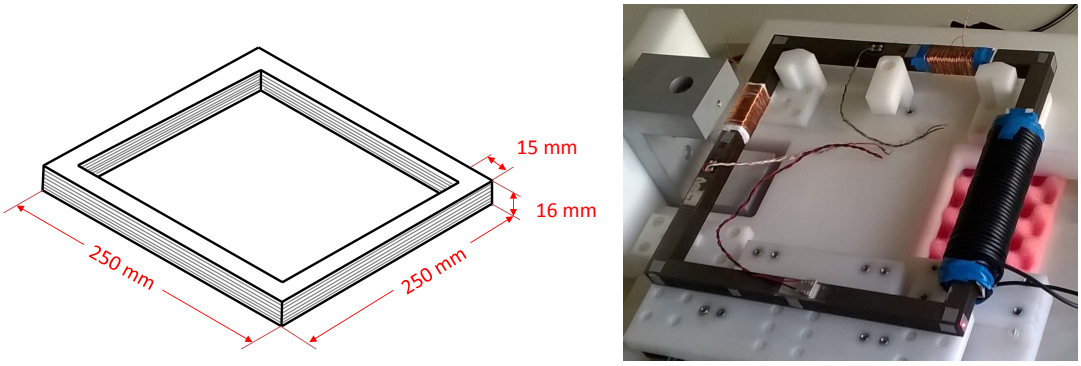

(a) (b)

Figure 4.3.1: *(a) schematic description of the ferromagnetic frame core. (b) the structure with the magnetization winding and B-coil sensors.*

4.3.2 Estimation of the displacement due to magnetostriction and Maxwell forces

Magnetostriction is a magneto-mechanical phenomenon that appears in ferromagnetic materials when the domains have to align along the direction of the magnetic field, resulting in a strain with constant volume, taking place twice the fundamental frequency of the magnetic field [32]. However, In many works, magnetostriction has been modeled as a force [77, 68, 71]. According to these two statements, magnetostrictive forces can be defined as the equivalent force field which creates the same strain as the magnetostrictive strain. Furthermore, the spatial distributions of magnetostrictive forces is inhomogeneous and difficult to interpret [105], because there is no established model for 3D magnetostriction capable of describing the spatial order decomposition of magnetostriction equivalent force. In contrast, the spatial decomposition of magnetic forces can be easily predicted as in the case of rotating machines (figure 4.3.2). Magnetostrictive strain causes the dimension of the core laminations to change and vibrate when the core is magnetized by an alternating magnetic field, which can lead to mechanical resonance [60, 108]. Moreover, the Maxwell forces present in the air gap can be responsible for higher noise if resonance happens [59, 89, 11]. As these forces occur at the same frequencies as magnetostriction [66], it is hard to quantify how much Maxwell efforts are greater or lower than magnetostrictive efforts. To make this difference, as men-

tioned earlier, we worked on a structure without any air gaps or overlaps and the only Maxwell forces that will be present, will appear at the circumference of the ferromagnetic structure. These forces can be due to magnetic field leakage lines or the presence of a magnetizing coil as shown in figure 4.3.3. Thereby, the Maxwell tensor $\sigma_{Maxwell}$ due to leakage magnetic field can be expressed as follows:

$$\sigma_{Maxwell} = \frac{B_{leakage}^2}{2\mu_0} \tag{4.3.1}$$

where $B_{leakage}$ is the magnetic flux density of leakage magnetic field lines (e.g. corners, coil) and $\mu_0 = 4\pi 10^{-7}$H/m is the vacuum permeability. As the circumferential magnetic flux density is very low in magnitude (except the coil position), the pressure or stress induced is weak, particularly, in the measurements positions (the lower part of the structure, figure 4.3.3).

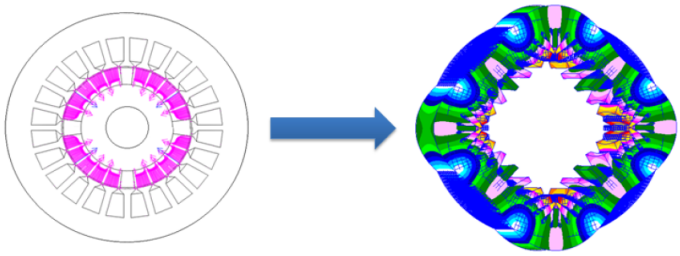

Figure 4.3.2: *Magnetic pressure due to Maxwell forces (left) and generated deformation of stator (right) [44].*

The magnetostriction model used for the computation of the magnetostrictive strain ε^{μ} was described in chapter 2. We remind that the proposed model aims to minimize the free energy inside the material.

In the finite element calculation, the magneto-elastic coupling is assumed to be weak. First, the magnetic simulation is carried out and the distribution of the magnetic field in the structure is produced. Then, a magneto-elastic problem is formulated by using the equivalent nodal method [114, 46, 81]. The general principle of this method is to calculate the equivalent forces to be applied to the nodes of the mesh in a structure calculation in order to reproduce the magnetostrictive deformation. These nodal forces are naturally functions, among others, of magnetic quantities initially calculated. The calculation of the nodal forces is done in two stages: computation and assembly of the elementary forces. These nodal forces equivalent to the magnetostriction are calculated for all the nodes of the problem and constitute the loading to be applied in the structural computation.

Figure 4.3.4 shows the results of simulation carried out on the structure. The computation has included Maxwell forces calculation and magnetostriction model to calcu-

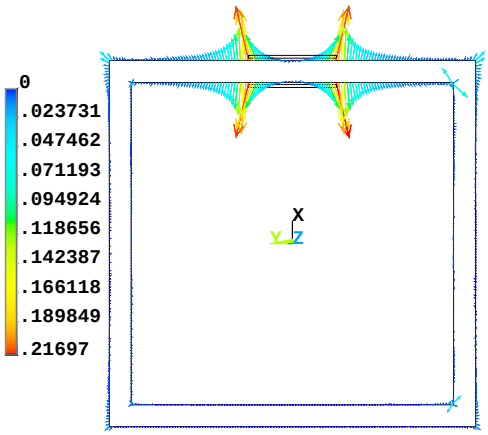

Figure 4.3.3: *Computed Maxwell forces (N/m) distribution on the ferromagnetic structure.*

late equivalent forces due to magnetostriction. These results show that at the measurement zones far from the excitation coil (top horizontal bar) the displacement due to the magnetostrictive strain is ten times greater than the displacement due only to Maxwell forces (due to leakage) $U_{Magnetostriction}$=10×$U_{Maxwell}$. Therefore, the displacement due to Maxwell forces $U_{Maxwell}$ caused by the magnetic field leakage, can be neglected in front of the displacement due to magnetostrictive strain $U_{magnetostriction}$. Hence, only magnetostriction will be considered as the main source of mechanical resonance in our study.

4.4 Mechanical part: determination of resonance frequencies of the ferromagnetic structure

This section presents the simulation and experimental modal analysis results conducted as part of a research collaboration with the acoustic and vibration team at the Roberval laboratory at UTC [67].

4.4.1 Simulated modal analysis

4.4.1.1 Description

In order to identify the eigenmodes of the structure, a modal analysis simulation has been carried out by the Finite Element Analysis (FEA). The software ANSYS was used

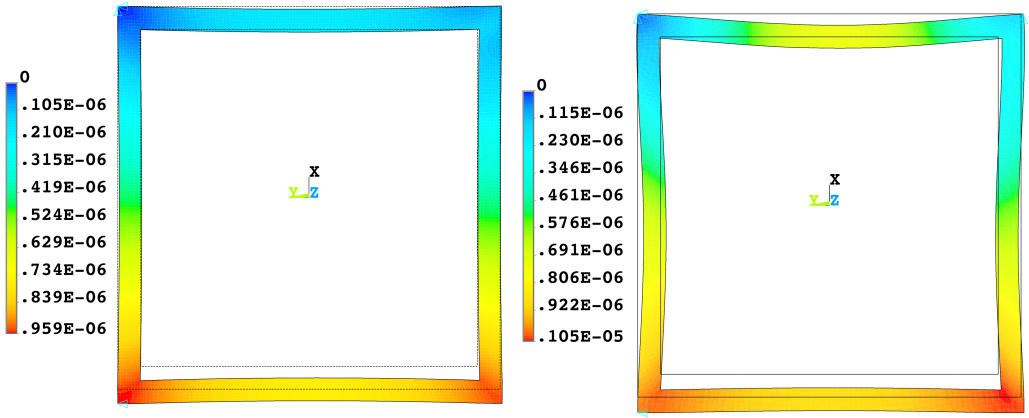

(a) *Only magnetostriction.* **(b)** *Magnetostriction and Maxwell forces.*

Figure 4.3.4: *Simulated displacement of the ferromagnetic structure in (m): due to only magnetostriction (a), due to magnetostriction and Maxwell forces (b).*

to perform the calculations. Since the structure is a set of laminated frame sheets, and to get close as possible to its real vibrational behavior, the structure is modeled as an assembly of 40 frame sheets of thickness 0.35 mm (the same as the real structure), with a contact condition between the sheets corresponding to a given friction coefficient (figure 4.4.1a). Based on measurement and by acting on this coefficient by fitting, we can best simulate the behavior between the sheets. In our case, it corresponds to 0.3 (steel-steel friction). Some experiments have shown that the vibrational behavior of a laminated structure is quite different from that of an homogeneous thick structure [116]. In this respect, another finite-element model is built, called homogeneous model made of homogeneous medium (isotropic) without any layers (figure 4.4.1b). To obtain both the in-plane modes and the out-of-plane modes at the same time, both models were modeled as a collection of three-dimensional block.

The material constants used in the calculations are shown in table 4.1. The same conditions as experimentation were respected (no boundary conditions) because the natural frequencies are very sensitive to the simple difference of boundary conditions.

3% Si-Fe NO Grade	M235-35A
Conventional density (kg.m^{-3})	7600
Poisson ratio ν	0,3
Young Modulus (GPa)	200

Table 4.1: *Typical physical properties.*

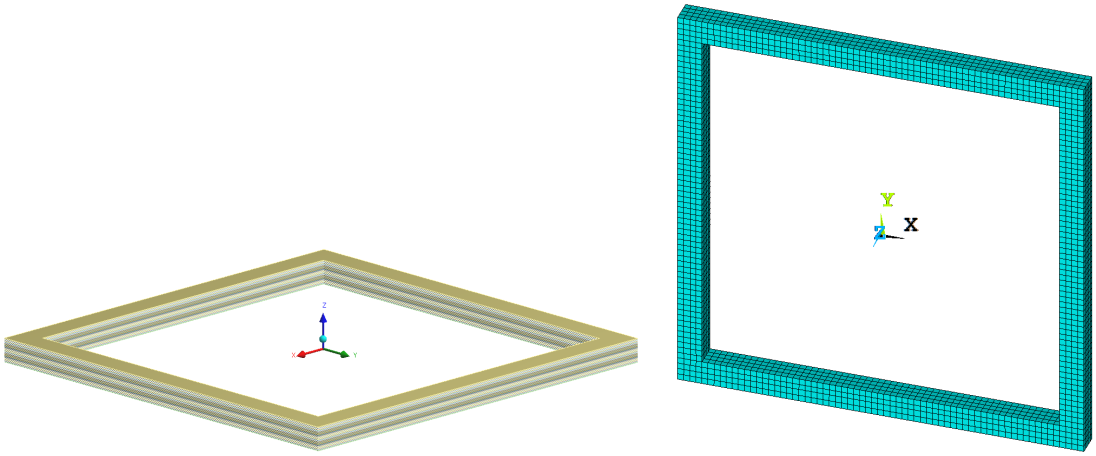

(a) *Laminated FE model.* **(b)** *Homogeneous FE model.*

Figure 4.4.1: *Finite-element models of the ferromagnetic structure.*

The vibration of the ferromagnetic structure can be classified into in-plane vibrations modes and out-of-plane vibrations modes. Results of the modal analysis of the laminated finite-element model are shown in figure 4.4.2 for in plane displacements and in figure 4.4.3 for out of plane displacements. Similar mode shapes are obtained for the homogeneous model, except for out of plane modes where the eigenfrequencies shows a significant gap. The comparison of obtained eigenfrequencies of the two finite-element models will be discussed in subsection 4.4.2.2.

In the investigated frequency range (0-3.5 [kHz]), we obtain six in-plane modes and six out-of-plane modes. The mode shapes of the out-of-plane modes are much more complicated than those of the in-plane modes. These results from FE simulation will be compared with the experimental modal analysis results in the following section.

4.4.2 Experimental modal analysis

In this part the dynamic behavior of the structure is studied without any electrical excitation at the magnetizing coil terminal. First the measurements made on a real structure are presented. Then, the experimental natural frequencies and modes shapes are detailed. At the end, the comparison between the experimental and the numerical modes is discussed.

4.4.2.1 Experimental set-up and procedure

Given the geometry of the structure, the modes are divided in two categories : the in-plane modes, in the (xOy) plane, and the out-of-plane modes with a z component.

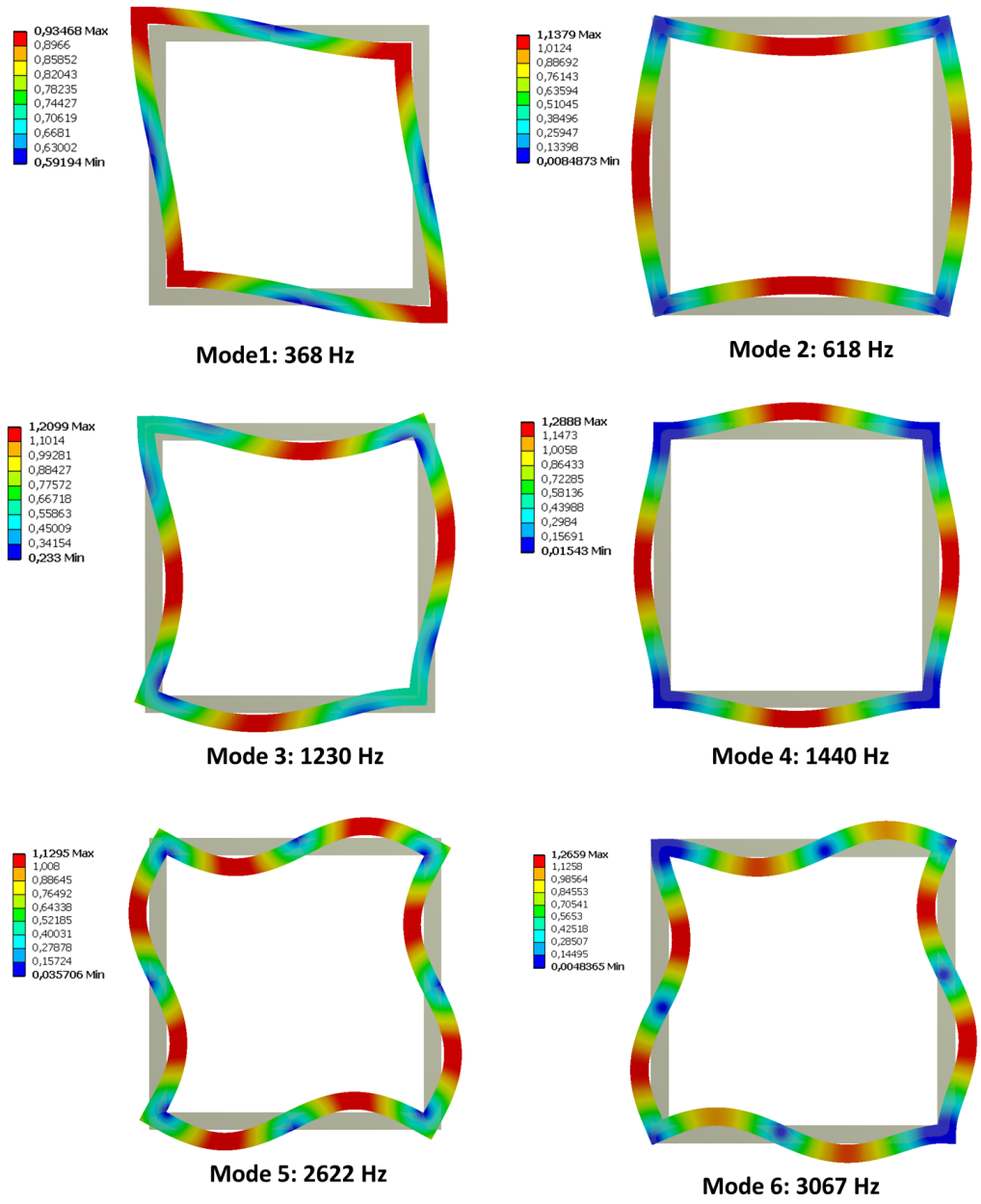

Figure 4.4.2: *Simulated in-plane modes shapes of the ferromagnetic frame in the range [0-3.5] kHz.*

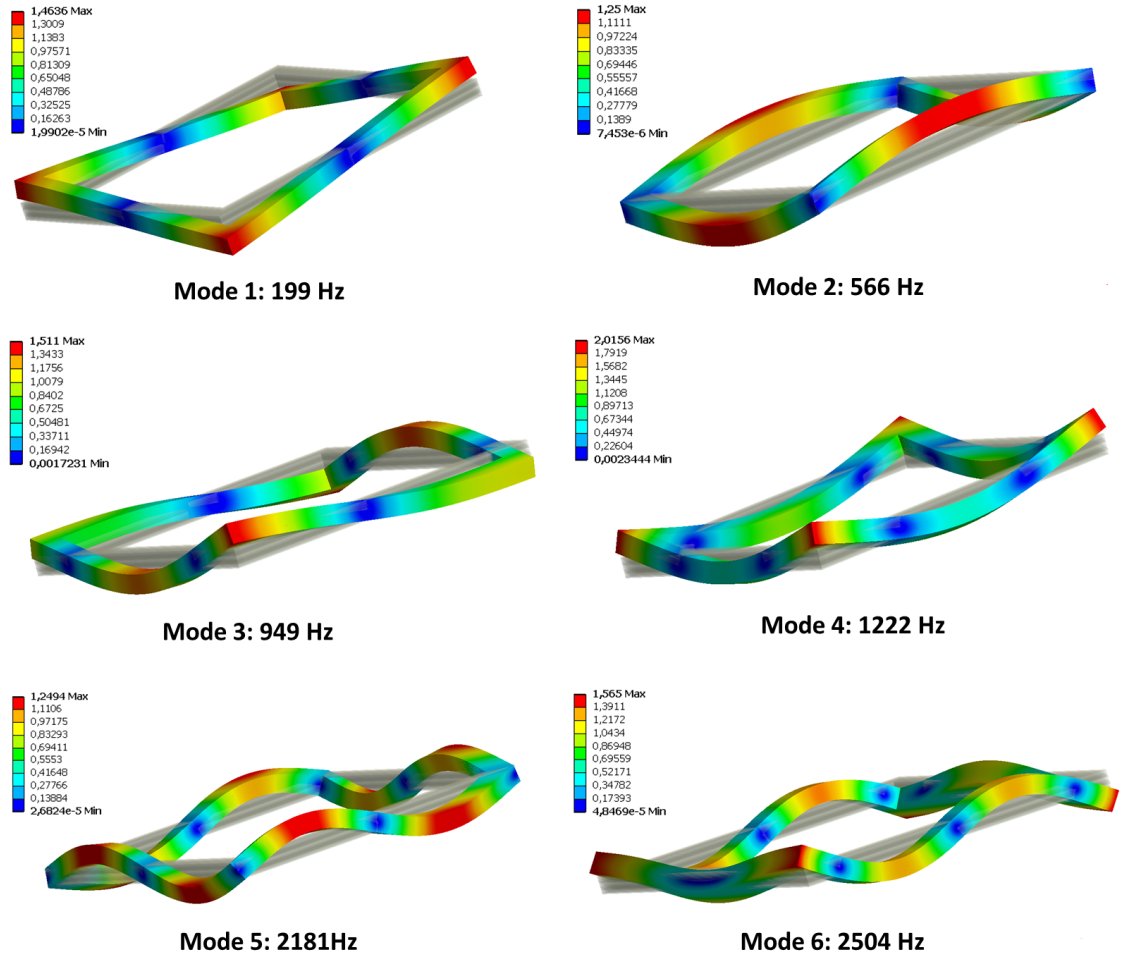

Figure 4.4.3: *Simulated out-of-plane modes shapes of the ferromagnetic frame in the range [0-3.5] kHz.*

Two different experimental setups were used to measure all these modes between 0 and 3.5 kHz.

Transfer function

The transfer function is a mathematical model defining the input-output relationship in the frequency domain of a linear physical system. Figure 4.4.4 shows a block diagram of a single input-output system. System response (output) is caused by system excitation (input). The causal relationship is loosely defined by the equation (4.4.1):

$$H_{ij}(\omega) = \frac{X_i(\omega)}{F_j(\omega)} \tag{4.4.1}$$

where ω is the excitation frequency, $X_i(\omega)$ is the Fourier transform of the response $x_i(t)$ in DOF[1] i, and $F_j(\omega)$ is the Fourier transform of a force $f_i(t)$ acting in DOF number j.

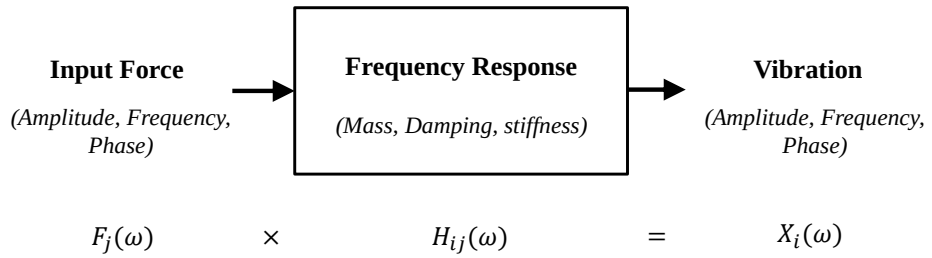

Figure 4.4.4: *Definition of the transfer function.*

An estimation of all mode shapes of the laminated structure can be obtained from only one row or one column of the transfer matrix [H]. A row of transfer functions can be obtained from an experiment by measuring the response in all DOFs, while the point of excitation is fixed to one DOF. To obtain a column of [H], the response is measured in one DOF while the point of excitation is moved between all DOFs. The second procedure is used to obtain all mode shapes for the structure under study.

In-plane modes

To conduct this in-plane measurements, a mono-directional accelerometer and a hammer with an impedance head were employed. The frequency response functions "acceleration over force" were measured on the four sides of the structure plane (see figure 4.4.5). Note that the accelerometer was fixed at the reference point 11, while the hammer moved over 48 points.

[1] Degree Of Freedom

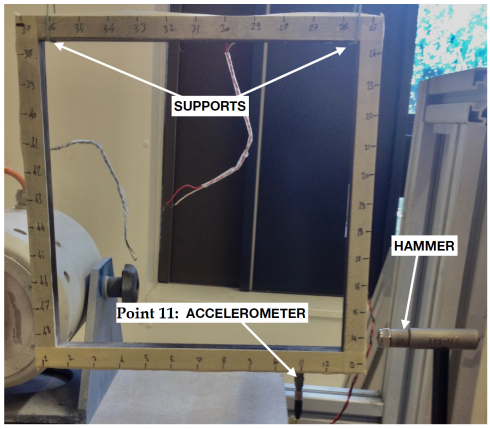

Figure 4.4.5: *Experimental set-up for in-plane modes.*

Out-of-plane modes

The out-of-plane measurements were done with a scanning laser vibrometer (figure 4.4.6 on the left). The excitation force, measured with an impedance head, was applied by a shaker fed with a white noise (figure 4.4.6 on the right). On the other side, the scanning vibrometer measured the acceleration over 1088 points.

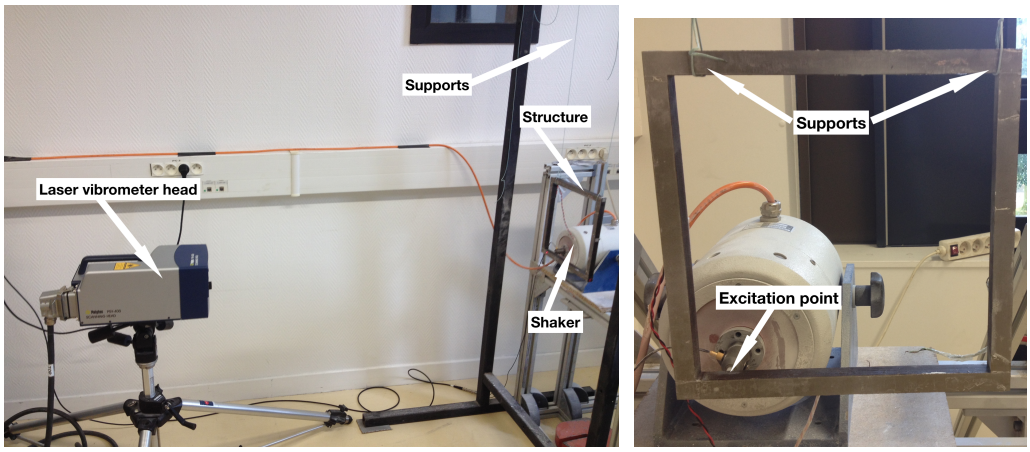

Figure 4.4.6: *Experimental set-up for out-of-plane modes.*

4.4.2.2 Comparison between simulated and experimental results

In figure 4.4.7, the mean Frequency Response Function (FRF) averaged over the 48 points is presented for the in-plane modes. We clearly see six resonant peaks over the studied range (0-3.5 kHz). The corresponding mode shapes are the same as simulation (figure 4.4.8). Similarly, the mean FRF of the out-of-plane experiment presented in

figure 4.4.9 shows also six resonant peaks. The corresponding mode shapes obtained by modal extraction, are shown in figure 4.4.10. Two legs of the ferromagnetic structure have a strange behavior in the modes 3 to 6. One could think that this result is related to measurement noise. However, the same measurements have been done a second time after having rotated the structure a quarter turn, and the same legs exhibit this behavior. We can therefore conclude that the local phenomena observed on these two legs are related to the structure itself. This could be explained by some local detachment of the layers inside the structure.

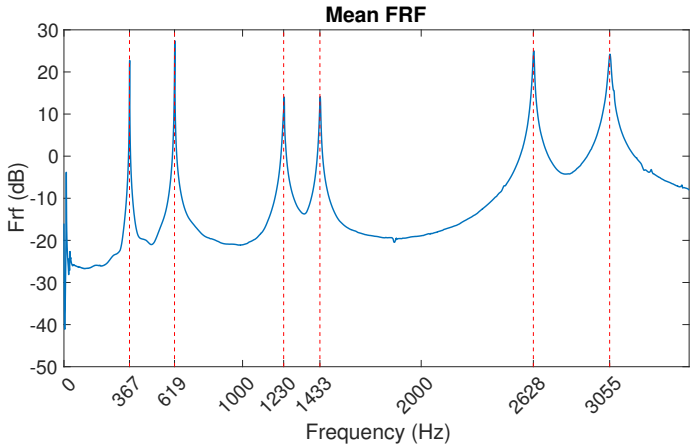

Figure 4.4.7: *Experimental mean FRF (acceleration) for in-plane modes: vertical lines correspond to simulated frequencies (laminated model).*

Figure 4.4.8: *In-plane modes shapes (measured).*

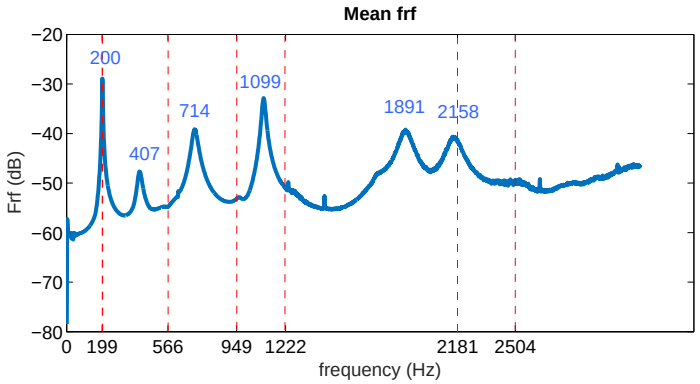

Figure 4.4.9: *Experimental mean FRF for out-of-plane modes: vertical lines correspond to simulated frequencies (laminated model).*

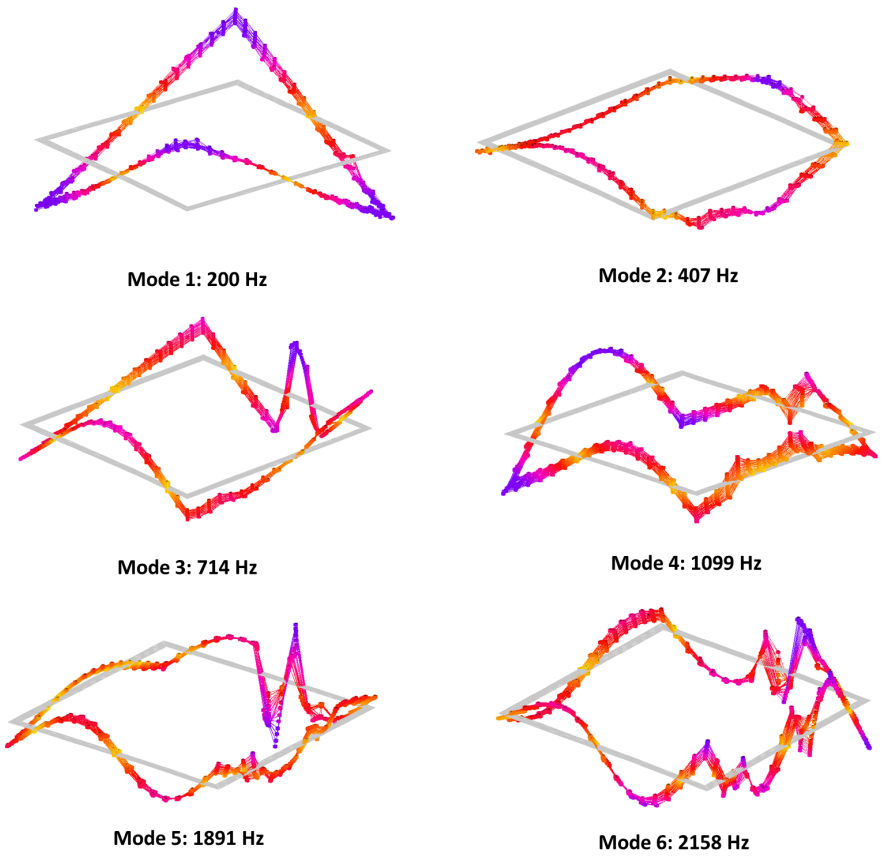

Figure 4.4.10: *Out-of-plane modes shapes (measured).*

Table 4.2 summarizes and gives a comparison between experimental and computed values of natural frequencies for laminated and homogeneous finite-element models. The results show that the natural frequencies of the in-plane vibrational modes obtained from the two models are very similar and all of the predicted modes were obtained with a good frequency accuracy by experiment. Moreover, authors in [116, 12] have shown that the natural frequencies of the in-plane modes are independent of the thickness of the laminations and a homogeneous medium model would be sufficient. For the out-of-plane modes however, except the first mode, the natural frequencies are quite different from simulation but remains acceptable for the laminated finite element model. In reality, the structure sheets assembly is maintained by varnish, this could modify the mechanical properties of the structure (steel + varnish). Structure with inter-laminar slip is much more complicated because of both the mutual elastic effects of adjacent laminations and the presence of varnish between them, which can lead to an increase or a decrease of the resonance frequency [6, 30]. On the other hand, the homogeneous finite-element model exhibits larger eigenfrequencies than those found by experiment

for out-of plane modes. As a result, the frequency dependence on the out-of-plane modes and thus, on the structure thickness should be considered to study the dynamic behavior of a laminated structure.

Thereby, to model the dynamic behavior of a laminated structure, the establishment of a unique model to predict the vibrational behavior can be a challenging task because it depends on many parameters like sliding, friction, clamping and impregnation. Hence, to study the effect of impregnation, a numerical model based on two different homogenization techniques is used. First, the numerical modal analysis is presented. Then, a comparison between the experimental and the numerical modes is discussed.

Modes	Frequency (Hz)		
	Measured	Computed (laminated model)	Computed (homogeneous model)
1	367	370 (0.81%)	366 (-0.27%)
2	619	620 (0.16%)	617 (-0.32%)
3	1230	1230	1228 (-0.16%)
4	1433	1430 (-0.2%)	1432 (-0.07%)
5	2528	2620 (3.6%)	2622 (3.7%)
6	3055	3060 (0.16%)	3061 (0.2%)

(a) *In-plane behavior.*

Modes	Frequency (Hz)		
	Measured	Computed (laminated model)	Computed (homogeneous model)
1	200	199 (-0.5%)	431 (115%)
2	407	566 (39%)	1191 (192.6%)
3	714	949 (37.1%)	1995 (67.3%)
4	1099	1222 (11.2%)	2435 (121.5%)
5	1891	2181 (15.3%)	out of range
6	2158	2504 (16.3%)	out of range

(b) *Out-of-plane behavior.*

Table 4.2: *Comparison between measured and computed eigenfrequencies.*

4.4.3 Numerical model of a homogenized structure

In this part the structure is modeled as a stack of 40 layers of steel separated by 39 layers of varnish perfectly bonded, i.e. with the continuity of the displacements at the interfaces, as shown in figure 4.4.11. Each material is considered as isotropic linear and elastic (table 4.3).

	Steel	Varnish
Young modulus E(GPa)	200	7
Density ρ(kg.m^{-3})	7600	3058
Poisson ratio ν	0.3	0.37
Thickness (mm)	0.35	0.046

Table 4.3: *Material properties of the steel and varnish layers.*

In order to model this multilayered structure with the finite element method using 3D solid elements, the domain has to be discretized with a very refined mesh. Indeed the maximal element size is limited by the thinnest layer thickness, i.e. 46 μm. With this size, more than 70 million elements are required to model the full structure. This is not reasonable. Therefore, instead of modeling all the layers, it is interesting to see if the multi-layer material can be homogenized and represented by an equivalent orthotropic material with E_x=E_y≠E_z and G_{xz}=G_{yz}≠ G_{xy}. To do so we used two different techniques. The first one is purely numerical and the second one is analytical.

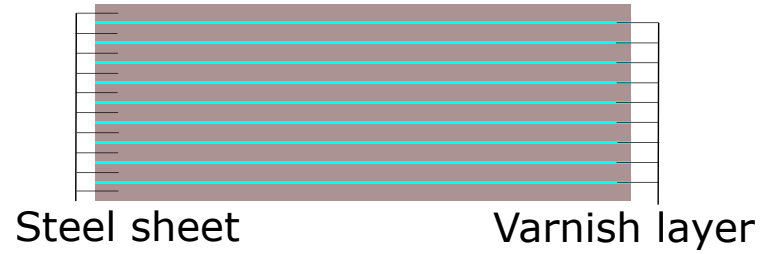

Figure 4.4.11: *laminated model with steel and varnish layers.*

4.4.3.1 Numerical method of homogenization

Here a small section of the frame is considered (L_x= 1 mm, L_y= 0.2 mm, L_z= 15.8 mm). All the layers are modeled with a refined mesh. We assume that all the layers are perfectly bonded together with the continuity of the displacements. The equivalent elastic modulus are then obtained with adapted configurations. For example the Young

modulus along the x-axis is obtained with a tensile test in the X direction. Each test is represented in figure 4.4.12.

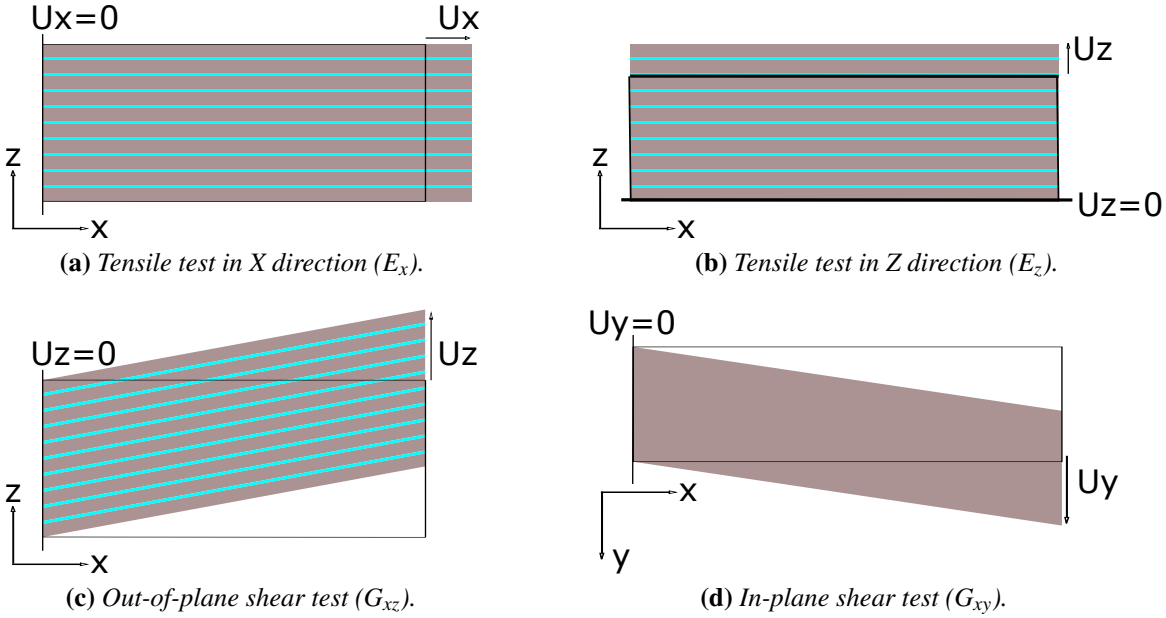

(a) *Tensile test in X direction (E_x).*

(b) *Tensile test in Z direction (E_z).*

(c) *Out-of-plane shear test (G_{xz}).*

(d) *In-plane shear test (G_{xy}).*

Figure 4.4.12: *Numerical tests used to get the equivalent elastic modulus.*

For each test the total strain energy is calculated. Then a homogeneous model is used to estimate the equivalent elastic modulus to have the same strain energy. The results are presented in table 4.4. Finally, the homogenized density ρ, Poisson ratio ν and Young moduli are obtained with a simple rule of mixture.

4.4.3.2 Analytical method of homogenization

Assuming that the Poisson's ratio is defined as the negative of the ratio of the normal strain in the transverse direction ε^T to the normal strain in the longitudinal direction ε^L:

$$\nu = -\frac{\varepsilon^T}{\varepsilon^L} \tag{4.4.2}$$

and the volume fraction of steel and varnish defined by:

$$\mu_V = \frac{V_V}{V} \tag{4.4.3}$$

$$\mu_S = \frac{V_S}{V} \tag{4.4.4}$$

where V is the total volume made of steel volume V_V and varnish volume V_S.

Analytical expressions of the equivalent elastic modulus are given by Juraj Sarlosi *et al.* [102], (S for steel and V for varnish):

$$E_x = E_y = \mu_S E_S + \mu_V E_V \tag{4.4.5}$$

$$E_z = \frac{1}{\frac{\mu_S}{E_S} + \frac{\mu_V}{E_V}} \tag{4.4.6}$$

$$G_{xz} = G_{yz} = \frac{G_S G_V}{\mu_V G_S + \mu_S G_V} \tag{4.4.7}$$

The other mechanical properties are obtained with rules of mixture (mean value) as follows:

$$\rho = \mu_S \rho_S + \mu_V \rho_V \tag{4.4.8}$$

$$\nu = \mu_S \nu_S + \mu_V \nu_V \tag{4.4.9}$$

$$G_{xy} = \mu_S G_S + \mu_V G_V \tag{4.4.10}$$

Results of the homogenization are summed-up in table 4.4.

	Numerical homogenization	Analytical homogenization
E_x(GPa)	177.6	177.6
E_z(GPa)	34.55	23.6
G_{xy}(GPa)	19.2	68.3
G_{xz}(GPa)	22.6	8.7
ν	0.308	0.308
ρ(kg.m^{-3})	7082	7082

Table 4.4: *Equivalent elastic moduli.*

Almost all the estimated equivalent modulus are similar with both methods, except G_{xy} that are significantly different. However, in the following this modulus has no significant effect on natural frequencies (see Table 4.5).

4.4.3.3 Comparison between the two homogenization

The ferromagnetic structure is now modeled as a homogeneous material with the previous equivalent properties. The natural frequencies and modes shapes are calculated with free boundary conditions. The results are presented and compared to the experimental results in table 4.5 (the percentage represents the frequency relative errors).

Modes	Frequency (Hz)		
	Measured	Numerically homogenized	Analytically homogenized
1	367	354 (-3.5%)	380 (3.5%)
2	619	631 (1.9%)	638 (3.1%)
3	1230	1198 (-2.6%)	1271 (3.3%)
4	1433	1330 (-7.2%)	1483 (3.5%)
5	2528	2584 (1.7%)	2707 (3%)
6	3055	2884 (-5.6%)	3160 (3.4%)

(a) *In-plane modes.*

Modes	Frequency (Hz)		
	Measured	Numerically homogenized	Analytically homogenized
1	200	197 (-1.5%)	179 (10.5%)
2	407	641 (57.5%)	625 (53.6%)
3	714	1057 (48%)	1012 (41.7%)
4	1099	1377 (31.6%)	1338 (28.2%)
5	1891	2746 (45.2%)	2544 (34.5%)
6	2158	3630 (68.2%)	3303 (53.1%)

(b) *Out-of-plane modes.*

Table 4.5: *Comparison between measurements, numerically and analytically homogenized models.*

First of all, the tendencies are similar with both homogenized set of parameters. Then, calculations match very accurately the experiment for in-plane modes. Besides, the cal-

culations give an accurate estimation for the first out-of-plane mode. However for higher out-of-plane modes the relative differences between measurements and calculations are important. These differences could be explained by some detachments between the layers, as mentioned previously. These local phenomena inside the structure could indeed reduce the stiffness of the structure and decrease the experimental natural frequencies for the modes that present a flexural behavior near the detachments.

The laminated structure model response was close to the experimental one. Despite, some differences for out of plane modes, the results of simulated modal analysis and the experimental measurements have shown a good agreement. Next, a numerical modal analysis has been presented and compared to experimental results. In the next section, magnetostriction induced resonance will be studied for the found modes.

4.5 Magnetization part: magnetostriction induced resonance

4.5.1 Magnetizing at resonance procedure

Figure 4.5.1 shows the experimental set-up used to study the influence of magnetizing frequency on the ferromagnetic structure displacement. The waveform and the amplitude of the current are adjusted by means of a signal generator which is connected to a power amplifier. Then, the current signal flows to the excitation coil of the ferromagnetic structure and a magnetic field is established, which in turn causes magnetostrictive strain in the stacked sheets. A differential and a current probes were used to monitor the voltage and the current respectively as the frequency increases. The laser interferometric vibrometer has the ability to measure magnetostriction deformation at low excitation [43], it can measure displacement up to a resolution of 0.1 nm. If we consider the dimension of the ferromagnetic structure, this corresponds to a strain resolution of 0.4 nm/m and a measurable frequency range of 0-3 MHz, which is largely enough for the displacement measurement in this manipulation.

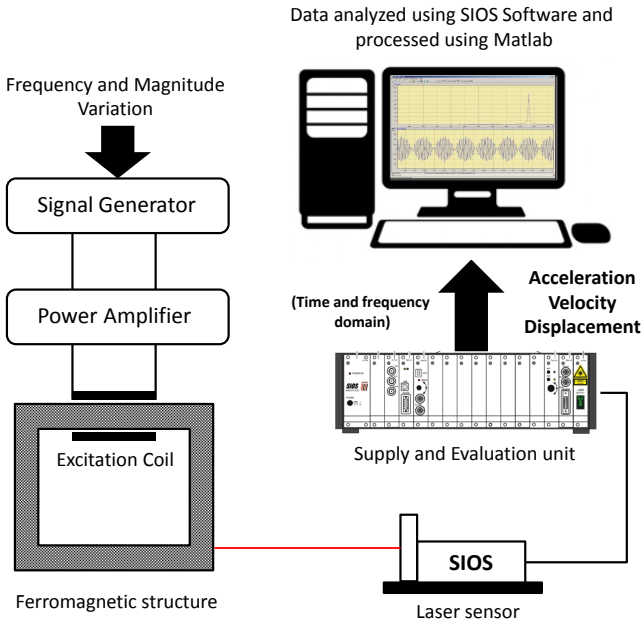

Figure 4.5.1: *A schematic diagram of the displacement measurement due to magnetostriction and magnetizing system.*

The ferromagnetic structure was magnetized under a maximum magnetic excitation of H = 35 A/m. Low current excitation is used since it is necessary to proceed in iso-excitation (same amplitude) for the studied frequency range. Furthermore, the interest is also to prove that the mechanical resonance due to magnetostriction can take place at low amplitudes of magnetic field.

4.5.2 Mechanical resonance excited by magnetostriction

The ferromagnetic structure can resonate at many frequencies with different modes shapes as it has been shown previously. Furthermore, a mechanical resonance can take place only if the force distribution of magnetostrictive strain and the structure mode shape are consistent in terms of spatial order and frequency. In the same way, to observe resonance that can be excited by magnetization, a frequency sweep of current is applied to the coil terminals producing a magnetic field in the ferromagnetic structure and a strain corresponding to magnetostriction strain appears. Pictures of the displacement measurements environment are shown in figure 4.5.2.

To illustrate the mechanical resonance induced by magnetostrictive strain, we selected the following vibration modes (see table 4.5):

- Modes 1, 2, 3 and 4 for in-plane modes.

- Modes 1, 3 and 4 for out-of-plane modes.

It is known that magnetostriction $\lambda = \frac{\Delta L}{L}$ occurs mainly at twice the excitation frequency f [32, 88]. Hence, for instance, in order to magnetically excite a mechanical resonance frequency of 1430 Hz (in-plane mode number 4), the magnetizing frequency has to be equal to 715 Hz. To do so, we will perform a magnetic frequency sweep below and above the resonant frequency, and the evolution of the response of the ferromagnetic structure displacement will be measured instantaneously.

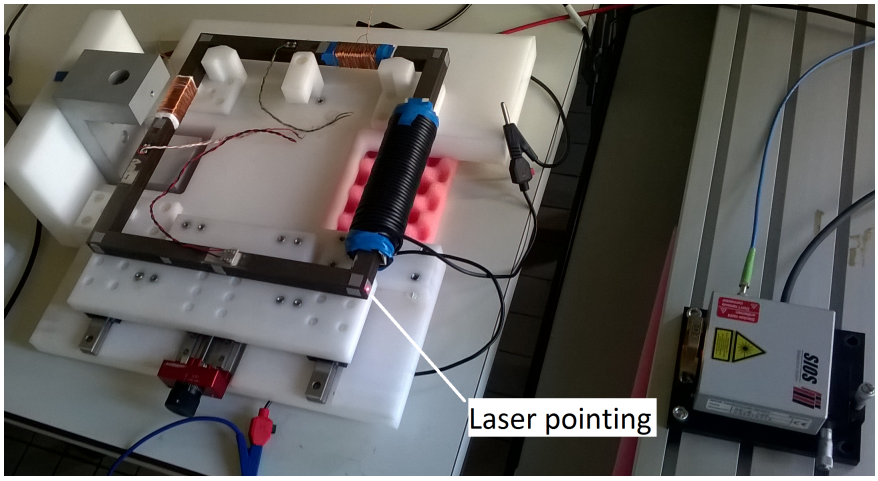

(a) *In-plane displacement measurements*

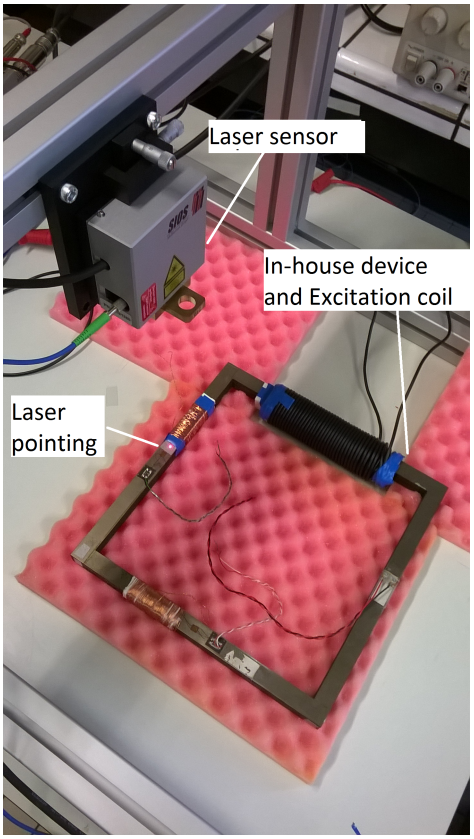

(b) *Out-of plane displacement measurements.*

Figure 4.5.2: *Measurements of displacements due to mechanical resonance by laser vibrometer.*

Figure 4.5.3 shows the results for the in-plane modes. We notice that peak-to-peak displacement at the resonance makes a significant increase. Moreover, the displacement at resonance varies from 2.3 to 14 times the displacement due just to magnetostriction (out of resonance). Due to resonance, at 394 Hz, the displacement is increased by a factor of 200 %, by 120 % for 640 Hz, 200% for 1250 Hz and 1300% for 1430 Hz. As shown in figure 4.5.3d, the so-called "breathing mode" (1430 Hz) is the most important in term of displacement.

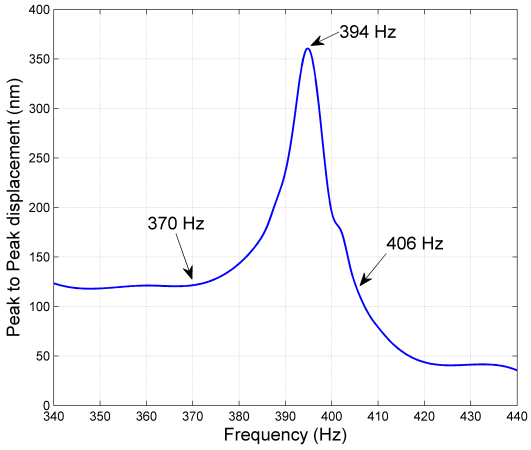

(a) *Mode 1: 394 Hz.*

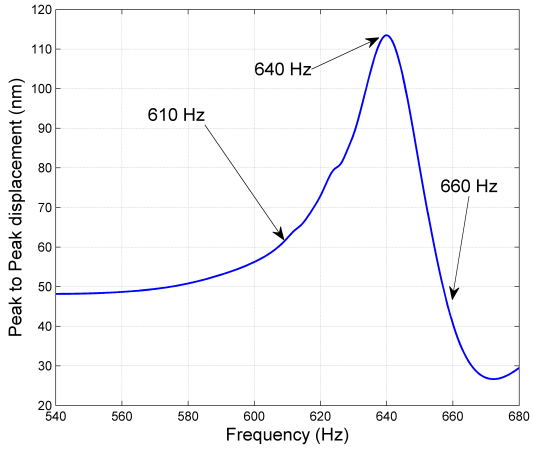

(b) *Mode 2: 640 Hz.*

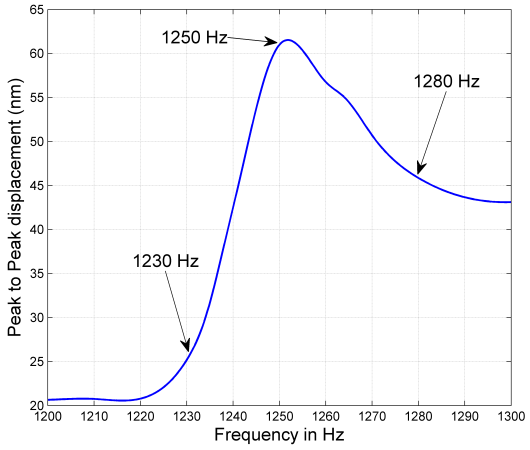

(c) *Mode 3: 1231 Hz.*

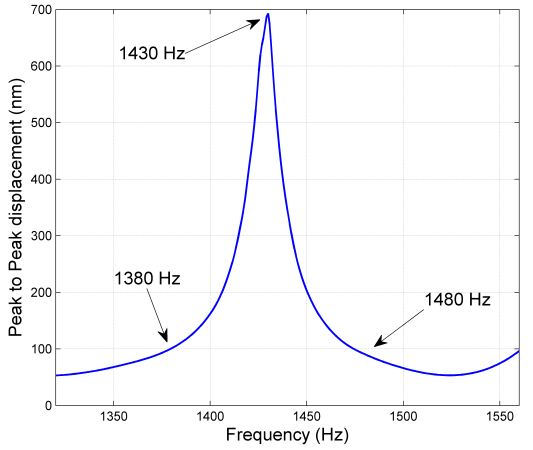

(d) *Mode 4: 1430 Hz.*

Figure 4.5.3: *In-plane behavior: displacement as a function of magnetizing frequency of the ferromagnetic frame (3% Si-Fe).*

Figure 4.5.4 illustrates the resonance peak displacement of the out-of-plane modes. As explained in the mechanical part, the simulated out-of-plane vibrational modes are different from the experimental one due to local phenomena (detachments of the layers inside the structure). For the chosen out of plane modes, the resonance occurs at the experimental natural frequencies. It can be seen that natural frequencies are slightly shifted of a few hertz, this is assumed to be due to boundary conditions (horizontal position of the ferromagnetic frame). As expected, the results presented in figure 4.5.4, confirm the mechanical resonance of the ferromagnetic structure in the out-of-plane direction. The peak displacement at resonance is notably significant, it has been increased by 263% for 215 Hz, by 533% for 780 Hz and by 214% for 1096 Hz.

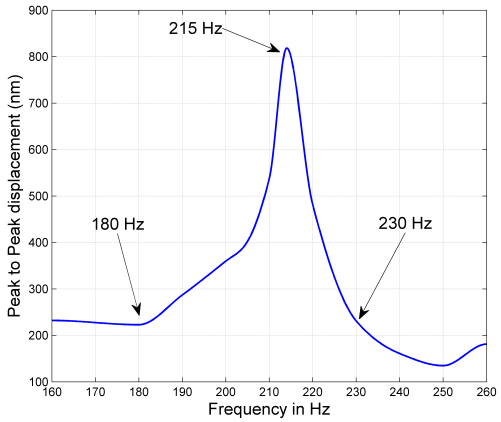

(a) *Mode 1: 215 Hz.*

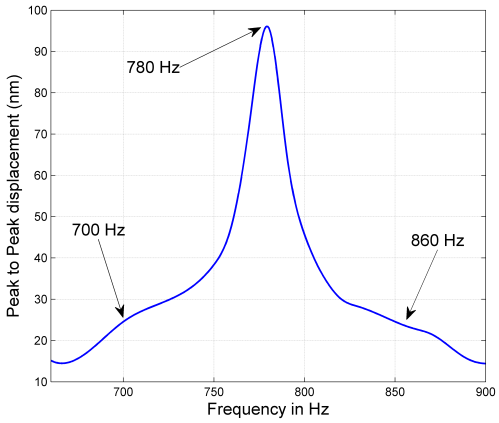

(b) *Mode 3: 780 Hz.*

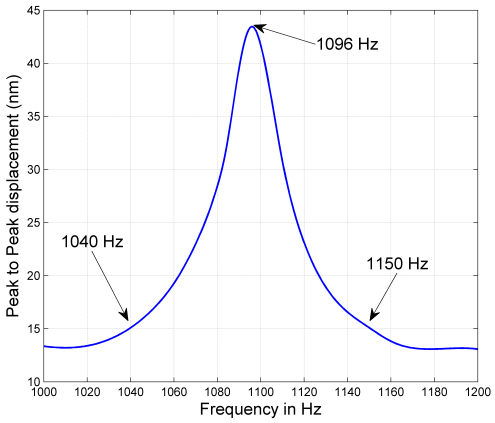

(c) *Mode 4: 1096 Hz*

Figure 4.5.4: *Out-of-plane behavior: Displacement as a function of magnetizing frequency of the ferromagnetic frame (3% Si-Fe).*

Figure 4.5.5 and figure 4.5.6 shows the peak amplitude of displacement spectrum below, at and above the resonance frequency for the in-plane and out-of-plane modes respectively. Likewise, the Fourier analysis confirms the same finding: at mechanical resonance, the spectrum line corresponding to resonance frequency tends to be very pronounced due to magnetostriction deformation generated in the ferromagnetic structure. Since the structure is excited with $f_{excitation} = \frac{f_{resonance}}{2}$, in some spectrum (figure 4.5.5a), we can clearly see the magnetizing frequency.

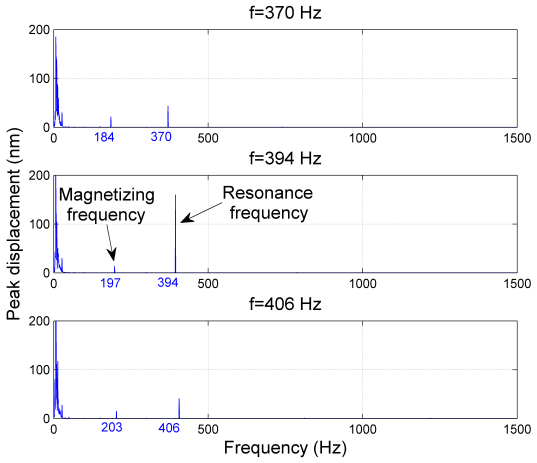

(a) *Resonance frequency: 394 Hz*

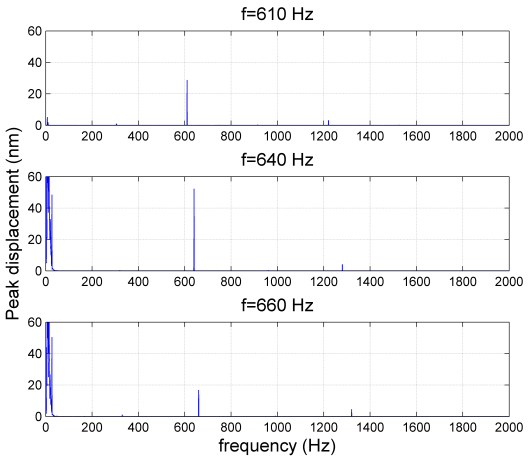

(b) *Resonance frequency: 640 Hz*

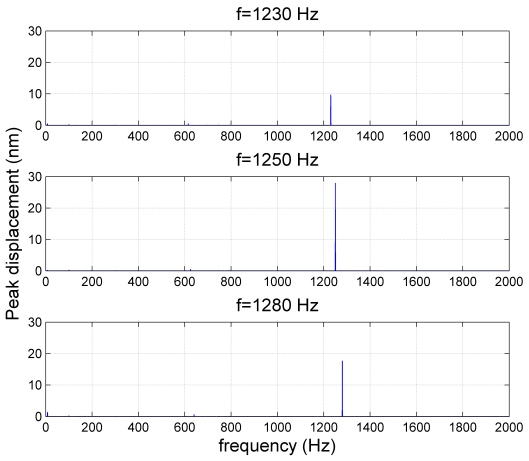

(c) *Resonance frequency: 1231 Hz*

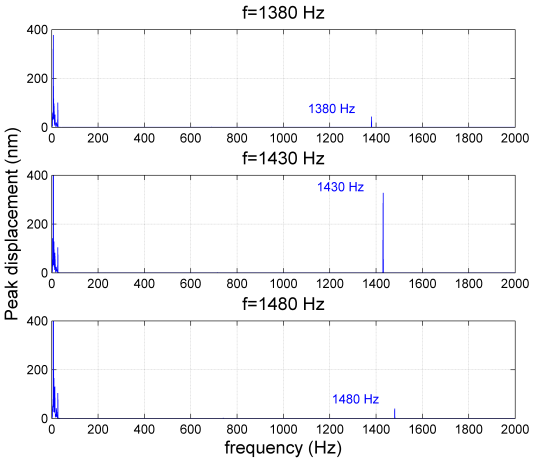

(d) *Resonance frequency: 1430 Hz*

Figure 4.5.5: *In-plane behavior: The spectrum of the displacement of the ferromagnetic frame below, at and above the resonance*

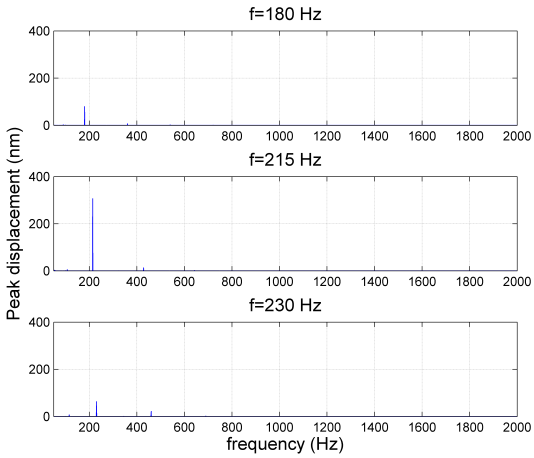

(a) *Resonance frequency: 215 Hz.*

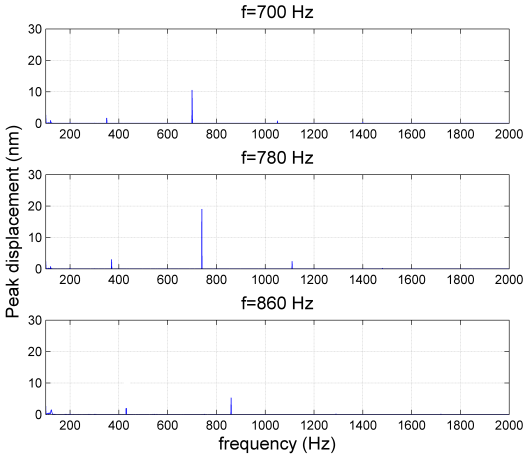

(b) *Resonance frequency: 780 Hz.*

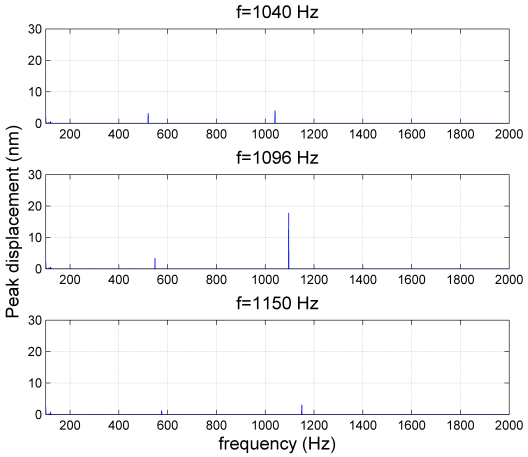

(c) *Resonance frequency: 1096 Hz.*

Figure 4.5.6: *Out-of-plane behavior: The spectrum of the displacement of the ferromagnetic frame below, at and above the resonance.*

4.6 Conclusion

This chapter has presented an investigation on mechanical resonance excited by magnetostrictive strain in an impregnated laminated structure, with an assembly without any lap joints or air gaps. The displacements of the structure due to resonance were measured by using the laser vibrometer, allowing measurements of the nanometer scale. The Finite Element results showed good agreement with the experiment in terms of eigenfrequencies and modes shapes for the in-plane modes shapes. Whereas, some differences

have been noticed for the out-of plane modes due to local phenomena (detachment of the layers inside the structure) leading to a lack of accuracy in calculating the eigen modes. To face this issue, a numerical homogenization has been proposed. Despite that, the differences between experiment and calculation last for higher out-of-plane modes that present flexural behavior near the detachments. The main conclusions are recalled hereafter:

1. Despite some frequency differences in out-of-plane modes, the experimental and the simulated laminated model have shown similar results. Nevertheless, the proposed homogenized model could not properly model the out-of-plane behavior, neither by numerical nor analytical methods, although the two methods have shown good agreement between them. More investigation is needed to understand these differences.

2. The increase of peak to peak displacement of the ferromagnetic structure at resonance is due to deformation of magnetostriction, for in-plane and out-of-plane directions.

3. The study reveals that magnetostriction alone is likely to excite all the resonances of the ferromagnetic structure when the frequency of magnetostriction excitation is consistent with a natural frequency of the ferromagnetic structure without necessarily knowing the spatial distribution of this deformation.

4. Resonance occurs even at very low excitation amplitude. Hence, the presence of harmonics (e.g. non linearity of the material, pulse width modulation (PWM) excitation) even with small amplitude of the magnetizing field can induce resonance at frequencies far from the fundamental frequency. It is necessary to consider their influence on magnetostriction deformation.

CONCLUSION AND PERSPECTIVES

General conclusions

Magnetostrictive materials provide a conversion of electromagnetic energy into mechanical energy. These materials see also their magnetic state influenced by mechanical stress, so they can be used in many mechatronic or electrical devices such as: actuators, sensors, transformers, energy harvesting systems and many other applications. The choice of these materials, the control of their behavior and their integration in devices requires not only a knowledge of their properties of use, but an understanding of their evolution under different types of solicitations: stress effect, frequency effect, type of excitation and so on. This thesis work was an opportunity to provide an answer to these scientific and technological issues. The work focuses on the study of magnetostriction in non-oriented Si-Fe alloy materials used for transformer application in a perspective of reducing vibration and noise.

The ultimate goal of the work presented here is to study magnetostriction phenomenon from two points of view: material (electrical steel) and device (laminated structure). Besides, an interaction between modeling and experimental approach has been conducted as well on two scales (material and device). In this respect, this thesis work offers a more complete study regarding existing works and made the link between the material and the device in term of behavior.

In the *first chapter* a state of the art was presented describing the magnetic and magnetostrictive behavior of ferromagnetic materials by making the connection between their micro structure and their response at the macroscopic scale with an emphasizes of the stress effect on these behaviors. It was noticed that these magneto-elastic effects are complicated and depend on several parameters. It has also been found that their modeling has been the subject of several studies with different approaches whose most used are phenomenological and multi-scale approaches.

Next, in the *second chapter*, after detailing the measurement procedures, an experimental characterization under uni-axial mechanical stress of magnetic and magnetostrictive behavior of Si-Fe material was presented. In addition to the stress, to study the anisotropy effect, 10 samples cut in several directions were used. These measurements have made it possible to identify the magneto-elastic response of the materials

in terms of magnetic induction and magnetostrictive deformation. The results obtained showed a strong dependence of the magnetic and magnetostrictive properties on mechanical stress. Also, the evolution of these properties also depends on the direction of the samples highlighting the anisotropy of the behavior even under mechanical stress. Furthermore, measurement results under stress and with two distinct excitation frequencies have highlighted the coupled effect of frequency and stress on magnetostrictive deformation.

At the end of this characterization, we created a rich experimental base allowing an identification of the model parameters and an in-depth confrontation with the modeling. The existing model based on an energetic, macroscopic and anisotropic approach has been improved and extended to take into account the effect of mechanical loading on magnetic and magnetostrictive properties. The modeling results showed a good agreement with those of the measurements for most of the studied directions. The main limitations of this modeling approach remain the large number of parameters and the bad restitution under large value compressive stress. It seems necessary to look into the optimization of certain energy terms and especially those related to the anisotropy and demagnetizing field because they control respectively the influence of the anisotropy and the stress effect magnetically speaking.

The *third chapter* had for ambition to study a laminated structure without and with air gaps respectively assembled with the previously characterized material. This approach going from the material to a device approaching a transformer structure is one of the strong points of this PhD work.

First of all, a simple laminated structure of square form was designed so that only magnetostriction takes place (without the magnetic forces). Magnetic and magnetostrictive measurements under two types of excitation (current and imposed voltage) and without applied stress have shown that the magnetostriction deformation obtained in both cases remains unchanged. These measurement results performed so far by strain gauges were compared to those obtained by the laser vibrometer and similar orders of magnetostriction magnitude were observed. The laser technique is a new measurement technique used in this thesis that allowed making measurements which could not be possible with the strain gauge. Namely, measurements along the height of the structure laminations which revealed that the deformation was not uniform throughout the lamination and could induce an increase in the magnetostrictive deformation when using non-oriented grain materials to manufacture transformer core. Next, the finite element calculation tool has been validated on a structure similar to the real one. The FE results showed a good match on the transverse direction but were not satisfying for the rolling direction. On the latter we found a larger deformation in experimentation than in the finite elements calculations. This is due to the random assembly of the structure and can be explained by the presence of TD sheets among the RD ones, which leads to higher deformation compared to the only RD sheets case. Then, a characterization under uni-

axial mechanical compressive stress was presented. The results of these measurements showed a significant increase in magnetostriction deformation and a degradation of the magnetic properties in the structure, hence, care must be taken about the importance of transformer assembly to avoid more noise and vibration.

A second structure including this time air gaps was set up to study the contribution of Maxwell forces and the magnetostriction to the total displacement of the structure. It was observed that the two phenomena can interact and interfere in an opposite way, and can even lead to a cancellation the total displacement with good control of the air gap material (Young modulus). The FE method which took into account just the magnetostrictive deformation was expanded to consider Maxwell forces as well. Also, an analytical calculation has been developed to quantify the total displacement of Maxwell's forces and magnetostriction. The results showed good agreement between them. On the other hand, the measurement results showed a partial agreement. Further steps in this direction should be considered later to conclude.

Staying in this vision of reducing noise and vibration caused by magnetostriction, in the *last chapter*, we established that the mechanical resonance induced by magnetostrictive strain in a laminated structure (e.g. transformer core) can have a significant influence on the magnitude of structure vibrations and, consequently, on the acoustic noise generated. Firstly, the vibration eigen modes were calculated by the FE method with a 3D model to obtain in-plane and out-of-plane modes. The results of simulation were validated by an experimental modal analysis (EMA) on the laminated structure. The in-plane modes have shown a good agreement between modeling and experiment, however, out-of-plane modes showed some differences. To address this problem, a numerical homogenization method has been proposed, despite that, the matching with experiment still not satisfying. These differences could be explained by some detachments between the layers observed in experiment. Secondly, the results showed that the structure would likely to resonate due to magnetostriction if magnetized at resonance frequencies implying excessive vibrations. Even worse, if harmonics are predominant in the magnetizing signal or a Pulse width modulation excitation (PWM) used in inverter, this may further increase the presence of resonance and hence high vibrations. Consequently, more care should be taken in such cases to control or avoid the phenomenon.

Prospects for future work

The contribution to the study of the magnetostriction phenomenon brought by this thesis work remains modest and incomplete, and needs to be further enriched. Given the limitations expressed by the simulation and experimentation results, extensions for our work can be found in the paragraphs that follow.

The model in its current configuration is limited to anhysteretic description of the magnetic and magnetostrictive behaviors. This limitation prevents its description of the

hysteresis phenomena, strongly present in the behavior of ferromagnetic materials. This can be interesting to estimate hysteresis losses in electrical machines. The use of the Sablik-Jiles-Atherton (SJA) model from the obtained anhysteretic curves is a possible solution. The question is whether it is easily integrated into our model or not.

Considering the stress effect coupled with anisotropy in the model has shown its limits. The current configuration of energy terms does not allow a satisfactory reproduction especially under compressive stress. An improvement of the energy terms, in particular, that of anisotropy is to be expected. It would be necessary also to consider a state of multi-axial stress; it would make the model more complete.

Also, it would be interesting to incorporate the model including the stress effect in the finite element tool and validate the results by comparing them with the measurements. The next step could be to enhance the finite element tool to predict acoustic emissions in order to conclude on the parameters influencing acoustic noise in electrical devices.

For experimental aspects, it seems essential to develop a device to apply a uni-axial and multi-axial stress on single sheet to target a wide range of electrical device applications. For larger structures, the limited tools of applying stress should be disregarded and more suitable applying stress devices must be considered, allowing the applied forces to be controlled precisely.

Measurements of the magnetostrictive deformation by the laser vibrometer are interesting but the setting up and the repetitive manipulation are time consuming. Moreover, vibrations of low frequencies appear probably due to building movement, making the measurements at low frequencies not possible. One of the solutions could be to develop a setup allowing an easy manipulation of the laser head for a quicker adjustment and a more adapted environment for making measurements by laser vibrometer (anti-vibration table or others). Also, in order to obtain more accurate magnetostrictive characterizations under mechanical stress, the laser vibrometer has a great potential for it. Provided, developing a setup adapted to overcome the difficulties related to accessibility, implementation and acquisition.

Appendix

APPENDIX A

CALIBRATION OF H-COIL AND B-COIL SENSORS

The calibration of the sensors consists of an estimation of their real cross section. To do so, we place our sensors inside a solenoid which has a uniform magnetic field, and then we measure the induced voltage of H-coil or B-coil.

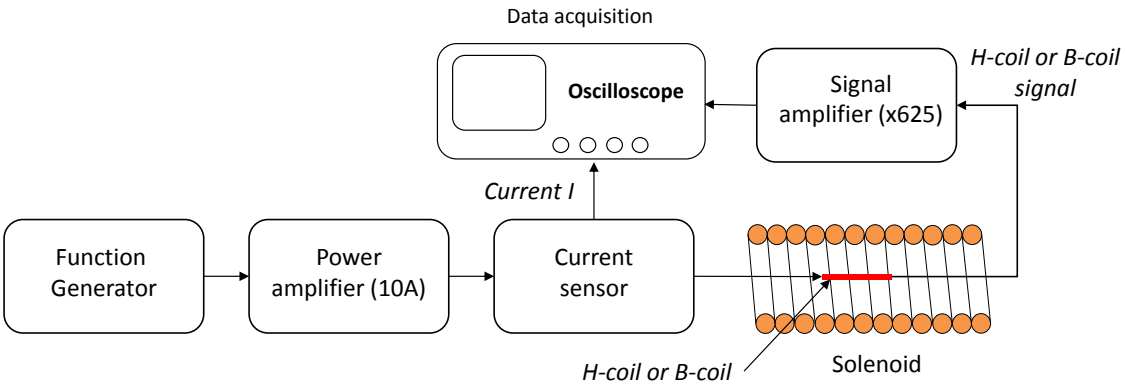

Figure A.1: *Description of the calibration procedure of sensors.*

A calibration procedure is executed using a 761 turns solenoid with a length of 542 mm and a diameter of 64 mm, as illustrated in figure A.1. At one end of the solenoid whose length is large compared to its radius, the magnetic field strength is given by:

$$H_s = \frac{N_s.I_s}{L_s} \tag{A.0.1}$$

- N_s : Number of turns of the solenoid

- L_s : The length of the solenoid
- I_s : The excitation current in the solenoid

The induced voltage between the sensors terminals is described by applying Lens's law:

$$V_{induced}(t) = N_{H/B-coil}.\mu_0.S_{H/B-coil}.\frac{dH_s}{dt} \tag{A.0.2}$$

- $N_{H/B-coil}$:The number of turns of the H-coil or B-coil
- μ_0 :The vacuum permeability
- $S_{H/B-coil}$:The desired section of the H-coil or B-coil

In the alternative regime, the current is linked to the induced voltage by:

$$\hat{V}_{induced} = N_{H/B-coil}.\mu_0.S_{H/B-coil}.\frac{N_s.\hat{I}_s}{L_s}.2\pi f \tag{A.0.3}$$

In table A.1 we summarize the numerical values of the parameters needed for the calculation of sensors sections:

Description	Value
N_s	761
L_s	0.562 m
N_{H-coil}, N_{B-coil}	100, 80
μ_0	$4\pi.10^{-7}H.m^{-1}$
f	50, 200, 500, 1000 Hz
I_{max}	0.5 A

Table A.1: *Numerical values of parameters used for calibration*

For each frequency we calculated the sections of sensors. As the induced voltage of the H-coil is very small, it has been amplified by a factor of 625 during the experiment. Each measurement was carried out 3 times to confirm the repeatability principal (A.1) and the average is taken (table A.2).

Frequency	S_{B-coil}(m²)	S_{H-coil}(m²)
50	2.811×10^{-4}	1.758×10^{-5}
200	2.903×10^{-4}	1.744×10^{-5}
500	2.826×10^{-4}	1.756×10^{-5}
1000	2.886×10^{-4}	1.440×10^{-5}

Table A.2: *The average section sensors measurement depending on frequency*

The sections of the sensors that will be taken for magnetic measurement are the following:

$$\begin{cases} S_{B-coil} = 2.85 \times 10^{-4} m^2 \\ S_{H-coil} = 1.75 \times 10^{-5} m^2 \end{cases} \tag{A.0.4}$$

These values correspond to the averaged values of the calculated cross section of the sensors independently of the frequency.

A.1 Evaluation of the uncertainties on H-coil and B-coil sections with the student law

As every measurement is prone to error, it is often stated that a measurement result is complete only when accompanied by a quantitative statement of its uncertainty. This uncertainty assessment is required in order to decide if the result is adequate for its intended purpose and to ascertain if it is consistent with other similar or previous results.

Here, we aim to estimate the section of coil sensors (H-coil and B-coil) from 3 tests (measurements for section calibration), as this number is small, **Student's t-distribution** is a good approach to construct confidence interval, which will enable us to say how confident we are that a given range would contain the true mean value of section.

Let n be the number of tests for section calibration that give us a value of section X_i and S^2 the variance.

The mean value on section calibration is :

$$\bar{X} = \frac{1}{n}\sum_{i=1}^{n} X_i \tag{A.1.1}$$

And the variance is written:

$$S^2 = \frac{1}{n-1}\sum_{i=1}^{n} (X_i - \bar{X})^2 \tag{A.1.2}$$

The confidence interval CI for the mean value of coil sensor section at a confidence level of $1-\alpha$ is given by:

$$CI_{1-\alpha} = [\bar{X} - t_\alpha . \frac{S}{\sqrt{n}} ; \bar{X} + t_\alpha . \frac{S}{\sqrt{n}}] \tag{A.1.3}$$

t_α is a correction coefficient extracted from Student table depending on degree of freedom $\nu = n-1$.

For the calibration made to find the coil sensors section, the uncertainties are given in the figures A.1-A.2 for a number of test $n = 3$ and two confidence levels $1-\alpha = 0.95\,(95\%)$ and $0.99\,(99\%)$. The calibration was made for frequencies: 50, 200, 500 and 1000 Hz.

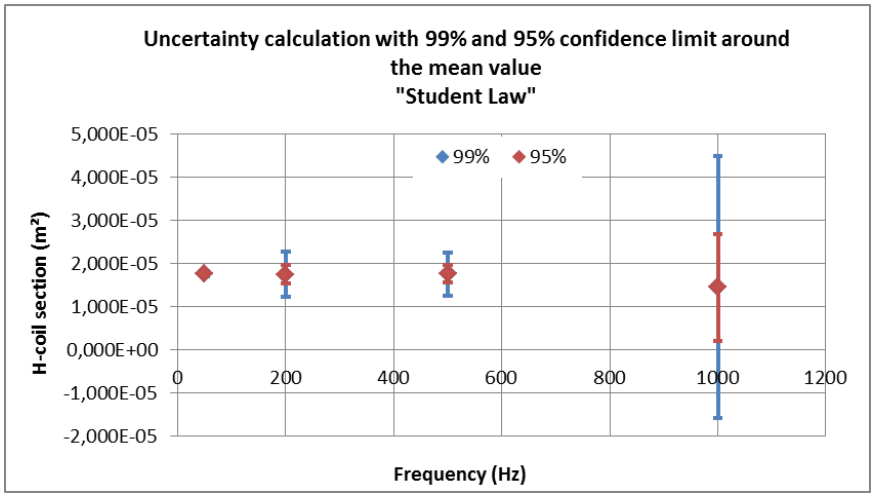

Figure A.1: *Uncertainty on H-coil sensor.*

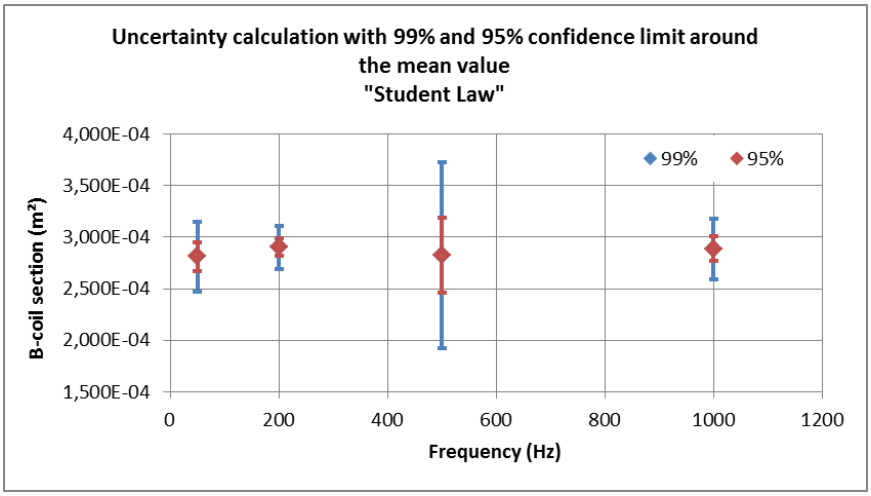

Figure A.2: *Uncertainty on B-coil sensor.*

A.2 H-coil and ampere's law comparison

After the calibration was carried out on the H-coil, the real section has been determined ($S_{H-coil} = 1.75\,10^{-5} m^2$). Next, the measurements of the magnetic field strength by H-coil (tangential component) will be compared to the measurements by ampere's law. The results of this comparison is shown in figure A.1. We remind that the H-coil was made of 100 turns. It can be observed that the magnetic field strength is almost the same for low and medium field, however, at high field strength the difference is significant. This difference can be explained by the magnetic field lines leakage, which correspond to a important quantity of the magnetic field according to the results of figure A.1. Hence, for the estimation of the magnetic field, we will use the ampere law.

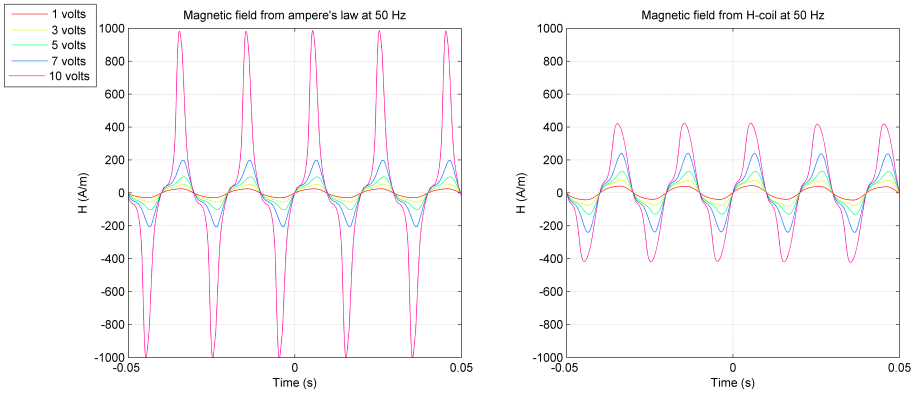

Figure A.1: *Comparison of the magnetic field measured by H-coil (a) and by ampere's law (b).*

APPENDIX B

FITTED AND MEASURED MAGNETOSTRICTION DEFORMATION FOR OTHERS DIRECTIONS

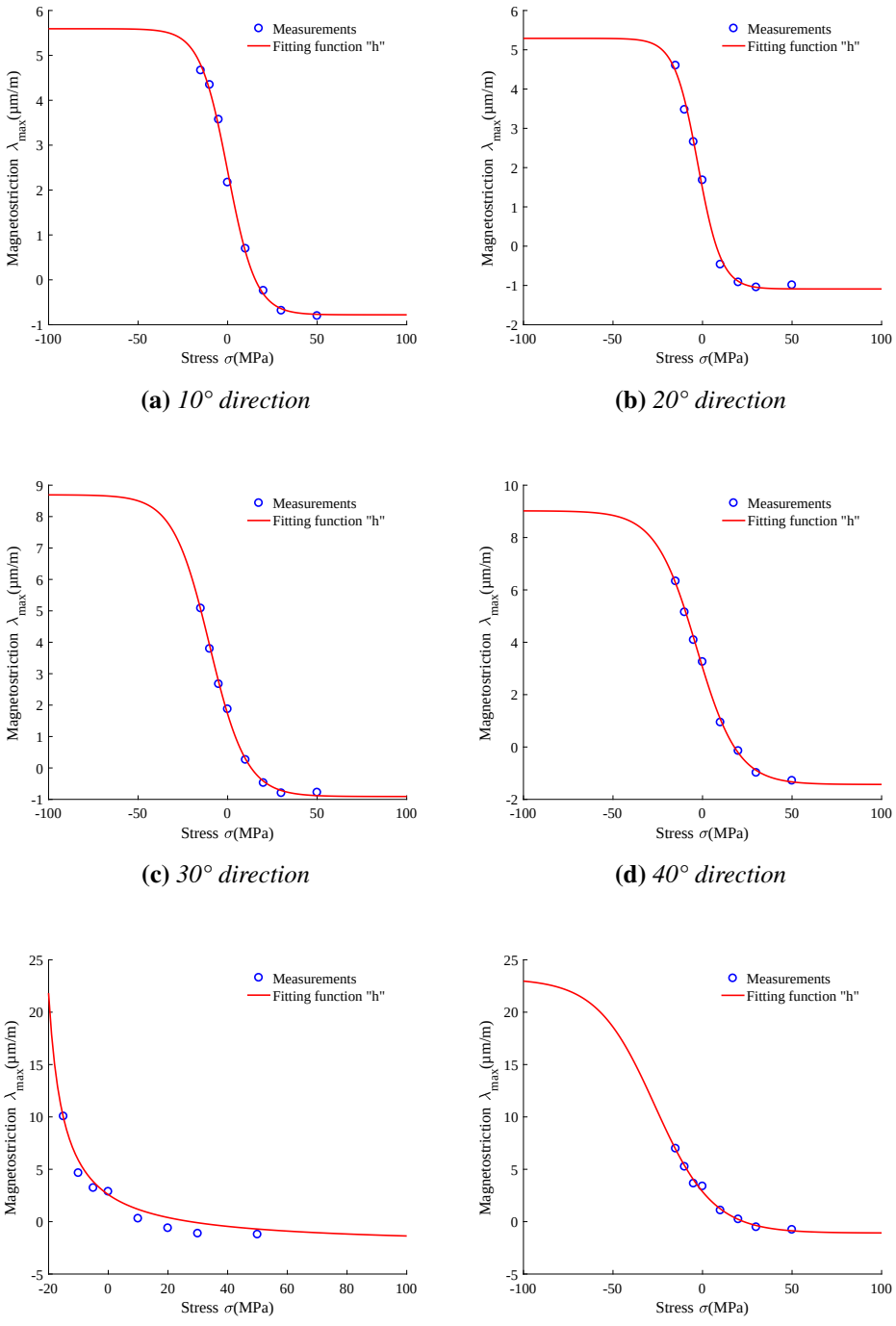

(a) *10° direction* **(b)** *20° direction*

(c) *30° direction* **(d)** *40° direction*

(e) *60° direction* **(f)** *80° direction*

Figure B.1: *Comparison between fitted and measured magnetostriction deformation for direction of cut:* 10°, 20°, 30°, 40°, 60°, 80°

APPENDIX C

OVERALL DRAWING OF THE CLAMPING DEVICE

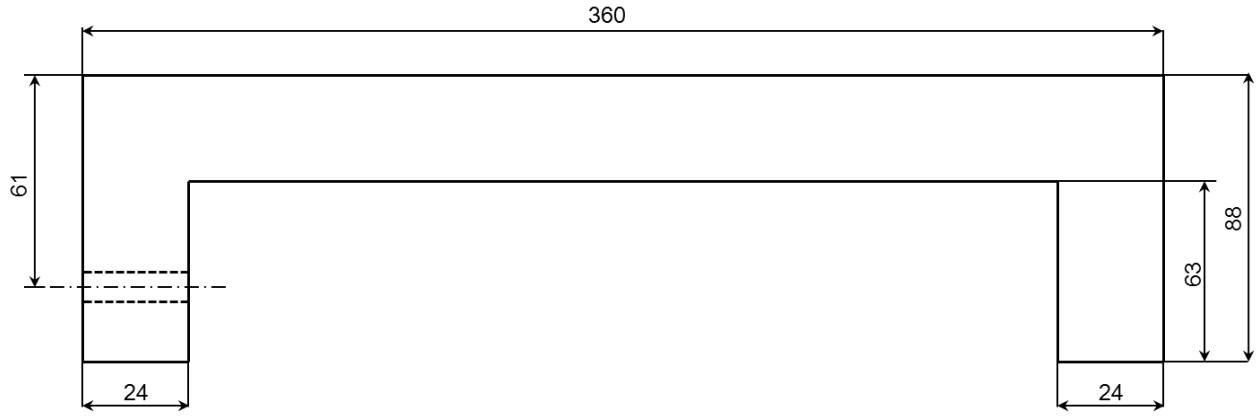

(a) *Front view*

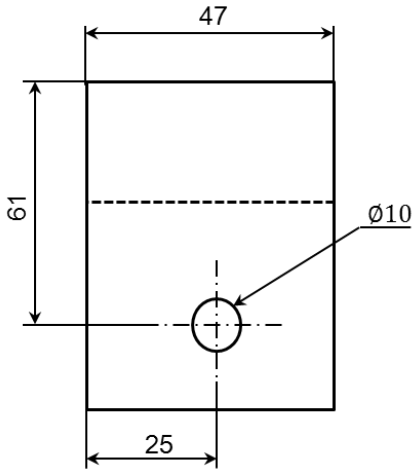

(b) *Left view*

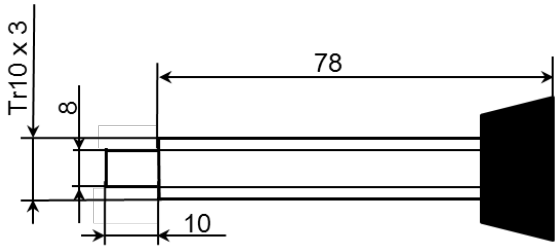

(c) *Clamping screw with trapezoidal thread*

Figure C.1: *Clamping device part and dimension in (mm)*

BIBLIOGRAPHY

[1] P. I. Anderson, A. J. Moses, and H. J. Stanbury. An automated system for the measurement of magnetostriction in electrical steel sheet under applied stress. *Journal of Magnetism and Magnetic Materials*, 215:714–716, 2000.

[2] P. I. Anderson, A. J. Moses, and H. J. Stanbury. Assessment of the stress sensitivity of magnetostriction in grain-oriented silicon steel. *IEEE Transactions on Magnetics*, 43(8):3467–3476, aug 2007.

[3] E. Antonelli, E. Cardelli, and A. Faba. Epstein Frame : How and When It Can Be Really Representative About the Magnetic Behavior of Laminated Magnetic Steels. *IEEE Transactions on Magnetics*, 41(5):1516–1519, 2005.

[4] U. Aydin, P. Rasilo, F. Martin, D. Singh, L. Daniel, A. Belahcen, M. Rekik, O. Hubert, R. Kouhia, and A. Arkkio. Magneto-mechanical modeling of electrical steel sheets. *Journal of Magnetism and Magnetic Materials*, 439:82–90, 2017.

[5] O. Barre. *Contribution à l'étude des formulations de calcul de la force magnétique en magnétostatique, approche numérique et validation expérimentale*. PhD thesis, 2004.

[6] C. F. Beards and J. L. Williams. The damping of structural vibration by rotational slip in joints. *Journal of Sound and Vibration*, 53(3):333–340, 1977.

[7] A. Belahcen. Vibrations of Rotating Electrical Machines Due to Magnetomechanical Coupling and Magnetostriction. *IEEE Transactions on Magnetics*, 42(4):971–974, 2006.

[8] A. Bergqvist and G. Engdahl. A Stress-dependent Magnetic Preisach Hysteresis Model. *IEEE Transactions on MagneticsIEEE*, 27(6):4796–4798, 1991.

[9] G. Bertotti. Dynamic Generalization of the Scalar Preisach Model of Hysteresis. *IEEE Transactions on Magnetics*, 28(5):2599–2601, 1992.

[10] A. Bossavit. Eddy-currents and forces in deformable conductors. *Mechanical Modelling of New Electromagnetic Materials*, 24:235–242, 1990.

[11] K. Bouayed, L. Mebarek, V. Lanfranchi, J. D. Chazot, R. Marechal, and M. A. Hamdi. Noise and vibration of a power transformer under an electrical excitation. *Applied Acoustics*, 128:64–70, 2017.

[12] L. Bouzek and R. Pechanek. Vibration behaviour of the asynchronous machine magnetic core. In *2013 15th European Conference on Power Electronics and Applications, EPE, 2013 15th European Conference on. IEEE*, volume i, pages 1–7, 2013.

[13] R. M. Bozorth. *Ferromagnetism*. Wiley-VCH, 1978.

[14] R. M. Bozorth and H. J. Williams. Effect of small stresses on magnetic properties. *Review of Modern Physics*, 17(1):72, 1945.

[15] N. Buiron, L. Hirsinger, and R. Billardon. A micro-macro model for magnetostriction and stress effect on magnetisation. *Journal of Magnetism and Magnetic Materials*, 197:868–870, 1999.

[16] M. Cazenave. *Méthode des éléments finis: Approche pratique en mécanique des structures.* Dunod, 2013.

[17] S. Chikazumi. *Physics of Ferromagnetism*. Oxford University Press on Demand., 1997.

[18] S. Chikazumi and C. D. Graham. *Physics of Ferromagnetism*. Oxford University Press on Demand, 2009.

[19] B. Cornut, A. Kedous-Lebouc, and Th. Waeckerlé. From metallurgy to modelling of electrical steels: A multiple approach to their behaviour and use based on physics and experimental investigations. *Journal of Magnetism and Magnetic Materials*, 160:102–108, 1996.

[20] D. J. Craik and M. J. Wood. Magnetization changes induced by stress in a constant applied field. *Journal of Applied Physics*, 3(7):1009, 1970.

[21] J. Craveur. *Modélisation par éléments finis-3e éd.: Cours et exercices corrigés*. Dunod, 2008.

[22] B. D. Cullity. Introduction to Magnetic Materials. pages 383–425. Addison-Alesley Series in Metallurgy and Materials, 1972.

[23] B. D. Cullity and C. D. Graham. *Introduction to magnetic materials*. John wiley edition, 2011.

[24] L. Daniel and O. Hubert. An analytical model for the ΔE effect in magnetic materials. *The European Physical Journal Applied Physics*, 45(3):31101, 2009.

[25] L. Daniel and O. Hubert. An equivalent stress for the influence of multiaxial stress on the magnetic behavior. *Journal of Applied Physics*, 105(7):07A313, 2009.

[26] L. Daniel, O. Hubert, N. Buiron, and R. Billardon. Reversible magneto-elastic behavior: A multiscale approach. *Journal of the Mechanics and Physics of Solids*, 56(3):1018–1042, 2008.

[27] L. Daniel, O. Hubert, and B. Vieille. Multiscale strategy for the determination of magneto-elastic bahavior: Discussion and application to Ni-Zn ferrites. *International Journal of Applied Electromagnetics and Mechanics*, 25(1-4):31–36, 2007.

[28] L. Daniel, M. Rekik, and O. Hubert. A multiscale model for magneto-elastic behaviour including hysteresis effects. *Archive of Applied Mechanics*, 84(9-11):1307–1323, 2014.

[29] M. J. Dapino. On Magnetostrictive Materials and Their Use in Smart Material Transducer. *Structural Engineering and Mechanics Journal*, 17(3):1–28, 2002.

[30] F. Druesne, J. Hallal, P. Lardeur, and V. Lanfranchi. Modal stability procedure applied to variability in vibration from electromagnetic origin for an electric motor. *Finite Elements in Analysis and Design*, 122:61–74, dec 2016.

[31] E. Du Trémolet de Lacheisserie. *Magnetostriction: theory and applications of magnetoelasticity*. CRC press, 1993.

[32] N. B. Ekreem, A. G. Olabi, T. Prescott, A. Rafferty, and M. S. J. Hashmi. An overview of magnetostriction, its use and methods to measure these properties. *Journal of Materials Processing Technology*, 191(1-3):96–101, 2007.

[33] M. Emura, F. J. G. Landgraf, W. Ross, and J. R. Barreta. The influence of cutting technique on the magnetic properties of electrical steels. *Journal of Magnetism and Magnetic Materials*, 255:358–360, 2003.

[34] M. Fall. *Mesure et modélisation multiéchelle du comportement thermo-magnéto-mécanique des alliages à mémoire de forme*. PhD thesis, Paris-Saclay University, 2017.

[35] F. Fiorillo. Mesures magnétiques - Mesurage des propriétés magnétiques des matériaux Mesures magnétiques Mesurage des propriétés magnétiques des matériaux. *Techniques de l'ingénieur*, 33(0), 2009.

[36] A. J. Fleming. A review of nanometer resolution position sensors: Operation and performance. *Sensors and Actuators, A: Physical*, 190(December):106–126, 2013.

[37] K. Fonteyn. *Energy-Based Magneto-Mechanical Model for electrical steel sheet*. PhD thesis, Aalto University, 2010.

[38] K. Fonteyn, A. Belahcen, R. Kouhia, P. Rasilo, and A. Arkkio. FEM for Directly Coupled Magneto-Mechanical Phenomena in Electrical Machines. *IEEE Transactions on Magnetics*, 46(8):2923–2926, 2010.

[39] N. Galopin. *Modélisation et caractérisation de matériaux actifs pour la conception de dispositifs magnéto-électriques*. PhD thesis, Université Paris-Sud 11, 2007.

[40] N. Galopin, K. Azoum, M. Besbes, F. Bouillault, L. Daniel, O. Hubert, and F. Alves. Caractérisation et modélisation des déformations induites par les forces magnétiques et par la magnétostriction. *Revue internationale de génie électrique*, 9(4):499–514, 2006.

[41] O. Geoffroy. Propriétés techniques des matériaux magnétiques Propriétés techniques des matériaux magnétiques. *Techniques de l'ingénieur*, 33(0), 2008.

[42] S. G. Ghalamestani. *Magnetostriction in electrical steel : numerical modelling and development of an optical measurement method*. PhD thesis, Ghent University, 2014.

[43] S. G. Ghalamestani, T. G. D. Hilgert, L. Vandevelde, J. J. J. Dirckx, and J. A. A. Melkebeek. Magnetostriction measurement by using dual heterodyne laser interferometers. *IEEE Transactions on Magnetics*, 46(2):505–508, 2010.

[44] J. Hallal. *Etudes des vibrations d'origine électromagnétique d'une machine électrique: conception optimisée et variabilité du comportement vibratoire*. PhD thesis, Université de Technologie de Compiègne, 2014.

[45] P. Hartemann. *Effets et matériaux magnétostrictifs*. Ed. Techniques ingénieur, 1999.

[46] T. Hilgert, L. Vandevelde, and J. Melkebeek. Comparison of magnetostriction models for use in calculations of vibrations in magnetic cores. *IEEE Transactions on Magnetics*, 44(6):874–877, 2008.

[47] A. Hubert and R. Schäfer. *Magnetic Domains: the Analysis of Magnetic Microstrutures*. Springer Science & Business Media, 1998.

[48] O. Hubert and L. Daniel. Effect of plastic straining on magnetostriction of ferromagnetic polycrystals — experiments and multiscale modeling. *Journal of Magnetism and Magnetic Materials*, 304:489–491, 2006.

[49] O. Hubert and L. Daniel. Multiscale modeling of the magneto-mechanical behavior of grain-oriented silicon steels. *Journal of Magnetism and Magnetic Materials*, 320(7):1412–1422, 2008.

[50] O. Hubert, L. Daniel, and R. Billardon. Experimental analysis of the magnetoelastic anisotropy of a non-oriented silicon iron alloy. *Journal of Magnetism and Magnetic Materials*, 254-255:352–354, 2003.

[51] O. Hubert, R. Waberi, S. Lazreg, H. S. Kim, and R. Billardon. Measurement And Two-Scales Modeling Of The E Effect. In *7th EUROMECH Solid Mechanics Conference*, 2009.

[52] A. Ilo, H. Pfützner, and T. Nakata. Critical induction - a key quantity for the optimisation of transformer core operation. *Journal of Magnetism and Magnetic Materials*, 215:637–640, 2000.

[53] M. Javorski. A Generalized Magnetostrictive-Forces Approach to the Computation of the Magnetostriction-Induced Vibration of Laminated Steel Structures. *IEEE Transactions on Magnetics*, 49(11):5446–5453, 2013.

[54] D. C. Jiles and D. L. Atherton. Theory of ferromagnetic hysteresis. *Journal of Magnetism and Magnetic Materials*, 61(1-2):48–60, 1986.

[55] D. C. Jiles and M. K. Devine. The law of approach as a means of modelling the magnetomechanical effect. *Journal of Magnetism and Magnetic Materials*, 144:1881–1882, 1995.

[56] D. C. Jiles, J. B. Thoelke, and M. K. Devine. Numerical Determination of Hysteresis Parameters for the Modeling of Magnetic Properties Using the Theory of Ferromagnetic Hysteresis. *IEEE Transactions on Magnetics*, 28(1):27–35, 1992.

[57] J. P. Joule. *On a new class of magnetic forces*. Ann. Elect. Magn. Chem, 1842.

[58] Y. Kai, Y. Tsuchida, T. Todaka, and M. Enokizono. Influence of stress on vector magnetic property under rotating magnetic flux conditions. In *IEEE Transactions on Magnetics*, volume 48, pages 1421–1424, 2012.

[59] F. Kako, T. Tsuruta, K. Nagaishi, and H. Kohmo. Experimental study on magnetic noise of large induction motors. *IEEE Transactions on Power Apparatus and Systems*, (8):2805–2810, 1983.

[60] K. Kamimoto, F. Ishibashi, S. Noda, S. Yanase, and T. Sasaki. Magnetostriction and motor vibration. *Electrical Engineering in Japan (English translation of Denki Gakkai Ronbunshi)*, 148(2):8–13, 2004.

[61] S. O. Kasap. *Principales of electronic materials and devices*. New York: McGraw-Hill, 2006.

[62] A. Kedous-Lebouc, B. Cornut, J.C. Perrier, Ph. Manfé, and Th. Chevalier. Punching influence on magnetic properties of the stator teeth of an induction motor. *Journal of Magnetism and Magnetic Materials*, 255:124–126, 2003.

[63] A. Kedous-Lebouc, O. Messal, and A. Youmssi. Joint punching and frequency effects on practical magnetic characteristics of electrical steels for high-speed machines. *Journal of Magnetism and Magnetic Materials*, 426(November 2016):658–665, 2017.

[64] Y. Y. Kim and Y. E. Kwon. Review of magnetostrictive patch transducers and applications in ultrasonic nondestructive testing of waveguides. *Ultrasonics*, 62:3–19, 2015.

[65] H. Krönmuller and M. Fähnle. *Micromagnetism and the microstructure of ferromagnetism solids*. Max-Plank-institut für Metallforschung, 1994.

[66] L. Lâftman. Magnetostriction and its contribution to noise in a PWM inverter fed induction machine. *Le journal de physique IV*, 8(PR2):567–570, 1998.

[67] O. Lahyaoui, V. Lanfranchi, N Buiron, J. D. Chazot, and C. Langlois. Investigation on Mechanical Resonance Induced by Magnetostriction in a Structure Based on Si-Fe Sheets. *IEEE Transactions on Magnetics*, 54(12):1–12, 2018.

[68] O. Lahyaoui, V. Lanfranchi, S. S. Mbengue, and N. Buiron. Macroscopic model of magnetostriction based on energy minimization. *2016 11th France-Japan and 9th Europe-Asia Congress on Mechatronics, MECATRONICS 2016 / 17th International Conference on Research and Education in Mechatronics, REM 2016*, (1):230–235, 2016.

[69] M. Liu. *Optimization of electromagnetic and acoustic performances of power transformers*. PhD thesis, Université Paris-Sud, 2017.

[70] M. Liu, O. Hubert, X. Mininger, F. Bouillault, and L. Bernard. Homogenized Magnetoelastic Behavior Model for the Computation of Strain Due to Magnetostriction in Transformers. *IEEE Transactions on Magnetics*, 52(2):1–12, 2016.

[71] M. Liu, O. Hubert, X. Mininger, F. Bouillault, L. Bernard, and T. Waeckerlé. Reduction of Power Transformer Core Noise Generation Due to Magnetostriction-Induced Deformations Using Fully Coupled Finite-Element Modeling Optimization Procedures. *IEEE Transactions on Magnetics*, 53(8):1–11, 2017.

[72] P. Marketos, S. Zurek, and A. J. Moses. Calculation of the mean path length of the Epstein frame under non-sinusoidal excitations using the double Epstein method. *Journal of Magnetism and Magnetic Materials*, 320(20):2542–2545, 2008.

[73] R. S. Masti, W. Desmet, and W. Heylen. On the influence of core laminations upon power transformer noise. In *Proceedings of ISMA*, pages 3851–3861, 2004.

[74] F. S. Mballa Mballa. *Modélisation du comportement magnéto-mécanique d'un acier Dual Phase à partir de sa description microstructurale*. PhD thesis, ENS Cachan, 2013.

[75] S. S. Mbengue. *Étude des déformations induites par l'aimantation des dispositifs électrotechniques: développement d'un modèle magnéto-élastique macroscopique*. PhD thesis, Université de Technologie de Compiègne, 2016.

[76] S. S. Mbengue, N. Buiron, and V. Lanfranchi. An Anisotropic Model for Magnetostriction and Magnetization Computing for Noise Generation in Electric Devices. *Sensors*, 16(4):553, 2016.

[77] S. S. Mbengue, N. Buiron, and V. Lanfranchi. Macroscopic modeling of anisotropic magnetostriction and magnetization in soft ferromagnetic materials, 2016.

[78] X. Mininger, N. Galopin, F. Bouillault, and M Gabsi. Analysis of electromagnetic strains on a structure such as switched reluctance machine. *The European Physical Journal-Applied Physics*, 39(2):191–196, 2007.

[79] M. Mizokami and Y. Kurosaki. Noise variation by compressive stress on the model core of power transformers. *Journal of Magnetism and Magnetic Materials*, 381:208–214, 2015.

[80] O. A Mohammed, T. Calvert, and R. McConnell. Coupled Magnetoelastic Finite Element Formulation Including Anisotropic Reluctivity Tensor and Magnetostriction Effects for Machinery Applications. *IEEE Transactions on Magnetics*, 37(5):3388–3392, 2001.

[81] O. A. Mohammed, T. E. Calvert, L. Petersen, and R. Mcconnell. Transient Modeling of Coupled Magnetoelastic Problems in Electric Machines. *IEEE Transactions on Magnetics*, 1:281–287, 2002.

[82] A. J. Moses. Measurement of magnetostriction and vibration with regard to transformer noise. *IEEE Transactions on Magnetics*, 10(2):154–156, 1974.

[83] A. J. Moses. Energy efficient electrical steels : Magnetic performance prediction and optimization. *Scripta Materialia*, 67(6):560–565, 2012.

[84] A. J. Moses, P. I. Anderson, T. Phophongviwat, and S. Tabrizi. Contribution of magnetostriction to transformer noise. In *Universities Power Engineering Conference (UPEC), 2010 45th International.IEEE*, pages 1–5, 2010.

[85] A. J. Moses, P. I. Anderson, and S. Somkun. Modeling 2-d magnetostriction in nonoriented electrical steels using a simple magnetic domain model. *IEEE Transactions on Magnetics*, 51(5):1, 2015.

[86] A. J. Moses, A. Ntatsis, T. Kochmann, and J. Schneider. Magnetostriction in nonoriented electrical steels: general trends. *Journal of Magnetism and Magnetic Materials*, 215:669–672, 2000.

[87] T. Nakata, N. Takahashi, M. Nakano, K. Muramatsu, and P. Miyake. Magnetostriction measurements with a laser Doppler velocimeter. *IEEE Transactions on Magnetics*, 30(6):4563–4565, 1994.

[88] A. G. Olabi and A. Grunwald. Design and application of magnetostrictive materials. *Materials and Design*, 29(2):469–483, 2008.

[89] P. Pellerey and V. Lanfranchi. Coupled numerical simulation between electromagnetic and structural models. Influence of the supply harmonics for synchronous machine vibrations. *IEEE Transactions on Magnetics*, 48(2):983–986, 2012.

[90] R. Penin, J. P. Lecointe, G. Parent, J. F. Brudny, and T. Belgrand. Grain Oriented Steel Rings for an Experimental Comparison of Relative Magnetostriction and Maxwell's Forces Effects. *IEEE Transactions on Industrial Electronics*, 61(8):1–8, 2013.

[91] R. Penin, G. Parent, J. P. Lecointe, J. F. Brudny, and T. Belgrand. Impact of mechanical deformations of transformer corners on core losses. *IEEE Transactions on Magnetics*, 51(4):5–9, 2015.

[92] O. Perevertov. Influence of the applied elastic tensile and compressive stress on the hysteresis curves of Fe-3%Si non-oriented steel. *Journal of Magnetism and Magnetic Materials*, 428:223–228, 2017.

[93] O. Perevertov, J. Thielsch, and R. Schäfer. Effect of applied tensile stress on the hysteresis curve and magnetic domain structure of grain-oriented transverse Fe-3%Si steel. *Journal of Magnetism and Magnetic Materials*, 385:358–367, 2015.

[94] T. Phophongviwat. *Investigation of the Influence of Magnetostriction and Magnetic Forces on Transformer Core Noise and Vibration*. PhD thesis, Cardiff University, 2013.

[95] T. P. P. Phway and A. J. Moses. Magnetisation-induced mechanical resonance in electrical steels. *Journal of Magnetism and Magnetic Materials*, 316(2 SPEC. ISS.):468–471, 2007.

[96] F. Preisach. Über die magnetische Nachwirküng. *Zeitschrift für Physik A Hadrons and Nuclei*, 94(5):277–302, 1935.

[97] A. Rafferty, S. Bakir, D. Brabazon, and T. Prescott. Calibration and characterisation with a new laser-based magnetostriction measurement system. *Materials and Design*, 30(5):1680–1684, 2009.

[98] M. Rekik. *Mesure et modélisation du comportement magnéto-mécanique dissipatif des matériaux ferromagnétiques à haute limite élastique souschargement multiaxial: application aux génératrices à grandes vitesses pour l'aéronautique*. PhD thesis, ENS Cachan, 2014.

[99] Z. Ren and A. Razek. Local Force Computation in Deformable Bodies using Edge Elements. *IEEE Transactions on Magnetics*, 28(2):1212–1215, 1992.

[100] M. Rossi and J. Le Besnerais. Vibration Reduction of Inductors under Magnetostrictive and Maxwell Forces Excitation. *IEEE Transactions on Magnetics*, 51(12):8403406, 2015.

[101] M. J. Sablik, H. Kwun, G. L. Burkhardt, and D. C. Jiles. Model for the effect of tensile and compressive stress on ferromagnetic hysteresis. *Journal of Applied Physics*, 61(8):3799–3801, 1987.

[102] J. Šarloši and J. Bocko. Effective Material Moduli for Composites. 4(7):289–292, 2016.

[103] S. Sathyan, A. Belahcen, J. Kataja, F. Henrotte, A. Benabou, and Y. Le Menach. Computation of Magnetic Forces Using Degenerated Air-Gap Element. *IEEE Transactions on Magnetics*, 53(6):3–6, 2017.

[104] J. W. Shilling and G. L. Houze. Magnetic Properties and Domain Structure in Grain-Oriented 3% Si-Fe. *IEEE Transactions on Magnetics*, 10(2):195–223, 1974.

[105] G. Shilyashki, H. Pfützner, P. Hamberger, M. Aigner, A. Kenov, and I. Matkovic. Spatial distributions of magnetostriction, displacements and noise generation of model transformer cores. *International Journal of Mechanical Sciences*, 118(September):188–194, 2016.

[106] D. Singh. *Effect of stress on magnetic properties of electrical steel sheet and core losses in electrical machines*. PhD thesis, Aalto University, 2017.

[107] R. Smith. *Smart material systems: model development*. Society for Industrial and Applied Mathematics, 2005.

[108] S. Somkun, A. J . Moses, and P. I. Anderson. Mechanical resonance in nonoriented electrical steels induced by magnetostriction under PWM voltage excitation. In *IEEE Transactions on Magnetics*, volume 44, pages 4062–4065, 2008.

[109] S. A Spornic, A. Kedous-Lebouc, and B. Cornut. Anisotropy and texture infuence on 2D magnetic behaviour for silicon, cobalt and nickel iron alloys. *Journal of Magnetism and Magnetic Materials*, 215-216:614–616, 2000.

[110] H. J. Stanbury. *Magnetostriction effects at angles to the rolling direction in grain oriented silicon steel*. PhD thesis, University college Cardiff, 1984.

[111] A. Tan-kim. *Contribution à l'étude du bruit acoustique d'origine magnétique en vue de la conception optimale de machines synchrones à griffes pour application automobile*. PhD thesis, Université de Technologie de Compiègne, 2015.

[112] E. Trémolet de Lacheisserie. Relations entre les coefficients d'anisotropie et de couplage magnétoélastique dans les cristaux cubiques et hexagonaux. *Journal de Physique*, 29(11-12):1066–1074, 1968.

[113] E. Trémolet de Lacheisserie. *MAGNETISME 1, Fondements*. EDP Sciences, cnrs edition, 1999.

[114] L. Vandevelde, J. Gyselinck, M. A. C. De Wulf, and J. A. A. Melkebeek. Finite-Element Computation of the Deformation of Ferromagnetic Material Taking Into Account Magnetic Forces and Magnetostriction. *IEEE Transactions on Magnetics*, 40(2):565–568, 2004.

[115] B. Vieille. *Modélisation de l'effet des contraintes sur le comportement magnétique des ferrites*. PhD thesis, ENS Cachan, 2012.

[116] H. Wang and K. Williams. Effects of Laminations on the Vibrational Behaviour of Electrical Machine Stators. *Journal of Sound and Vibration*, 202(5):703–715, 1997.

[117] B. Weiser, A. Hasenzagl, T. Booth, and H. Pfützner. Mechanisms of noise generation of model transformer cores. *Journal of Magnetism and Magnetic Materials*, 160:207–209, 1996.

[118] B. Weiser, H. Pfützner, and J. Anger. Relevance of magnetostriction and forces for the generation of audible noise of transformer cores. *IEEE Transactions on Magnetics*, 36(5):3759–3777, 2000.

[119] P. Weiss. L'hypothèse du champ moléculaire et la propriété ferromagnétique. *Journal de Physique Théorique et Appliquée*, 6(1):661–690, 1907.

[120] B. Wiele. *Numerical Study of Magnetic Processes: Extending the Landau-Lifshitz-Gilbert Approach from Nanoscale to Microscale*. PhD thesis, Ghent University, 2010.

[121] E.P. Wohlfarth. *Ferromagnetic Materials*. North-Holland, 1980.

[122] H. H. Woodson and J. R. Melsher. *Electromechanical Dynamics: Part I (Discrete Systems) and Part II (Fields, Forces, and Motion)*. John Wiley and Sons, 1968.

[123] X. G. Yao, T. Phway, A. J. Moses, and F. Anayi. Magneto-Mechanical Resonance in a Model 3-Phase 3-Limb Transformer Core Under Sinusoidal and PWM Voltage Excitation. *IEEE Transactions on Magnetics*, 44(11):4111–4114, nov 2008.